UNIVERSITÉ DE GENÈVE

Archive ouverte UNIGE

https://archive-ouverte.unige.ch

Thèse 2014

Open Access

This version of the publication is provided by the author(s) and made available in accordance with the copyright holder(s).

Nuclei identification with the AMS-02 silicon tracker and measurement of cosmic ray nuclei fluxes

Saouter, Pierre

How to cite

SAOUTER, Pierre. Nuclei identification with the AMS-02 silicon tracker and measurement of cosmic ray nuclei fluxes. Doctoral Thesis, 2014. doi: 10.13097/archive-ouverte/unige:40681

This publication URL: https://archive-ouverte.unige.ch/unige:40681

Publication DOI: 10.13097/archive-ouverte/unige:40681

© This document is protected by copyright. Please refer to copyright holder(s) for terms of use.

UNIVERSITÉ DE GENÈVE
Section de Physique
Département de Physique Nucléaire et Corpusculaire

FACULTÉ DES SCIENCES
Professeur Martin Pohl

Nuclei Identification with the AMS-02 Silicon Tracker and Measurement of Cosmic Ray Nuclei Fluxes

THÈSE

présentée à la Faculté des Sciences de l'Université de Genève
pour obtenir le grade de Docteur ès sciences, mention Physique

par
Pierre Erwan SAOUTER
de
Bordeaux, France

Thèse N° 4706

GENÈVE
Atelier d'impression ReproMail
2014

UNIVERSITÉ DE GENÈVE

FACULTÉ DES SCIENCES

Doctorat ès sciences
Mention physique

Thèse de *Monsieur Pierre Erwan SAOUTER*

intitulée :

"Nuclei Identification with the AMS-02 Silicon Tracker and Measurement of Cosmic Ray Nuclei Fluxes"

La Faculté des sciences, sur le préavis de Monsieur M. POHL, professeur ordinaire et directeur de thèse (Département de physique nucléaire et corpusculaire), Monsieur M. BOURQUIN, professeur honoraire (Département de physique nucléaire et corpusculaire), Monsieur D. RAPIN, professeur (Département de physique nucléaire et corpusculaire), Monsieur L. DEROME, docteur (Laboratoire de physique subatomique et de cosmologie, Institut National Polytechnique, Université de Grenoble, France) et A. OLIVA, docteur (Centro de Investigaciones Energéticas, Medioambientales y Tecnológicas, Madrid, España), autorise l'impression de la présente thèse, sans exprimer d'opinion sur les propositions qui y sont énoncées.

Genève, le 27 août 2014

Thèse - 4706 -

Le Décanat

N.B. - La thèse doit porter la déclaration précédente et remplir les conditions énumérées dans les "Informations relatives aux thèses de doctorat à l'Université de Genève".

Résumé en Français

Depuis leur découverte au début du $20^{\text{ème}}$ siècle, les rayons cosmiques, ou astro-particules, continuent de poser, inlassablement, la question de leur origine. Divers modèles astrophysiques ont été avancés pour tenter de fournir une compréhension globale des mécanismes de production, d'accélération et de propagation de ces particules dans notre Galaxie. Bien que, depuis quelques années, un nombre croissant d'évidences expérimentales identifie les restes de supernova, résidus de violentes explosions d'étoiles, comme la source la plus probable des rayons cosmiques, aucune preuve décisive de ce scénario n'a pu être apportée. Dans une large mesure, les modèles théoriques sont validés dans leur capacité à reproduire les données de rayons cosmiques observées sur terre. Réciproquement, les observations permettent de contraindre les paramètres des modèles et de réduire certaines sources d'incertitudes. En ce sens, des mesures expérimentales systématiquement plus précises permettent d'établir des contraintes autrement plus efficaces sur les modèles.

L'expérience AMS-02 s'inscrit dans cette volonté de surpasser les expériences existantes en termes de qualité et de précision des mesures réalisées. AMS signifie "Alpha Magnetic Spectrometer", ou spectromètre magnétique de Alpha en français, Alpha étant l'ancien nom de la Station Spatiale Internationale (ISS). Il s'agit d'un des détecteurs les plus complexes envoyés dans l'espace et dont la conception fut en grande partie guidée par les progrès technologiques réalisés sur les grands accélérateurs de particules. Associé aux conditions uniques de détection des rayons cosmiques primaires dans l'espace et avec une durée opérationnelle estimée à plus de 10 ans, AMS-02 pourra mesurer avec une très grande précision les spectres des différentes particules cosmiques dans un intervalle d'énergie allant de quelques centaines de MeV à plusieurs TeV. Muni de son puissant aimant permanent, AMS-02 peut aussi distinguer la matière de l'antimatière avec une sensibilité surpassant de 3 ordres de grandeur les précédentes recherches expérimentales dans l'espace. La détection d'un seul noyau d'anti-carbone constituerait une évidence presque irréfutable de l'existence, quelque part dans l'univers, d'anti-étoiles.

Le succès d'une mission aussi complexe, illustré par déjà 3 années de collecte de données dans l'espace et l'analyse de dizaines de milliards d'événements cosmiques, est la récompense de l'effort continu de centaines de scientifiques, chercheurs, ingénieurs et techniciens, pendant plus de dix-huit ans. La collaboration a vu se succéder deux générations de chercheurs post-doctorants et bientôt quatre générations d'étudiants. La construction du détecteur fut jalonnée d'étapes diverses, de succès mais aussi de déceptions, en partie liées aux liens complexes qu'entretient un projet de telle envergure avec les ressorts politiques et financiers internationaux. Malgré les périodes de doute, les collaborateurs, issus de 16 pays à travers le monde, n'ont admis aucun compromis dans la construction du détecteur.

Une thèse réalisée en 5 ans donne l'opportunité d'aborder le travail de physicien expérimental de bien des manières. J'ai commencé avec un séjour en Hollande, au Centre Européen de

Recherche et Technologie Spatiale (ESTEC), où AMS-02 fut soumis à des tests de vibrations mécaniques et d'excursions thermiques visant à simuler les conditions extrêmes attendues lors du décollage de la navette et pendant l'opération du détecteur en orbite. Les résultats de l'ESTEC et l'annonce par le Sénat américain de l'extension de son programme spatial justifièrent un détour technique d'envergure pour le détecteur : remplacer son aimant supra-conducteur par l'aimant permanent utilisé lors du vol précurseur d'AMS-01. Ainsi, j'ai participé activement à la qualification des échelles au silicium et au nouveau câblage du détecteur initié par le changement de configuration de l'aimant. Il s'ensuivit plusieurs tests faisceaux au CERN pour la vérification du bon fonctionnement du nouveau modèle intégré d'AMS-02. En août 2010, AMS-02 fut transporté à bord d'un avion cargo de l'armée américaine vers la base de lancement du Kennedy Space Center (KSC), à Cape Canaveral en Floride. Jusqu'au 16 mai 2011, date de lancement de la mission STS-134, avec AMS à bord de la navette Endeavour, j'ai participé à plusieurs activations du détecteur depuis le KSC, visant à optimiser diverses procédures d'acquisition des données et les outils de contrôle pour la future opération du détecteur dans l'espace. J'ai également contribué à la documentation des protocoles de communication orale imposés par la NASA. AMS-02 fut installé sur l'ISS le 19 mai 2011. J'eus alors la chance de faire partie de l'équipe responsable de la première activation du détecteur sur l'ISS avec l'arrivée au sol des premières données scientifiques à peine une heure plus tard. Ce fut un moment riche d'émotions partagées avec les membres d'AMS-02 et les collaborateurs de la NASA. Pendant deux mois, nous nous succédâmes pour contrôler les opérations du détecteur depuis le Jonhson Space Center à Houston au Texas, tout en préparant la relève au CERN avec la création d'un centre de contrôle d'AMS-02, le POCC (Payload of Operation and Control Center). Jusqu'à la fin de ce travail de thèse, je continuerai à participer activement aux opérations du détecteur depuis le CERN.

Le travail de thèse présenté dans ce manuscrit est articulé autour d'un thème central, celui des noyaux cosmiques. Les noyaux sont identifiés dans AMS-02 par des mesures redondantes de leur charge électrique absolue $|Z|$, estimée à partir de la déposition d'énergie dans les divers détecteurs composant AMS-02. Le traceur au silicium (le tracker) est réparti en 9 plans à différentes positions verticales et fournit autant de mesures indépendantes de la charge Z. La mesure brute du tracker est affectée par un certain nombre d'effets, qu'ils soient physiques ou le résultat de bruit électronique, qui dégradent la mesure de la charge. Un premier travail fut donc consacré au développement d'une procédure détaillée pour la calibration du tracker et l'optimisation de ses performances en termes d'identification des différents noyaux cosmiques. De la calibration résulte une excellente capacité d'identification jusqu'au silicium (Z=14). Au-delà de cette limite, la réponse du tracker se dégrade rapidement en raison de non-linéarité dans les courbes de réponse de l'électronique. L'excellente performance du tracker, combinée à la mesure de la rigidité par la reconstruction de la trajectoire des particules dans le détecteur, nous a naturellement conduit à une analyse des flux différentiels de noyaux cosmiques. Nous proposons dans ce travail une nouvelle méthode d'extraction des flux reposant sur la distribution de charge du tracker. Nous présentons les résultats préliminaires pour les flux de noyaux cosmiques allant du lithium (Z=3) jusqu'au neon (Z=10), dans un intervalle d'énergie allant de quelques GV à environ 1 TV.

Abstract

Since their discovery in the beginning of the 20^{th} century, cosmic rays, or astro-particles, still pose the fundamental question of their origin. Several astrophysical models have been put forward to attempt to provide a general understanding of the production, acceleration and propagation mechanisms of these particles in our Galaxy. Although there is growing evidence from the experimental data that supernovae remnants, residuals of violent explosions of stars, are the most likely source of cosmic rays, there as yet not been any conclusive proof to this scenario. To a large extent, the models are validated by their ability to reproduce the cosmic ray data observed at Earth. Reciprocally, the observations can help constrain parameters of the models, therefore reducing the impact of various sources of uncertainties. In this respect, new data of systematically higher precision helps constraining the models even more efficaciously.

The AMS-02 experiment aims at measuring cosmic rays with an un-precedented level of statistics. AMS stands for Alpha Magnetic Spectrometer, Alpha being the old name of the International Space Station. AMS-02 is one of the most complex detectors ever sent to space, the design of which is intimately related to the technological progresses made at particle accelerator experiments. Given the unique conditions of cosmic ray detection in space and the expected long duration of the mission (over 10 years), AMS-02 will measure with high precision the spectra of different cosmic ray species in an energy range from few hundreds of MeV to few TeV. Thanks to its powerful magnet, its large acceptance and long exposure time, AMS-02 will be capable of distinguishing matter from anti-matter with a sensitivity 3 orders of magnitude higher than previous experiments in space. The detection of a single cosmic anti-carbon nucleus would be almost a conclusive evidence for the existence, somewhere in the universe, of anti-stars.

The operational success of the mission, evident from 3 years of data taking and tens of billions of cosmic events analyzed, is the reward of the continuous effort of hundreds of scientists, researchers, engineers and technicians during 18 long years. The collaboration has seen the succession of 2 generations of post-doctoral researchers and almost 4 generations of students. The construction of the detector was punctuated by several steps, marked by successes but also disappointments, in part related to the complex connections such a big project maintains with international political and financial motivations. Despite strong moments of disillusion, the collaborators, coming from 16 different countries, have admitted no compromise in the detector's construction.

Five years of PhD gives the opportunity to grasp the work of an experimental physicist in many ways. I began with a journey to the Netherlands, at the European Space Technology Research Center (ESTEC) where AMS-02 experienced mechanical vibration and thermal excursion tests simulating the harsh conditions of the shuttle launch and operations of the detector on orbit. The results from ESTEC and the announcement from the american senate

of the extension of their space program, motivated a crucial technical detour for AMS-02 : the replacement of its super-conducting magnet by the permanent magnet used in the precursor flight of AMS-01. I was involved in the qualification tests of the new tracker silicon modules and the cabling of the detector initiated by the new tracker configuration. This work was followed by several test beams at the European Organization for Nuclear Research (CERN) to assess the proper functioning of the new integrated model of AMS-02. In august 2010, AMS was flown on-board a cargo plane of the american army to the launch site of the Kennedy Space Center (KSC) in Cape Canaveral, Florida. Until the 16^{th} may 2011, launch date of the STS-134 mission, I will participate in several activations of the detector on ground to optimize data acquisition procedures and detector monitoring tools for future operations of the detector in space. On the 19^{th} may 2011, AMS-02 was installed on the International Space Station, and I will join the team of cadres responsible for the first operation of AMS in space with the first scientific data received on ground few hours later, a truly emotional moment for all the co-workers present in the Nasa control room. During the following two months, we took over the operations of the detector from the Johnson Space Center in Houston, Texas, while preparing the certification of the main control center, the POCC (Payload of Operation and Control Center), in CERN, Switzerland. Until the end of my PhD, I have participated actively to the detector operations from the POCC.

The work presented in this thesis manuscript evolves around a central theme : nuclei cosmic rays. Nuclei are identified in AMS-02 by the redundant measurement of their absolute electric charge $|Z|$. The silicon tracker offers nine such independent measurements of the particle charge. The tracker response is naturally degraded by a number of effects. A first work was dedicated to the elaboration of a procedure to accurately calibrate the tracker response and optimize its performances in terms of nuclei identification. The results of the calibration show an excellent identification power for nuclei up to silicon ($Z = 14$). Above this limit, the tracker's response is degraded due ton non-linearities in the response of the electronics. The excellent performance of the tracker, combined to the measurement of the particle rigidity, naturally lead us to an analysis of the differential fluxes of cosmic ray nuclei. We propose a new method to extract nuclei fluxes based on the charge distribution of the tracker. We present preliminary results for the fluxes of nuclei from lithium ($Z = 3$) to neon ($Z = 10$), in a range of energy between few GeV up to about 1 TeV.

Remerciements

J'aimerais exprimer ma plus sincère gratitude au Professeur Martin Pohl, directeur de cette thèse. Durant ces cinq années de doctorat, son soutien et son expérience approfondie de la physique expérimentale m'ont été d'une précieuse aide. Ma reconnaissance va toutefois au-delà du travail présenté ici. Je connais le Professeur Pohl depuis plus de dix ans et je dois reconnaître qu'il fut l'un des professeurs les plus impliqués dans la cause estudiantine à l'Université de Genève. Son engagement pour rendre la physique accessible est particulièrement apprécié par les nouveaux étudiants. Enfin, lors de périodes plus difficiles que d'autres, son soutien et sa flexibilité furent pour moi d'un grand réconfort.

J'aimerais ensuite remercier les membres du jury pour avoir accepté d'évaluer ce travail. Leurs commentaires après la lecture de la première version de ce manuscrit m'ont permis d'en améliorer le contenu. Je les remercie par ailleurs pour l'ensemble des discussions particulièrement intéressantes tenues au sein de la collaboration d'AMS.

Mes sincères remerciements à Alberto Oliva, que je peux légitimement considérer comme le superviseur non-officiel d'une grande partie de mon travail. Sans lui, j'aurais certainement lutté longtemps avant de me faire une place dans la collaboration d'AMS, et je porte en grande estime notre proche collaboration. Je lui suis très reconnaissant de tout ce qu'il m'a appris.

Le groupe d'AMS Genève au sein du DPNC est plutôt restreint. J'ai commencé en étant le seul étudiant sous la supervision de quatre professeurs. La qualité des discussions qui en découla me furent certainement très profitables. Le Professeur Divic Rapin nous a toujours tous impressionnés par son infaillible mémoire et nous devons à jamais garder à l'esprit qu'il fut jadis appelé le *Dieu du câblage*. Il m'a inculqué une vision unique du raisonnement scientifique pour laquelle je le remercie sincèrement. Le groupe s'agrandit par la suite avec l'arrivée de Marion Habiby. Voisine au bureau, je la remercie pour avoir rendu la vie de tous les jours plus agréable. La même reconnaissance va à Silvio Orsi et Mercedes Paniccia. J'aimerais enfin remercier Maurice Bourquin et Catherine Leluc pour leur intérêt constant dans l'avancement de mon travail.

Je dois enfin rendre hommage à tous les membres de la collaboration AMS, sans lesquels ce magnifique projet scientifique n'aurait jamais pu voir le jour. Les longues heures de surveillance au Cern ont certainement donné un caractère plus humain à cette entreprise.

Il m'est arrivé d'ignorer, par égoïsme, ce que je dois à mes amis. Perdre l'un d'eux aide aussi à ouvrir les yeux. La vie est courte et je dois tellement plus à mes amis que ce que les mots peuvent exprimer. Gaetano, tu dois venir en premier. Merci pour l'aide que tu m'as apportée durant mon doctorat ; sans toi je serais probablement toujours en train d'essayer de lancer root sur windows. Tu as toujours été pour moi une source d'inspiration à bien des niveaux. Tu es l'artiste des couleurs de l'esprit, mon ami. Xavier, Nabil, je suis à la fois plus musclé et plus grand que vous deux ! Tâchons de garder toujours contact, malgré les chemins qui se séparent. Audrey, tu as certainement joué un grand rôle à faire de nous tous le groupe d'amis que nous sommes. Sans Saint-Luc, reconnaissons-le, nous aurions bien moins de souvenirs à partager. A Saint-Luc résonne aussi le nom de Matthieu. Très cher, vous êtes unique et si vous n'existiez pas, et bien, il faudrait vous créer. Tellement d'autres personnes pour lesquelles je manque de place pour un mot personnel : Léo, Elisabeth, Imam, Laurence, Denis et tous ce que j'oublie de citer. Merci à tous. Damien, tu es parti trop tôt mon ami, je ne t'oublierai jamais.

Quant à ma famille, et bien, d'un point vue pratique, je lui dois d'être là. Blague à part, je suis extrêmement reconnaissant à mes parents pour m'avoir appris l'ouverture d'esprit afin de me garder de juger trop hâtivement les autres et de m'avoir insufflé la curiosité de découvrir le monde. J'admire ma soeur pour la vie "exotique" qu'elle mène et je souhaite la bienvenue à bébé Samir parmi nous.

A quoi ressemble la vie avec un étudiant en physique ? Ne le demandez pas à son conjoint, vous risqueriez d'avoir un point de vue totalement biaisé. Ou peut-être serait-ce seulement l'expression de la vérité... On ne réalise pas toujours tout ce que l'on doit à notre moitié, et combien on peut lui rendre la vie difficile. Je ne pourrai jamais être suffisamment reconnaissant. Merci d'être là pour moi Elodie. Je t'aime.

Acknowledgements

I must make a brief account, in english, of my previous acknowledgment section to make sure the credits are appreciated by all those concerned, included does who do not speak french.

My deepest gratitude goes first of all to Professor Martin Pohl, the director of this thesis. His guidance throughout these five years and his deep expertise in experimental physics has really helped me gain a valuable experience in the field of cosmic ray physics. My recognition goes however beyond the accomplishment of this thesis. I have known Prof. Pohl for over 10 years now and he has certainly been one of the Physics faculty collaborators most committed to the cause of students, in particular in making physics accessible to poorly trained minds. Also, in times of troubles, his support and flexibility was of precious comfort.

I would like to thank the members of the jury for accepting to evaluate this work. The feed-back from their careful reading of the manuscript was certainly most profitable to me, in particular to improve the final version. I am also thankful for all the precious discussions within the AMS collaboration.

My most sincere acknowledgments go to Alberto Oliva, whom I could easily consider as the unofficial supervisor for a large part of my work. Without him, I would have certainly struggled a long time before finding my place inside the collaboration and I value a lot the close collaboration we entertained. I am extremely thankful for all he has taught me.

The AMS Geneva group at DPNC is rather small. I started being the only student working under the supervision of four Professors. The resulting high quality group discussions was certainly very profitable to me. Divic Rapin has always impressed all of us with his infallible memory and we shall always keep in mind he was once called the *God of Cabling.* He has brought me a very unique way of looking at physics and I warmly thank him for that. The group later gain some working force with the arrival of Marion Habiby. Being neighbors in the office, I thank her for making the everyday life more pleasant. The same recognition goes to Silvio Orsi and Mercedes Paniccia. I also would like to thank Maurice Bourquin and Catherine Leluc for their constant interest in the advancement of my work.

Table of Contents

1 Introduction **15**
- 1.1 A Brief History of Cosmic Rays 15
- 1.2 Experimental Observations 17
- 1.3 Modern Detection Methods 18
  - 1.3.1 Balloon Flights 19
  - 1.3.2 Satellite Experiments 20
  - 1.3.3 Ground-based Detectors 22
- 1.4 Recent Experimental Results 23
  - 1.4.1 Antimatter Searches 24
  - 1.4.2 The Positron Excess 24
  - 1.4.3 Discrepant Hardening Observed in Cosmic-ray Spectra 25
- 1.5 Structure of the Thesis 27

2 Cosmic Ray Phenomenology **29**
- 2.1 Interpretation of the Energy Spectrum 29
  - 2.1.1 Cosmic Rays up to the Knee 30
  - 2.1.2 Around the first Knee 31
  - 2.1.3 From the first Knee to the Ankle 31
  - 2.1.4 Ultra-high Energy Cosmic Rays and the GZK Cut-off 32
  - 2.1.5 Anisotropy Searches 33
- 2.2 Composition below the Knee 34
  - 2.2.1 Nuclei Relative Abundances 35
  - 2.2.2 Refractory Elements and Neon 22 36
  - 2.2.3 Other Interesting Particles 37
- 2.3 Origin : the SNR Paradigm 37
  - 2.3.1 Basic Facts 37
  - 2.3.2 Diffusive Acceleration 38
  - 2.3.3 Experimental Evidence 40
  - 2.3.4 Other Astrophysical Objects 40
- 2.4 Cosmic Ray Propagation 42
  - 2.4.1 Propagation Models 42
  - 2.4.2 Constraints from Observations and Secondary to Primary Ratios 43
  - 2.4.3 Modeling the Galactic Diffuse Gamma Ray Emission 45

3 The Alpha Magnetic Spectrometer 51
- 3.1 The AMS-02 Detector . . . 51
  - 3.1.1 The Permanent Magnet . . . 52
  - 3.1.2 The Silicon Tracker . . . 53
  - 3.1.3 The Time-of-Flight system . . . 54
  - 3.1.4 The Transition Radiation Detector . . . 55
  - 3.1.5 The Rich Imaging Čerenkov Counters . . . 56
  - 3.1.6 The Electro Magnetic Calorimeter . . . 57
  - 3.1.7 The Anti-Coincidence Counters . . . 58
  - 3.1.8 The Star Tracker and the Global Positioning System . . . 59
  - 3.1.9 Electronics . . . 60
  - 3.1.10 The Trigger Logic . . . 61
  - 3.1.11 The Data Acquisition System . . . 63
- 3.2 AMS on the International Space Station . . . 64
  - 3.2.1 AMS on ISS . . . 65
  - 3.2.2 Thermal Environment and Thermal Control . . . 67
  - 3.2.3 The Data Flow from ISS . . . 67
  - 3.2.4 AMS Payload Operation Control Center . . . 68

4 The Silicon Tracker 71
- 4.1 Silicon Sensors . . . 71
- 4.2 Front-end Electronics and Signal Digitization . . . 72
- 4.3 The Ladder Design and Tracker Structure . . . 72
  - 4.3.1 Ladders . . . 72
  - 4.3.2 Tracker Layers . . . 73
  - 4.3.3 K5 and K7 Routing Schemes . . . 74
  - 4.3.4 Ladder Naming Convention . . . 74
- 4.4 Quality Tests and Pre-flight Performances . . . 75
- 4.5 Signal Processing . . . 77
  - 4.5.1 Signal Detection and Calibration . . . 78
  - 4.5.2 Clusterization . . . 78
  - 4.5.3 Track Reconstruction . . . 78
  - 4.5.4 Signal Corrections . . . 79

5 Nuclei Identification and Tracker Calibration 81
- 5.1 Draw Chart of the Calibration Procedure . . . 81
- 5.2 Data Sample . . . 82
  - 5.2.1 Event Selection . . . 82
  - 5.2.2 Charge Sample Selection . . . 83
- 5.3 Charge Measurement . . . 84
  - 5.3.1 Ionisation Energy Loss . . . 84
  - 5.3.2 Charge Collection . . . 84
  - 5.3.3 Charge Equalization and Linearization . . . 85
- 5.4 VA Equalization . . . 86
  - 5.4.1 P and N-Side Response Functions . . . 86
  - 5.4.2 Equalization Procedure . . . 86
  - 5.4.3 VA Classification . . . 90
  - 5.4.4 Equalization Results . . . 90
  - 5.4.5 Discussion . . . 93
- 5.5 Charge Loss Correction . . . 93

5.5.1 Traversing Position Estimation 93
5.5.2 Charge Loss Description 94
5.5.3 Application of Correction Factors 97
5.5.4 Results 97
5.6 Energy Dependences 97
5.6.1 Energy Dependence Description 98
5.6.2 Energy Dependence Correction 99
5.6.3 Results 100
5.7 Final Equalization and Linearization 100
5.8 Time Stability 101
5.9 Charge Identification Performance 101
5.10 Software Implementation 103

6 Nuclei Flux Measurements **107**
6.1 Nuclei Identification with AMS-02 107
6.2 Flux Formula and Analysis Strategy 108
6.2.1 Nuclei Counting Method 110
6.2.2 Flux Normalization Factor 111
6.2.3 The Monte Carlo Simulation 112
6.3 Data Selection 113
6.3.1 Data Sample 113
6.3.2 Selection Cuts 114
6.4 Reconstruction Efficiencies 114
6.4.1 ToF Reconstruction Efficiency 116
6.4.2 Tracker Reconstruction Efficiency 118
6.4.3 Layer 1 Pick-up Efficiency 123
6.4.4 Trigger Efficiency 126
6.4.5 Summary 128
6.5 Geometrical Acceptance 129
6.6 Exposure Time 132
6.7 Nuclei Counting Method 132
6.7.1 Charge Templates 133
6.7.2 Inner Tracker Template Fit 135
6.7.3 Contamination and Pure Sample Selection 137
6.7.4 Layer 1 Template Fit 139
6.7.5 Corrected Nuclei Counts 139
6.7.6 Fit Systematics and Total Error 141
6.8 Nuclei Fluxes 143
6.9 Conclusion and Outlook 154

7 Conclusions **157**

List of figures **158**

List of tables **166**

Bibliographie **169**

Appendices **175**

A VA Equalization DataBase **177**

B ToF Beta Reconstruction Efficiency **179**

C Track Reconstruction Efficiency **183**

D Layer 1 PickUp Efficiency **187**

E Trigger Efficiency **191**

Chapitre 1

Introduction

"L'homme de l'avenir est celui qui aura la mémoire la plus longue."

F. Nietzsche

In the introduction of his excellent review on *The Origin of Galactic Cosmic Rays* [1], Pasquale Blasi recalls a quote from physicist Bruno Rossi who wrote in his 1962 review of cosmic rays that "It is quite possible that future historians of science will close the chapter on cosmic rays with the fiftieth anniversary of Hess' discovery". Blasi points out that actually very little of the current experimental data was available at the time of this claim. It is quite ironic to quote his own opinion, more than 50 years later : "I am pretty sure that historians of science will not close the chapter on cosmic rays with the 100^{th} anniversary of their discovery. Too many loose ends need to be put in place.". In this chapter we provide a brief introduction to the field of experimental cosmic ray physics. After a snapshot at the discovery of these cosmic particles and the main experimental observations of the last century, we describe a few of the detection techniques used nowadays, whether in space, in the atmosphere or on ground. We then present some recent exciting experimental results before introducing the structure of this thesis.

1.1 A Brief History of Cosmic Rays

Summarizing in a few lines a scientific discovery is a dangerous exercise. A the edge of any paradigmatic crisis, contemporary physicists are often more remembered. We will not try here to do full justice to those who should be rewarded but are forgotten, but simply apologize for omissions, provided our presentation of the *science* is accurate. An extensive review of the discovery of cosmic rays is given in [2].

Electroscopes are known to spontaneously discharge with time at least since the observations of Charles Augustin Coulomb in 1785. More then one century later, in 1900, Elster and Geitel understood that the phenomenon was due to the presence of ions in the atmosphere. With the discovery of spontaneous radioactivity by Henri Becquerel a few years earlier, in 1896, it became widely accepted that the origin of these ions was the natural radioactivity from the

Earth's soil. Between the years 1900 and 1908, a number of studies with improved versions of the electroscope (better insulation and sensitivity) were performed to study the level of radioactivity at different locations. Ernest Rutherford, David J. Cooke, A. S. Eve and others conducted measurements on ground and in the middle of the ocean but found no significant reduction of the ionization level. Elster and Geiter measured the ionization level at the bottom of a salt mine and reported a 30% decrease. It was at the time simply interpreted as the fact that some materials in the soil must be less radioactive. In 1909, Theodor Wulf decided to study this ionization in the atmosphere and conducted his measurements on top of the eiffel tower. Although he measured an unexpected increase of the ionization, incompatible with a radiation originating from Earth, his results suffered from rather poor precision. In the same years, Domenico Pacini compared the ionization rate on mountains at different altitudes, on lakes and on the see. His measurements clearly showed that the Earth's soil cannot be the only origin of natural radioactivity. Pacini was in fact the first to suggest that a sizable cause of ionisation must come from the atmosphere. To improve Wulf's measurements, Karl Bergwitz and Albert Gockel flew balloons up to an altitude of 4000 m and observed no reduction of the ionization. A few years later, Victor F. Hess and later Werner Kolhörster [3, 4] observed in successive balloon flights at much higher altitudes that above a given altitude, the ionization level in air increased indeed with altitude, indicating a potential extra-terrestrial source of the ionizing radiation. Many alternative hypotheses were tested at first, such as atmospheric disturbances and thunderstorms. Hess also performed a flight during an eclipse on the 12th April 1912 to exclude a potential solar origin (night measurements had already been carried out). In 1925, Robert A. Millikan repeated the atmospheric measurements with much higher precision and extended them to under-water detection. The results remained best compatible with the hypothesis that the source of the ionizing radiation was coming from above the Earth's atmosphere. Millikan was the first to coin the term *Cosmic Ray.* The discovery of cosmic rays set a new paradigm in terms of the Universe's exploration since there was now more to it than the known stars, dust and gas, visible through the usual photons. Hess dedicated the rest of his life to improving cosmic ray detection techniques. He was awarded the Nobel Prize in 1936 for the "discovery of cosmic radiation".

At first, the nature of the cosmic radiation remained un-determined. Scientists were expecting either a form of electromagnetic radiation or some other neutral component. On the contrary, in 1929, Bothe and Kolhörster measured the absorption characteristics of the radiation using Geiger-Muller counters and concluded it must consist of charged particles [5]. The same conclusion was supported by worldwide surveys by J. Cay, Kolhörster, B. Rossi and A. Compton that showed that the rate of ionization strongly depended on the geomagnetic latitude[1] [6]. Only charged entities could be so strongly affected by the Earth's magnetic field. Further measurements showed an greater cosmic ray intensity coming from the West than from the East, establishing that the particles must be mainly positively charged. The cosmic radiation therefore represented a natural source of high energy particles. In fact, before the 1950s and the construction of big accelerator experiments on ground, particle physics was essentially practiced through the study of the cosmic radiation, leading to many discoveries. The same year Hess was given the Nobel Price, so was Carl Anderson for the discovery of the positron [7], proving the existence of anti-matter and confirming Dirac's theory of the electron. Anderson was studying the tracks of cosmic particles inside a cloud chamber in the presence of a magnetic field. Other important examples are the muon in 1936 [8] and the pion in 1947 [9]. While the positron and muon were discovered using cloud chambers, the pion was observed exposing nuclear emulsions. The development of the *Geiger-Muller* detector allowed to detect individual cosmic rays and perform very high precision arrival time measurements. Operating such detectors in fast coincidence, Pierre Auger (after hints from Rossi) was able to observe correlations in the arrival time of particles in detectors separated by large distances, giving birth to the concept of Extensive Air Showers (EAS). Detection of air showers allowed to measure particles with extreme energies, far beyond what will ever be achievable on Earth.

---

[1] The effect was actually discovered accidentally by Clay during a trip from Java to Genova.

The cosmic ray history illustrates the deep connection existing between the development of particle physics instrumentation and cosmic ray research. In the recent years, the collaboration between the two fields has reached a new frontier, with the successful operation in space of the most complex cosmic ray detectors ever built. AMS-02 is one of the latest examples of such particle physics experiment in space.

1.2 Experimental Observations

With particle discovery dictated by the ever more sophisticated accelerator experiments, the key interest of cosmic rays became the exploration of the Universe. What is the origin of these cosmic particles ? How and where are they accelerated to such extreme energies ? What is their composition ? How do they propagate in the galaxy or the Universe before reaching our detectors ? A hundred years after their discovery, all these questions are still matter of intense research. Yet, in the recent years, a consistent picture of the origin of cosmic rays has emerged. We summarize here the main experimental observations since their discovery. A detailed discussion of the phenomenology of cosmic rays is given in Chapter 2.

In the 1940s, balloon detectors flown at high altitudes revealed that the flux of cosmic rays consisted mainly of protons [10]. Using cloud chambers and photographic plates sent up to the stratosphere, heavier nuclei components were identified, up to a nuclear charge value $Z \approx 40$. It became clear that the relative abundance of these nuclei was very similar to the one observed for the solar system composition, with proton and helium largely dominating the particle flux and elements heavier then iron ($Z = 26$) or nickel ($Z = 28$) found to be extremely rare. These observations suggested a same origin, nuclei-synthesis in stellar environments. Significant deviations from the solar system abundances were however clearly identified and have been best explained in terms of propagation effects when cosmic rays interact with the interstellar matter in the Galaxy.

Using large arrays of detectors to measure the properties of extensive air showers, it was observed that the energy spectrum of cosmic rays follows a rather smooth power-law over a wide energy range. However, in 1958, a significant kink in the spectrum was found at energies around 10^{15}eV [11], the interpretation of which is still under debate. With ever more sophisticated and increasingly larger arrays of detectors, combined with fluorescence light detection techniques, the energy spectrum has since then been measured in great details and over a wide energy range. Combining direct measurements of cosmic rays from high up in the atmosphere or in space and indirect detections from ground, cosmic rays are observed to span an energy range from few MeV up to 10^{21} eV, while the flux drops dramatically from more than 1000 particles per second and square meter at GeV energies to less than 1 particle per km^2 per century at 100 EeV. A plot of the all-particle energy spectrum is presented in Chapter 2 (Figure 2.1). In addition to the knee, other structures have been revealed. Below few tenths of GeV ($\sim$ 30 GeV), the spectral shape bends down due to the influence of a magnetized wind originating from the sun which modulates and partially inhibits the access of low energy cosmic rays to the inner solar system. At these energies, there is a significant anti-correlation between the eleven-year solar cycle activity and the intensity of cosmic rays. Moreover, low energy cosmic rays must penetrate the Earths magnetic field to reach the top of the atmosphere and eventually our detectors. Therefore, below few tenths of GeV, the flux of cosmic rays depends both on time and location. Above 100 GeV, the flux is well described by a power-law with spectral slope ~ -2.7 that holds to a good approximation up to the *knee*, somewhere around 4×10^{15}eV. At the knee, the spectrum starts falling more steeply with a spectral index around -3.1. The shape holds up to a second structure at $\sim 4 \times 10^{18}$eV, the *ankle*, where the flux flattens out again. At energies around 10^{20} eV, the flux seems to undergo a significant suppression, perhaps the evidence of a feature predicted by theory as the GZK-cutoff[2].

The main paradigm around the origin of cosmic rays up to knee is that they are accelerated at the shock fronts of supernova remnants, violent phenomena resulting from the explosion of a parent star. The explosion results in the expulsion of metal-enriched ejecta traveling at supersonic speeds, thus creating a shock wave where diffusive acceleration processes are assumed to take place. Supernova events are not rare, about 3 of such explosions taking place in typical Galaxies each century. Only a small fraction of the power represented by the explosion is needed to account for the observed density of cosmic rays. The mechanism of acceleration itself has been deeply studied since the 1950s and a lot of progress has been made towards understanding how particles can be accelerated up to the region of the knee. Although there is compelling indirect evidence that at least some cosmic rays are accelerated in supernova remnants, it remains controversial whether energies up to the knee can be reached or not. Pinpointing the arrival directions of cosmic rays could be very useful in this respect. Observation of small-scale anisotropies in the arrival directions could help identify potential sources. Anisotropy studies have been conducted by many experiments but none have been found (see 2.1.5). This is expected since our best account of cosmic ray propagation inside the Galaxy tells us that cosmic rays propagate diffusively, being scattered many times by magnetic fields before reaching the Earth. Added to confinement time estimations of about 10^7 years, cosmic rays most likely completely loose track of their origin.

Above the knee our understanding of the origin of cosmic rays becomes even weaker, in large part due to the fact that the measurements cannot disentangle different species. It is believed that somewhere in between the knee and the ankle a transition occurs between cosmic rays of galactic origin and extragalactic origin, the ankle marking the turning point where the extragalactic component starts dominating the all-particle flux. The rationale for this idea is that with increasingly high energies, the confinement of cosmic rays by galactic magnetic fields becomes inefficient. Several theoretical models are able to reproduce the features observed in the all-particle spectrum but they essentially differ in the assumed or inferred composition at these energies (see Sec. 2.1). At the highest energies, composition measurements are even more challenging and our general understanding of the origin of these particles is extremely poor. A source of valuable information comes from anisotropy studies. At these high energies, since the particle confinement is limited, one can expect correlations in arrival directions of particles with their sources, presumably of extra-galactic origin. This very tempting scenario has recently been supported by measurements of the Pierre Auger Observatory which has shown a potential correlation with the position of Active Galactic Nuclei [12].

1.3 Modern Detection Methods

Due to the rapidly decreasing flux of cosmic rays, experimental cosmic ray physics is divided in two different observational categories : satellite or balloon experiments, and ground experiments. For energies up to several hundreds of TeV, the flux is high enough to consider experiments in space or high up in the atmosphere to measure the arriving particles. Above these energies, the big surfaces or/and long exposure times required to provide statistically significant measurements of the arriving flux are not yet technologically achievable in space. The solution is then to move to indirect detection from ground of the extensive air showers produced when cosmic rays interact with the constituents of the atmosphere. In the following, we describe a few instruments that currently represent the state-of-art in cosmic ray detection, whether in space or on ground. A few selected results from these experiments will be presented in Section 1.4.

---

[2] From the authors Greisen, Zatsepin and Kuzmin.

1.3.1 Balloon Flights

Since the first balloon flights measuring cosmic rays in the nineties, the technological progress has been tremendous and balloons remain a very popular approach to cosmic-ray studies. Balloon missions are both cheaper and often more convenient to conduct than space experiments. Some of the most important measurements remain dominated by balloon measurements, such as nuclei isotopic compositions and secondary to primary nuclei ratios. One of the main difficulties in interpreting balloon measurements is to deal with the presence of a given amount of residual atmosphere which requires to accurately model the resulting interactions cosmic rays may undergo before being detected.

ATIC

The Advanced Thin Ionization Calorimeter (ATIC) is an experiment primarily devoted to the measurement of energy and composition of cosmic rays. It is composed of several layers of bismuth germanate scintillating material that allow to measure the particle energy, while the charge is obtained using a silicon matrix. ATIC completed three successful flights since the year 2000 and was able to measure the energy spectra of nuclei up to iron from 50 GeV to hundreds of TeV. ATIC also published in 2008 [13] the observation of an excess of electrons in the energy range 300 to 800 GeV compared to the expected galactic background. Since ATIC cannot distinguish electrons from positrons, this result can be compatible with the famous positron excess measured the same year by the PAMELA collaboration, the Fermi LAT experiment, and more recently confirmed by AMS-02 (see 1.4.2). A picture of ATIC is shown in Figure 1.1 (left plot), taken from the ATIC website [3].

CREAM

The Cosmic Ray Energetics and Mass experiment (CREAM) consists of various particle physics detectors optimized to discriminate nuclei from proton to iron in a range of energy between 10^{11}eV and 10^{15}eV. The balloon was flown successfully six times above Antarctica at an altitude ranging between 38 and 40 km, above roughly 99.5% of the atmosphere. The energy range covered is large and intended to overlap the region where air shower detections can be used. Direct measurements at these energies have the potential to provide an energy calibration for the indirect measurements. The instrument consists of several complementary detecting devices : a Timing Charge Detector, a Čerenkov Detector, a Transition Radiation Detector, a Čerenkov Camera, a Silicon Charge Detector, scintillating fiber hodoscopes, and a tungsten-scintillating fiber calorimeter. CREAM has up to now produced the best measurements of secondary to primary nuclei ratios, an essential information for the constraint of cosmic ray propagation models (see Sec. 2.4). A picture of the CREAM instrument is shown in Figure 1.1 (right plot), taken from the CREAM website [4].

---

[3] `http://atic.phys.lsu.edu`

[4] `http://cosmicray.umd.edu/cream/`

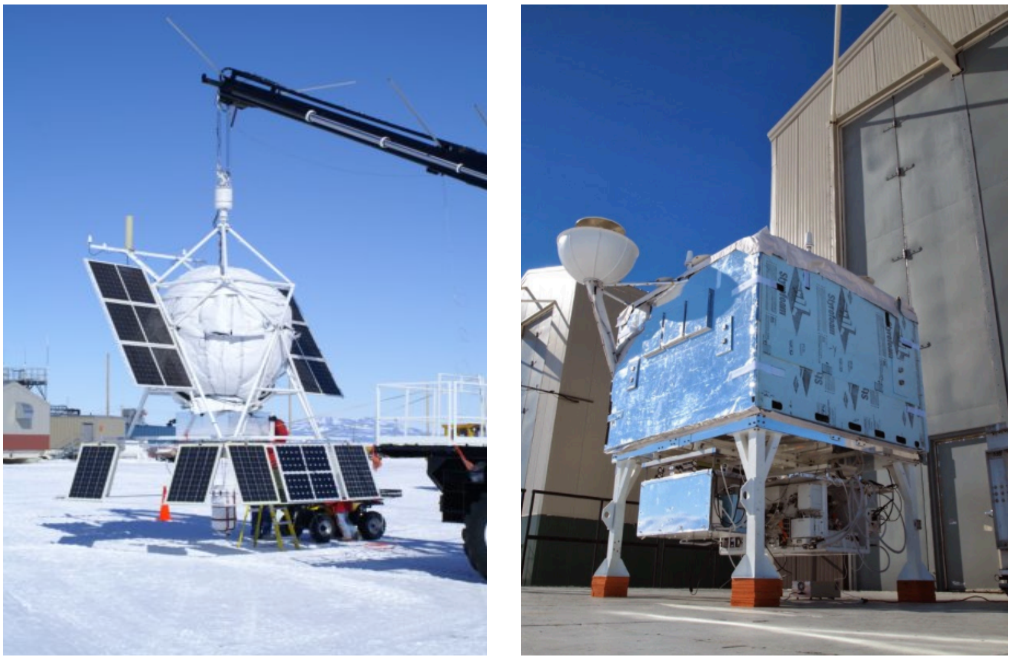

Figure 1.1 – Pictures of the ATIC (left) and CREAM (right) instruments.

1.3.2 Satellite Experiments

For a long time, the technology of particle physics detection on ground was judged too challenging to be implemented in space. The majority of space experiments were dedicated solely to the measurement of the cosmic electro-magnetic radiation or to the exploration of the Earth magnetic structure. The qualification flight of the AMS experiment in 1998 validated the use of modern particle physics technology in space. The PAMELA instrument was however the first long duration particle physics experiment in space.

PAMELA

The Payload for Anti-Matter and Light-nuclei Astrophysics (PAMELA) is an Italian particle detector that has been taking data in space since June 2006. It is installed on the Russian satellite Resurs-DK1 and follows an orbit at an altitude between 350 km and 610 km. With its magnetic spectrometer, it was the first experiment to measure with high precision cosmic anti-matter. The instrument combines a plurality of particle physics detection techniques, such as a a Magnetic Spectrometer, based on a neodymion-iron-boron permanent magnet and a precision tracking system, a sampling imaging Calorimeter, a Time of Flight System, an anti-coincidence system made of plastic scintillation counters, and a dedicated neutron counter. The PAMELA measurements led the route to several unexpected results. Most famous is the observed excess in the positron to electron ratio, starting at an energy of about 50GeV (see 1.4.2) which was later confirmed by the FERMI and AMS-02 collaborations. PAMELA also measured a break in the spectral index of proton and helium nuclei, challenging the standard view of a smooth power-law spectrum for all cosmic species up to the knee (see 1.4.3).

FERMI

The FERMI instrument, previously named GLAST, consists of a Large Area Telescope (LAT) and a Gamma Ray Burst Monitor (GBR). The LAT is the main instrument on-board and comprises a tracker and calorimeter system that allow to perform precise measurements of the energy and arrival direction of photons that convert into electron-positron pairs in the detector material. The energy range covered by the LAT is between 10 keV and 300 GeV. The conversion is ensured by high-Z conversion foils placed on top of the tracker planes. Anti-coincidence counters allow to select photons against the high background of charged particles which are up to a thousand time more abundant. The main goal of FERMI is to measure the diffuse galactic γ-ray emission and various γ-ray sources. Such measurements have the potential to bring crucial information to the cosmic ray picture. Figure 1.2 shows the entire sky observed by FERMI for γ-rays with energies above 1 GeV. Despite the fact that the detector is optimized for photon detection in the GeV range, it can also detect electrons. Without a magnet on-board, it is not possible to separate directly electrons from positrons. However, the FERMI collaboration was able to distinguish the two leptonic components using the properties of the Earth magnetic field. This allowed the collaboration to measure the ratio of positron to electrons up to 870 GeV and confirm the excess observed by PAMELA (Figure 1.4).

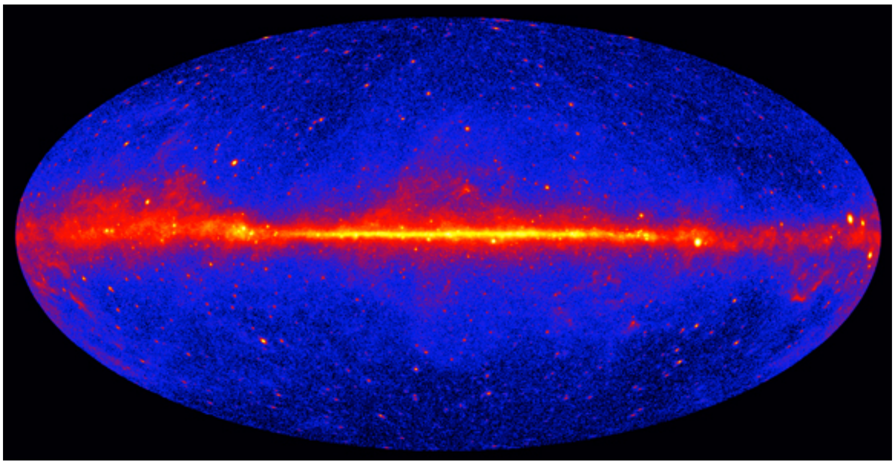

FIGURE 1.2 – The entire sky observed by FERMI for γ-rays with energies above 1 GeV [14]. Brighter colors indicate brighter sources. One can observe the concentrated emission around the galactic center.

The Alpha Magnetic Spectrometer

The AMS story starts with a precursor flight in 1998 with a simplified qualification model (AMS-01) of what was designed to be the final AMS-02 instrument. The AMS-01 detector was flown on-board the Space Shuttle Discovery during the STS-91 mission, demonstrating the feasibility of large-scale particle physics detectors in space. AMS-01 successfully collected more than 100 million particles which led to several publications. Based on the experience gain from AMS-01, AMS-02 took another 14 years to be built. It is now taking data on the International Space Station and has set the new reference for precision measurements in space. The AMS project is reviewed at length in Chapter 3. AMS will cover a variety of physics topics such as heavy anti-matter, dark matter, cosmic ray chemical composition and anisotropies, as well photon studies.

Future : DAMPE, ISS-CREAM and HERD

The Dark Matter Particle Explorer (DAMPE) is one of the five satellite missions of the Chinese Academy of Sciences (CAS) space science program, with a launch date planned to be in 2015-2016. DAMPE is designed to increase the sensitivity and energy reach for electrons, photons and cosmic ray particles (proton and heavy nuclei). The energy range is planned to be from 5 GeV to 10 TeV for electrons and photons and 100 GeV to 100 TeV for cosmic ray nuclei, with extremely good energy resolution. The main scientific goals of DAMPE are to identify potential Dark Matter signatures and help in the understanding of the origin and propagation mechanisms of high energy cosmic rays, as well as potential new discoveries in high energy gamma astronomy.

ISS-Cream is a mission based on a transformation of the CREAM (1.3.1) instrument for accommodation on the International Space Station (ISS). The goal is to extend the energy range of direct measurements of cosmic rays to the highest energy possible, around 10^{14} eV, very close to the knee. The long exposure above the atmosphere offers orders of magnitude greater statistics without the secondary particle background inherent to balloon experiments. ISS-CREAM is planned for launch onboard the SpaceX-6 spacecraft in December 2014.

The High Energy Cosmic Radiation Detection facility (HERD) is planned for launch and installation onboard the Chinese space station around 2020. HERD will perform accurate, high statistics measurements of electrons, γ-rays up to TeV energies and cosmic ray nuclei up to PeV energies. Extending the direct measurements of cosmic rays to energies around the knee may have the potential to improve fundamentally our understanding of the cosmic ray picture. The disentanglement of the various cosmic ray components at these energies will help discriminate different theoretical models.

1.3.3 Ground-based Detectors

When a cosmic ray enters the Earth's atmosphere, it interacts with its constituents and forms an extensive air shower. Electromagnetic showers initiated by photons or electrons can be distinguished from hadron initiated showers based on several observable properties. Different detection techniques can be used. Figure 1.3 gives an illustration of the various instrumentations and techniques used to detect extensive air showers on ground. The classical approach uses an array of scintillation detectors which measures the local density of charged particles at ground, which allows in turn to estimate the position of the shower core and the total number of particles in the shower. The latter is directly correlated to the particle energy. Combined with measurements of the arrival time of the particles at neighboring detectors, it is possible to reconstruct the arrival direction of the primary particle. Examples of experiments using such technologies are the KASKADE [15], KASKADE-Grande [16] or the older AGASA [17]. With arrays of hundreds of scintillation detectors, they measure cosmic rays with energies around the knee up to around 10^{18}eV. Based on the same shower reconstruction methodology, another detection technique uses Čerenkov light detectors. Due to a much deeper collection volume with respect to scintillators, they are usually more sensitive to showers with large zenith angles, allowing a much greater sky coverage. Horizontal showers, initiated by very high energy neutrinos, are also believed to be detectable. An example of experiment using such devices is the Pierre Auger Observatory [18], currently the largest operating experiment in the world. It consists of an array of 1600 water Čerenkov tanks distributed over an area of 3000 km^2 in the high fields of the Andes in Argentina. The Pierre Auger collaboration was able to detect the highest energies ever observed in the Universe, above 10^{19} eV.

Another category of experiments uses the fact that light charged particles in extensive air showers travel with relativistic speeds and emit Čerenkov radiation. Arrays of photomultipliers equipped with light collecting cones inside imaging telescopes with large collection areas can be used to measure the Čerenkov emission. Detectors based on Čerenkov light detection are mainly designed to measure photon initiated showers in the TeV region. Recent experiments include H.E.S.S. [19], MAGIC [20] and VERITAS [21].

Finally, at very high energies (E $\geq 10^{17}$eV), shower particles excite nitrogen molecules in the atmosphere which results in the emission of fluorescence light. The instrumentation is rather similar to the one used for Čerenkov light detection. The Fly's Eye experiment [22] was operated during more than 10 years and consisted in two stations of 67 spherical mirrors. It was upgraded with its successor, the High Resolution Fly's Eye (HiRes) which took data up to 2006. The Pierre Auger Observatory also uses four fluorescence light sites (each comprise six telescopes) overlooking the 1600 surface detectors which makes it a hybrid detector. The detection of the same shower by the two complementary methods provides very important cross-checks in terms of the energy measurement. The KASKADE-Grande can also be operated in hybrid mode. The Telescope Array (TA) [23] is located in Utah, USA, and consists of 576 scintillator stations and three fluorescence detector sites. Fluorescence measurements are difficult because they require that the atmospheric conditions are well known. Moreover, the detectors can only be operated during cloudless and moonless nights which significantly reduces the duty cycle of these detectors.

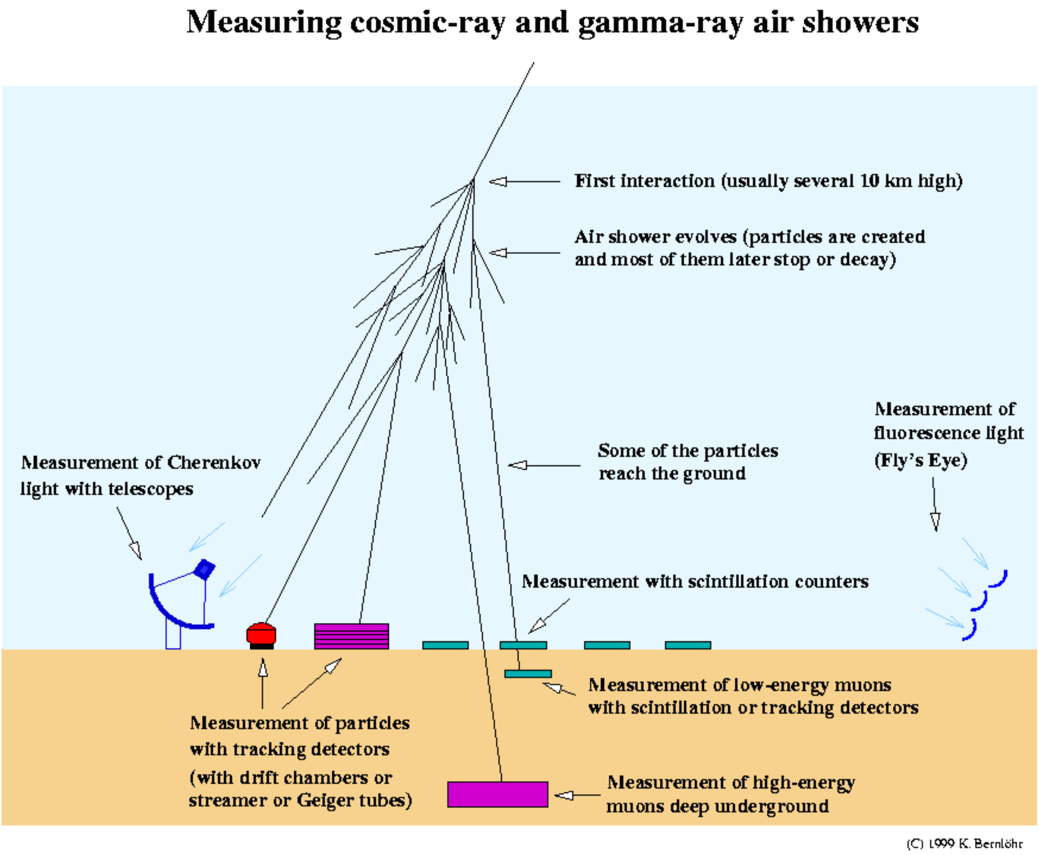
Measuring cosmic-ray and gamma-ray air showers
First interaction (usually several 10 km high)
Air shower evolves (particles are created and most of them later stop or decay)
Measurement of fluorescence light (Fly's Eye)
Measurement of Cherenkov light with telescopes
Some of the particles reach the ground
Measurement with scintillation counters
Measurement of low-energy muons with scintillation or tracking detectors
Measurement of particles with tracking detectors (with drift chambers or streamer or Geiger tubes)
Measurement of high-energy muons deep underground
(C) 1999 K. Bernlöhr

FIGURE 1.3 – Illustration of the various instrumentations and techniques used to detect extensive air showers on ground (credits K. Bernlöhr [6])

1.4 Recent Experimental Results

In the last ten years, cosmic ray experiments have revealed some of the most exciting and unexpected results, continuously challenging our understanding of cosmic particles. whether these results are signs of new physics or limitations of the current theoretical models remains an open question. We present in this section a few selected topics which have caught the scientific community's attention in the recent years.

1.4.1 Antimatter Searches

Within the standard picture of the Hot Big Bang theory, matter and anti-matter are produced in equal amounts. There is however growing experimental evidence that the Universe we live in is made only of matter. Moreover, the characteristic intense emission of photons expected from matter antimatter annihilations has never been observed. This limits further the plausibility that large amounts of antimatter subsist somewhere in the Universe. Nevertheless, the observation of a single anti-nucleus other than anti-hydrogen in the flux of cosmic ray particles would be strong evidence for the existence of primordial heavy antimatter. In 1998, AMS-01 established an upper limit of 10^{-6} for the anti-helium/helium flux ratio in the Universe. AMS-02 will reach a sensitivity of 10^{-9}, therefore extending the volume of the Universe which can be tested for the existence of primordial antimatter.

1.4.2 The Positron Excess

As discussed in 1.4.1, primordial antimatter seems rather rare in our Universe. Antimatter is detected in the cosmic ray flux only in the form of antiprotons and positrons. These particles are however thought to be of secondary origin, the result of interactions of primary cosmic rays with the dilute interstellar gas. Supposing a secondary origin, the associated fluxes can be computed using the knowledge of the respective production cross-sections for cosmic ray species interacting with the interstellar matter and models of particle propagation in the Galaxy. The observations of $\bar{p}$ and low energy e^+ (up to 10 GeV) are well reproduced by the models which supports the secondary origin hypothesis [24]. At higher energies, the positron flux has however been hard to account for by the models. One convenient way to study the positron spectrum is through the positron fraction, defined as the number of positrons divided by the sum of electron and positrons. Assuming secondary positrons and that electrons are both of primary and secondary origin, one expects that the positron fraction is a monotonically decreasing function of energy above few GeV. The grey band in Figure 1.4 shows the typical expectations calculated by the models, the band serving as a conservative estimate of the uncertainties in the modeling. The PAMELA collaboration was the first [7] to report a clear excess of the number of positrons above 10 GeV with respect to expectations [26]. The excess was confirmed in a publication from the FERMI collaboration [27] and recently by the AMS-02 collaboration [28]. The disagreement between the PAMELA and AMS-02 points below 10 GeV is the result of solar modulation effects which evolve with time but are negligible above few GeV. The disagreement with the Fermi points at few tenths of GeV has not been explained but may be the result of systematic uncertainties in the scale of the measured energy [8].

There is thus a clear and indisputable excess of light antimatter measured at Earth. The question is, obviously, where does it come from ? Many theoretical scenarios have been advanced to explain the excess. A popular explanation is that nearby astrophysics objects such as pulsars are the accelerators that produce this genuine source of primary cosmic antimatter. The physics of pulsars predicts the production of positrons (and electrons) and it was shown that a set of pulsars suitably distributed in age and distance could account for the observed excess.

---

6. `http://www.mpi-hd.mpg.de/hfm/CosmicRay/ShowerDetection.html`

[7] Hints of a rising positron fraction were actually already observed since 1969 by Agrinier et al. [25].

[8] The contribution of some proton background could also be an explanation

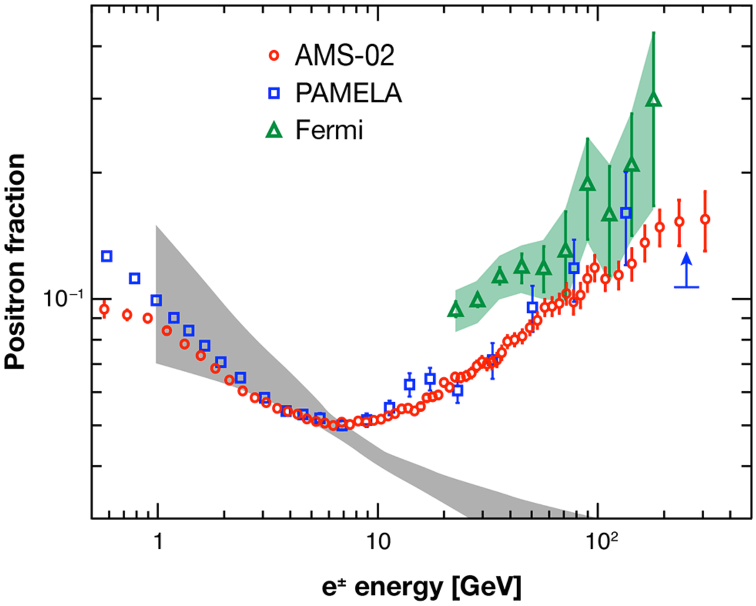

FIGURE 1.4 – Recent measurements of the positron fraction [29]. The grey band is the expectation from models of particle interaction and propagation in the Galaxy. The current measurements show a clear deviation from the predictions above 10 GeV.

An exciting alternative however is that these positrons are produced by the decay or self-annihilation of dark matter particles. Dark matter is the dominant part of the matter density of the Universe, yet nothing is known about its nature. Identifying the excess of positrons as the signature for dark matter would certainly be one of the greatest discoveries of modern physics.

Crucial measurements that would allow to favor the pulsar hypothesis would be to observe anisotropies in the arrival direction of positrons or a structure in their energy cut-off indicating multiple sources. If dark matter particles are at the origin of the excess, then the flux should be isotropic while pulsars are point sources and could contribute to some anisotropy. However, given the assumption that multiple pulsars contribute to the excess, the expected anisotropy is quite small. Moreover, electrons are efficiently deflected by magnetic fields which further reduces the level of anisotropy expected. The needed sensitivity to disentangle the two scenarios in terms of anisotropy measurements is currently far above what our experiments are capable of.

1.4.3 Discrepant Hardening Observed in Cosmic-ray Spectra

The first hint of deviations from a smooth power-law in the spectra of cosmic ray nuclei between 50 GeV and 100-200 TeV came from the ATIC-2 balloon experiment [30]. A significant difference in the spectra of protons and helium nuclei (the proton spectrum being steeper) was found. In addition, deviations from a single power-law in the spectra of all nuclei from protons to heavier nuclei were observed. The same results were obtained by the CREAM collaboration [31]. They measured with excellent charge resolution the fluxes of nuclei from proton to iron between 2.5×10^{12} to 2.5×10^{15} eV. CREAM showed that the measured proton and helium spectra are both harder and flatter with respect to extrapolations from low energy measurements. The proton spectrum is also observed to be significantly steeper than the helium one. The helium flux measured by CREAM is not compatible with an extrapolation of the low energy measurements performed below 100 GeV. For heavier nuclei, CREAM measured fluxes that are consistent with previous experiments below 200 GeV per nucleon but above, their data are systematically higher than what a single power-law fit from lower energies would indicate. The conclusion is that the CREAM data are best fitted with a broken power-law, the break-point being in the range 200-250 GeV/nucleon. PAMELA brought the most recent support for the spectral break claim with high precision measurements of the proton and helium fluxes between 1 GeV and 1 TeV [32]. PAMELA identified a clear break in both the spectrum of proton and helium around 230-240 GeV. A single-power law fit is rejected at 99% confidence level. Moreover, PAMELA observes a clear difference between the spectral shapes of proton and helium prior to the respective hardening of the spectra, the proton spectrum being softer. The fluxes measured by the different experiments discussed here are presented in Figure 1.5.

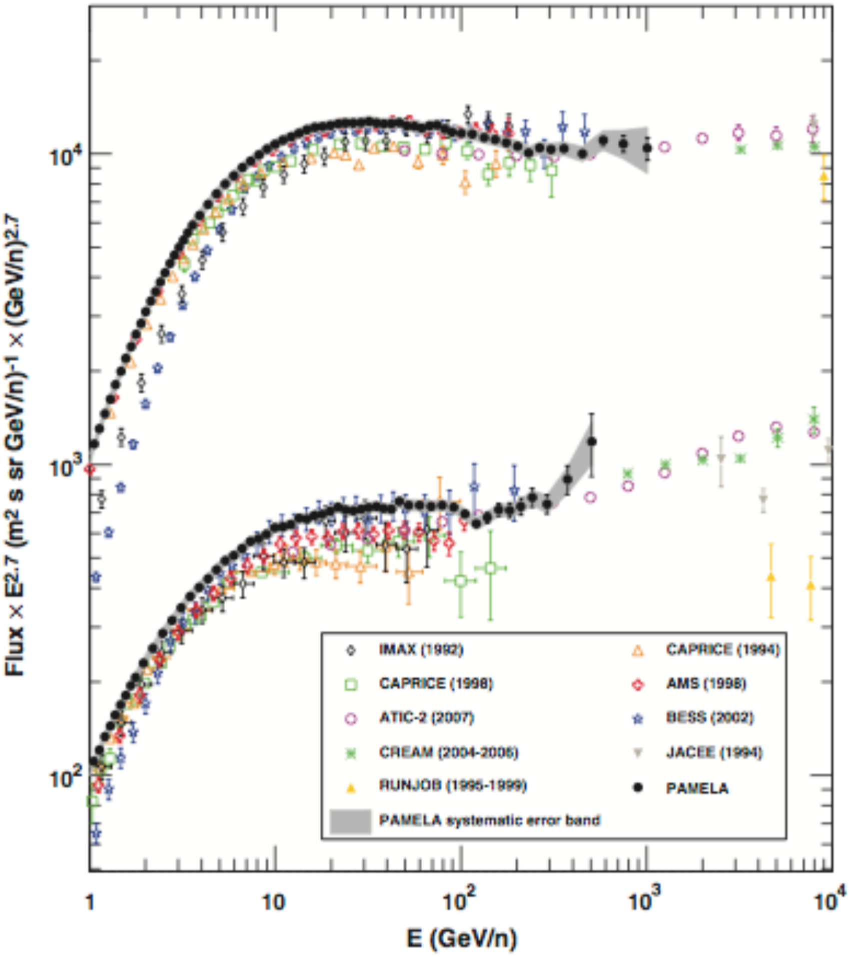

FIGURE 1.5 – Measured energy spectra for proton and helium nuclei. The black points from PAMELA indicate a clear deviation from a smooth power-law. An extrapolation of the proton break observed by PAMELA seems consistent with the flux measured by the ATIC (open purple circles) and CREAM (green squares) experiments at higher energies. A pronounce discrepancy is however observed for the helium flux. Plot taken from [32].

These results challenge the standard picture of a smooth spectrum of cosmic rays below the knee. Many explanations have been proposed. One scenario is that against what is usually assumed in standard propagation models (a steady state continuous source distribution), the true cosmic ray source distribution is probably discrete in time and space. A non-uniform distribution of sources could result in structures in the cosmic ray spectra. Local or younger sources could dominate the high-energy parts of the spectra [33], a scenario that has also been advanced to explain the observed excess of positrons (1.4.2). It has also been suggested that the hardening could result from a source effect connected with subtleties of the acceleration mechanisms taking place inside the source [34]. Some authors have assumed a break in the slope of the diffusion coefficient [35] used to describe cosmic ray propagation in the Galaxy. In a recent work, Tomasseti [36] was able to reproduce the observed spectra assuming that the hardening results from a spatial dependence of the cosmic ray diffusion properties in different regions of the Galaxy. It seems likely that a realistic description of the Galaxy requires all of the above ingredients. The question is whether some effect truly dominates to explain the spectral features recently observed. It is worth mentioning that the AMS-02 collaboration has recently presented preliminary measurements of the helium and proton fluxes which are consistent with no spectral hardening [37, 38]. Confirming or infirming the presence of a spectral break in the proton and helium spectra (as well as for heavier nuclei) is of fundamental importance because the parameterization of these fluxes are the standard input to the modeling of secondary cosmic ray production in the interstellar medium. In particular, the impact of the spectral hardening observed by PAMELA on the modeling of the secondary positron production was studied in [39].

1.5 Structure of the Thesis

The work presented in this manuscript concerns the detection and precise measurement of cosmic ray nuclei using the AMS-02 detector. In Chapter 2, we give an overview of the phenomenology of cosmic rays, emphasizing on the role played by cosmic nuclei measurements in constraining theoretical models. We present a detailed discussion of the AMS-02 instrument and its operation on the International Space Station in Chapter 3. After the activation of AMS-02 in space, almost two years have been dedicated to the optimization of the performances of the various sub-detectors. A dedicated procedure to accurately calibrate the response of the silicon tracker and optimize its performance in terms of charge resolution was developed. After a detailed description of the silicon tracker in Chapter 4, the calibration procedure and its results are presented in details in Chapter 5. Based on the excellent nuclei identification capabilities of the tracker, an analysis to measure nuclei fluxes is presented in Chapter 6, with preliminary flux results for nuclei from lithium ($Z = 3$) to neon ($Z = 10$).

Chapitre 2

Cosmic Ray Phenomenology

> *"A theory which is not refutable by any conceivable event is non-scientific. Irrefutability is not a virtue of a theory (as people often think) but a vice. Every genuine test of a theory is an attempt to falsify it, or refute it."*
>
> K. R. Popper

The evolution of cosmic ray physics is to a large extent driven by new experimental results. However, experimental data alone is of limited interest if not compared to a general theory of the origin, acceleration and propagation mechanisms of these cosmic particles. Understanding the origin of cosmic rays has long been intrinsically related to the understanding of what are the potential acceleration processes taking place in different astrophysical environments and capable of explaining the observed energies. Since a few years, there is growing evidence that supernova remnants are at the origin of most of galactic cosmic rays. This scenario does however not yet explain the spectral features observed at Earth, in particular that the energy spectrum of all cosmic ray species tend to follow a smooth power law with spectral index close to -2.7. Earth measurements reflect the properties of cosmic rays locally and it is evident that once injected from their sources into the interstellar medium, charged particles are affected by a number of processes that can potentially alter their spectra. Propagation models do their best at simulating these effects. They must incorporate many ingredients, some of them being rather poorly understood at the present time.

In this Chapter, we give an overview of the phenomenology of cosmic rays. After a detailed discussion of the cosmic ray energy spectrum, we make the case for the SNR paradigm, presenting the main theoretical and experimental evidence gathered in the last 50 years. We then give a brief account of propagation models. A practical case is presented to emphasize the importance of new measurements like the ones from AMS-02 in better constraining the existing models.

2.1 Interpretation of the Energy Spectrum

Due to the huge energy range spanned by cosmic ray observations, it is natural to start our discussion from the broad view of the overall cosmic ray energy spectrum. The left plot in Figure 2.1 shows a compilation of various measurements of the differential flux (flux of particles per unit time, surface and solid angle, per unit energy interval) of cosmic rays reaching the Earth. The flux is multiplied by E^2 for clarity and to enhance the visibility of features in the spectrum.

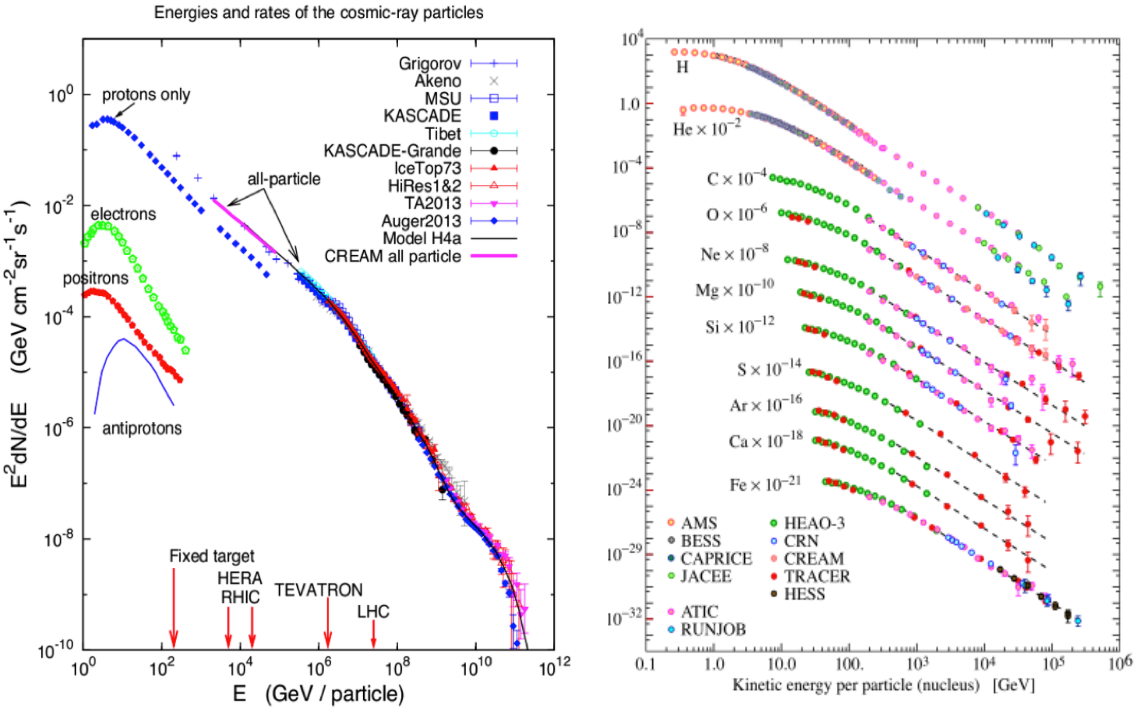

FIGURE 2.1 – Left : Various components of the cosmic ray flux measured by different experiments. Picture taken from [40]. Right : Relative flux of primary cosmic ray nuclei from hydrogen to iron [41].

2.1.1 Cosmic Rays up to the Knee

Up to a little above 100 TeV (slightly below the knee), the various flux components can be measured individually and the primary cosmic ray fractions are found nearly constant, as can be appreciated in the right plot of Figure 2.1. The fact that the spectra appear very smooth with a power-law shape for all species suggests particles are accelerated through non-thermal, scale invariant, processes. Although currently direct measurements do not extend up to the knee region, there is a comforting agreement between the extrapolation of the all-particle spectrum obtained by direct detection methods (magenta solid line in left plot of Figure 2.1) and the spectrum measured by air shower experiments covering the energy region close to the knee. The apparent smoothness of the spectrum below the knee has recently been challenged by results of the PAMELA experiment which show a break in the spectrum of proton and helium elements around 230 GeV (see 1.4.3).

Cosmic rays up to the knee are mainly thought to be of galactic origin and the standard paradigm is that they are accelerated at the shock fronts of supernova remnants (SNRs), violent explosive phenomena observed to take place in most galaxies, in particular in our Milky Way. Cosmic rays then propagate diffusively through our Galaxy, being deflected many times by randomly oriented magnetic fields before reaching our detectors. In this conventional picture, cosmic rays rapidly loose track of their origin. Although there is compelling evidence that these particles are indeed produced by SNRs, there is yet no conclusive proof that the acceleration mechanisms invoked do take place in such environments.

2.1.2 Around the first Knee

There are multiple experimental evidences that the average mass of cosmic rays increases with energy across the knee region, heavier elements progressively dominating the all-particle spectrum. This observation suggests that the knee is the result of sequential cut-offs in the spectra of different nuclei. The justification for this interpretation is that most acceleration processes we can think of are rigidity dependent, meaning they scale with the particle magnetic rigidity, $R = pc/Ze$. If the maximum energy at which a proton can be accelerated is $E_{p,\max}$, then nuclei of nuclear charge Z (fully ionized at such energies) can reach an energy $E_{Z,\max} = Z \cdot E_{p,\max}$. This explanation also naturally reproduces the smooth spectra observed right after the knee. What are the exact values for these maximum energies is a matter of assumptions on the source and acceleration of cosmic rays as well as the description of the propagation mechanisms. As already mentioned, one of the most popular scenarios for the source assumption is that cosmic rays are accelerated in SNRs. Due to the finite lifetime of the shock front, the maximum energy attainable is around $E_{\max} \sim Z \times (0.1 - 5) \times 10^{15}$eV for a particle of charge Z (see Sec. 2.3). Many models have been studied using as input different assumptions on the properties of the SNRs, like magnetic field strength, available energy, evolving medium, etc. Different estimations of the maximum attainable energy are obtained. While first SNR models calculated a maximum energy around 0.1 PeV, the most recent and presumably more realistic models predict a factor 10 higher cut-off. Another popular explanation of the knee is related to propagation effects. With increasing energy, galactic magnetic fields are less able to confine cosmic rays which results in a leakage of particles from the Galaxy. Such effect is rigidity dependent and predicts a superposition of different energy cutoffs for different elements. This scenario alone predicts a knee position much lower than what is actually observed. It seems likely that a combined approach assuming both energy cut-offs at the acceleration site and leakage of particles from the Galaxy is the most reasonable scenario to envisage [42]. Other approaches have been considered to explain the knee. For example, acceleration of cosmic rays by γ-ray bursts. Other authors consider the interaction of cosmic rays with particles like massive neutrinos or photo-disintegration of cosmic rays in dense photon fields. Also energy transfers through nucleon-nucleon interactions into gravitons or very high energy muons have been suggested. Most of these more exotic models have either not been capable of reproducing satisfactorily the observed knee or have been strongly disfavored by other data.

2.1.3 From the first Knee to the Ankle

There is a wide consensus that the ankle marks the turning point where cosmic rays of extragalactic origin start dominating the all-particle flux. However, in the region in between the knee and the ankle, it is not clear what are the relative contributions of the galactic and extragalactic components. The KASKADE-GRANDE and ICETOP collaborations have in fact identified a third structure, called the second knee, somewhere in between 10^{16} and 10^{18} eV [43, 44]. Their measurements disentangle light nuclei (p and He) from heavier elements and show that the spectrum of the light component tends to show a ankle-like feature at around 10^{17}eV. The authors naturally interpret this as a transition from galactic to extra-galactic origin of the light component of cosmic rays. At 10^{18} eV, they measure a comparable flux of Fe-like cosmic rays and light nuclei. Although the scenario described here is tempting, this interpretation is not supported by measurements of the HiRes [45], TA [46] and Pierre Auger [47] collaborations which report a composition significantly dominated by the light component at 10^{18}eV. Moreover, based on the current interpretation of the knee, authors in [48] have shown that considering different energy cut-offs in individual particle spectra (from p to Iron) does not suffice to reproduce the observed all-particle spectra. Around 10^{16} eV, there is already a strong deficit of particles in the models. To account for this depletion, various assumptions on the nature of the extra component have been considered. Some authors (see [42]) have introduced in their models a significant contribution of ultra-heavy elements with Z ranging from 28 to 92. Based on the same principle of successive cut-offs in the spectra of the various nuclei species, these models are able to reproduce the observed spectra as well as the position of the second knee. It is very interesting to notice that the position of the second knee is then almost precisely at a factor 92 higher then the first knee. A model by Berezinsky and collaborators [49] explains the position of the second knee as the result of proton energy losses due to interactions with photons of the cosmic microwave background $\mathrm{p} + \gamma_{CMB} \rightarrow \mathrm{p} + \mathrm{e}^{+} + \mathrm{e}^{-}$. To reproduce the observed spectra, this explanation would require that the composition of cosmic rays at those energies is significantly dominated by protons [50], by more than 80%. Wether the composition at these energies is rather light than heavy is a controversial question based on the current contradictory experimental measurements.

Few of the previous models can be extended to higher energies and explain the position and shape of the ankle. The model of Berezinsky naturally reproduces the ankle energy and shape but predicts a composition significantly dominated by protons. If we expect extragalactic cosmic rays to be accelerated in processes similar to the galactic ones, then we also expect the composition at the source to be somewhat similar to the one observed at lower energies. Both models assuming a mixed or heavy dominated composition allow to reproduce the observed data quite well. A purely proton dominated composition could imply very different astrophysical pictures such as top-down scenarios or the existence of unexpectedly strong magnetic fields in SNRs. Moreover, different scenarios also have deep implications for the interpretation of what happens at higher energies. It is clear from these discussions that a better understanding of the cosmic ray composition in the region between the knee and the ankle (and above) is of fundamental importance to distinguish different models.

2.1.4 Ultra-high Energy Cosmic Rays and the GZK Cut-off

The ankle is usually interpreted as a superposition of two cosmic ray components, with a transition in abundance from the first to the second, the latter having a softer spectrum. The explanation is that charged particles with energies above the ankle cannot be confined in the Milky Way by the galactic magnetic field. With conservative approximations for the size of the galaxy (a disk of 20 kpc) and the strength of galactic fields (1 μG), the gyro-radius being defined as $R \sim E/(qB)$, the maximum energy a relativistic particle confined in the galaxy can have is around 10^{18} eV. If sources local to our galaxy were to produce such high energy events, small scale anisotropies should be observed in the arrival directions of cosmic rays, pin-pointing back to their origin. None of such objects have been identified in our Galaxy and it is therefore believed that above the ankle the flux is dominated by particles of extra-galactic origin.

At energies above 5×10^{19} eV, theory predicts that protons should interact inelastically with photons of the Cosmic Microwave Background (CMB) producing pions via a delta resonance, and therefore loosing energy :

$$\mathrm{p} + \gamma_{\mathrm{CMB}} \rightarrow \Delta^{+} \rightarrow \mathrm{p} + \pi^{0} \tag{2.1}$$

$$\mathrm{p} + \gamma_{\mathrm{CMB}} \rightarrow \Delta^{+} \rightarrow \mathrm{n} + \pi^{+} \tag{2.2}$$

This implies an upper-limit for the energy of cosmic rays somewhere around 10^{20}eV, an expected drop of the cosmic ray flux named Greisen-Zatsepin-Kuzmin cut-off (GZK cut-off) [1]. The HiRes and the Pierre Auger Observatory have provided experimental evidence for a significant suppression in the flux of cosmic rays with energies exceeding 4×10^{19}eV [51]. Above this energy, the flux is 50% lower than what would be expected from a power-law based extrapolation of the lower energy data. Both results are shown in Figure 2.2.

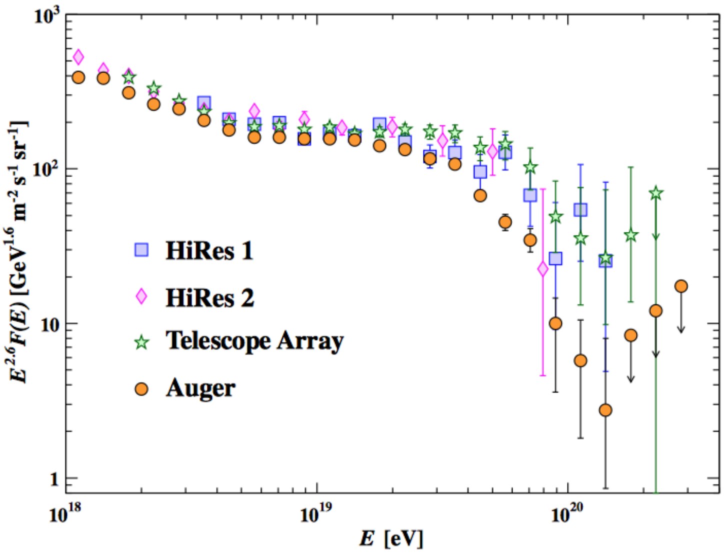

FIGURE 2.2 – Flux of UHE cosmic ray particles measured by various experiments [41]. The differential cosmic-ray flux is multiplied by $E^{2.6}$. A significant suppression of the the flux of cosmic rays is observed above 4×10^{19} eV.

The question arises wether the suppression observed is the result of the predicted GZK effect or simply due to a threshold in the maximum energy attainable in the acceleration sites. As anticipated, the precise understanding and interpretation of the apparent GZK suppression depends again on the composition at those energies. Since intermediate mass nuclei are predicted to break up more rapidly when interacting with the CMB background, one essentially expects either a light or, on the contrary, a rather heavy composition at GZK energies. The precision of the current data does not allow such distinctions. There is yet another support for the GZK effect. The Pierre Auger collaboration has reported a correlation (see below) between their highest energy events and the position of Active Galactic Nuclei, compact regions inside massive galaxies thought to host a supermassive black hole. The significance of the measured correlations is still controversial and more data at these extreme energies are needed.

2.1.5 Anisotropy Searches

Potential anisotropies in the arrival direction of cosmic rays could help understand their origin, wether source regions or individual contributors can be identified. Two type of analysis are usually conducted. Large scale anisotropies would be connected to the propagation of cosmic rays through the galaxy. For example, a large-scale anisotropy is expected if the Earth moves relative to a cosmic ray rest system, a so-called *Compton Getting* effect [52].

---

[1] Greisen,Zatsepin and Kuzmin conducted in parallel the first estimation of the energy threshold at which the process was to take place.

Small-scale anisotropies searches obviously aim at finding individual sources of cosmic rays in the sky. It is important to recall that below 10^{15} eV, our current understanding suggests that particles propagate diffusively and are confined for thousands of years in the Galaxy, such that they loose complete track of their origin. Hence we do not expect any anisotropies on small scales for GCRs. Below 1 GeV, clear large-scale anisotropies are detected due to solar wind and the Earth magnetic field. The latter deviates positive and negative particles in opposite directions creating an "East-West" effect. This effect is used by the Fermi collaboration to distinguish electron and positrons. At ultra-high energies, above the ankle ($E > 10^{19}$ eV), CRs are too energetic to be confined by the galactic magnetic field, which means anisotropies could be expected (assuming inter-galactic fields are sufficiently weak). Anisotropy studies at these energies become however extremely challenging due to the very low particle fluxes.

Small scale anisotropies in galactic cosmic rays were investigated by the KASKADE and Tibet experiments in the TeV and PeV energy ranges. Special attention was given to the galactic plane region and to the distinction from extensive air showers of photons. Tibet found a small excess at TeV energies most probably correlated with the well-known Crab Nebula [53]. At energies above 0.3PeV, the KASKADE collaboration did not find any significant excess in either charged or photon like samples [54]. The Super-Kamiokande [55] and Tibet [56] experiments have reported observations of large-scale anisotropies in the same regions of the sky at about 10 TeV, consistent with a co-rotation of galactic cosmic rays with the local galactic magnetic field environment. At the same energies, the Tibet and Milagro experiments have identified another region in the sky presenting an excess of γ-rays. There is yet no conclusive interpretation for this excess but some authors suggest a relation to the Geminga pulsar as a local source of cosmic rays [57].

Many different groups have been looking for large-scale anisotropies at the highest energies. Although there are some claims of an observed excess of showers coming from the direction of the galactic plane at 10^{18}eV in the AGASA and SUGAR data, this is not confirmed by the Auger and HiRes data. Clustering of arrival directions within small angular regions of the sky could indicate potential point sources. The most convincing, yet not conclusive, claim of small-scale anisotropies comes from the Pierre Auger collaboration, who has measured a correlation of their very highest energetic events ($E > 5.7\times10^{19}$ eV) with the positions of various active galactic nuclei (AGN). A sky map with the referenced positions of known AGNs is reported in Figure 2.3 (blue asterisks). Filled circles represent the arrival directions of the PA events while squares are high energy events reconstructed with the HiRes telescope. The correlation is not confirmed by the HiRes data. A recent review of anisotropy studies with the Pierre Auger data is given [12].

2.2 Composition below the Knee

We will not discuss further the controversies around the measurement of the cosmic ray composition above the knee region and concentrate on the wealth of data provided by direct measurements. The flux of cosmic rays incident at the top of the atmosphere consists of all stable charged particles and nuclei with lifetimes of the order of 10^6 years or longer. Among these particles, about 87% are protons (fully ionized hydrogen), while the remaining fraction is composed mainly of helium nuclei (more than 9%) and other elements, as heavy as iron or nickel. There is also a small amount of electrons and anti-matter positrons and anti-protons. Some authors argue that we should also include under the cosmic ray denomination a small flux of electromagnetic radiation (ranging from radio frequencies to TeV gamma rays). These photons are undoubtedly of cosmic origin and the component discussed here is associated both

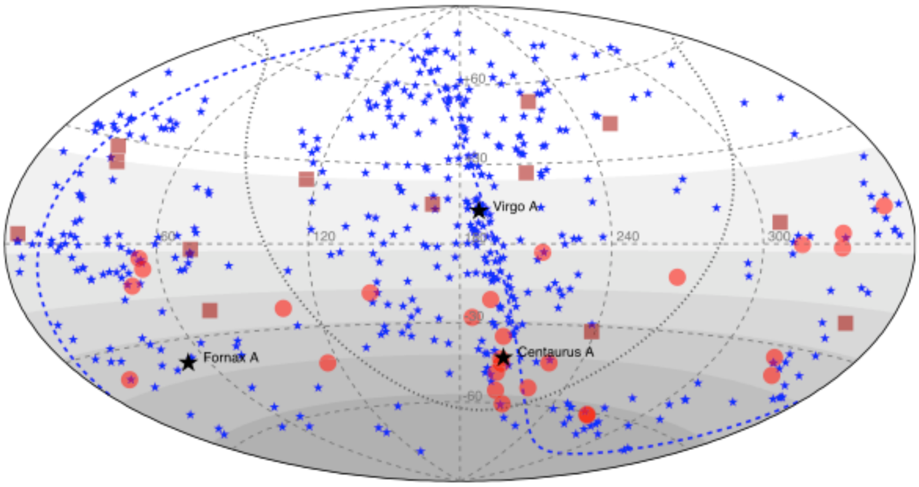

FIGURE 2.3 – Sky map in equatorial coordinates presenting the arrival directions of cosmic ray showers measured at the Pierre Auger observatory (filled red circles). The blue asterisks indicate the position of AGNs from different catalogs. The squares correspond to events measured with the HiRes telescope. Picture taken from [58].

to potential sources of cosmic rays and to the interactions of cosmic rays with interstellar matter during their propagation through the galaxy. The observation of this electromagnetic component has brought in the recent years new insights into the understanding of the cosmic ray origin (see 2.3.3).

2.2.1 Nuclei Relative Abundances

Figure 2.4 shows the measured abundance of cosmic ray nuclei at around 1 GeV per nucleon normalized to the silicon abundance (×100). The filled black points are a collection of experimental results from different experiments [59]. Solar system abundances are also shown for comparison (filled triangles). Focusing on elements with the nuclear charge number Z below 28 (nickel), one observes that for the most abundant species (H, He, C, O, Fe), there is a good agreement between galactic and solar system abundances, indicating that most cosmic ray elements originate from stellar nucleosynthesis. There are however clear deviations, most striking for lithium ($Z = 3$), beryllium ($Z = 4$) and boron ($Z = 5$). These elements are not abundant end-products of stellar fusion, as they are rapidly transformed into heavier and more stable elements. The best accepted explanation to date is that these elements are created by the interaction of heavier nuclei with the interstellar matter through so-called *spallation* reactions. This implies an important conceptual distinction between cosmic rays detected at Earth. *Primary* cosmic rays are those particles that were produced and accelerated at some astrophysical source, while the *secondary* component relates to the products of the interactions of the primary particles with the interstellar gas. A third population is sometimes identified, consisting of products of the interaction of the secondary particles with the interstellar gas. Although its flux is almost negligible, its consideration is important to account for anti-proton measurements. These categorical distinctions cannot be made at the detection level but are fundamental for the interpretation of the experimental results.

The ratio of secondary to primary nuclei is one of the most interesting observable for theoretical models of cosmic ray propagation. Since the secondary component is produced through

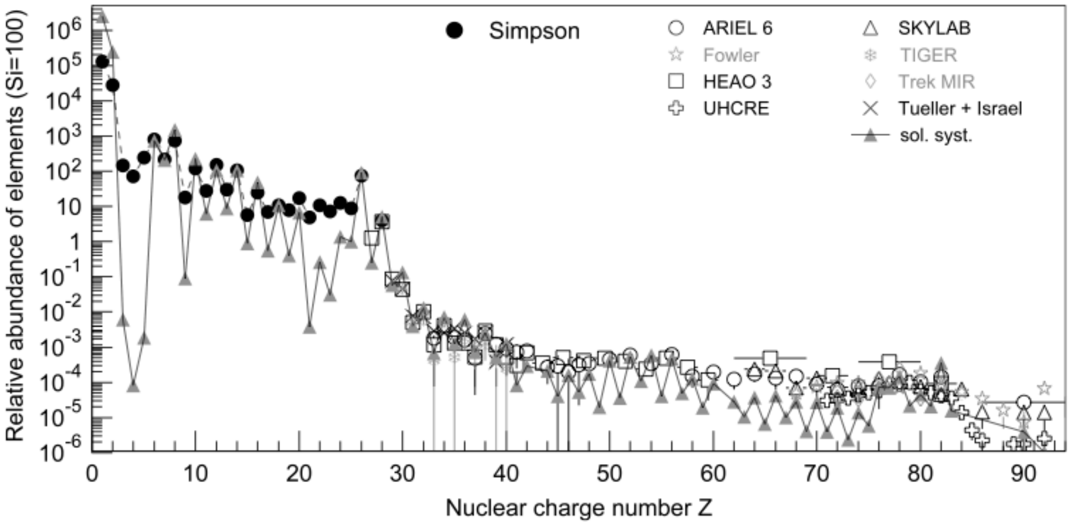

FIGURE 2.4 – Relative abundance of cosmic ray nuclei at an energy around 1 GeV/n (normalization to Si ×100). Filled triangles represent solar system abundances [58]. The black points are a compilation by Simpson [59] of different experimental results. Courtesy of Prof. Israel for the Advanced Explorer experiment [3].

spallation reactions with the interstellar medium, this ratio provides constraints on the density of matter traversed by cosmic rays. This estimation assumes that we now the confinement time of cosmic rays in the Galaxy and have a precise knowledge of nuclear interaction cross-sections, which is not the case in reality. We discuss this topic in more details in 2.4. Confinement time estimations can be obtained from measurements of radio-isotopes like ^{10}Be, ^{26}Al, ^{36}Cl and ^{54}Mn, considering the fact that isotopes with shorter life-times are not observed [60].

2.2.2 Refractory Elements and Neon 22

Precise composition measurements have shown a significant over-abundance of ^{22}Ne and refractory nuclides with respect to solar compositions. It became evident that these anomalies could not be explained by nucleosynthetic processes but rather by dependences on atomic parameters. It is observed that elements with lower value of the first ionization potential (FIP) are systematically in excess relative to higher FIP ones. Authors in [19] have shown that the galactic cosmic ray composition is best described in terms of a predominance of refractory elements (low FIP values) relative to volatile ones (high FIP) and that among the volatile elements, the abundance of heavier elements is also enhanced. The mass dependence is most likely explained by a dependence of the acceleration efficiency of cosmic rays to the mass-to-charge ratio of the accelerated species. The observed composition can be interpreted in the context of acceleration by supernova shock waves. The over abundance of ^{22}Ne is best explained by the scenario of a star exploding in the metal enriched environment of Wolf-Rayet type stars, pointing to *super-bubbles* as astrophysical sites for cosmic ray production, hence supporting the main SNR paradigm.

---

[3] `http://www.srl.caltech.edu/ACE/`

2.2.3 Other Interesting Particles

Anti-matter particles like anti-protons and positrons are thought to be largely of secondary origin. Wether a significant portion of these particles is of primary origin is a crucial question. As was discussed in 1.4.2, the observed excess of positrons in the flux of cosmic rays is of high interest for scenarios of new physics like dark matter. The alternative explanation establishes pulsars as the source of these positrons, therefore adding new input to the picture of the cosmic ray origin. The existence of anti-stars somewhere in the universe is not forbidden but if they were to be at the origin of a small flux of primary anti-matter such as anti-protons and positrons, then they should also produce heavier anti-matter nuclei. The observation of only one single anti-helium nucleus would be strong evidence for the existence of large amounts of anti-matter in the Milky Way. Either heavy anti-matter will be detected in the near future by the ever more sophisticated instruments like AMS-02, or even more stringent upper limits will be placed (see 1.4.1).

2.3 Origin : the SNR Paradigm

The combination of the theory of diffusive shock acceleration and diffusive propagation in the Galaxy to explain the observed cosmic ray properties is usually what one refers to as the current *supernova remnant* paradigm. Although no definite proof has been provided, it is yet our most convincing account of the origin of galactic cosmic rays. Following the lines of the recent and detailed review given in [1], we summarize in this section the main ingredients of the SNR model.

2.3.1 Basic Facts

As discussed in section 2.2, the most reasonable way to explain the apparent similarity between the observed cosmic ray composition and the solar system elemental abundances is to assume that cosmic rays are produced in similar stellar fusion processes and that discrepancies between the solar and GCR composition results from secondary productions. The presence in the cosmic ray flux of long-life radio isotopes like ^{10}Be or ^{36}Al, with respect to the absence of isotopes with shorter lifetimes, gives an estimation of the propagation time of cosmic rays of the order of 10^7 years for particles with GeV energies [60]. This estimation is consistent with the time-scale needed to interpret the observed ratio of secondary to primary nuclei like boron and carbon. This is yet the best argument to support the assumption that cosmic rays propagate diffusively in the Galaxy, being deflected many times by randomly oriented magnetic fields. Based on the observed fluxes at the top of the atmosphere, the energy density of cosmic rays amounts to $\sim$1 eV/cm^3. The power required to sustain such intensities in our Galaxy is estimated to be 10^{41} ergs/s. In 1934, Baade and Zwicky [61] already suggested that with the observed rate of 3 supernova events per century in a typical galaxy, only a 10% efficiency in particle acceleration by these objects would be necessary to account for the observed cosmic ray density. The acceleration mechanism itself remained a mystery until Fermi proposed his theory of diffusive shock acceleration in 1949 [62] where particles are accelerated through collisions with moving magnetized clouds. The concept developed by Fermi was further elaborated based on the clouds being the strong shock fronts powered by SN explosions and propagated from a SN remnant to the interstellar medium. Diffusive acceleration at the strong shocks of SNRs started giving a more comprehensive picture of the cosmic ray story. Many problems remain however to solve.

2.3.2 Diffusive Acceleration

Fermi considered the situation in which charged particles are reflected from *magnetic mirrors* associated either with some moving magnetized clouds or with irregularities in some large scale magnetic field. He showed that such encounters allow the particles to gain energy stochastically. The gain in energy was however calculated to be only second order in v/c (where c is the speed of light) which made the process quite inefficient in terms of cosmic ray acceleration given the low values of v observed in astrophysical environments. Only few GeV could be achieved by this mechanism. Although incapable of accounting for the high energies observed in cosmic rays, the concept that the electric field induced by moving magnetic fields could accelerate charged particles was revolutionary in itself. Moreover, the theory proposed by Fermi had the very interesting feature of producing particles according to a power-law distribution :

$$N(E)dE = const \times E^{-\nu} dE \tag{2.3}$$

where $\nu = 1 + (\alpha\tau_{Esc})^{-1}$, the parameter α encoding the properties of the acceleration process and where τ_{esc} is taken to be the time the particle remains in the acceleration region before escaping. Nothing in the theory did however tell us what should be the value of ν and if it should match our observations of fluxes at Earth.

First-Order Diffusive Acceleration

During a supernova explosion in the interstellar medium (ISM), metal enriched ejecta are created and travel through the ISM at highly supersonic speeds close to 10^4 km s^{-1}. This results in a strong shock front wave propagating at supersonic velocities. When crossing the shock front, particles are scattered by magnetic instabilities and turbulent motions. Their velocity distribution becomes rapidly isotropic with respect to the shock front reference system. The application of the Fermi acceleration mechanism to such situations was formulated independently by several physicists in the 1970s, leading to the theory of first order diffusive acceleration. The most important feature predicted by the theory is that particles now gain energy each time they cross the shock, irrespective of the arrival direction. The average fractional energy increase for particles performing a round-trip through the shock was calculated to be :

$$\left\langle \frac{\Delta E}{E} \right\rangle = \frac{4}{3}\left(\frac{v}{c}\right) \tag{2.4}$$

Now being first order in v/c, the acceleration mechanism is much more efficient. The resulting spectrum of particles remains a power law with a spectral index identical for all particles, mainly dependent on the properties of the shock front. For strong shocks (characterized by a big compression factor), the spectral index takes the value -2, not so far from cosmic ray observations at Earth.

There is a crucial limitation to the picture discussed here. The concept of maximum energy is not naturally embedded in the theory, and the energy cut-off has no limit. This is an artifact of the assumption, within most common models of diffusive acceleration, that the shock front is stationary in time. The question remains : can first-order diffusive acceleration explain energies up to the knee ? The definition of the maximum energy is rather ambiguous because it can be based on very different considerations. The age of the SNRs or more precisely of its shock front relates this energy threshold to the maximum acceleration time. The best models tend to show that the highest energies are achieved during the accelerated ejecta dominated phase of the remnant evolution which is indeed much shorter than the total SNR life-time. It is also reasonable to assume the existence of a spatial boundary at which particles can escape the acceleration region which further limits the total acceleration time. The predictions of the most realistic models available barely reach an energy of 10^{14} eV, which is insufficient to explain the knee.

Non-linear Diffusive Acceleration

The next step in the quest to explain higher energies came from the consideration of non-linear effects in the diffusive acceleration process, hence the theory of non-linear diffusive acceleration. In almost all realistic cases, the assumptions within the most common models of diffusive acceleration break down. SNRs have a finite age ($\sim 10^6$-10^7 years) and the stationary shock front assumption is probably appropriate for very small time phases of the evolution. The pressure exerted by the accelerated particles on the shock front must affect the shock dynamics and therefore the acceleration process itself. Interestingly, these plasma instabilities have been theoretically linked to a mechanism of magnetic field amplification that can account for acceleration to much higher energies than in the stationary model. Even more convincing is the fact that the existence of these magnetic field amplifications is yet the best explanation for the observed bright and narrow X-ray rim of thermal emission observed from virtually all young SNRs (see 2.3.3). Such magnetic fields must in turn affect the shock region which again affects the resulting spectra of accelerated particles. All these effects show the intrinsically non-linear nature of the acceleration process taking place. The description of magneto-hydrodynamic effects is extremely difficult and strong efforts are put in this field of study to achieve a better understanding of the global picture of cosmic rays acceleration.

The Escape Problem

A realistic description of front shocks must take into account the fact that the shock is observed to slow down in time, most likely due to mass accumulation. In some regions the shock might be broken, allowing some particles to escape. It is reasonable to expect that at some distance from the shock the particle density drops which also favors an escape of the particles at the tails of the distribution. All these effects tend to further limit the maximum energy attainable through the acceleration. The physics of particle escape from SNR shocks remains one of the most poorly understood aspects of the SNR paradigm. In the absence of a reliable formal description, the common practice has been to introduce a spatial boundary (usually at some fraction of the shock radius) at which the particles are free to leave the acceleration region. Formally, this is introduced in the models as a transition in the value of the diffusion coefficient, going from small values in the shock region to values close the ones expected for the propagation in the Galaxy.

Particle Spectra

Considering all the uncertainties in the models, a precise modeling of the particle spectra is difficult. It requires the knowledge of the instantaneous spectrum of all accelerated particles at any time of the SNR evolution, the associated temporal evolution of the maximum accelerated energy as well as a description of the mechanisms of particle escape. Moreover, an exact calculation should take into account different types of SNRs and the environments in which the explosion takes place. A detailed simulation is clearly not feasible. The main approach is to consider different characteristic cases and study the resulting variations in the obtained spectra. In [63], authors found that all spectra end up being very close to the initially predicted E^{-2} power law. This result is problematic because to account for the spectral index of the fluxes observed at Earth (~ 2.7), one must require a diffusion coefficient in the propagation through the Galaxy proportional to $E^{0.7}$. Such diffusion values would imply very strong small-scale anisotropies that are currently not observed.

2.3.3 Experimental Evidence

There are now very few doubts that cosmic rays are accelerated in supernova remnants. The important questions are wether all cosmic rays come from SNRs and can diffusive acceleration explain energies up to the knee. No conclusive element has yet been found to answer either of these questions. The evidence for the presence of cosmic rays inside SNRs is given by few independent facts, all based on the detection of electromagnetic radiation. Gamma-rays associated to the production of neutral pions have been seen in several SNRs. Very bright X-ray emission in the shape of rims are detected from almost all young SNRs, giving strong support for the existence of magnetic field amplification in the shock regions.

Figure 2.5 shows a picture of the famous SN-1572 remnant, also known as the Tycho SNR. This remnant was made famous because it was first observed in the sky by the Danish astronomer Tycho Brahe back in 1572. The image is taken by the Chandra X-ray observatory, an X-ray telescope orbiting up to 139.000 km above the Earth surface. Low energy X-rays (reddish emission) are associated with the expanding debris of the explosion while the blueish rim corresponds to a much higher energy component usually associated to the presence of very high energy electrons at the shock front producing synchrotron radiation. To explain the observed radiation, one must assume the presence of magnetic fields of the order of $\sim 300\mu$G. In the context of non-linear diffusive acceleration, such magnetic fields could easily accelerate protons to several hundreds of TeV, very close to the knee. Recently, the Fermi-LAT [64] and VERITAS [65] collaborations have measured the source in the GeV and TeV range. Several authors have modeled the observed spectrum and found it is best explained by a hadronic origin [66, 67]. The models use however very different assumptions on the type of environment around the shock. Another system for which the same conclusions are obtained through analysis of the multi wavelength spectrum is SNR RXJ1713.7-3946. X-ray rims are observed for virtually all young SNRs.

A very interesting astrophysical scenario is when a SNR is found close to a molecular cloud. The cloud constitutes a target for the potential cosmic rays accelerated by the SNR which are expected to produce γ-ray emission due to $\mathrm{pp} \to \pi^0 \to 2\gamma$.

2.3.4 Other Astrophysical Objects

A useful qualitative understanding of the potential astrophysical sources capable of accelerating cosmic rays at the observed energies is provided by the famous Hillas criterion. The latter is a simple geometrical condition that implies that the Larmor radius of a particle cannot exceed the accelerator size, otherwise the particle will escape the acceleration region and not gain further energy. The acceleration region is characterized by its size R and magnetic magnetic flux density B. Based on Faraday's law, $\nabla \times E = -\partial B/\partial t$, one can write $E/R \sim B/(R/u)$, where R is the typical size of the acceleration region and u the speed of the shock front, assuming the acceleration process taking place is some kind of diffusive acceleration. Thus $E \sim Bu$ and for a particle of charge Ze accelerated by the induced electric field :

$$E_{\max} = \int zeEdx = zeBuR \tag{2.5}$$

The relation can be re-written in a more convenient form, unit wise :

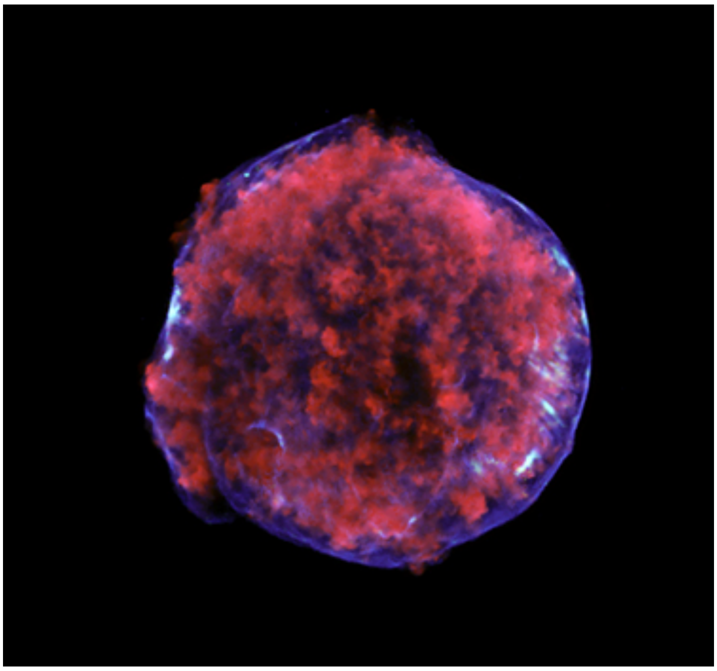

FIGURE 2.5 – Remnant of SN-1572 as seen in X-ray light from the Chandra X-ray Observatory [5]. The blueish rim at the edge of this type Ia SNR is the first evidence for magnetic filed amplification at the shock front of SNRs.

$$E_{\max} \leqslant 10^{18} \times Ze \times u \times B_{\mu G} \times R_{kpc}[eV] \tag{2.6}$$

where $B_{\mu G}$ is the magnetic field measured in micro Gauss, R is measured in kilo parsecs and Ze is the charge of the accelerated particle. The best way to understand this relation is to look at Figure 2.6. This plot, called the Hillas plot, shows a classification of astrophysical sources in terms of their magnetic field B and size R. The blue (red) line represents the conditions for B and R to explain different energies of proton (iron) cosmic rays, while the grey blobs represent conservative approximations of the size and magnetic field for different astrophysical objects. The lines for proton and iron have been drawn for different properties of the shock front, namely non-relativistic shocks ($u/c = 1/300$) like the ones we have discussed for SNRs, and potential relativistic shocks ($u/c = 1$) assumed to take place in Active Galactic Nuclei (AGNs). Based on this picture we see that SNRs are expected to accelerate protons to energies slightly higher than 10^{12}eV. In fact, based on equation 2.3.4 and characteristic values of u,B and R, one finds a maximum energy around 10^{14} eV. This is in reasonable agreement with the predictions of diffusive acceleration. This suggests that as expected, this picture is too simplistic if one were to add predictions of non-linear diffusive acceleration. Accelerating iron nuclei to 10^{20} eV, based on a non-relativistic shock front, clearly requires huge magnetic fields which seem to be only achievable in so-called magnetars, a particular type of neutron star with an extremely powerful magnetic field. Based on relativistic shocks however, active galactic nuclei (extra-galactic objects) are a suitable candidate to accelerate cosmic rays to the highest energies. This simple conclusion has been given support by the results of the Pierre Auger collaboration who claims the observation of a correlation of their highest energy events (> 57EeV) with the position of known AGNs (2.1.5).

---

[5] `http://chandra.harvard.edu/photo/2011/tycho/`

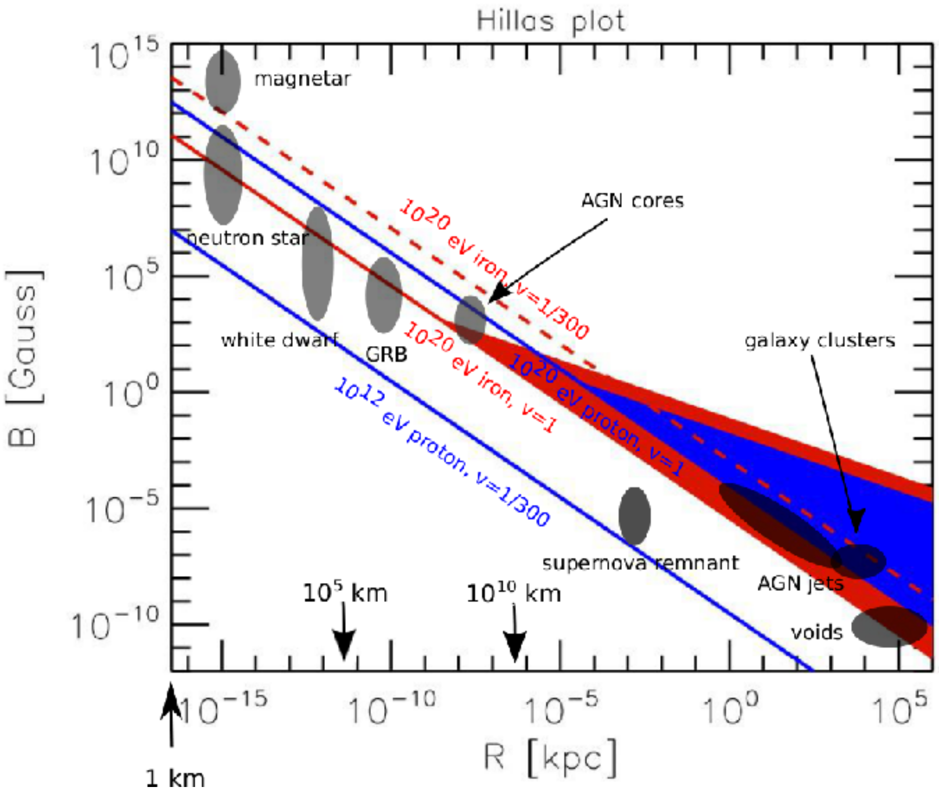

FIGURE 2.6 – Hillas plot : the lines represent the maximum energy of a proton (blue) and iron (red) in different accelerator sites (β=1/300 for non-relativistic shock, β=1 for relativistic shocks). The gray blobs in the plot are characteristic of the astronomical objects magnetic field sizes and radii. Any class of objects above the diagonal line will be able to accelerate the proton/iron nuclei to the marked energies. Picture taken from [68].

2.4 Cosmic Ray Propagation

Modeling the spectra of cosmic rays observed at Earth is extremely challenging. The reason is that what we measure is essentially the convolution of a complex interplay between different physical processes occurring at very different temporal and spatial scales. Cosmic rays originate from some production mechanism assumed to be similar to nuclear synthesis in stellar environments. They are then accelerated inside the sources, at some point escape from the acceleration region and propagate through the Galaxy (or the Universe for extra-galactic cosmic rays) until they are eventually detected at Earth. Propagation models incorporate the knowledge from direct cosmic ray measurements, the interaction cross-sections from accelerator experiments, the gas distribution and galactic magnetic field configurations from astronomical observations, to try to fill the gap between production and acceleration at the source and Earth observations. We will give in this section a brief review of these various ingredients. Precision measurements from AMS-02 will be extremely useful in better constraining some parameters of the propagation models.

2.4.1 Propagation Models

The most constraining information we have in our hands is the experimental observation at Earth (by balloons or satellite experiments) of cosmic ray spectra. These measurements reflect the properties of cosmic rays locally and it is evident that once injected from their sources into the interstellar medium, charged particles are affected by a number of processes that can potentially alter their spectra. The Galactic Magnetic Field leads to the diffusion of cosmic rays. Higher energy particles tend to be more efficiently diffused and escape the Galaxy more rapidly while the lower energy component remains confined for longer durations. The irregularities in the magnetic field itself can lead to so-called diffusive re-acceleration of the particles. The presence of Galactic winds leads to a form of convection. Finally, while traversing the interstellar medium, cosmic rays suffer a number of energy losses and spallation processes. Energy losses predominantly affect electrons and positrons through Compton and synchrotron radiation as well as Coulomb interactions, ionization and bremsstrahlung at the lowest energies. Nuclei may undergo spallation processes where the destruction of the impinging particle leads to a secondary flux consisting of γ-rays from neutral pions decay (the galactic diffuse γ-ray emission, see 2.4.3), electrons and positrons (from the charged pions), protons and other nuclei. One also expects a copious amount of neutrinos to be produced in these interactions. Spallation is determined by the nuclear cross-sections involved and by the density and distribution of the interstellar gas. The latter is essentially composed of hydrogen and helium, an essential ingredient to the calculation of the spallation rate.

All these ingredients are combined into a transport equation for a given cosmic ray species. To solve the equation, one must make a certain number of additional assumptions. Conventional propagation models, that are able to reproduce quite well a number of observed data, typically assume a steady state of the cosmic rays. This is justified by the observation that the global structure of the Galaxy is apparently stable over billions of years and that the propagation process should be as well. This points to the question of the assumed geometrical structure of the galaxy, or in this context the shape of the diffusion region. For simplicity, one can usually adopt a cylindrical symmetry, which is also in rough agreement with observations of another spiral Galaxy, NGC 463. The diffusion coefficient is usually taken to be constant inside the diffusive region. The half thickness of the diffusive halo, L, is typically larger than the half-thickness of the galactic disk, $h \sim 0.1$ kpc. The transport equation is solved using numerical integration techniques available as standard tools in software packages such as the GALPROP [6], DRAGON [7] or USINE [69] codes. Assuming most of the ingredients discussed are known to a very deep level (which is not the case in reality), propagation models become useful to probe the parameter space of an unknown parameter by requiring a match to the known observables.

2.4.2 Constraints from Observations and Secondary to Primary Ratios

The distribution of neutral hydrogen in the galaxy has started being established already since the 1950s through the observation of a specific transition radiation line at $\lambda = 21.1$ cm. Molecular hydrogen H_2 is harder to detect because it has no electric dipole moment and no rotational transitions can be observed. Few detections were however performed by the Copernicus satellite in absorption in the ultraviolet and showed molecular hydrogen must be present in large quantities in the interstellar gas. Later, new surveys started establishing more precisely the distribution of H_2 through the observation of the strong radiation line of carbon monoxide, CO. The fact is that wherever CO is detected, there must be molecular hydrogen since the excitation mechanism for the CO molecules is related to the collisions with H_2. The main observation is that both distributions of neutral and molecular hydrogen are confined to the plane of the Galaxy but exhibit very large differences with increasing distance from the Galactic center, as can be seen in Figure 2.7. Without any feeding mechanism, the interstellar gas would end up cooling down which is in contradiction with the observation of various phases of wide temperature differences. The standard picture is that the gas is continuously fed by new matter, probably coming in great part from supernova.

---

[6] `http://galprop.stanford.edu`

[7] `http://www.desy.de/~maccione/DRAGON/`

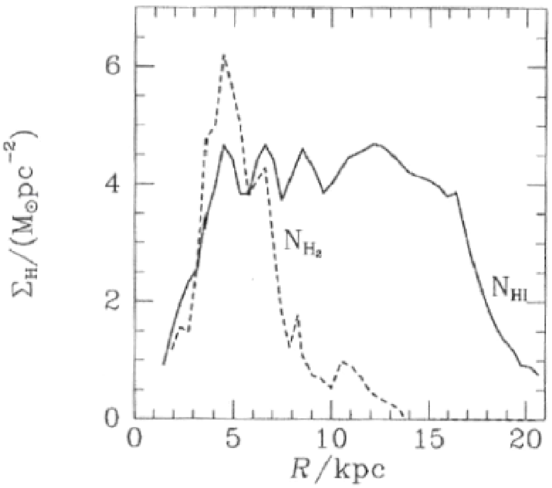

FIGURE 2.7 – Radial distribution of atomic and molecular hydrogen as deduced from radio surveys of the Galaxy in the 21-*cm* line of atomic hydrogen and from millimetre surveys of the molecular emission line of carbon monoxide [70].

Regarding the structure and magnitude of the Galactic magnetic field, a variety of techniques give complementary informations. We do not discuss this lengthy topic here but a summary of these techniques and results is given in Chapter 12 of Longair [71]. The magnetic fields form spiral patterns (in galaxies presumably like ours) and are usually modeled by a typical average equipartition strength of about 10 μG.

Secondary-to-primary nuclei flux ratios can be extremely useful to constrain propagation models. In the simple but widely used leaky-box model, one can demonstrate that such ratios are independent from the source injection spectrum. This is not true anymore in a more realistic diffusion model but the dependence is almost negligible [72]. In combination with measurements of abundance of radio-active isotopes, one can estimate the effective column density traversed by cosmic rays, hence the value of the propagation diffusion coefficient.

Maurin et al. have however shown [73] that due to the large uncertainties in almost all ingredients of the models, very different combinations of the propagation parameters can still remain consistent with the observed B/C ratio, which is currently the best measured ratio. In [74], Hooper and colleagues have studied how the expected measurements of AMS-02 of the stable and unstable secondary-to-primary ratios can help constrain the propagation models. Their conclusion is that within the most simple models, parameters can be very tightly constrained by AMS-02 measurements. Again, this ability is significantly reduced if other free parameters are added to the models. Even in the context of more complicated models, the authors claim that AMS-02 data remain of great interest. It would for instance be sensitive to even small amounts of galactic convection. Preliminary results on the boron over carbon ratio have been presented by AMS-02 at the 2013 ICRC conference [75], and should soon be published. AMS-02 results are consistent with previous measurements, showing however an increased precision at high energies. On another hand, it is worth mentioning that without the superconducting magnet from the initial design of the experiment, the loss of resolution at low rigidities will probably not allow to measure the unstable ratio ^{10}Be to ^{9}Be. Such ratio, extensively used in Hooper's work, is useful to constrain the time interval of nuclei since spallation.

2.4.3 Modeling the Galactic Diffuse Gamma Ray Emission

To illustrate the use of propagation models and the role played by some of the ingredients discussed above, we give a practical example based on the modeling of the observed diffused galactic gamma-ray emission. Our discussion follows the lines of the work done by Delahaye et al. [76], which illustrates the level of uncertainties one is dealing with when considering only the effect of uncertainties in nuclear cross-sections and in the assumptions of injection spectra of cosmic-rays based on Earth measurements, hence the importance of new cosmic ray measurements such as the ones expected from AMS-02.

The Galactic Diffuse Gamma Ray Emission

The interaction of high energy cosmic rays with protons and nuclei of the interstellar medium produces charged and neutral pions, π^+, π^- and π^0. Charged pions decay into muons which in turn decay into electrons and positrons of relativistic energies. Neutral pions decay into two γ-rays, inducing a broad photon spectrum with a maximum centered around 70 MeV. This energy peak is a characteristic signature for the process and has been observed in the emission emanating from the Galactic plane. The galactic emission also comprises a leptonic component coming from electrons via inverse Compton scattering and Bremsstrahlung. The hadronic component is expected to dominate although the relative contributions with energy and position in the Galaxy remains uncertain. The analysis of the gamma ray spectra can therefore provide information on the associated spectra of leptons and nucleons in different locations in the Galaxy, a precious information in the discussion of cosmic ray origin. Since the diffuse emission represents a foreground to the extra-galactic diffuse emission and to faint point source detection, its precise measurement and understanding (i.e. modeling) is also of great interest for galactic and extra-galactic astrophysics. In the following, we discuss solely the modeling of the hadronic component of the diffuse gamma ray emission.

Experimental Observations

The EGRET experiment [77] was the first to perform a detailed analysis of the spectral and spatial properties of the diffused gamma-ray emission. Compared to conventional propagation models that were well reproducing the particle spectra measured by balloon and satellite experiments, the EGRET data showed an excess of emission above 1 GeV. This excess led the scientific community to a variety of interpretations (a favorite being the signature of dark matter) and modifications of the propagation models to account for the excess. Among these studies, strong efforts were dedicated to the re-evaluation of the π° production rate in pp-interactions (see for example [78]). It was however shown that the re-calculations with the most recent Monte Carlo codes produced gamma-ray fluxes consistent with previous calculations. More than 10 years after EGRET, the Fermi-LAT mission measured the diffuse emission with an unprecedented precision and observed no excess above 1 GeV [8] [80]. Considering the unprecedented accuracy of the Fermi data, and the new measurements of particle spectra at Earth by experiments like PAMELA, several authors have decided to re-investigate the modeling of the photon emission process.

---

[8] A re-analysis of the EGRET data [79] a few years later showed an experimental issue with the calculation of the instrument sensitivity above the GeV scale which seemed to remove the previously observed excess.

Gamma-ray Emissivity of the ISM

The hadronic component of the diffuse emission is the result of interactions between high energy cosmic ray nuclei (mainly protons and helium) and the interstellar gas (mainly hydrogen). Since photons remain essentially un-affected by their journey through the galaxy, the observed γ-ray emission is the line-of-sight integral over the total emissivity of the interstellar medium (ISM). The total emissivity is the product of the density of the various ISM elements with their specific γ-ray emissivities, which are essentially the rate at which a nucleus of atomic mass A produces γ-rays of energy E per unit of energy and solid angle. In these terms, the differential γ-ray flux observed at Earth can be expressed as :

$$\phi_\gamma(l,b,E) = \int_{los} ds \sum_A n_A(\boldsymbol{x})\epsilon_A(\boldsymbol{x},E) \tag{2.7}$$

where A denotes all the ISM elements. The position $\boldsymbol{x}$ is determined by the galactic longitude l and latitude b and the depth s along the line of sight (los). E is the energy of the photon and $\epsilon_A(\boldsymbol{x},E)$ the associated emissivity. For an hydrogen atom of the ISM, ϕ_p and ϕ_{He} (the impinging proton and helium fluxes), the specific emissivity can be expressed as :

$$\begin{aligned}
\epsilon_H(\boldsymbol{x},E) &= \int_{T_{min}}^{+\infty} dT\{\frac{d\sigma}{dE}(p(T)+H\rightarrow\gamma(E))\times\phi_p(\boldsymbol{x},E) && (2.8)\\
&= +\frac{d\sigma}{dE}(\alpha(T)+H\rightarrow\gamma(E))\times\phi_\alpha(\boldsymbol{x},E)\} && (2.9)
\end{aligned}$$

where the integral runs over the kinetic energy per nucleon of the projectile. One sees from this formula that the fluxes of impinging nuclei need to be known at any position $\boldsymbol{x}$ along the line of sight. This can be done using the fluxes measured at the Earth in combination with some choice of propagation model to compute the fluxes at any location in the Galaxy.

Following the work of Huang et al. [81], the authors consider only proton and helium nuclei impinging on the ISM. For the ISM itself, they assume a constant composition in the Galaxy of the form : 90% protons, 10% helium, 0.02% carbon and 0.04% oxygen. It is then possible to re-express the previous γ-ray flux at Earth in terms of an effective emissivity ϵ_{eff} that encodes the assumed composition of the ISM and the choice of photo-production cross-sections. The red curve in Figure 2.9 shows the calculated emissivity, using as input proton and helium fluxes the results of the BESS spectrometer as parametrized by Shikaze et al. [82]. The cross-sections used are the ones from Huang et al. [81], that we discuss below. The black dots show the data from Fermi. Although the agreement with Fermi is good, there is a tendency for overestimation which is problematic since one expects, although in some rather unknown proportions, additional contributions from the leptonic channel. In this sense the hadronic emissivity should at best always be below the Fermi points and not above. The discrepancy consists of several non-independent factors. One should consider that the Fermi data are averaged over regions of different galactic latitudes, where the assumed distribution of neutral and molecular hydrogen is perhaps not totally reliable (see Figure 2.7). This means the propagated proton and helium fluxes might also be over-estimated. Finally, and core of the present discussion, the uncertainties in the chosen production cross-sections can significantly affect the result.

Photo-production Cross-Section

Over time, several choices of parametrization of the differential and total photo-production cross-sections have been made, depending on the energy range studied, on the available data from accelerator experiments and on the status of simulation codes. The production of γ-rays through π^0 production is thought to be the main mechanism for the hadronic component of the diffuse emission from cosmic ray interactions with the ISM. A number of parameterizations describe this production process in terms of γ-ray production in pp collisions. In this sense, the work of Kamae et al. [83] has been a reference. It was realized that other channels make substantial contributions depending on the energy, such as the direct production of γ's, the production of ($\Sigma^{\pm}$,Σ^0), ($K^{\pm}$,K^0) and η particles. Taking into account the presence of helium nuclei in cosmic rays and in the ISM contributes up to 30% more secondary particles produced. Although in much weaker proportions, other elements enter the composition of the impinging flux and ISM. This should be included in a precise parametrization of the cross-sections. All these ingredients are discussed in the work of Huang et al. [81]. For protons with energies below 2.5 GeV, the cross-sections are given by the parametrization of Kamae et al., which is actually expected to be quite robust up to energies of 50 GeV. Above 20 GeV, the cross-sections are calculated with the DPMJET-III Monte Carlo simulation of pp, p-*nucleus* and *nucleus-nucleus* collisions. In between these ranges of energy, the cross-sections are obtained by linear interpolation between the two previous descriptions. Figure 2.8 gives an example of the predicted γ-ray spectra with the contribution from the different channels.

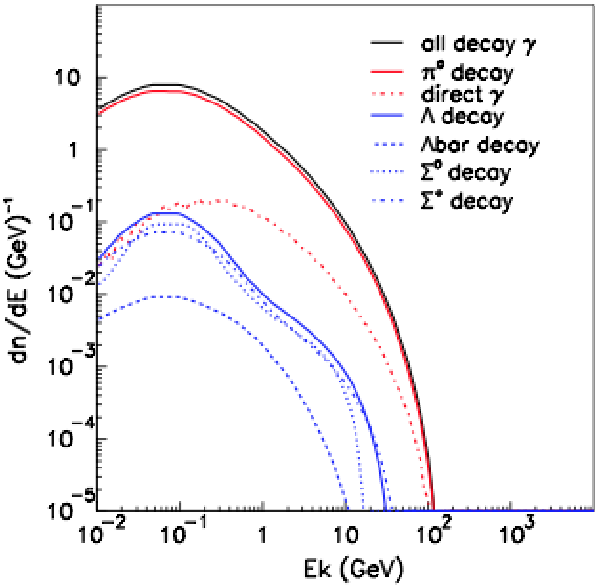

FIGURE 2.8 – Predicted gamma-ray energy spectra from each secondary particle produced in p+ISM interactions for a photon energy of 150 GeV, here only from baryon decay contributions. Plot taken from [81].

The magenta curve in Figure 2.9 corresponds to the emissivity calculated using the Kamae and al. model of the γ production cross-section, which considers pp interactions only. The result is systematically lower than the Huang et al. prediction (red curve). This is expected since the Kamae el al. model is quite restrictive in the number of possible interactions considered (only *pp*). Delahaye et al. [76] then play the game of adding by hand a parametrization of the missing nuclear cross-sections. This is usually done using some scaling function to the better known pp interaction cross-sections :

$$\frac{d\sigma}{dE}(A_i[T] + A_t \to \gamma[E]) \quad = \quad w(A_i, A_t, T, E) \times \frac{d\sigma}{dE}(p[T] + H \to \gamma[E]) \tag{2.10}$$

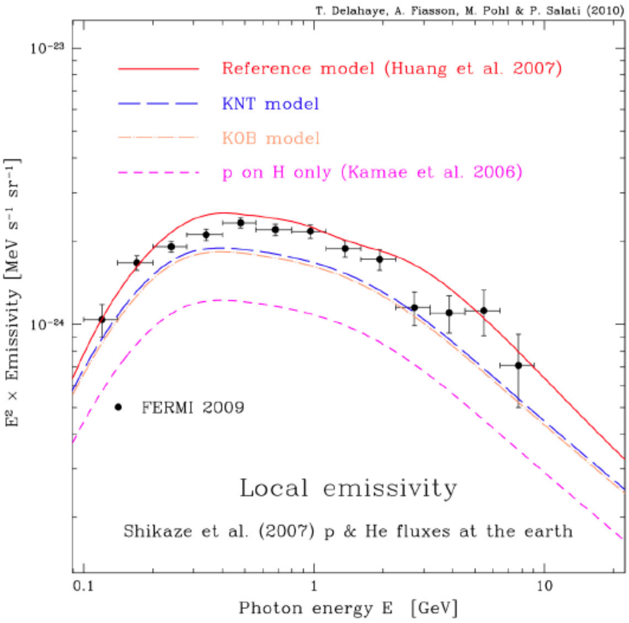

Figure 2.9 – Parameterization of the diffused gamma rays emission [76]. Black points are the local effective emissivity of the ISM per hydrogen atom measured by the Fermi collaboration. The lines correspond to the predictions based on different photo-production cross-section parameterizations.

where w is the so-called nuclear weight factor. It depends on both the target and projectile. The weight factors are related to the number of two-body reactions taking place during the collision between two nuclei (the *nucleus-nucleus* interaction being understood as a collection of incoherent *nucleon-nucleon* collisions). The authors investigate two standard prescriptions used to define the weight factor : the Orth and Buffington (OB) and the Norbury and Townsend one (NT),

$$w_{OB} = ((A_i^{3/8})^2 + A_t^{3/8} - 1)^2 \tag{2.11}$$

$$w_{NT} = (A_i A_t)^{0.8} \tag{2.12}$$

The common practice is to assume that these factors do not depend on the kinetic energy per nucleon of the impinging cosmic ray nor on the outgoing photon energy. This is known to be wrong, especially around the energy threshold for π^0 production. Moreover, it was found that the scaling model fails to predict correct cross-sections at energies below 10 GeV. Such limitations are addressed in the work of Huang et al. Combined with the Kamae et al. *pp* cross-sections, both OB and NT models yield predictions varying within 4% between 100 MeV and 1 TeV. This can be appreciated in Figure 2.9 where the blue (orange) dashed lines are the results for the KNT (KOB) predictions. The parametrization of the Huang et al. model (red curve) is based on the Kamae one at low energies. This is indeed where the differences between the scaling models and Huang et al. are minimized. One still observes differences as much as 54% at 4.5 GeV. This illustrates clearly the level of uncertainties in the photon emissivity calculation due to different assumptions on the parameterization of the cross-sections. The Huang et al. parametrization certainly gives the most precise account of the photon production cross-sections, especially at higher energies where DPMJET has brought considerable improvements. Despite these improvements, standard scaling models appear to be potentially more robust at low energies where standard models tend to over-estimate the emissivity.

Another interesting exercise is to estimate the effect of adding additional elements to the ISM composition. Based on reasonable composition assumptions, we can draw a simple table of the relative additional contribution to the γ-ray flux from each specie. These numbers are summarized in Table 2.4.3. From this table we recover the 30% increase in the predicted γ-ray flux one expects when adding helium to the picture. The importance of adding further contributions is relative to the precision one ought to be achieving, the effect of adding carbon and oxygen being less than 1%. In this perspective, high precision measurements of the nuclei elemental abundance from new experiments like AMS-02 are fundamental. Finally, possible energy dependences should be considered.

A	A/H [%]	w_{NT}	A/H $\times$ w_{NT} [%]
He	10	3.03	33.7
C	0.02	7.3	0.16
O	0.04	9.18	0.41

Table 2.1 – Contribution of the most abundant nuclei species to the diffuse γ-ray emission according to the simple scaling model of Norbury and Townsend. First column gives the assumed ISM abundance normalize to proton. The third column uses the same normalization to produce the expected additional γ-ray flux (in % of the proton contribution).

Nuclei Fluxes at Earth

In Figure 2.10, the authors [76] have plotted the predicted emissivities using the cross-sections from Huang et al. and varying the parameterizations of the proton and helium fluxes measured at Earth. The red curve corresponds to a parameterization of the BESS measurements. The green curve uses the parametrization from Donato et al. based on the same BESS parametrization only below 20 GeV/n.The blue and orange dashed curves refer to the parameterizations done by Lavalle [84] of the CREAM and ATIC data respectively. The spread among the curves of the four different parameterizations can reach as much as a factor 2 at TeV energies. This clearly illustrates the importance of new precision measurements of the nuclei fluxes at higher energies, as well as measurements of the diffuse gamma-ray emission at the same energies. The results from AMS-02 should help decrease significantly some of the current uncertainties.

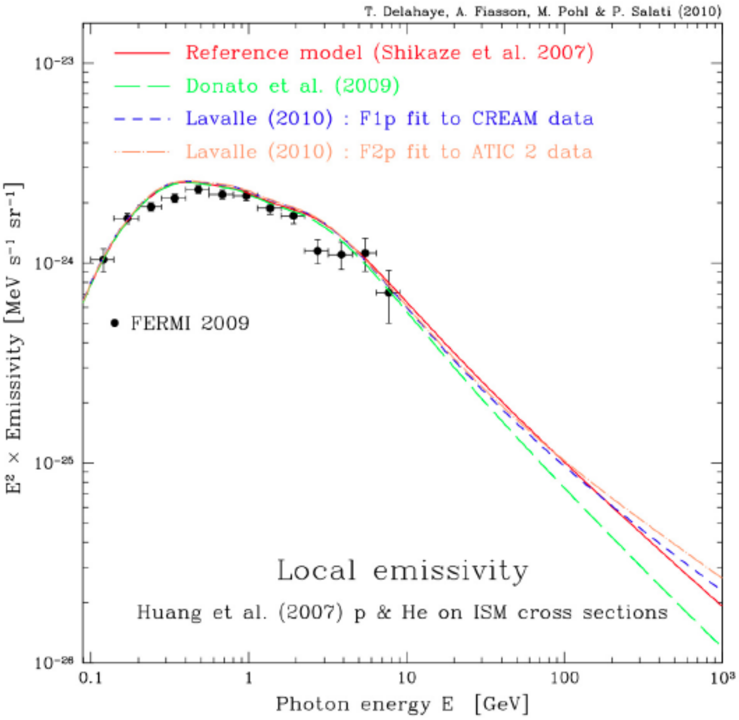

FIGURE 2.10 – Black points are the local effective emissivity of the ISM per hydrogen atom measured by the Fermi collaboration. The lines correspond to the predictions based on different parameterizations of the CR proton and helium fluxes measured at Earth. Delahaye et al. [76].

Chapitre 3

The Alpha Magnetic Spectrometer

> *"C'est la qualité de l'oeuvre qui doit porter et légitimer la technologie et non l'inverse."*
>
> Jean Zeitoun

The Alpha Magnetic Spectrometer (AMS-02) is a state-of-the art particle physics detector operating as an external module on the International Space Station since May 2011. In orbit at an average altitude of 400 km, the main objective of the experiment is to perform accurate, high-statistics, long-duration measurements of the spectra of charged cosmic rays from 0.5 GeV to few TeV energy, and for particle charges up to nickel ($Z = 28$) and perhaps above. These measurements will help addressing fundamental questions in the search for dark matter and antimatter. Moreover, the absolute fluxes of most chemical species in cosmic rays, as well as their secondary to primary ratios, will help constrain models of acceleration and propagation of cosmic rays in the galaxy. Due to its large acceptance and long duration, foreseen to be as much as the ISS lifetime, AMS-02 will also provide an accurate description of the influence of solar activity on the cosmic ray fluxes.

The AMS story is long, starting back in 1998 with a precursor flight using a reduced qualification model of the current AMS-02 instrument. Details about the AMS-01 mission and the scientific results achieved can be found in [85]. In this chapter, we give an overview of the AMS-02 experiment, addressing individually all its sub-detectors. We also discuss the main aspects of operating the detector in space, from the data acquisition chain and the data transfer to ground, up to the final reconstruction of events on ground.

3.1 The AMS-02 Detector

Figure 3.1 gives a schematic view of AMS-02 emphasizing the working principle of the magnetic spectrometer. Figure 3.2 shows a more detailed drawing of the various components constituting the detector. The full instrument weighs a total of 8.4 tons for a volume of 64 cubic meters. The core of the detector is a permanent magnet of hollow cylindrical shape that provides a transverse field of ∼0.15 T. Nine layers of precision silicon tracker are placed along the particle trajectory, inside and outside the field of the magnet. The main trigger for the

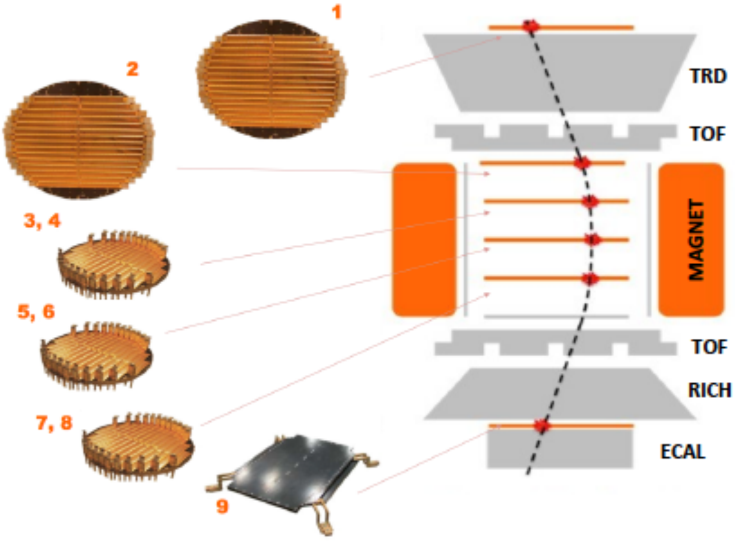

FIGURE 3.1 – Schematic view of the AMS-02 spectrometer [88], presented in the bending plane of the magnetic field. Pictures of the nine silicon tracker layers are also shown.

experiment is given by the Time of Flight system (ToF). The two units, above and below the magnet case, consist of two layers of plastic scintillators oriented in orthogonal directions. The ToF also determines if a particle is crossing the magnet with upward or downward direction and provides a sensitive measurement of the relativistic velocity β with a resolution around 1%. An array of anti-coincidence counters (ACC) surrounds the magnet and acts as a veto against particles traversing the detector sideways. At the top of the instrument is found a transition radiation detector (TRD) which provides excellent particle identification capabilities in separating $e^{\pm}$ from p. At the bottom of the instrument, a Ring Image Cherenkov detector (RICH) provides a high precision measurement of the β with a resolution at the level of 1 *per mille*, as well as a good charge discrimination power. Below the last layer of the silicon tracker stands an Electromagnetic Calorimeter (ECAL) of 17 radiation lengths, serving accurate energy measurements for $e^{\pm}$ and powerful particle identification [86]. In the following section, we give a comprehensive review of all the AMS-02 sub-detectors. Since a significant part of this thesis was dedicated to the charge measurement calibration of the silicon tracker, we discuss in details this detector in Chapter 4. More details on the various sub-detectors can be found in [87] and references therein.

3.1.1 The Permanent Magnet

The permanent magnet of the AMS-01 precursor flight has been reutilized in the AMS-02 construction[1]. A picture of the magnet can be appreciated in Figure 3.3. It is composed by 64 sectors arranged in a cylindrical shape with inner radius of 115 cm, outer radius of 129.9 cm and a height of 80 cm. Each sector is assembled from 100 high grade Nd-Fe-B blocks glued together with epoxy. This arrangement results in a dipole magnetic field of 0.15 T in the ma-

---

[1] The initial design of AMS-02 included a super-conducting magnet. However, due to the announcement by Nasa of an increase of the ISS lifetime, it was decided to profit from this extension by replacing the magnet. The operation of a super-conducting magnet limits the endurance of the experiment to about 3 years due to the incapacity of re-filling the cryostat in space.

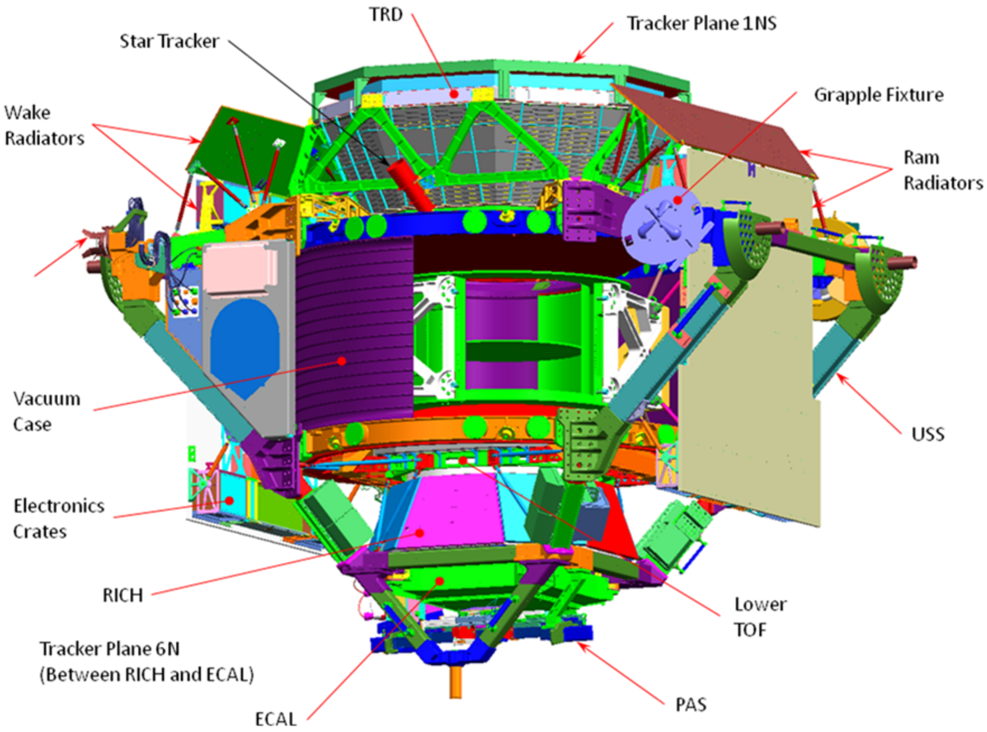

FIGURE 3.2 – Detailed drawing (to scale) of AMS-02 [89]. The various detectors are labelled.

gnet center, with a negligible dipole moment outside the magnet case ($\sim 10^{-2}$ T) to avoid any torque forces on the space shuttle while transportation and on the ISS during the mission.

Due to the almost uniform magnetic field inside the magnetic bore, the permanent magnet also defines the natural reference frame for AMS with its origin at the center of the magnet, as can be observed un Figure 3.3. The Z axis runs along the cylinder's axis of symmetry, with positive values in the direction of the top of the instrument. The X axis is aligned to the magnetic field lines while the Y coordinate describes the bending direction. With this choice of reference, the bent trajectories of all charged particles traversing the magnet are contained in the $Y-Z$ plane.

3.1.2 The Silicon Tracker

The AMS-02 tracking system is composed by 2284 double-sided silicon micro-strip detectors covering an effective area of 6.4m^2. These sensors are arranged in 6 planes placed at different vertical positions in the detector, as shown in Figure 3.1. Six layers are arranged into 3 double-sided planes placed inside the magnetic bore, together with another single-sided plane. The two remaining single-sided planes are placed at both vertical extremities of the instrument. When a particle traverses the silicon material, it produces a signal through ionization. This signal allows to estimate the particle traversing position on the silicon surface, with an accuracy better than 10μm in the bending direction (Y), and 30μm in the non-bending one (X). Moreover, the deposited ionization energy is proportional to the square of the particle charge ($I \propto Z^2$) and can therefore be used to identify the particle. Any charged particle is deviated from its trajectory under the influence of a magnetic field. The reconstruction of the particle trajectory by the tracker is multi-purposed, allowing to extract several complementary informations about the particle :

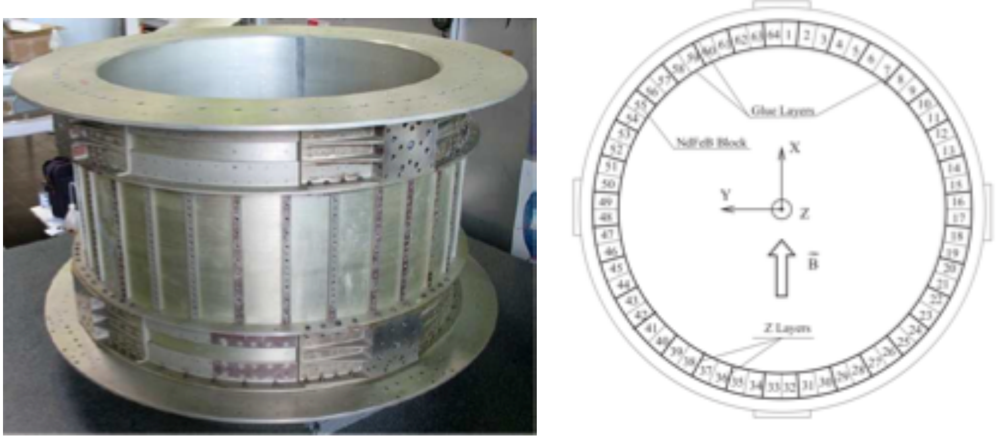

FIGURE 3.3 – *Left* : Picture of the AMS-02 permanent magnet. The very same magnet was operated during the STS-91 Space Shuttle Discovery mission in 1998. *Right* : Magnetic field configuration of the AMS-02 magnet. The uniformity of the field inside the magnet defines the reference frame for the instrument, with its X axis running along the magnetic filed lines, and its Y coordinate describing the bending direction. Pictures taken from [90].

- the particle rigidity from the curvature ($R = pc/Ze$),
- the associated signals in the other detectors,
- the particle charge by the energy deposition in the silicon,
- and the particle charge sign by the sign of the curvature.

The bending power of the magnet is a fixed quantity for a permanent magnet configuration and the capability of the tracker to measure the curvature of the particle in the magnetic field through deviations from a straight line is limited by the resolution in the position determination. This leads to the concept of *Maximum Detectable Rigidity* (MDR). It is defined as the rigidity at which the error on the rigidity measurement is 100%. The rigidity resolution of the tracker is essentially related to two main contributions : the relative position resolution and effects of multiple-scattering inside the detector. With increasing strength of the magnetic field, the bending power increases and allows to probe, with a fixed position resolution, particles of higher rigidities. The multiple scattering component however scales as B/β and is affected by increasing strengths of B. This effect dominates the lowest energies, below 40 GV. Using the AMS-02 inner tracker only, the MDR is around 400 GV for carbon nuclei. However, when adding the two external layers in the measurement of the particle trajectory, one can reach an MDR of about 10 TV. This is due to the increased level arm, which allows to determine with a higher precision the incident and exit angles of the particle trajectory entering and exiting the inner tracker.

3.1.3 The Time-of-Flight system

The Time-of-Flight system (ToF) consists of four layers of 12 cm wide plastic scintillator counters. The layers are arranged into two planes placed above, the upper ToF (UToF), and below the magnet, the lower ToF (LToF). A picture of the lower ToF plane is shown in Figure 3.4. Within a layer, the paddles overlap to minimize geometrical inefficiencies. The paddles of the two layers constituting a plane are positioned in orthogonal directions to provide a rough

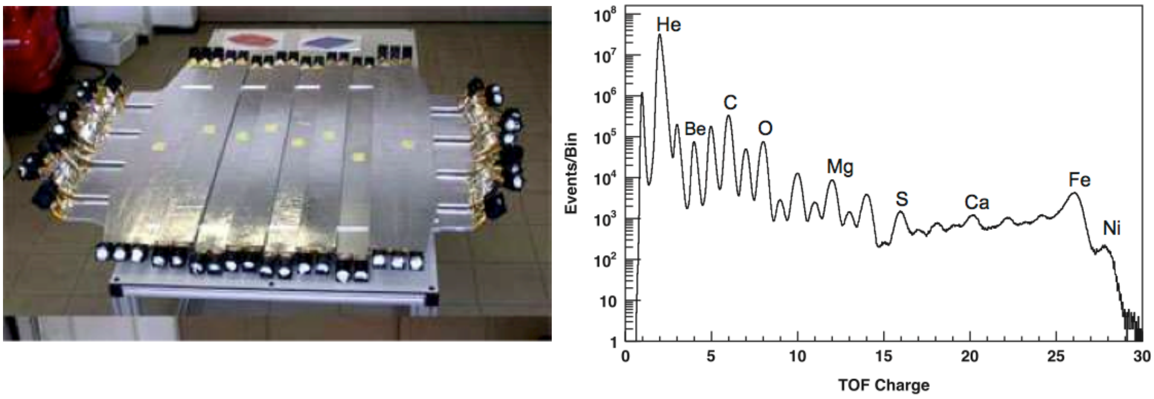

FIGURE 3.4 – The lower ToF plane (left) [90] and the charge measured by the upper ToF plane (right) in a data sample with a pre-scaled H component [91].

bi-dimensional measurement of the position. Each plane has a sensitive area of 1.2 m^2. Both extremities of a paddle are connected through plexiglass light guides to either 2 or 3 photomultiplier tubes (PMTs). The PMT choice and light-guide design was studied considering the proximity of the ToF system to the magnet and the potential effect of residual magnetic field on the electron multiplication process. The PMTs are operated at a high voltage of 1.6×10^3V to further reduce the magnetic field influence.

The ToF covers the full AMS-02 geometrical acceptance. Since the ToF also provides a fast and reliable response to the energy loss of charged particles, it is naturally used to provide the main trigger for the experiment (see 3.1.10). The impact point of a particle can be estimated through the time difference of signals measured by the two ends of the same paddle. The time resolution is measured to be approximately 180 ps for $Z = 1$ particles and below 100 ps for particles with $Z \geq 2$ (48 ps for $Z = 6$), which is enough to discriminate down-going particles from up-going ones at the level of 1 out of 10^9, an important sensitivity requirement for the search for anti-matter. The resulting resolution on the particle velocity measurement is, below few GV, of the order of 4% for protons and 1% for ions [91]. The measurement of the energy loss being to first order proportional to the square of the particle charge, the ToF also provides a complementary measurement of the particle charge with a resolution sufficient to distinguish nuclei up to charge 28 (Nickel) and above (see Figure 3.4, right plot).

3.1.4 The Transition Radiation Detector

The Transition Radiation Detector (TRD) is placed on top of AMS, just below the tracker plane 1 and above the upper ToF. The main purpose of the TRD is to identify electrons and positrons among the overwhelming flux of protons and nuclei traversing the detector. The identification principle is based on the electromagnetic transition radiation (TR) emitted when a charged particle traverses the boundary between two media with different dielectric constants, as the result of the particle's field reformation. The intensity of the TR is roughly given by $I = (\gamma q^2(\omega_{p1} - \omega_{p2})^2)/(3c)$ where γ is the Lorentz factor of the particle ($\gamma = E/mc^2$), ω_{p1} and ω_{p2} the plasma frequencies of the two media, related to the respective dielectric constants, q the charge of the particle and c the speed of light. For particles of the same charge, large mass differences correspond to differences in the γ factor, and hence in the probability of emitting TR. This is the principle that allows to distinguish positrons from protons in the TRD. The discriminating power of the TRD does however decrease when the proton γ factor exceeds 300

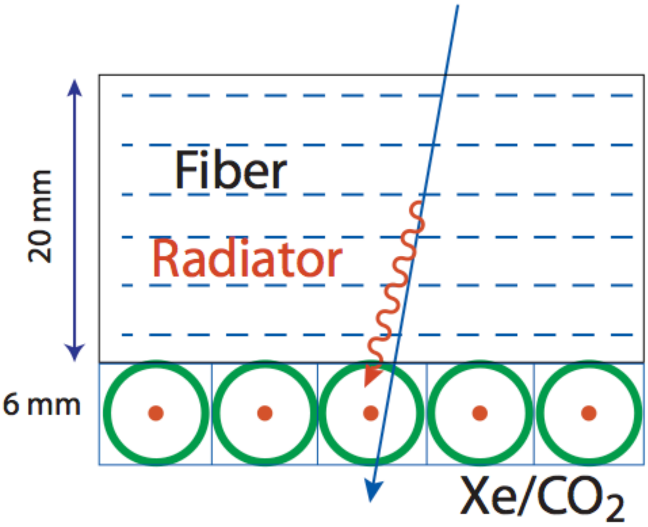

FIGURE 3.5 – Detection principle of the TRD [92]. The Figure depicts a single element of the fleece radiator and proportional chamber layered combination. The AMS-02 TRD is made of 20 of such elements.

where the probability of TR emission then becomes significant.

The working principle of the AMS-02 TRD system is depicted in Figure 3.5. The TR takes places in the 20 mm thick fiber fleece radiator made of alternating polyethylene and polypropylene layers. The radiation is detected in the 6mm diameter straw tubes filled with a 20%-80% Xe-CO_2 gas mixture. The photon detection principle is based on proportional wire chambers, where the ionization energy loss obeys the Bethe-Bloch formula. The transition radiation probability (emission of 1 photon due to transition radiation) is very low but can be increased through the dedicated choice of materials and multiplying the number of radiator layers. The AMS-02 TRD follows this approach with 20 of such layers. Operating efficiently and reliably such a large gaseous detector in space was among the greatest technological achievements of the AMS mission.

3.1.5 The Rich Imaging Čerenkov Counters

The Rich Imaging Čerenkov Counter (RICH) is placed below the lower ToF plane. It provides a high resolution measurement of the particle velocity β needed for the precise estimation of the mass of the particle, which can be expressed as :

$$m = \frac{p\sqrt{1-\beta^2}}{\beta} \tag{3.1}$$

The tracker provides the measurement of the momentum ($p = RZ$), with a resolution of the order of 8% over a wide energy range. This error propagates to the same level of uncertainty in the mass estimation. To keep the mass uncertainty as minimal as possible, the goal of the RICH is to measure the velocity with a precision of 1 *per mille*. The precise knowledge of the mass is fundamental to address topics such as the isotopic composition of nuclei.

The detection principle is based on the Čerenkov electromagnetic emission produced by a particle travelling in a medium with a speed greater than the speed of light in that medium. A cone of emission is created along the particle trajectory. The opening angle of this cone is

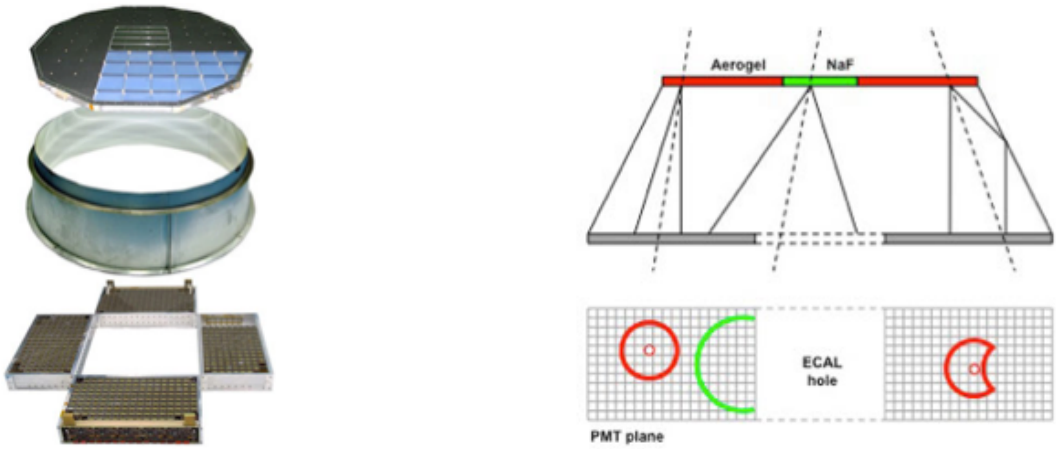

FIGURE 3.6 – Left : exploded view of the various elements of the RICH instrument. From top to bottom : the radiator plane, the conical reflector walls and the bottom layer of PMT detectors. Right : Example of the type of events reconstructed by the RICH. Particles can either emit Čerenkov radiation in the NaF part of the radiator or the silicon aerogel. The ring of the Čerenkov emission cone is reconstructed by the PMTs detected signals. Pictures taken from [89].

related to the particle velocity through $\beta = 1/\cos\theta n(\omega)$ where n(ω) is the refraction index. Moreover, for a particle of charge Ze, the number of radiated photons per frequency unit and unit length is given by $dN^2/(d\omega dx) = \alpha Z^2 \sin^2\theta$. The RICH measurement therefore also provides an independent measurement of the particle charge.

The structure of the RICH detector is shown in Figure 3.6. The detector has a truncated conical shape with an upper radius of 60 cm, a lower radius of 67 cm and height of 60.5 cm. The lower plane shows a 64×64 cm^2 central hole designed to minimize the material in front of the electromagnetic calorimeter. The top plane (grey) holds a dual radiator configuration : a 3 cm thick layer of silica aerogel tiles with low refractive index ($n \approx 1.05$), and a central, 0.5 cm thick, square of sodium fluorine (NaF) crystals of higher refractive index ($n \approx 1.334$) to maximize the Čerenkov light collection above the central hole. The lower plane supports 680 light guides connected to multi-pixel photomultipliers. Most of the photons created in the radiator are directly directed to the bottom plane PMTs. For large opening angles and inclined particles, the photons produced are reflected on the lateral mirrors covering the inner surface of the RICH. Based on the spatial coordinates of the triggered PMT pixels, the Čerenkov cone can be reconstructed. Up-going particles can be ignored since they will not produce any signal in the RICH. The measured velocity resolution reaches $\Delta\beta/\beta = 1.4 \times 10^{-3}$ for single charged particles and $\sim 10^{-4}$ for nuclei. The charge identification capability has been proven to be efficient with a good resolution up to iron (Z=26) [93].

3.1.6 The Electro Magnetic Calorimeter

The AMS-02 Electromagnetic Calorimeter (ECAL) is a lead-scintillating fiber calorimeter providing precise 3-dimensional reconstruction of the longitudinal and lateral electromagnetic shower development. A picture of the ECAL detector is shown in Figure 3.7. The detector is composed of 9 so-called *superlayers* arranged as a square parallelepiped, for a total surface

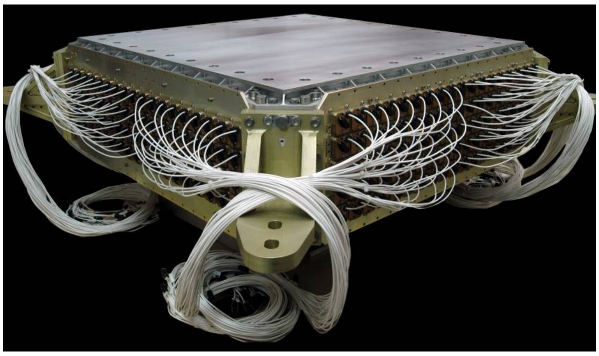

FIGURE 3.7 – Picture of the ECAL detector [90]. Each wire is connected to the PMTs inserted in the lateral slots on all sides of the structure.

at the basis of 65.8×65.8 cm^2 and a height of 16.5 cm. Each super-layer is 18.5 mm thick and consists of 11 lead foils interleaved with layers of scintillating fibers. In a given super-layer, all the fibers run in the same direction. A 3-D imaging capability is however provided by alternating the fibers direction along the X and Y axis in different super-layers. Four layers sample the X coordinate while 5 layers measure the shower development along the Y coordinate. The fibers are connected to 324 photo-multiplier tubes which read the signal.

The main purpose of the ECAL is to provide a high discrimination power between leptons and hadrons, based on the very different characteristic profiles of electromagnetic and hadronic induced showers. When photons and light leptons reach the calorimeter, they interact with the lead material through electromagnetic processes and produce a electromagnetic shower dominated by Bremsstrahlung photons and electron-positron pair products. When reaching the bottom of the ECAL, the particles have either reached the critical energy for absorption in the calorimeter material or start leaking out the detection volume. For electrons and photons entering the central part of the ECAL and with energies below the TeV, the shower is fully contained and the measured energy deposition is directly proportional to the energy of the primary particle. The ECAL energy resolution for electron and photons has been measured [94] and can be described as a function of energy as :

$$\frac{\sigma(E)}{E} = \frac{10.4\%}{\sqrt{E(GeV)}} + 1.4\% \tag{3.2}$$

In combination with the TRD, the ECAL allows for a proton rejection at the level of 10^{-6}. The ECAL can be used as γ-ray observatory, since the direction of the incoming particle can also be obtained through reconstruction of the shower axis. For the purpose of dedicated photon analysis, the ECAL can also be used as an independent standalone trigger.

3.1.7 The Anti-Coincidence Counters

The flux of cosmic ray particles traversing AMS is isotropic. The best analyzing power is for particles traversing the detector from top to bottom, with redundant measurement of the particle properties along the trajectory. It is therefore important to be able to identify and reject particles entering the detector sideways. Such particles don't contribute to valuable information and can cause spurious triggers by interacting with the detector material. This is illustrated in Figure 3.8 where the type of events accepted and rejected based on the ACC information are shown.

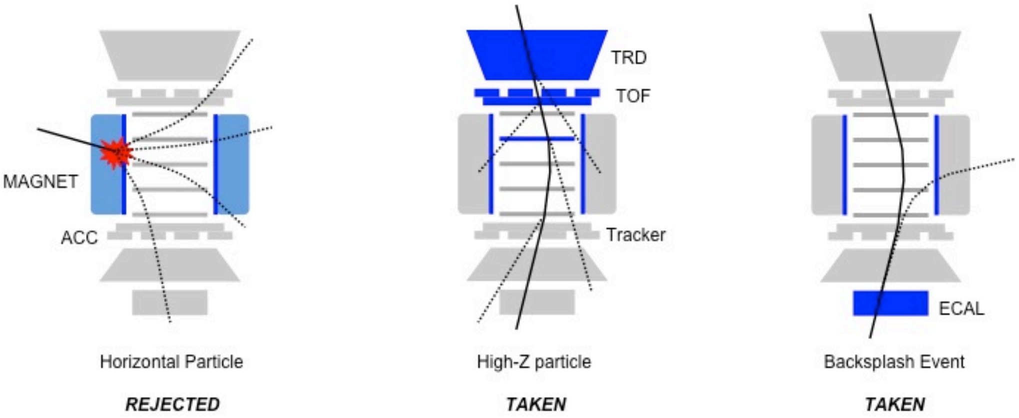

FIGURE 3.8 – Illustration of the ACC purpose in rejecting certain types of events in the AMS trigger [89].

The ACC is composed of an array of 16 scintillation counters inserted into the inner bore of the magnet case such that it surrounds the inner tracker. The signal detected by the scintillators is guided through wave-length shifter fibers to 16 PMTs, 8 on top of the magnet bore, 8 at the bottom. The detection inefficiency has been designed to be lower than 10^{-5}. An impact point determination is also possible. The ACC information is mainly used in the different trigger decisions (see 3.1.10).

3.1.8 The Star Tracker and the Global Positioning System

AMS-02 is able to detect photons in two ways, either through a direct detection in the ECAL (with a dedicated standalone trigger), or from pair conversion in the tracker (a photon converts into a positron-electron pair, the trajectories of which can be reconstructed by the tracker). Both methods deliver an estimate of the photon energy and its arrival direction with respect to the AMS-02 reference frame, within an accuracy better than 1°. To correlate any photon measurement with the position of known astrophysical objects, it is crucial to know the position of AMS in the sky to an even better accuracy. To perform this orientation estimation, AMS-02 is equipped with a Star Tracker, which gives the position of AMS with respect to fixed stars in the sky, i.e. in the sidereal system. Although the International Space Station data bases provide the same information, the Star Tracker is designed to achieve a much higher precision.

The Star Tracker is composed of two CCD cameras placed on opposite sides of the instrument such that if one camera faces the sun (and therefore cannot be used to take pictures of the sky), the other one can always be used. Each camera is made of 512×512 pixels and positioned on top of the magnetic bore edges with a 40° orientation with respect to the AMS-02 zenith. A picture of one camera is shown in Figure 3.9. The pictures taken by the cameras are compared to reference stellar maps and the relative position of AMS deduced.

The time variability of γ-ray sources is one of the main topics related to cosmic photon detection. Such studies require excellent timing capabilities. This is achieved by a Global Positioning System unit (GPS) that allows to synchronise the data acquisition with an epoch of the GPS constellation time. A picture of the GPS unit is shown in Figure 3.9.

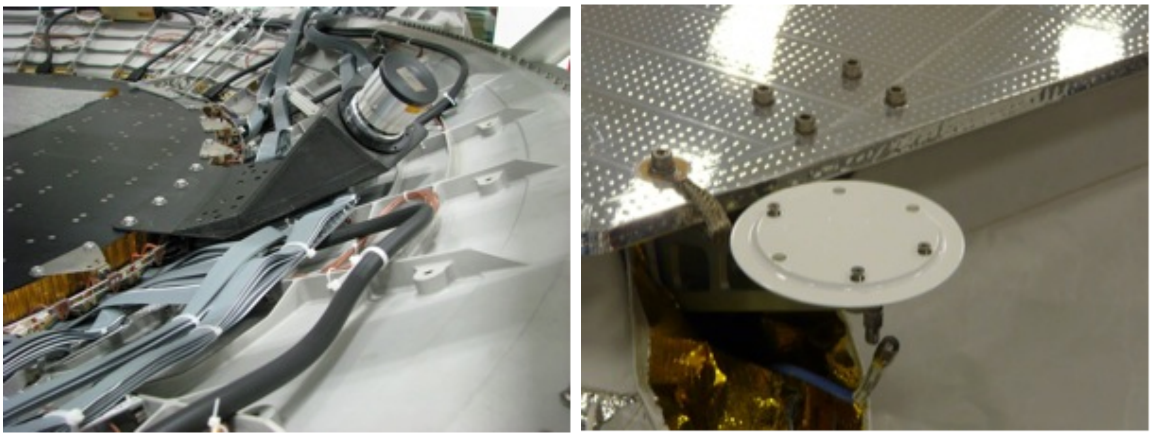

Figure 3.9 – Left : picture of one Star Tracker camera placed on top of the magnet case [90]. The camera points at a 40° w.r.t. the AMS zenith. Right : The GPS receiver integrated on top of AMS [89].

3.1.9 Electronics

The main challenge faced by the design of the AMS-02 electronics was to adapt well-known particle physics electronics to the requirements of space operations. A list of the main challenges faced and the solutions adopted for the integration are listed in Table 3.1. The requirements for the AMS-02 electronics are more demanding than for usual space electronics due to the level of expectations in terms of performances, complexity and resource constraints such as total power consumption and total weight. One must also consider the fact the AMS-02 mission will operate in excess of 10 years with respect to the initial design of the experiment. The durability of the electronics over the years will therefore be of important concern.

Challenges		**Solutions**
Static Loads	$40 + 10 + 10$g	Mechanical Design and Test
Vibration	$6.3g_{\text{rms}}$	Mechanical Design and Test
Depressurization	1 to 0 bar/2 min	Mechanical Design and Test
Zero G	Floaters	Conformal Coating
Vacuum	No Convection	Waste Heat Conduction
Thermal	$-40, +80$°C Survival $-30, +50$°C Operation	Parts Selection Mechanical Design and Testing
Radiation	∼KRad/year	TID Testing
Heavy Ion	Latch Ups, Bit Flips	Beam Testing, Error D/C
Atomic O Solar UV	Etching Aging	Material Selection Mechanical Shielding
EMC	Noise Requirements	Ground, Filter, Screen
Mag. Field	Up to ∼ 500 Gauss	Testing, Placement

Table 3.1 – List of the various technical challenges faced by the design of space qualified electronics for AMS-02. Table adapted from [90].

For the best physics performances, the various sub-detectors must meet clear operational constraints : the gas gain of the TRD must be carefully controlled, the relative timing accuracy of the ToF must be of the order of 100 ps, signals as small as a few femtocoulombs must be detectable in the silicon tracker and single photons must be measurable in RICH and in the ECAL requiring a very wide operational dynamic range. All these requirements and many more add up to more than 300K electronic channels that generate about 3.7 MBit of data for each trigger.

3.1.10 The Trigger Logic

The main purpose of the AMS-02 trigger logic is to take a fast and efficient decision wether a particle crossing the detector has the potential to be well measured by the various sub-detectors or not. The decision is tuned to the particle properties, such as its type (photon, lepton, hadron), its charge, potentially its energy and, to some extent, it's trajectory through the detector (for example, if the particle is in the acceptance of a specific tracker configuration or not). The AMS trigger uses the combined information coming from the ToF, ACC and ECAL sub-detectors, which are analyzed inside a dedicated electronics board, the JLV1 [95]. The processing of all the different signals takes about 1 μs which represents a significant contribution to the dead time of the experiment. This is the time while the detector is in a *busy* state and cannot detect new particles. In order to minimize this dead time, a complex decision tree architecture is adopted with three different stages : the Fast, Level1 and Level3 trigger logics. Only if the conditions of the previous stage are met can the next level be considered. At present, only the Fast and Level 1 Trigger are used for the data acquisition. Following the lines of the presentation given in [96], we give below a brief description of the two trigger levels.

Fast Trigger

The Fast Trigger (FT) is used to make extremely fast decisions that do not contribute to any dead time and activate the Level-1 trigger logic or not. It is based on the signals received by ToF and ECAL. The ToF FT signals are constructed from combination of the digital signals received from the ToF paddles (six signals per plane) and correspond to three different categorical information about the particle :

- **Charged Particle (CP)** : signal constructed from a logical *OR* of all digital signals received from the ToF paddles. The CP is set if at least one paddle signal is above a High Threshold value (HT).
- **Charged Particle in Tracker Acceptance (CT)** : the signal uses only the signals from the paddles inside the Tracker acceptance.
- **Big Z Particle (BZ-TOF)** : same as CP but the digital signals must be above a so-called Super-High Threshold (SHT), which is normally associated to heavier particles (nuclei) traversing the detector.

ECAL produces only two signals based on signal detection in the x or y super-layers. The detection requires a minimum number of neighboring cells are found to have a signal above a given threshold value. The two signals are both logically *OR*ed and *AND*ed to produce two different patterns. The ToF and ECAL signals can then be combined in different logics to produce three different FT categories that can eventually be combined to produce a general FT signal :

- **FTC** : if any of the CP or CT conditions are set.
- **FTZ** : this a dedicated trigger for the detection of potential *strangelets*, particles expected to have a very high charge but to be very slow with respect to ions with the same

charge and rigidity. The FTZ uses the combination of the top and bottom ToF planes in a extended decision time window.
- **FTE** : it is based on the activation of one of the two trigger patterns. If the FTE is alone (no FTC nor FTZ), the trigger is usually representative of a photon detected in the ECAL material only.

Level 1

Based on the existence of a FT, the JLV1 board enters the Level 1 (LVL1) logic evaluation, which takes exactly 1 μs. The following conditions are tested :

- **Charged Particles** : the FT opens a 240 ns gate to latch the CP and CT charged particle signals. Both events with 3 out of 4 ToF planes and 4 out of 4 ToF planes inside the trigger are accepted. The first condition is used to construct the unbiased trigger sample.
- **Big Z Particles** : builds the trigger for ions with looser conditions on the ACC than in the standard Charged Particle trigger.
- **ACC** : the signals coming from anti-coincidence counters are used to veto triggers associated with particles traversing horizontally the AMS detector (see Figure 3.8). ACC signals are also associated with high activity in the detector, typical of heavy nuclei interactions with the detector material.
- **ECAL-F signals** : FTE signals are used to build the unbiased electromagnetic trigger.
- **ECAL-A signals** : used for non converting photons detected in the ECAL only.

These new LVL1 triggers are added to FTE and FTZ signals to produce 8 different LVL1 sub-triggers. Pre-scaling factors from 1 to 1024 can be applied on any sub-trigger. The 8 sub-triggers can finally be *OR*ed to produce the general LVL1 trigger for the experiment. Among the various combinations offered by the trigger flexibility, 7 sub-triggers were carefully chosen for data taking on ISS :

1. **Unbiased charged** : ToF 3/4 (HT) with a 128 pre-scaling factor.
2. **Single charged** : ToF 4/4 (HT), N_{ACC}=0.
3. **Normal ions** : ToF 4/4 (SHT), N_{ACC}<5.
4. **Slow ions** : ToF 4/4 (SHT), extended gate to latch the signals to account for slow *strangelet* particle.
5. **Electrons** : ToF 4/4 (SHT), both x and y ECAL super-layers.
6. **Photons** : an ECAL shower.
7. **Unbiased EM** : ECAL signal over threshold, pre-scaling factor of 1024.

The normal ion trigger was initially defined with no constraint on the number of ACC signals. In the first months of data taking on the ISS, the event size associated with nuclei detection showed to be higher than expected due to abundant interactions of nuclei within the detector material. In order to respect downlink and buffering capabilities onboard the instrument, it was decided to add a maximum number of ACC counts in the trigger definition.

Live-Time

The constraint of minimizing the experiments dead-time depends on several factors. As we have seen, the FT initiates a 1μs time window for the LVL1 evaluation to take place. Based on a LVL1 trigger, the various sub-detectors start the digitization of the signals. Although carried out in parallel, a 200 μs additional dead-time is introduced. Finally, the compression of the collected signals can take up to $\sim$300μs. The associated dead-time is kept as low as possible by allowing the compression to take place in parallel to the digitization of the following event. This strategy is efficient as long as the buffer for the compression is not full, which usually depends on the data acquisition conditions, in particular the trigger rate. To evaluate precisely the live-time, a 20 ns scaler is used to sample continuously the status of the data acquisition, wether it is ready to accept a new event or is in a *busy* state.

3.1.11 The Data Acquisition System

When a charged particle crosses the top and bottom plane of the ToF instrument, or when a particle produces a shower in the ECAL, a trigger signal is initiated and sent to the various sub-detectors to record the potential associated detections. All sub-detectors in AMS-02 are equipped with dedicated Front-End electronics (FE) with a maximum readout time of 90μs which represents, for a trigger rate of 2kHz, a 16% dead-time for the experiment. While the Data Acquisition System (DAQ) collects the signals from these 200K analog channels, its main goal is to minimize the additional dead-time due to signal digitization. A schematic view of the DAQ architecture is represented in Figure 3.10. A dedicated simplified nomenclature has been adopted to identify uniquely each sub-detector : U stands for the TRD, S for the ToF and Anti-Cincidence Counters, E for the electromagnetic calorimeter, T for the Tracker, R for the RICH, and LV1 for the Level-1 trigger module. The architecture adopts a tree-like structure with roughly 300 computational nodes : 264 xDR nodes (DR for Data Reduction and x specifying a sub-detector) that collect the signals from the detector Front-End electronics and perform a first packaging treatment of the data, 28 JINF nodes that collect the data from the xDRs ; 8 SDR nodes that produce the trigger signal based on ToF and ACC information as well as 2 JLV1 nodes that collect both analog and digital information to produce the LV1 trigger. Finally, 4 JINJ nodes collect the data from the JINF, SDR and JLV1 nodes.

All nodes are interconnected through serial wired links and a dedicated communication protocol is used, based on a master-and-slave hierarchy. Data is sent from a slave to its master only upon the master's request. The typical transmission speed is about 7.6 Mbytes/s. Upon a LV1 trigger signal generated by the JLV1 module based on ToF, ACC and ECAL systems, and delivered to the xDRs via the JINFs, each xDR node collects, processes and stores in a internal buffer all the information related to the event. The content of this buffer is further retrieved by the master node upon request. To minimize the dead-time, event buffering is performed at each level of the architecture.

The 4 JMDCs are the main computers on-board the experiment. The JMDC provides the monitoring and the control of the entire AMS instrument. It also contains a large buffer (called JBUX) to store the data, avoiding any science loss when interruptions in the transmission between the ISS and the ground take place. All the data is sent to ground through dedicated NASA interfaces (see 3.2.1) and one can interact with AMS from ground through the JMDC computer. New software and new operation procedures can thus be constantly uploaded to the experiment if needed, despite AMS being in space. This flexibility, added to the high transmission bandwidth provided by NASA for transferring the collected data to ground, makes the AMS mission a truly unique space experiment.

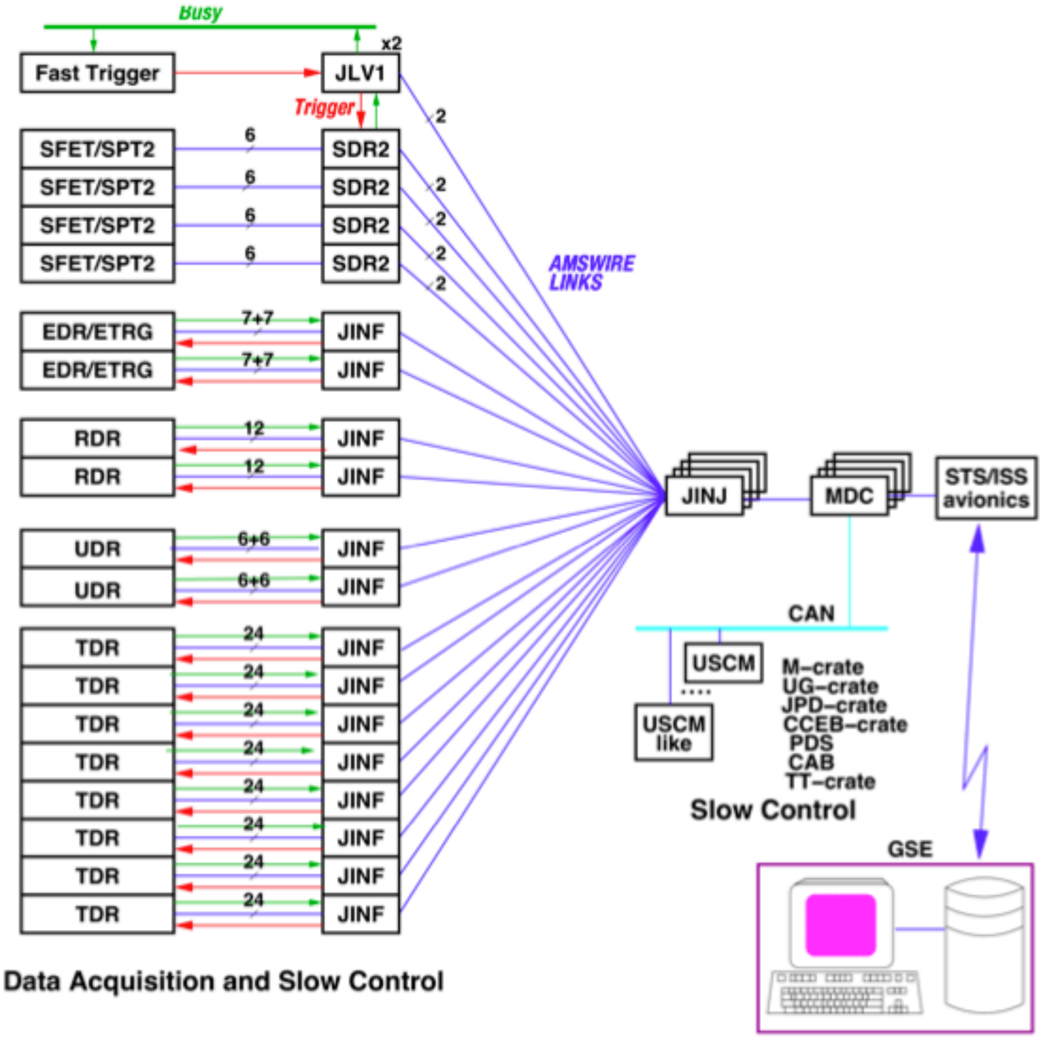
Busy
x2
Fast Trigger
JLV1
Trigger
2
SFET/SPT2
SFET/SPT2
SFET/SPT2
SFET/SPT2
6
6
6
6
SDR2
SDR2
SDR2
SDR2
2
2
2
2
AMSWIRE LINKS
EDR/ETRG
EDR/ETRG
7+7
7+7
JINF
RDR
RDR
12
12
UDR
UDR
6+6
6+6
TDR
24
JINJ
MDC
STS/ISS avionics
CAN
USCM
USCM like
M-crate
UG-crate
JPD-crate
CCEB-crate
PDS
CAB
TT-crate
Slow Control
GSE
Data Acquisition and Slow Control

FIGURE 3.10 – Diagram of the AMS-02 Data Acquisition architecture [90].

The data acquisition is organized in 23 minutes run, such that 4 runs are taken by orbit. Each two runs are intervened by a full calibration of the various sub-detectors. Twice per orbit, a dedicated procedure is used to identify and correct single electronic upsets (bit flips) in all acquisition nodes.

3.2 AMS on the International Space Station

On the 16th of May 2011, NASA's Space Shuttle Endeavour was launched from Cape Canaveral at the Kennedy Space Center (KFC). Few hours later, the first successful power-on of the AMS-02 electronics inside the shuttle was performed from the Johnson Space Center (JSC, Houston Texas) with a first monitoring on ground of various temperatures and electrical currents. On the 19th may, AMS-02 was powered off for installation on the International Space Station. At 4:46 a.m. the same day, AMS-02 was attached to its mission site (Figure 3.11) and the first activation of the full detector in space took place less than an hour later, with the first science data arriving to ground. No damage on any of the sub-detectors due to the shuttle launch was found and all functioning proved to be as expected. Since then, AMS-02 has been collecting cosmic ray data at a rather steady rate of about 10^9 particles per month, almost 90% of which correspond to completely ionized hydrogen.

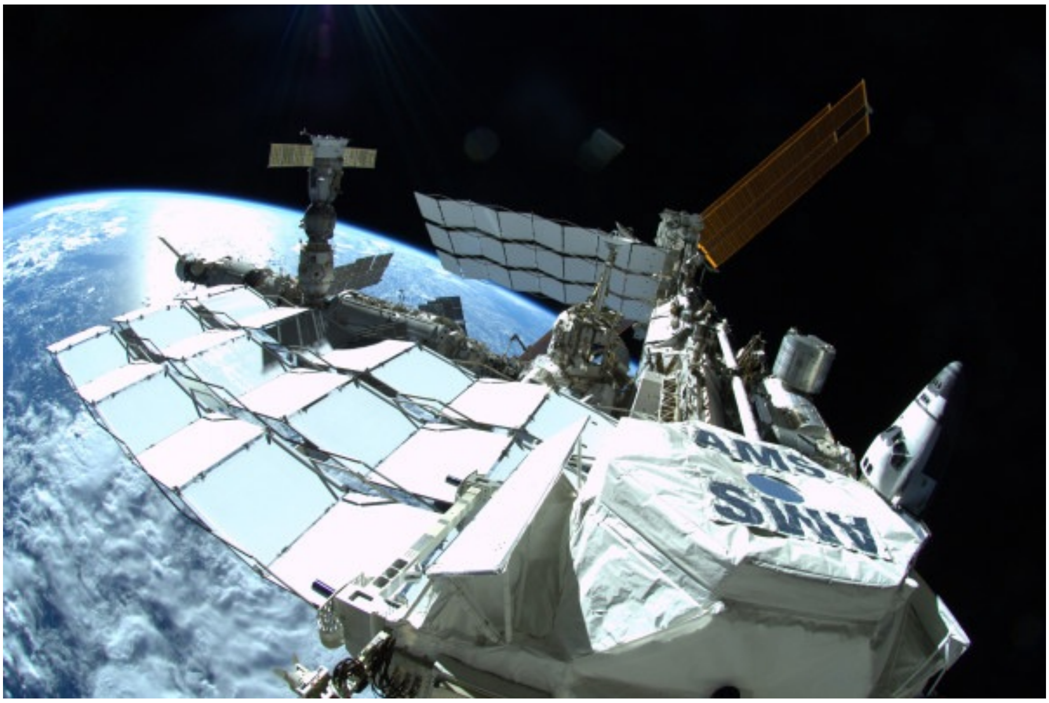

FIGURE 3.11 – Picture of the AMS-02 instrument place on its mission site on the ISS. Credits to Nasa.

The operation of AMS-02 in space is extremely challenging due to the very harsh and constantly changing thermal conditions. Whether AMS-02 is directly facing the sun or deep space results in significant temperature variations, sometimes within a single ISS orbit. The ISS completes 15.7 orbits per day at an altitude ranging from 330 km to 410 km. The performance of the various sub-detectors strongly depends on the precise understanding and control of the effects caused by such important temperature excursions.

3.2.1 AMS on ISS

NASA provides 3 different electrical interfaces to AMS-02 on ISS (see Figure 3.12). After AMS was physically attached to its mission site, all connectors were attached to the payload. The first interface provides the power to the AMS payload. The other two interfaces are data transmission links : the Low Rate Data Link (LRDL) and the High Rate Data Link (HRDL).

Power Interface

The power on the ISS is provided by the eight large solar array panels. The power is distributed to the AMS-02 payload through two feeds with a maximum power draw allocation of 2000 W. To meet the high constraints imposed by NASA in terms of isolation, grounding, inrush current, etc., a dedicated power distribution system (PDS) was developed to distribute the ISS power input to the various sub-detectors. It has been designed to minimize the number of units directly attached to the ISS feeds and to provide the best monitoring, control and protection of the power delivered to each sub-system.

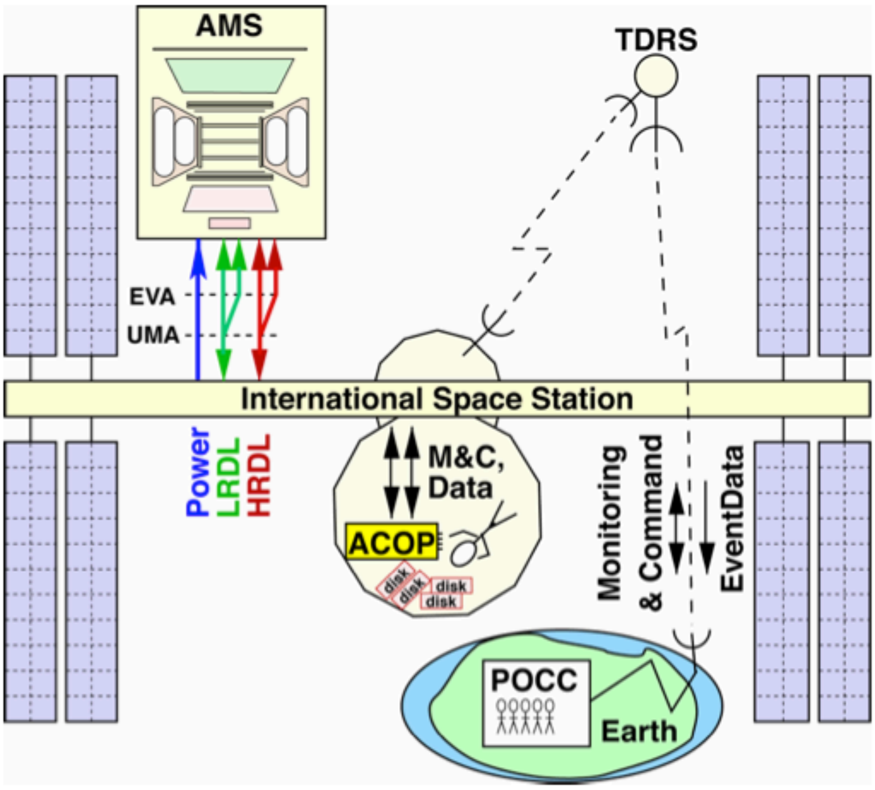

FIGURE 3.12 – Scheme of electrical interfaces between AMS-02 and the ISS [90]. TDRS : Tracking and Data Relay Satellite, POCC : Payload Operations and Control Center, M&C : Monitoring and Command.

Low Rate Data Link

The LRDL is a dual serial bus link (1553B) that is split to each of the four JMDCs. To avoid single point failures, there are two such splitters which can be selected by an astronaut by swapping a cable at the bottom of the experiment during an extra-vehicular activity (EVA). Data sent from JMDC to ground using the LRDL proceeds through various units of NASA and then via radio beam to Earth using Tracking and Data Relay Satellites (TDRS). Around 20 KBits/s of data bandwidth on the LRDL is allocated to AMS-02. The expected duty cycle is about 70%. In addition, ten highly summarized bytes per second of critical health data are transmitted with near to 100% duty cycle. In nominal conditions, all commands to operate AMS-02 originate from the POCC (see 3.2.4) and follow the inverse path. The maximum command rate is about 1 Kbit/second.

High Rate Data Link

A parallel path of data transmission is organized throughout the High Rate Data Link and represents the main path for the data out of AMS-02. The transmission is based on fiber optics communication. Transmission speeds up to 90 MBit/s can be reached on-board the ISS, and the radio down link supports up to 43 Mbit/s, with a duty cycle of about 70%. The high rate link is crucial for the proper operations of AMS-02 considering the high event acquisition rate of the experiment. The average trigger rate is about 600 Hz, but can reach up to 2kHz in regions of low Earth magnetic field. The resulting average event size is about 2kBytes which represents a substantial amount of data to be downlinked to ground. The needed downlink rate is on average 10 Mbits/s. AMS currently operates with a steady value of 13 Mbits/s which can be increased upon request depending on ISS activities.

3.2.2 Thermal Environment and Thermal Control

The primary external factor influencing the temperature of the detectors is related to solar illumination which depends on the angle between the ISS orbital plane and the direction to the Sun, called the *beta* angle (see Figure 3.13). Based on the ISS's orbital inclination (51.6°), the beta angle varies between -75.1° and 75.1° with a strong seasonal modulation. When the beta angle is above 70°, the orbit is entirely exposed to the sun and represents the biggest criticality for AMS.

Since the response of the various sub-detectors is temperature dependent, the operating temperatures must be kept within well defined limits. This constraint is even more complex due to the fact different parts of the instrument are exposed to various amounts of sun-light and undergo very different temperature variations at the same time. All sub-detectors have their own specific thermal requirements for best performances, as well as destructive limits never to be reached. The internal heat distribution inside the detector is complex. All the elements are thermally interconnected by radiation and conduction through common support structures and cabling. A dedicated Tracker Thermal Control System (TTCS) has been developed to maintain the temperature of the inner tracker stable within 1°C. It consists of a two-phase, mechanically pumped loop system, where the cooling liquid is carbon dioxide, CO_2.

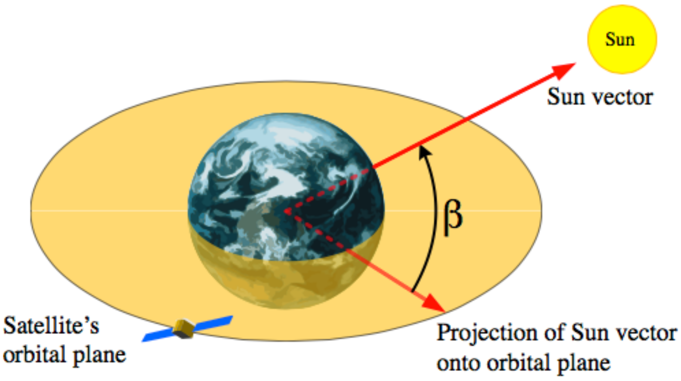
Sun
Sun vector
β
Satellite's orbital plane
Projection of Sun vector onto orbital plane

FIGURE 3.13 – Illustration of the beta angle definition (*Wikipedia*).

A dedicated team controls continuously the thermal conditions of the experiment from ground, analyzing the data received from the payload and performing risk assessments studies for singular events to take place on the ISS or expected high beta angle periods.

3.2.3 The Data Flow from ISS

Two categories of data are buffered into the main JMDC computer : *science data* (SCI), the data associated to the measurement by the various sub-detectors of a traversing particle, and *housekeeping data* (HK), consisting of various informations such as temperature readings, memory program checks (upsets and bit flips) related to the general health and status of the experiment. The latter information is crucial for fast reaction against potential damage of the payload in case of unexpected events. This is why the HK data, in parallel to being buffered in the JBUX, is also directly transferred to ground through the LRDL for real-time assessment of the payloads condition. The buffered SCI and HK data are transferred to ground through the HRDL based on the First In First Out logic (FIFO). This stream can thus be few hours late due to low bandwidth availability or loss of satellite connexion. NASA delivers a schedule of available satellite connexions for each orbit of the ISS. This schedule is loaded inside the JMDC which automatically enables the playback from the buffer. Un-expected losses of transmission from the ISS are unavoidable contingencies of space operations. To avoid any loss of science data, a final copy of the data is sent to a laptop computer on-board the ISS through a wired link. The laptop has a 500 GB hard memory capacity, which allows to buffer approximately one continuous week of data if needed. The data from the laptop are downloaded weekly. The system is flexible enough such that the buffering in JMDC can be by-passed if real-time data is needed on ground. The data are received on ground by high rate radio frequency antennas and directed to the Marshall Space Flight Center (MSFC). A full copy of the data remains in the legal possession of NASA. The data is then copied to CERN and a copy of the housekeeping data is sent to the Taiwan control center (see 3.2.4).

Data from the AMS-02 sub-detectors are collected by the JMDC in blocks of information. These blocks are separated into frames for transmission to ground. One frame corresponds to approximately 4kbytes of information. At ground, the frames are merged into packets before being copied to the CERN location. A dedicated de-framing program then recovers the original block files. These are fed to the event reconstruction software that produces the standard Root [97] files for the analysis. The reconstruction is a time consuming process and new arriving data is queued to already running processes on available computing resources at CERN. In parallel to this standard production, a special reconstruction is immediately started on dedicated machines to provide fast reconstruction of high-level event variables for a close to real-time monitoring of the detectors.

3.2.4 AMS Payload Operation Control Center

The Payload Operation Control Center, the POCC, is located on the French border side of CERN, in Prevessin. It is a single building fully dedicated to the control of AMS-02 operations on-board the ISS. The control center was certified by NASA authorities prior to starting operations. The POCC is occupied every single day of the year, day and night, by a team of experts that monitor the health and status of the payload in successive shifts of 8 hours. A picture of the CERN POCC is shown in Figure 3.14. Five positions are occupied :

- **LEAD** : is the main responsible for the operations inside the POCC. LEAD deals with direct communication with NASA collaborators responsible for ISS activities management (Debris Avoidance Maneuver, astronaut crew activity, etc.). LEAD is the only authority in the POCC to allow commanding actions to the payload.
- **DATA** : the DATA shifter controls the flow of data from the ISS to ground and to the various locations on earth, primarily the CERN POCC.
- **THERMAL** : monitors the hundreds of temperature readings provided by sensors placed in various places in the detector. It continuously assesses potential risks due to up-coming events associated with unexpected temperature excursions.
- **PM** : controls the proper functioning of the RICH, the ECAL and the ToF sub-detectors.
- **TEE** : controls the proper functioning of the TRD and the Silicon Tracker.

Two years after the beginning of the science activities on the ISS, a second POCC center was opened in CIU, Taiwan. Profiting from the different time zones, PM and TEE shifters are

FIGURE 3.14 – Picture of the AMS POCC at Cern Prévessin [89]. A big central screen displays the position of the ISS at any moment in time.

substituted by people in Taiwan during night time in Europe. The LEAD and THERMAL positions remain at all time occupied at CERN, only location allowed to communicate with NASA teams through the official International Voice Loop System (Ivods).

Chapitre 4

The Silicon Tracker

The AMS-02 tracker was build on the model of experiments performed at particle accelerators, where the typical resolution achieved on the position of detected particles is of the order of 10μm. AMS being an experiment in space, constraints on the volume, weight and power consumption of the detector where essential contingencies of the design. In this section, we present the tracker system starting from the basic detecting units, the silicon sensors, up to the full tracker structure as implemented in AMS-02. We also describe how the signal induced in the silicon is digitized and further processed for on-board calibration and data reduction.

The construction of the tracker is described in detail in [98]. Preliminary studies of the charge reconstruction using ion test beams are published in [99].

4.1 Silicon Sensors

The tracker system is composed of 2284 double-sided silicon micro-strip detectors called sensors, with surface dimensions of 72×41 mm^2 and a 300μm thick n-doped silicon substrate. Each face of a sensor is implanted with metallic strips running in orthogonal directions, providing a bi-dimensional measurement of the particle's position. The sensor metallization is such that p-side strips measure the bending coordinate Y, while n-side strips measure the non-bending one X. A schematic view of a double-sided silicon sensor is given in Figure 4.1. The junction side (or p-side) is composed of 14μm wide p$^+$ doped strips, for an implantation (readout) pitch of 27.5 μm (110 μm) ; the opposite ohmic side (the n-side) has 15μm wide strips, for a larger implantation (readout) pitch of 104 μm (208 μm). This makes a total of 2568 implanted strips for 640 readout strips on the p-side and 384 implanted strips for 192 readout strips on the n-side. The discrepancy in the number of implantation and readout strips is justified by the size and power consumption requirements for the payload. One expects the highest resolution on the position to be achieved when all implanted strips are directly readout by the electronics. The configuration discussed here does however not necessarily imply a significant loss of resolution. Indeed, a solution exists by coupling capacitively the strips together such that one can partially recover the information of the signal deposited in between two readout strips. The technological challenge is then to find a compromise between the optimization of the capacitive coupling, which requires a high capacitance between strips, and the limitation of noise, which requires this same capacitance to be minimized. The sensors are biased via the punch-through technique [87, 100], the bias voltage being common to all sensors of a given ladder (see 4.3). The p and n sides are separately connected in different daisy chains to the front-end electronics, respectively named the S and K-side hybrids.

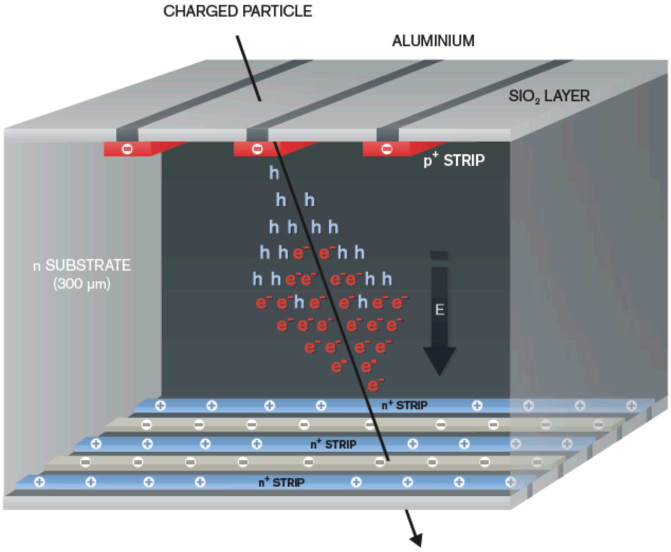

FIGURE 4.1 – Schematic view of a double-sided silicon sensor. Plot created by N. Saouter [1].

4.2 Front-end Electronics and Signal Digitization

The tracker front-end electronics (TFE) provides the coupling between the strips and the digitization system. The low noise capacitive coupling is made through 700 pF capacitor chips. The front-end hybrid design is based on a high dynamic range, 64 channel chip, developed on the basis of the VA and Viking chips [101]. A total of 10(6) VA chips are used to read the signals from the p(n)-side. Each VA readout channel consists of a charge sensitive amplifier, a CR-RC semi-Gaussian shaper and a sample-and-hold stage. The chips are glued on a hybrid circuit board connected to the ladders by a flexible Upilex cable. The dynamic range for a unique channel is around 100 MIPs, with a linear response up to 75 MIPs. The power consumption criteria of $\sim$ 0.5 mW per channel defines the final optimization of the hold delay value. Figure 4.2 shows the structure of the connection between the p-side of a silicon sensor and the associated p-side electronics.

The main electronics for the signal digitization and online reduction are grouped on the so-called Tracker Data Reduction Board (TDR). The analog output from the TFE are multiplexed and sent through coaxial cables to three 12 bits Analog to Digital Converters (ADC) that amplify and digitize the signals. The digitization frequency is 5MHz, a compromise between signal quality and the total reading time of about 80 μs. The flow of data from the ADCs to the memory buffers is controlled by a Field Programmable Gate Array (FPGA) while a Digital Signal Processor (DSP) is programmed to collect the events from the buffers and execute either on-line calibration or data reduction procedures.

4.3 The Ladder Design and Tracker Structure

4.3.1 Ladders

The 2284 silicon sensors are assembled in basic functional elements called ladders. Each ladder is composed of 9 to 15 sensors for a total of 192 ladders and an active area of 6.75

---

[1] `http://www.weworkarts.com/we.html`

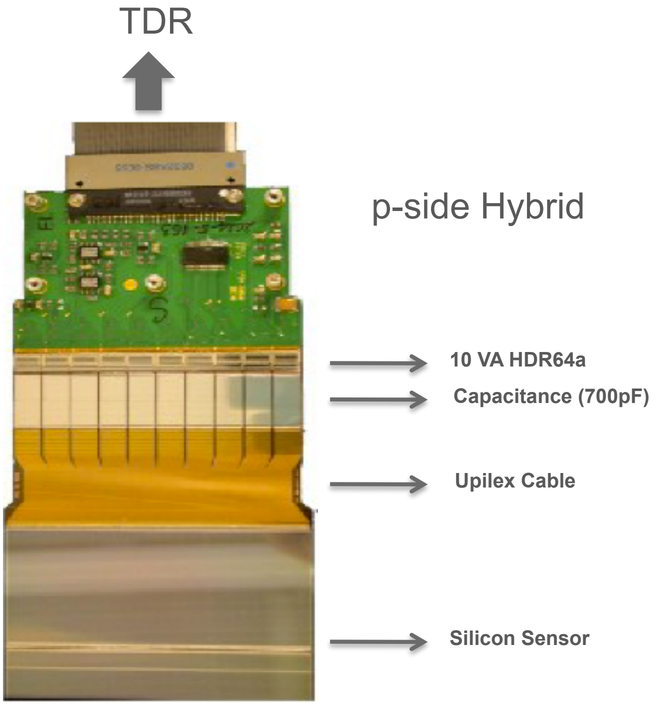

Figure 4.2 – Architecture of the connection between the p-side of a sensor and the associated S-side Hybrid. One can recognize the 10 VAs used to amplify and shape the signals from the p-side strips.

m^2. The p-side of sensors are arranged such that the strips run in the longitudinal direction of the ladder while the n-side strips are orthogonal to the ladder length. This implies different routing schemes to distribute the signals from both sides to the respective electronics. On the p-side of a ladder, the strips between different sensors are simply daisy-chained together through metallic bonds. On the n-side, signals of alternating sensors are distributed, by means of a Upilex cable, to the same readout channel, i.e., the 192 strips of the first (second) three VAs receive the signal from the readout strips of sensors 1,3,5,... (2,4,6,...). This results in an ambiguity in position between alternating sensors. The differences in the routing schemes can be appreciated in Figure 4.3 which illustrates the connection of both sides of a silicon ladder to the front-end electronics. For protection, the ladders are electromagnetically shielded with a 50μm metalized upilex foil while the hybrids are enclosed in a 0.3mm thick aluminum box.

4.3.2 Tracker Layers

The ladders are arranged in 9 different layers, in a configuration that can be appreciated from Figure 3.1. The 6 circular support planes are composed of a low density aluminum honeycomb structure enclosed in a thin carbon fiber structure. To minimize the effects of multiple scattering, the density of the support structure was kept as low as possible. The average density for the external support planes is 0.032 gcm^{-2} and 0.016 gcm^{-2} for the internal support planes. The total average thickness of a tracker plane is about 1% of the radiation length, making the tracker a very transparent detector. The ambiguity resulting from the n-side routing scheme is resolved by using a different routing scheme on ladders of the external planes with respect to internal planes (see 4.3.3). Figure 4.4 shows the structure of the inner tracker planes attached on the mounting structure to be placed inside the magnetic bore.

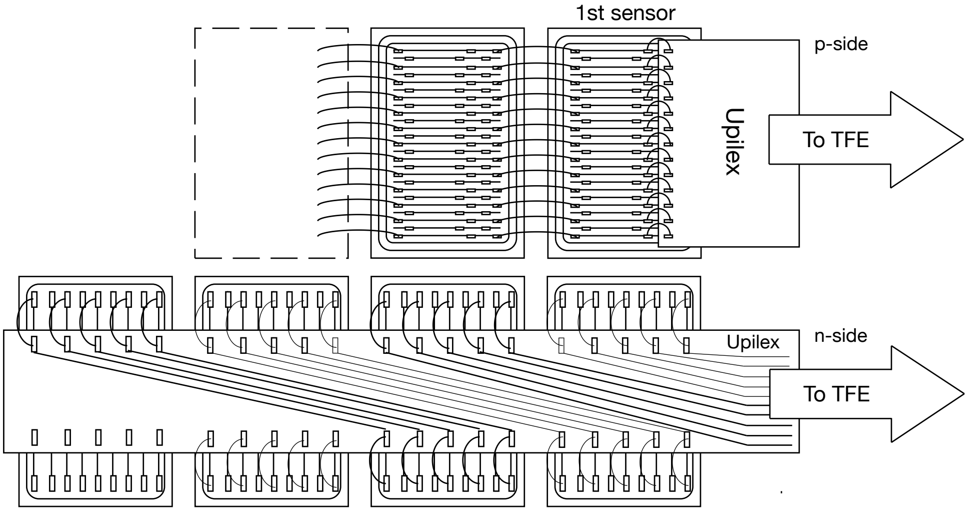

FIGURE 4.3 – Schematic view of the signal routing for both sides of a typical AMS-02 ladder [98]. The specific routing of the n-side introduces an ambiguity in the hit position.

4.3.3 K5 and K7 Routing Schemes

Ladders on the outermost planes present a different signal routing scheme of the n-side strips to their readout electronics. In total, 61 ladders out of the total 192 present this peculiarity. Figure 4.5 illustrates the two different routings. The standard K5 routing scheme is such that 1 out of 2 implanted strip is readout by the electronics. On the special K7 ladders, a sensor is separated into 7 sub-groups of 32 readout channels. Two subgroups on each edge of the sensor possess a specific routing scheme alternating between 1 out of 1 strip and 1 out of 2 strips read out by the electronics. This means that for portions of these 4 subgroups, the K5 routing scheme is still applied. The 3 remaining middle groups have the exact K5 routing scheme. Following the front-end electronics nomenclature, we distinguish three cases : S (readout electronics for the p-side strips), K5 and K7.

The special K7 scheme is expected to show a different charge collection behavior compared to the standard K5 scheme. In order to take into account such potential differences, each reconstructed cluster is classified according to the readout scheme it belongs to. The association is based on the subgroup affiliation since going to a lower level inside a subgroup would imply an unresolvable distinction for clusters with more than 2 strips.

4.3.4 Ladder Naming Convention

Due to the high number of readout channels associated with the silicon tracker, one needs an efficient naming scheme to link the detector objects to the electronic slots. The ladder themselves have a unique identifier related to the intrinsic number of sensors and their construction history (see [98]). The position of a ladder in the tracker is referenced by an identification number, the *TkID*. A plane can be divided in slices, also called slots, in the direction of the AMS-02 x-axis. Each slot can be identified by a number running from 1 to 15, the numbering starting at the most positive y-side value. External planes have 15 slots, numbered from 1 to 15 while internal planes have 14 slots, also numbered from 1 to 15 but with slot number 8 missing. Each slot is divided in two on each side of the x-axis, inducing a positive and negative sign according to the positive and negative coordinates on the x-axis. A half slot can house a single ladder but not all the slots are occupied. Based on this description, the TkID of a given

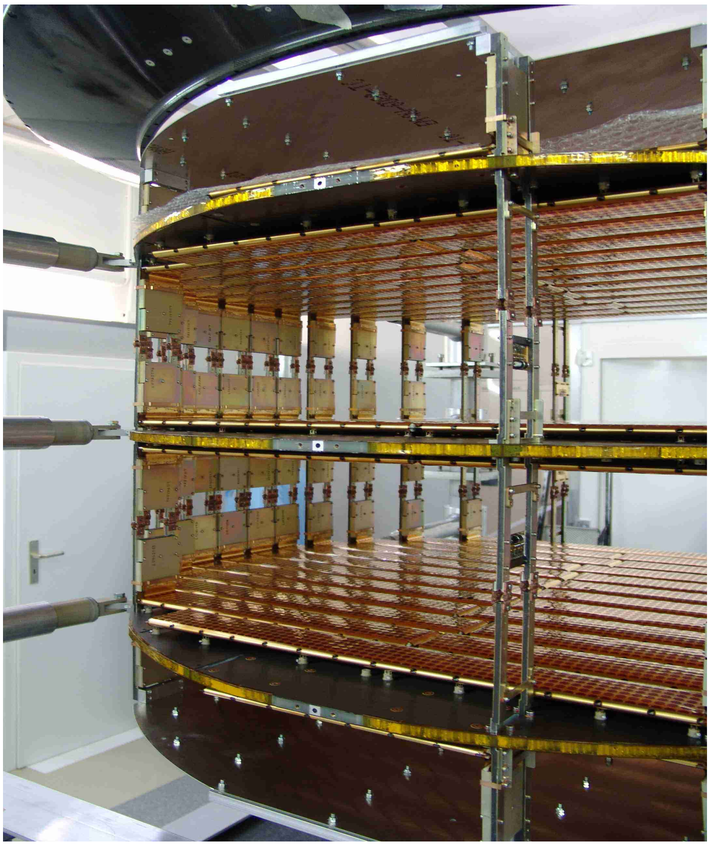

FIGURE 4.4 – The AMS-02 inner tracker planes [90]. One can appreciate the double layered structure of each plane with the two columns of ladders running parallel.

ladder is obtained through :

$$\text{TkID} = (\text{Layer}_{\text{Old}} \times 100 + \text{slot}) \times \text{sign} \tag{4.1}$$

$\text{Layer}_{\text{Old}}$ refers to the old naming convention of the tracker layers, before the superconducting magnet design was abandoned for the permanent magnent one. Hence the current layer 1 is layer 8 in the old geometry while layer 9 has no old affiliation. The naming scheme for layer 9 is shown as an example in Figure 4.6.

4.4 Quality Tests and Pre-flight Performances

The main criteria for defining the sensor quality are related to strip noise levels and operation voltages. The total leakage current must be measured to be less than 2 μA. At the single strip level, leakage currents must be under 2 nA for the p-side and 10 nA for the n-side. A strip not meeting this requirement is flagged as hot and a sensor possessing more than 6 hot strips (4) on the p-side (n-side) is rejected. At the production time, 96.1% of all sensors passed the selection criteria [98]. The performance of the silicon tracker, in terms of momentum resolution, is related to the precision in the alignment of the sensors in the ladders. The alignment relies on a very precise cut of the wafers and was measured to have a precision of 4 μm rms. The silicon ladders are then daisy chained for biasing and readout. For final acceptance, each front-end hybrid must have less than one percent defective channels. For the estimated noise, on the p-side and n-side, typical values are around 2 to 3 ADC counts. This is to be compared

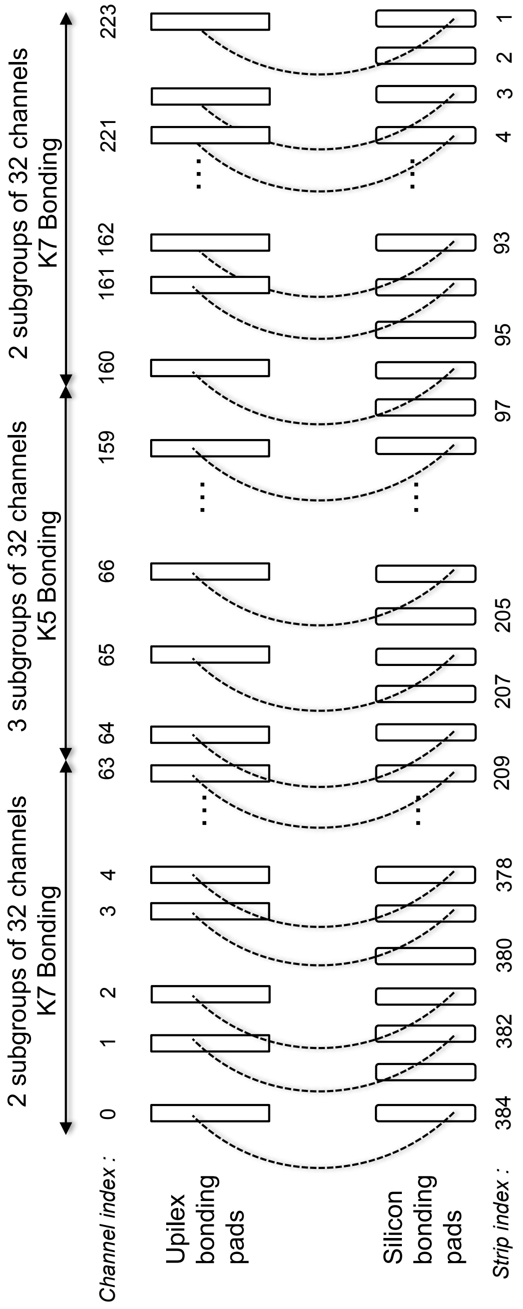
2 subgroups of 32 channels
K7 Bonding
3 subgroups of 32 channels
K5 Bonding
2 subgroups of 32 channels
K7 Bonding
Channel index :
0
1
2
3
4
63 64
65
66
159
160
161 162
221
223
Upilex
bonding
pads
Silicon
bonding
pads
Strip index :
384
382
380
378
209
207
205
97
95
93
4
3
2
1

Figure 4.5 – Schematic illustration of the special K7 routing scheme. A sensor is separated into 7 sub-groups of 32 readout channels. Two sub-groups on each edge of the sensor possess a specific routing scheme alternating between 1 out of 1 strip and 1 out of 2 strips (usual K5 implementation) readout by the electronics.

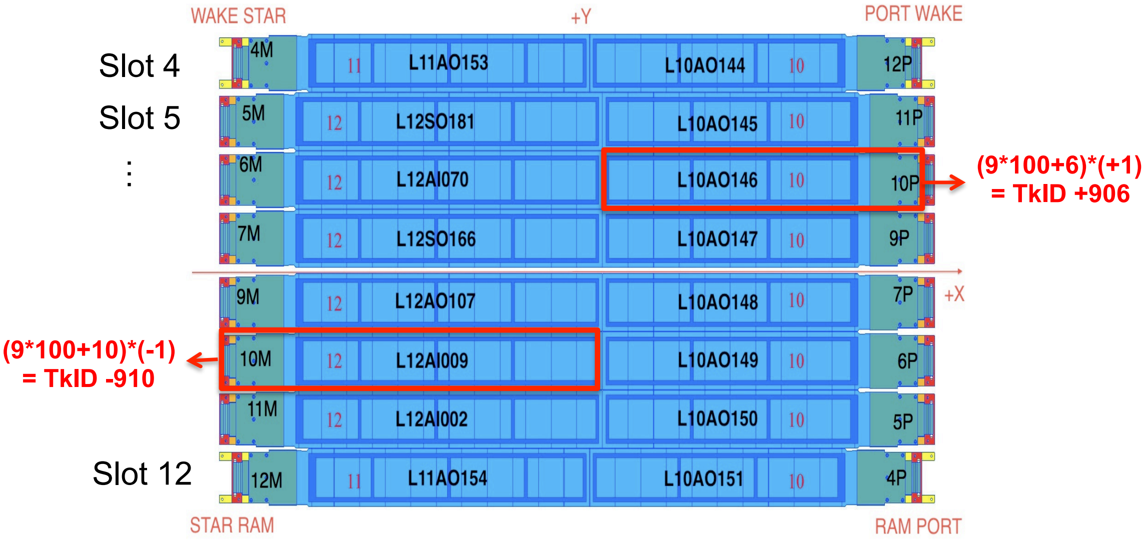
WAKE STAR
+Y
PORT WAKE
Slot 4
Slot 5
⋮
Slot 12
4M
11
L11AO153
L10AO144
10
12P
5M
12
L12SO181
L10AO145
10
11P
6M
12
L12AI070
L10AO146
10
10P
(9*100+6)*(+1)
= TkID +906
7M
12
L12SO166
L10AO147
10
9P
9M
12
L12AO107
L10AO148
10
7P
+X
(9*100+10)*(-1)
= TkID -910
10M
12
L12AI009
L10AO149
10
6P
11M
12
L12AI002
L10AO150
10
5P
12M
11
L11AO154
L10AO151
10
4P
STAR RAM
RAM PORT

Figure 4.6 – Example of the different naming schemes for the tracker layer 9.

with the typical 30 ADC counts associated to the signal of a minimum ionizing particle.

In the construction phase of the detector, a limited number of ladders has been exposed to several particle beams in order to evaluate their performances, in terms of position resolution but also in terms of their charge identification capabilities. In June 2003, four AMS-02 ladders were operated in a proton beam at the CERN Proton Synchrotron (PS) to study the influence of the VA hold delay on the performance for singly charged, minimum ionizing particles. A six ladder telescope was placed in proton and ion beams at the CERN Super Proton Synchrotron (SPS) in October 2002 and 2003. In September 2004, a four ladder telescope and a 11 ladder tracker were used to study the photon detection capabilities via pair production in an electron beam at the CERN SPS. A detailed description of the ladders, as well as the results of these performance studies can be found in Ref. [100]. Furthermore, the complete tracker has been tested with cosmic rays at ground during the AMS pre-integration phase in 2008. The response of the ladders to different ions and the properties of the charge collection measurement were analyzed in details in [102, 99].

4.5 Signal Processing

The final goal of the silicon tracker is to reconstruct the particle trajectory all the way through the AMS-02 instrument. The signals deposited in the silicon by traversing particles sets the basis for the track reconstruction algorithms. The signals must however be primarily filtered such that they are efficiently discriminated from the detector noise. This is done using the information of the onboard calibration of the tracker, combined with clusteritzation algorithms. The particle rigidity is determined from the curvature of the reconstructed track. One can then associate the signals from other sub-detectors, determine the particle charge by the multiple energy loss measurements, and find the particle charge sign by the curvature sign and the directional information from the ToF.

4.5.1 Signal Detection and Calibration

The signal collected by a readout strip is amplified and digitized by the front-end electronics and the TDR. The resulting ADC values include the following contributions : a constant offset (pedestal), a coherent common noise component, identical for all 64 channels of a given pre-amplifier chip, the channel noise and an eventual signal, i.e. the charge accumulated on strips due to the passage of an ionizing particle in the depleted silicon. The strip pedestal and noise values are determined during the calibration.

The calibration is performed by the TDR twice per orbit when AMS-02 is around the equator. This allows to take into account the potential high temperature excursions experienced along different orbits. Dark current fluctuations at the sensor level and the electronic noise from the readout chain both contribute to the channel noise σ. Based on the noise properties, channels can be tagged either as noisy (if $\sigma > 5$ ADC counts), dead ($\sigma < 0.1$ ADC) or non-gaussian if the noise distribution deviates too much from a gaussian distribution. Such channels are excluded from the event reconstruction and the subsequent analysis. The results of the calibrations, in terms of pedestal and noise values for each channel, are stored in a memory buffer for further use in the data reduction process and in the offline analysis. Details of the calibration procedure can be found in [100, 103]. The time stability and in-flight performances of the silicon tracker are discussed in [103].

4.5.2 Clusterization

Particles traversing a silicon sensor induce a signal on the strip nearest to its impact point on the silicon surface. The diffusion of charge carriers inside the silicon volume, added to the capacitive coupling between the strips, typically results in a spreading of the ionization signal on more than one strip, resulting in an ensemble of strips called a *cluster*. The task of the reconstruction algorithms is then to recognize clusters among simple fluctuations of the readout channels. During data acquisition, pedestal values and common noise values are subtracted from the channel raw signals on an event-by-event basis. The resulting signals are compared to the channel noise values from the closest calibration in time. A valid signal is defined by the threshold applied to the strip signal-to-noise ratio (SN). A channel with SN above a value SN_{Seed} is considered as a *seed* for a potential cluster. All the neighboring channels are tested and if their SN is greater than a value $\mathrm{SN}_{Neighbour}$, they are added to the cluster. The choice of SN_{Seed} and $\mathrm{SN}_{Neighbour}$ were obtained through careful studies and were also adjusted to the different tracker layers. In the first weeks of operation of AMS on the ISS, the thresholds values were further tuned to meet the event size requirements of the data transfer allowance.

4.5.3 Track Reconstruction

The set of clusters reconstructed for a given event trigger of AMS-02 is the basis for reconstructing the associated particle track in the detector. Given the large size of the tracker (more than 196k channels), the average number of clusters reconstructed per event is around 100. Since a track contains at most 18 clusters (p and n side measurement of each of the 9 layers), the high cluster multiplicity makes the track finding task challenging. Moreover, an accurate knowledge of the sensor and ladder geometries, to the level of a few microns, is necessary to optimize the tracker performances in terms of the maximal detectable particle rigidity, which implies a very precise alignment of the detector [104]. More details on the track reconstruction algorithms can be found in [88].

4.5.4 Signal Corrections

The energy deposited in a sensor is usually collected by a cluster of adjacent read-out strips. The total cluster amplitude is defined as the sum of the individual cluster strip signals, which is proportional to the energy deposited in the silicon by the particle. These raw integrated signals must be corrected for two simple effects. The first one is related to the multiplexed reading of the VA channels. It was observed during the qualification phase of the ladders that there was an positional asymmetry in the signal collection due to the fact that channels are always read in the same order. This effect is corrected by a simple side-dependent factor that is applied to all ADC raw signals. The correction essentially amounts in subtracting a fraction of a channel's signal and adding it to the next channel. The traversing position of a particle can be estimated using the center of gravity (CoG) of the two strips with highest signal. Figure 4.7 shows the CoG distribution for the n-side before and after correcting for the asymmetry effect. The specific implantation structure of the n-side can clearly be distinguished where the three peeks match the position of the implanted strips. One must also correct the signals for the track inclination. A particle traversing the silicon with a greater inclination will deposit more energy. The correction consist in normalizing the cluster amplitude to a vertically traversing particle, i.e., to a traversing silicon thickness of 300μm. This is again a multiplication factor corresponding to the cosine of the particle track inclination.

The effects described here do not depend on the charge of the traversing particle nor on its energy. These corrections can therefore be applied to the raw signals, irrespective of the particle nature.

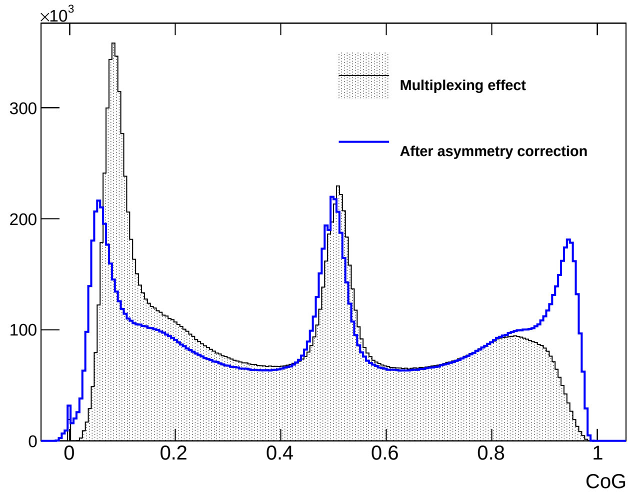

FIGURE 4.7 – Asymmetry in the n-side signal CoG distribution due to the multiplexed reading of the VA chips (blue filled curve). Correcting for this effect allows to partially recover the original symmetry of the signal (blue curve).

Chapitre 5

Nuclei Identification and Tracker Calibration

The silicon tracker is the only subdetector that can separate positive from negative particles, hence matter from anti-matter, using the measurement of the particle magnetic rigidity ($R = p/Z$), and the information of up-going or down-going particle coming from ToF. On top of this crucial measurement, the tracker measures with an excellent resolution the magnitude of the charge of the traversing particle, offering up to nine independent measurements of the specific energy loss. The same energy loss is in fact measured twice in each layer due to the double-sided readout. The single layer charge identification capability provides an important tool for tagging the nuclear fragmentation appearing at different levels in the detector. The tracker response to different nuclei is naturally degraded by a number of detector effects. A precise calibration is thus essential for many physics topics. The main goal behind the calibration procedure presented in this chapter is to construct a single charge estimator for the tracker which is independent of energy and presents the best nuclei identification performance.

Most of the material presented in this section is the result of an effort to publish the results of the tracker calibration in a refereed paper. The paper is currently in the process of review by the AMS-02 collaboration for submission to a journal. The calibration procedure has been developed in close collaboration with Dr A. Oliva[1].

5.1 Draw Chart of the Calibration Procedure

Figure 5.1 presents a draw chart of the different steps used to calibrate the tracker response to different nuclei. The strip cross-talk correction and the path length correction have already been discussed in Section 4.5. In the following sections, we discuss the main remaining effects degrading the tracker measurement and how they have been taken into account. After correcting for gain differences in the response of the VA electronic chips in Section 5.4, we account for the charge collection efficiency dependence with the particle impact position and traversing inclination (Sec. 5.5). The dependence of the energy loss with the particle velocity is described in Section 5.6 before a final equalization of the VA responses is applied (Sec. 5.7). The results of the separate p-side and n-side calibrations are finally combined to produce a single tracker charge estimator with optimized charge identification performances (Section 5.9).

---

[1] Alberto.Oliva@cern.ch

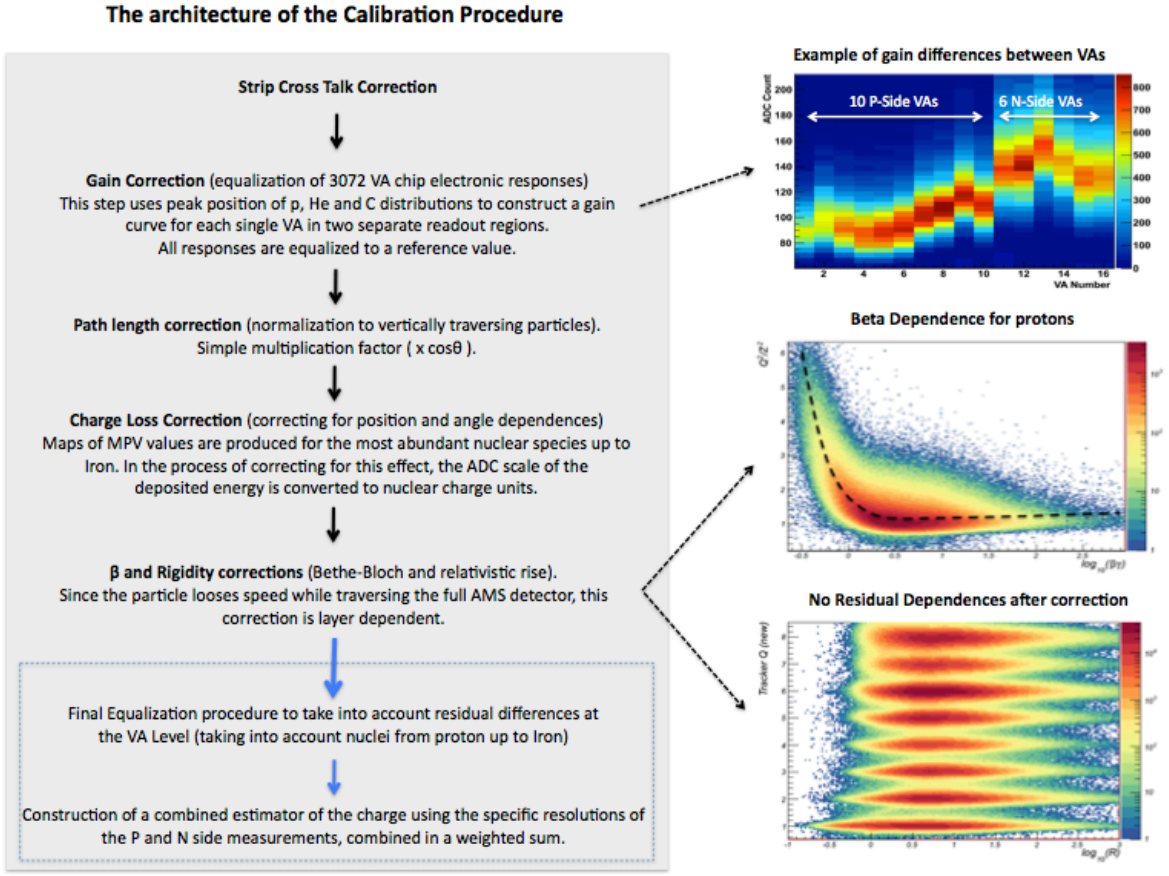

The architecture of the Calibration Procedure

Strip Cross Talk Correction

Gain Correction (equalization of 3072 VA chip electronic responses)
This step uses peak position of p, He and C distributions to construct a gain curve for each single VA in two separate readout regions.
All responses are equalized to a reference value.

Path length correction (normalization to vertically traversing particles).
Simple multiplication factor (x cosθ).

Charge Loss Correction (correcting for position and angle dependences)
Maps of MPV values are produced for the most abundant nuclear species up to Iron. In the process of correcting for this effect, the ADC scale of the deposited energy is converted to nuclear charge units.

β and Rigidity corrections (Bethe-Bloch and relativistic rise).
Since the particle looses speed while traversing the full AMS detector, this correction is layer dependent.

Final Equalization procedure to take into account residual differences at the VA Level (taking into account nuclei from proton up to Iron)

Construction of a combined estimator of the charge using the specific resolutions of the P and N side measurements, combined in a weighted sum.

Example of gain differences between VAs
10 P-Side VAs
6 N-Side VAs
ADC Count
VA Number
Beta Dependence for protons
$\log_{10}(\beta\gamma)$
No Residual Dependences after correction
Tracker Q (new)
$\log_{10}(R)$

FIGURE 5.1 – Draw chart of the architecture of the charge calibration procedure of the silicon tracker.

5.2 Data Sample

We use a data sample corresponding to two years of data where the contribution of singly charged particles ($Z = 1$) has been strongly suppressed. This allows to speed up considerably the calculations as the proton sample constitutes about 90% of all the triggers. The response of the electronics to proton particles has been systematically cross-checked using a non prescaled stream of data.

5.2.1 Event Selection

We select triggers based on the ToF system. We apply a set of quality cuts to remove events with bad reconstruction status or errors during acquisition. We remove events acquired in the South Atlantic Anomaly by applying a geometrical cut on the geomagnetic longitude and the latitude coordinates. Only events with both a track reconstructed in the tracker and in the ToF are selected. Up-going particles are removed by imposing a positive β measured by the ToF. The quality of the reconstructed track is ensured by requiring a minimum number of hits attached to the track and imposing a maximum chi-square value of the track fit. This latter cut remains quite loose ($-0.01 \leq \chi^2_{x,y} \leq 10^3$) in order to maximize the statistics for the charge studies. Whenever more than one track has been reconstructed by the tracker, we loop on the different tracks and select the track with the highest overall energy deposition, most likely to be the nucleus track if a nucleus passed through the detector.

5.2.2 Charge Sample Selection

To characterize the behavior of the electronics as a function of the nuclear charge Z, a selection of samples of different nuclear species is needed. This selection can be performed looking at the truncated mean (S_T) of cluster signals S_i associated to a particle track :

$$S_T = \frac{\sum_{i=1}^{n} S_i - S_{max}}{n-1} \tag{5.1}$$

where n is the number of clusters entering the truncated mean calculation. Figure 5.2 gives an illustration of the selection procedure, where the square root of the truncated mean calculation is used for its direct proportionality to the charge of the particle ($\sqrt{S_T} \propto Z$). The good discrimination, already at this stage, between the different charge peaks was possible using a set of correction factors derived from proton data acquired in the integration phase of the experiment [102]. The truncated mean distribution is fitted with a multi-gaussian function from which we extract single gaussian contributions to define 1 standard deviation selection ranges around the peak values. This definition ensures a contamination from the $Z+1$ and $Z-1$ populations lower than 1% up to oxygen. In order to avoid any bias in the selection, the cluster from the layer under study is removed from the truncated mean. Since the raw n-side measurement presents better performance, we also use it to define the charge samples on the p-side.

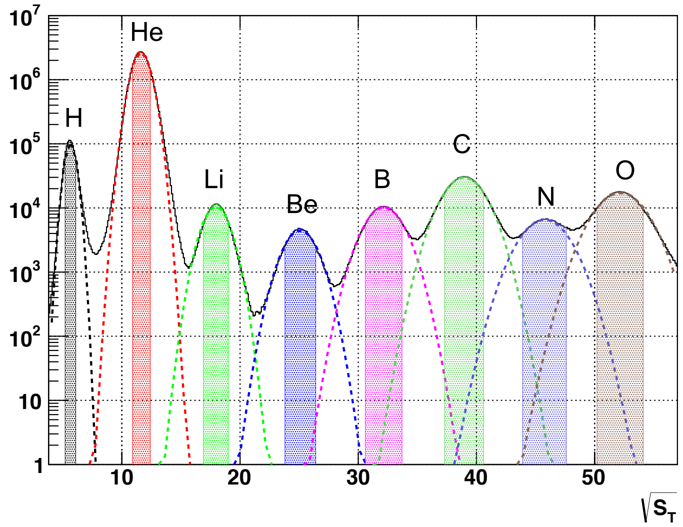

FIGURE 5.2 – Illustration of the nuclei selection procedure. The black curve represents a typical n-side truncated mean distribution in units of $\sqrt{ADC}$. The peaks of nuclei up to oxygen ($Z=8$) are clearly visible. The gaussian fits allow to select the different nuclei with minimum contamination from neighboring charges, as indicated by the colored hashed areas.

When correcting for the different effects degrading the charge resolution of the tracker (Section 5.3.3), one can profit from each step of the correction procedure to improve the charge samples definition. In particular, the improvement in resolution allows to define new samples, for nuclei above oxygen that could otherwise barely be discriminated from the tracker truncated mean distribution. In addition, to select nuclei heavier than silicon, one can profit from the excellent charge identification power of the ToF instrument [91]. In general, multiple measurements of the charge are performed by the various detectors in AMS-02 and can be used in the selection procedure. A review is given in Ref. [105].

5.3 Charge Measurement

The operation of a silicon sensor is related to the properties of p/n junctions (or diodes) operated in reverse biased mode. When a particle traverses a silicon sensor, electron-hole pairs are created by ionisation along the particle trajectory. Due to the electric field in the depleted volume, electrons and holes migrate to opposite sides (see Fig. 4.1). The opposite sign of the collected signals has an impact on the VA response function which are therefore different for the two sides, in particular for what concerns saturation effects. This implies a separate calibration of the two sides (Sec. 5.4).

5.3.1 Ionisation Energy Loss

The deposited ionisation energy is proportional to the square of the particle charge ($dE/dx \propto Z^2$), therefore allowing to distinguish different nuclear species. The analog readout and the high dynamic range of the front end electronics of the ladders are designed to identify nuclear species from hydrogen up to iron and above. The full description of the ionisation energy loss is given by the Bethe-Bloch formula which takes into account the properties of the traversed material and density correction effects in the ultra-relativistic regime. An important dependence of the energy loss rate is upon the energy of the traversing particle. The typical shape of this dependence is shown in Figure 5.14 (right plot) for a selected sample of carbon nuclei measured with AMS-02. A minimum is found around a kinetic energy of Mc^2 of the ionizing particle. From lower energies up to this minimum, the energy loss rate decreases as v^{-2}. It presents a logarithmic rise at high energy. At a given kinetic energy per nucleon, the dE/dx gives a sensitive measure of the particle charge.

The energy deposition is in itself a statistical process and its distribution at a given energy is described by a Landau function. It was shown in [106] that for such a probability distribution, while the mean ionisation energy loss over-estimates by large factors the peak position of the distribution, the Most Probable Value (MPV) and the Full Width at Half Maximum (FWHM) are more representative of the distribution. In terms of ADC signals, the distribution of deposited energy must be convoluted with a Gaussian function that models the contributions of noise and resolution from the silicon and the electronics.

5.3.2 Charge Collection

The cluster amplitude depends on the impact position of the particle on the sensor and on its inclination, as can be seen in Figure 5.3 for a selected sample of helium nuclei measured by the n-side. The *Impact Point* (IP) is defined as the distance, in units of readout strip pitch, of the particle impact point on the sensor surface to the closest readout strip. For a particle impinging directly on a readout strip, $IP = 0$, while $IP = \pm 0.5$ when the particle traverses in between two readout strips. The θ_{XZ} angle corresponds to the projection of the particle inclination on the xz plane of AMS-02[2].

The observed dependence can be understood in terms of a loss of collection efficiency when a particle traverses the sensor surface in between two readout strips, while the maximum charge collection efficiency appears when the particle impacts vertically on a readout strip. For the former case, at higher inclinations, the signal tends to be distributed to a larger number of strips which partially compensates the loss of collection and attenuates the effect. The total effect can amount to differences up to more than 30% for the lighter nuclei ($Z < 6$). As the charge increases, the deposited energy is collected by an increasing number of readout strips and the effect is attenuated. An example is shown in Figure 5.11 where we discuss the procedure to correct for this effect.

---

[2] Concerning the p-side measurement, the relevant angle becomes θ_{YZ}, the particle inclination projected on the yz plane.

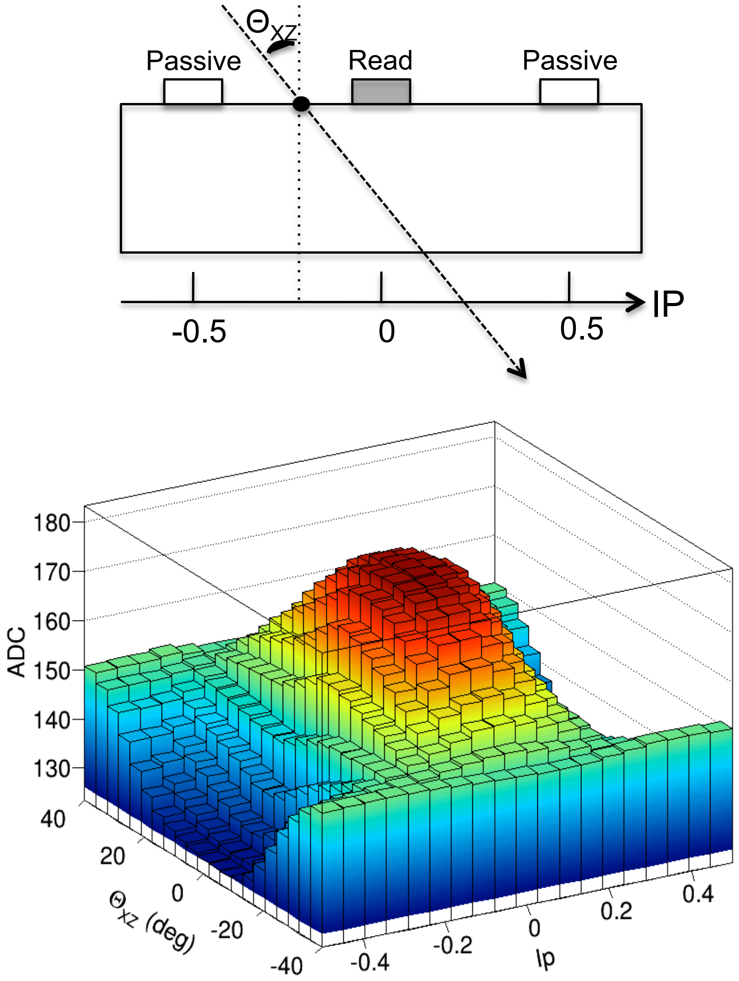

FIGURE 5.3 – Dependence of the raw signal on the impact position of the particle and its inclination for a selected sample of helium nuclei. The maximum of collection efficiency appears when the particle traverses at vertical incidence, impinging directly on a readout strip, i.e. $IP = 0$ and $\theta_{XZ} = 0$.

5.3.3 Charge Equalization and Linearization

The charge resolution of the tracker is degraded by a number of detector effects that need to be carefully taken into account and corrected for. In-flight calibration of the Tracker is done using the statistics accumulated over two years of operation, allowing to perform a precise equalization and linearization of the amplifier chips' responses. This is achieved using the characteristic energy deposition of the most abundant nuclear species. The next sections describe the procedure that has been implemented to accurately calibrate the tracker response to different nuclear species and optimize its performances in terms of charge resolution.

5.4 VA Equalization

5.4.1 P and N-Side Response Functions

During a test beam in 2003, the nucleus identification power of four ladders was studied [87]. It was found that the n-side performance is better than that of the p-side in terms of charge separation. On the n-side, the single ladder measurement showed a clear separation of the nuclei species up to silicon ($Z = 14$). Above silicon, the resolution is degraded due to saturation effects in the front-end electronics. For the p-side, the situation is more complex as a significant overlap between nuclei is also seen around the boron ($Z = 5$) to neon ($Z = 10$) region. This feature is due to a gain transition in the response of the electronics, as can be seen in Figure 5.4 where the correlation between the charge and the cluster signal measured both at the time of the test beam and with ISS data is presented. The p-side response function was deliberately chosen to saturate at lower pulse heights so as to maximize the spatial resolution using charge sharing between neighboring strips. The cluster signal is roughly proportional to Z^2, as we expect from the properties of ionisation, albeit the specific transitions and non-linearities due to electronic effects.

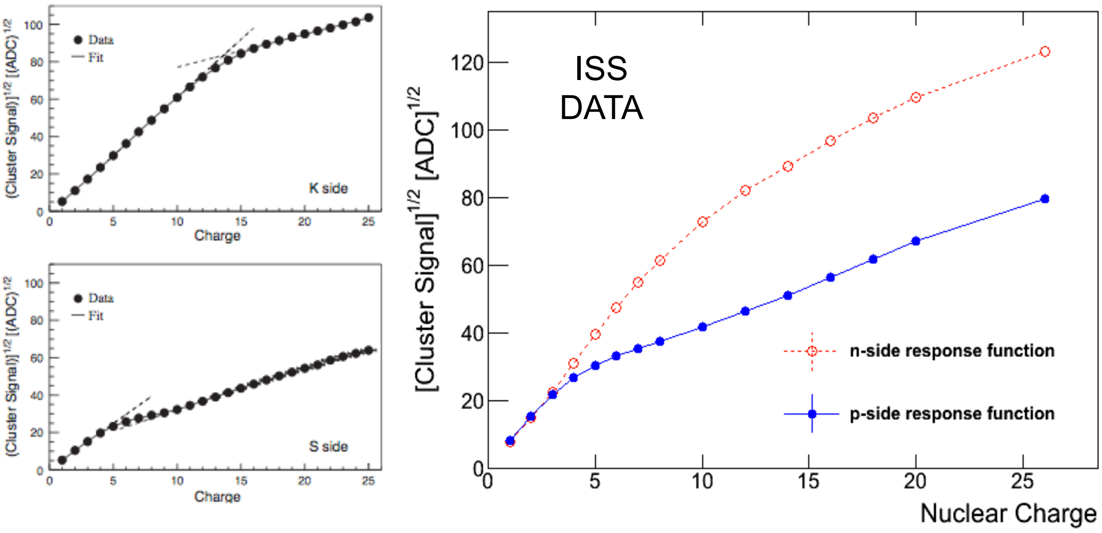

FIGURE 5.4 – *Left* : Correlation between the charge and the raw cluster signal for the p-side (top plot) and n-side (bottom plot) measurements of a single tracker ladder during the 2003 test beam [87]. *Right* : the same correlation is measured for another AMS-02 tracker ladder with ISS data for the p-side (solid blue) and n-side (solid red).

5.4.2 Equalization Procedure

The correlation between the charge and the cluster signal shown in Figure 5.4 is a property of the electronics and an optimum characterization can only be done considering the basic electronic unit, the VA. In Figure 5.5, we present an extreme case where the gain differences between different p-side VAs in a single ladder (here TkID +307) amount to as much as 22%. Due to the loss of collection efficiency in regions between readout strips (Figure 5.3), the events are classified in two categories : readout region, i.e. particles passing on or near a readout strip, and not-readout region, i.e. particles passing near a passive strip. The classification is done according to the η parameter, that is the particle traversing position on the surface of a sensor expressed in units of strip pitch :

1. readout region : $\eta \in [0.,0.15[\cup [0.85,1.]$
2. not-readout region : $\eta \in [0.35,0.65[$

The dependence with the inclination of the particle is neglected in order to save statistics. We further impose a cut on the β of the particle to be greater than 0.95 to get rid of the low energy dependence of energy loss in matter (Sec.5.3.1).

Considering the very high number of electronic chips constituting the silicon tracker (3072), and differences in acceptance due to the position of the chips in the tracker, added to edge effects, even two years of data suffers statistical limitations for the equalization procedure. In particular, the study of the response function was only possible using the 3 most abundant nuclear species, hydrogen, helium and carbon, for the n-side measurement, and only the two most abundant species for the p-side measurement. At this stage, the response functions are therefore only adjusted in the first linear regime, up to silicon ($Z = 14$) for the n-side and up to the CNO region for the p-side. The residual differences at higher charges are compensated in a final equalization step described in Section 5.7.

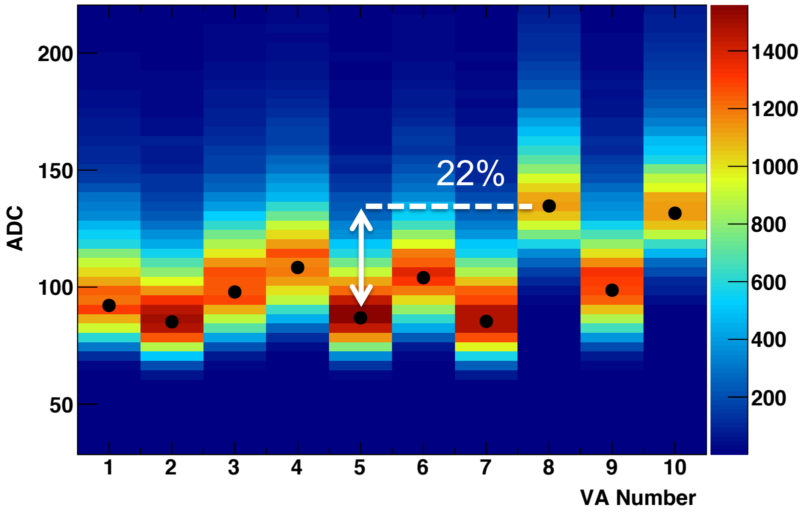

Figure 5.5 – The scatter plot presents the cluster signal, in units of ADC, for a selected sample of helium nuclei, vs the 10 p-side VAs of a single AMS-02 ladder (TkID +307). For this extreme case, the maximum difference in the peak position (black points from fitting) amounts to 22%.

For each VA, the energy loss distribution for each nuclear species is fitted using a Landau function convoluted with a Gaussian noise contribution from which we extract the Most Probable Value (MPV) to characterize the peak position of the distribution. Figure 5.6 shows an example of the fit results for 6 n-side VAs and 5 p-side VAs of a same ladder (TkID +103). One clearly sees that for the n-side VAs (6 upper plots), the signal distribution peaks at higher values in the readout region (red) compared to the non-readout region (black). For the p-side (5 lower plots), since the readout strip configuration is different, we actually do not see the same effect as for the n-side. The statistics in the readout region (blue) is substantially lower than for the non-readout region (black). This effect seems to be a characteristic of VAs with a low gain (see discussion below). We use a sub-sample of known high quality VAs (from detailed studies of individual response functions) to compute reference MPV values, to which all the VA responses are equalized. The gain correction factor for each VA can be obtained using the mean of the reference distributions through the following relation :

$$\mathrm{MPV}_{VA} = a \times \mathrm{MPV}_{Ref} + b \tag{5.2}$$

Substituting to this relation the measured and corrected cluster amplitudes, we have

$$\mathrm{ADC}_{Corrected} = \frac{1}{a} \times (\mathrm{ADC}_{Measured} - b) \tag{5.3}$$

The left plot in Figure 5.7 illustrates the procedure for the 6 n-side VAs of a typical ladder. In an ideal case, we would expect the offset b to be zero since we do not expect any signal for a zero energy deposition. It was however observed that for several VAs, the value of the offset is significant, in particular for VA characterized by a very low gain. For such cases, the signal over noise (SN) threshold used to trigger the cluster reconstruction is closer to the peak value of the proton energy loss distribution. Consequently, the peak of the proton distribution is shifted to higher values. Such a bias is not present for higher charge nuclei for which the characteristic energy deposition is far above the SN threshold. The resulting MPV_{VA} versus MPV_{Ref} relations present a significant deviation from linearity, observed both in a lower fit quality and in the offset values. It was considered to neglect the proton peak values when extracting the gain correction factors for these VAs. Although this showed slightly better results for high charges, it tends to be less efficient for the proton equalization. It was finally decided to include the offsets in the equalization procedure as a compromise to an overall improvement of low charge and higher charge resolutions. The right plot in Figure 5.7 shows the result of applying the equalization factors to the fitted MPV values for all three nuclei samples combined. The RMS of the MPV distribution is reduced by a factor 3 after equalization (red distribution). One still observes a few outliers to the distribution which correspond to pathological cases for which a reliable equalization factor could not be obtained (see 5.4.3). For each VA, we provide an estimation of the fit quality based on an adapted RMS criteria :

$$\mathrm{RMS}_{\mathrm{VA}} = \sqrt{\sum_{P_i} \left(\frac{MPV_{VA,\eta,Z}}{MPV_{Ref,\eta,Z}} - 1 \right)^2 / N} \tag{5.4}$$

This value helps assessing the reliability of the correction factors and trace back more easily potentially biased equalizations. All the information relative to the equalization procedure for each VA is saved in a dedicated data base easily accessible within the official analysis software (see 5.4.3).

One cross-check to our method consisted in computing the correction factor $1/a$ for the two readout regions separately. The mean of the distribution of the difference between the two factors is centered at 0.002 with an RMS of 0.029 and only very small skewness to the distribution. This validates the assumption that the response function of a given VA does not depend on the readout region. A single correction factor was therefore extracted combining both readout regions, as discussed above.

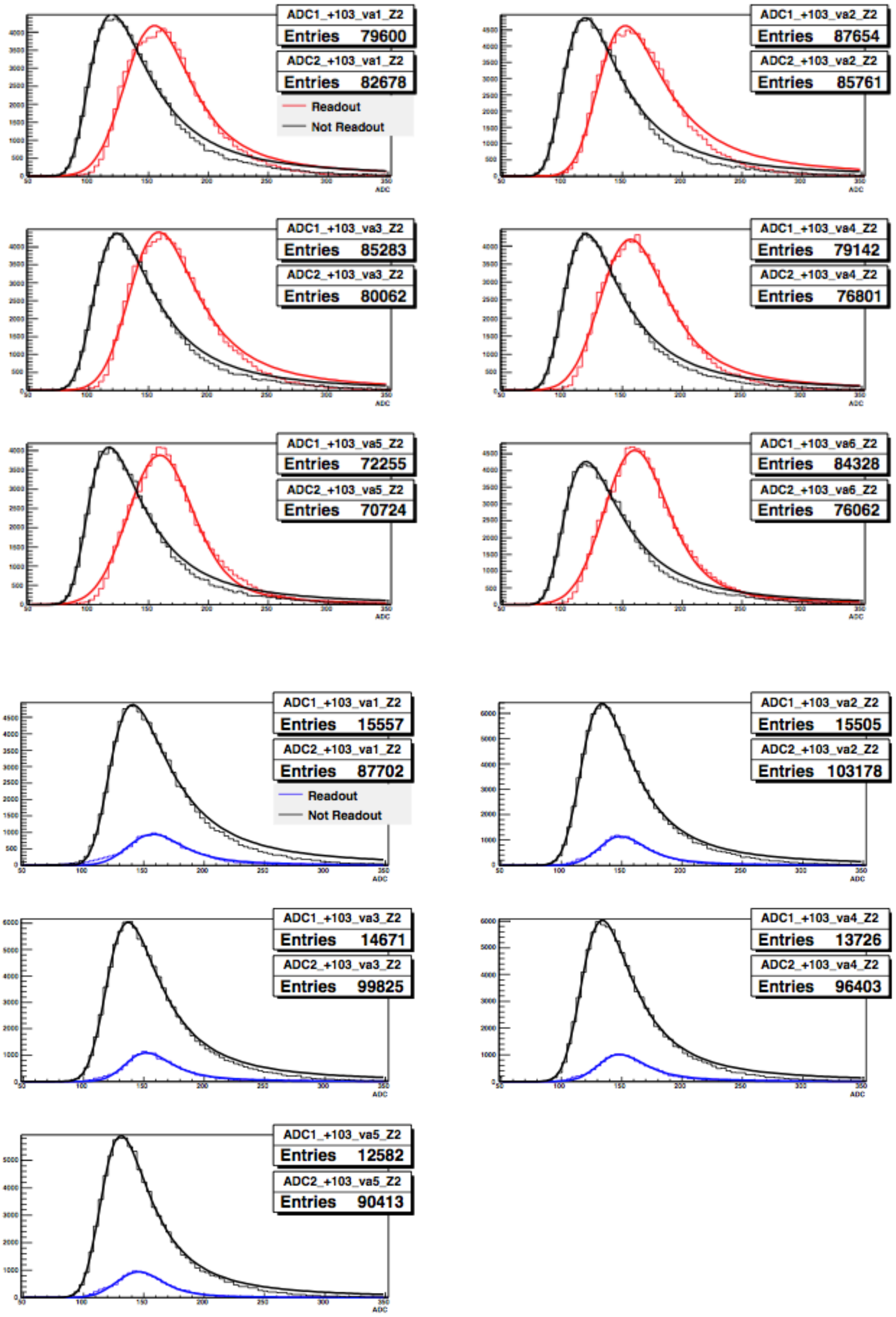

FIGURE 5.6 – Landau convoluted with gaussian fit of 6 N-side VAs and the 5 first P-side VAs of ladder +103. For each VA, two separate categories are defined depending on the impact position of the particle (see text).

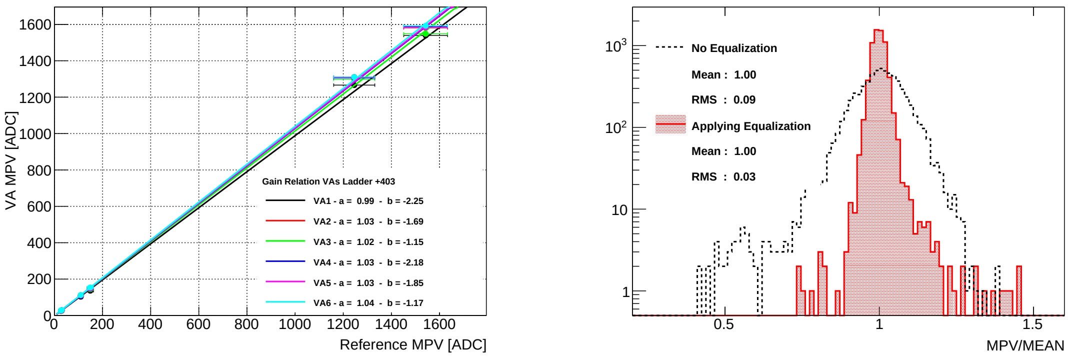

Figure 5.7 – *Left* : Relation of the MPV values for a given VA as function of the reference MPV values. Horizontal error bars are the RMS of the reference MPV distributions. The inverse of the slope value gives the equalization factor for the given VA. *Right* : distribution of n-side MPV values before (black) and after (red) applying the equalization factors. All three nuclei sample are combined in this plot.

5.4.3 VA Classification

Based on the VA signal distributions, it is possible to classify VAs according to different quality levels. We have defined three categories : golden, silver and bad VAs. Golden VAs are defined as VAs with well-defined charge distributions in both the readout and non-readout regions. Silver VAs are characterized by particularly low gain values compared to the bulk of high quality VAs. Formally, we attach the low gain attribute for VAs with an MPV position farther away than 2.5 times the RMS from the mean of the overall MPV distribution (all VAs together). The silver category also includes VAs with higher noise levels. Finally, the bad VA category includes all units that are either dead (permanently and tagged as such) or with very low detection efficiency. We also include in this category VAs with pathological behaviors. Figure 5.8 shows the example of ladder −210 which contains all three types of VAs.

In general, for most physics studies, both the golden and silver category can be used. In Appendix A, a detailed example of the format used to save the information from the equalization procedure (including the VA classification) in a dedicated data base is presented. Out of the 3072 VA chips constituting the tracker, 93% are found to be golden VAs while the remaining population is equally shared between the silver and bad category.

5.4.4 Equalization Results

The VA equalization factors are applied offline and are not used at the level of the track reconstruction since they are not relevant for the spatial resolution and systematics. The result of the equalization procedure is shown in Figure 5.9 for both the n and p-side measurements (top and bottom plot respectively). On the n-side, we observe an improvement up to neon but no significant improvement at higher charges. This is expected considering that saturation effects in the front-end electronics appear around that region. For the p-side, we observe that the charge resolution is worse than for the n-side, as expected from previous studies [87]. There is however a significant improvement from the equalization procedure since many new charge peaks are visible which would otherwise be hidden. Although non-linearities in the response function of the electronics appears around the CNO group, the overall improvement, even at higher charges, simply translates the high level of non-uniformities between different VAs that the equalization procedure already helps compensating.

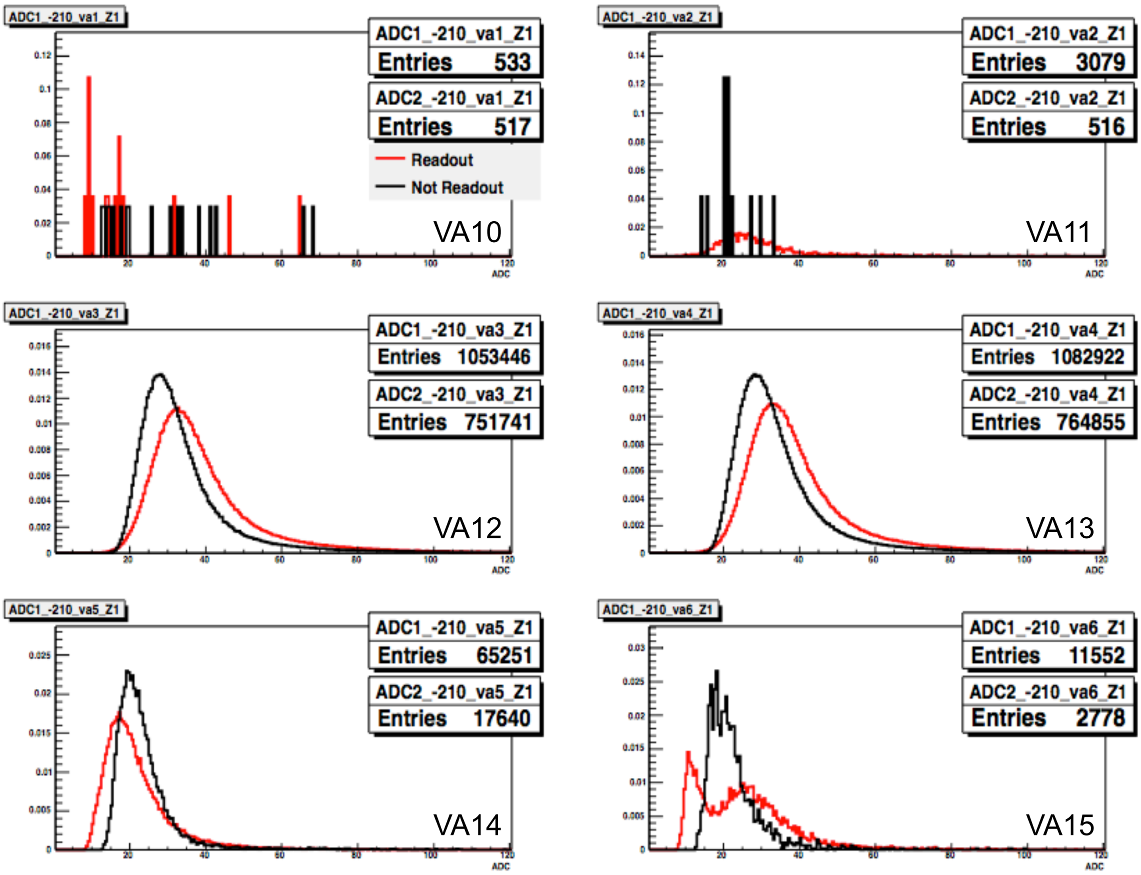

FIGURE 5.8 – Cluster signal signal distribution (in ADC) for ladder −201 in the two readout and non-readout regions. Three different type of VA categories can be identified among these 6 n-side VAs. VA 10 ,11 and 12 are tagged as bad VAs (10 and 12 are dead while 15 shows very pathological behavior). VA 12 and 13 are golden VAs and VA 14 is considered as silver since the signal has a well defined shape but has a very low gain.

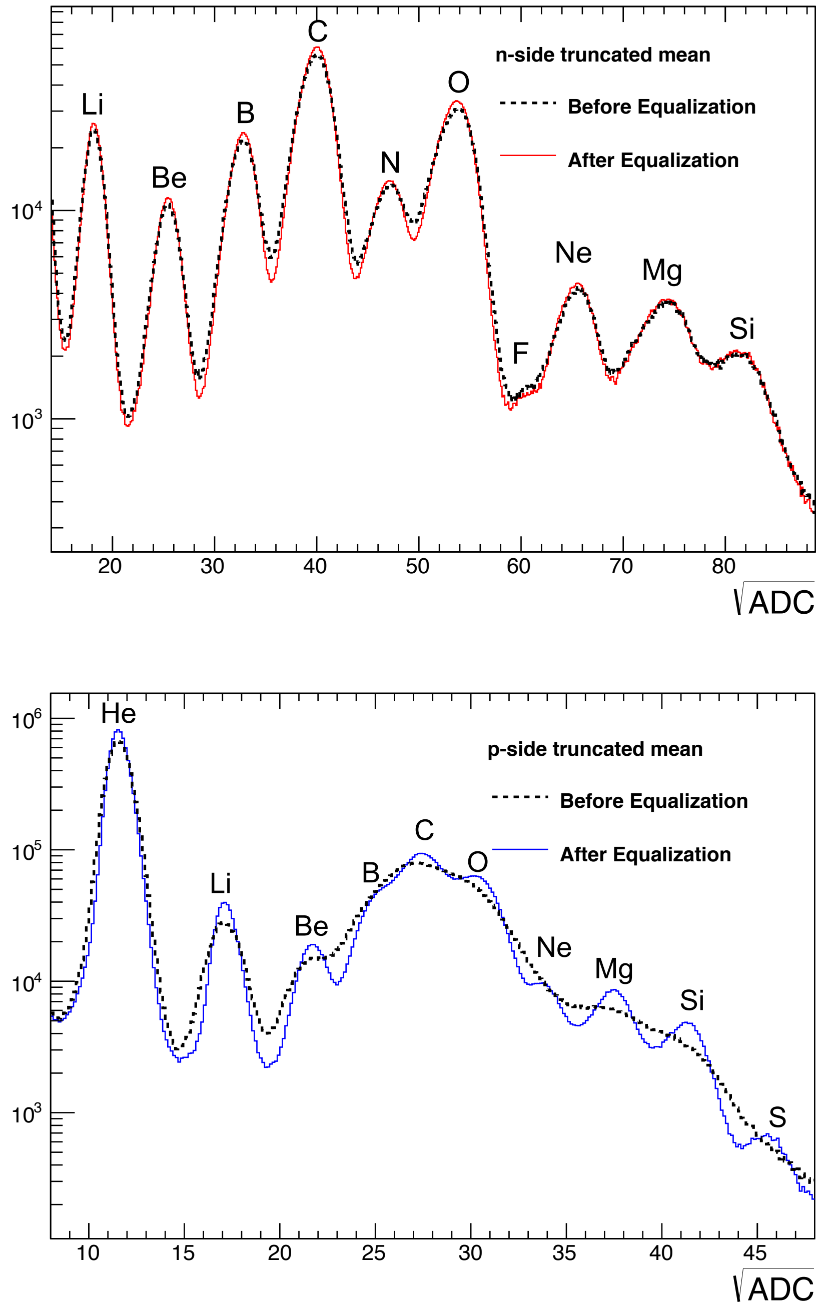

FIGURE 5.9 – Effect of the VA equalization on the overall charge separation power for a selected range of nuclei for the n (top) and p-side (bottom) measurements. Dashed lines indicate the results before applying the equalization.

5.4.5 Discussion

We have studied in detail the distributions of fitted MPV values in the two readout regions. Figure 5.10 shows the average (all VAs together) relative difference [3] between the two readout regions for each individual layer and the three most abundant nuclei species. The average relative difference is systematically lower for the layer 2. This systematic shift is not yet fully understood but is thought to be the result of a different signal-to-noise threshold setting for the layer 2, which can result, as discussed above, in a biased MPV estimation in the non-readout region where the signal peaks at lower values close to the threshold. After applying the equalization factors, we ran the equalization procedure again on all VAs. We observe that for the layer 2, the new MPV values tend to be over-corrected (with respect to other layers) in the readout region while being under-corrected in the non-readout region. This is a small effect that comes as no surprise since a single gain correction factor is extracted from the combination of both the readout and non-readout regions.

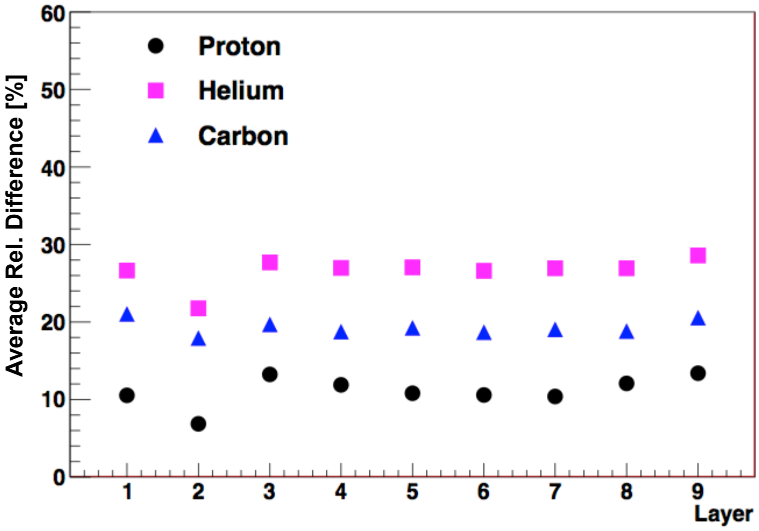

FIGURE 5.10 – Average relative difference between fitted MPV values in the readout and non-readout regions, for individuals layers. A distinctive feature appears for layer 2, probably due to different signal-to-noise thresholds settings for cluster reconstruction.

5.5 Charge Loss Correction

Once the VA responses are equalized, we can combine the statistics of all VAs of a given side to produce 3-dimensional description plots of the type of Figure 5.3. As mentioned in Section 5.3.2, the effect of charge collection can induce differences as much as 30% in the collected signal. Such effect must therefore carefully be taken into account.

5.5.1 Traversing Position Estimation

The traversing position of the particle impinging a silicon sensor can be estimated in several ways. The Impact Parameter (IP) used in Figure 5.3 is certainly the most precise estimation but is a quantity that depends on the quality of the reconstructed track. At low rigidities, where the effects of multiple scattering are important, the estimation becomes less reliable. Moreover, the IP is not available at the level of the cluster identification, before any track is reconstructed. The coordinate of the passage of the particle can also be estimated by the center of gravity (CoG) of the cluster signals. For vertical tracks, test beam studies [87] have shown that the best spatial resolution is obtained with the center of gravity calculated with the seed strip of the cluster and its two neighboring strips with the highest signal. For inclined tracks, the algorithm can be adapted to include more than two strips in the calculation.

---

[3] The relative difference for a given VA is defined as $(MPV_{\mathrm{VA},\eta_1,Z} - MPV_{\mathrm{VA},\eta_2,Z})/(MPV_{\mathrm{VA},\eta_1,Z} - MPV_{\mathrm{VA},\eta_2,Z})$.

In the first iteration of the calibration procedure, we used the IP as the position estimator to extract the correction factors, while the CoG was used when applying the same correction factor to the raw signals. It was however observed that subtle differences appear in the shape of the charge loss effect when describe in terms of the two different estimators. Therefore, using different estimators for the correction factor extraction and for the correction application introduces biases. For consistency, since the IP is not available when applying the correction factors, it was finally decided to use only the CoG estimator.

5.5.2 Charge Loss Description

We produce 3-dimensional description plots of the type of Figure 5.3 for nuclei from proton to iron and for the three different signal routing schemes, K5, K7 and 3S (see 4.3.3). The traversing position of the particle is estimated through the CoG. To be free of any energy dependence (see 5.3.1), we select the signal in the region of minimum ionisation, imposing tight cuts on the reconstructed particle energy : β greater than 0.97 and $\beta\gamma \in (3.98, 7.94)$. The signal, expressed in ADC units, is normalized to the square of the corresponding nuclear charge. This allows a better comparison between different species and simplifies the implementation of the correction procedure. From Figure 5.3 it is evident that the charge loss effect is symmetric between positive angles and negative angles, positive and negative impact positions. We can profit from this symmetry and apply a folding procedure to improve the statistical power of the description. This is particularly useful to describe the heaviest nuclei which suffer from much lower natural abundances. The resulting signal distributions are fitted using a Landau function convoluted with a gaussian noise contribution. The fit is performed with `Root` using the `Minuit` minimization package [97]. The fit function maximum is used as the main parameter to describe the signal peak in the bin. The MPV is found not to be the most reliable description of the peak position due to the convolution with the gaussian function which in some cases shifts the MPV to lower values. Figure 5.11 shows the observed charge collection behavior for the K5 and S readout schemes in terms of the fit results for helium ($Z = 2$), carbon ($Z = 6$) and oxygen ($Z = 8$) nuclei. The general behavior of the charge collection is similar but the absolute scale of the effect tends to decrease with higher charges. The K7 case shows similar behaviors, as one would expect from the similar routing schemes. Its description suffers however from lower statistics since only 32% of the tracker ladders present this specific routing scheme. Moreover, these ladders populate external layers which have a lower acceptance. Figure 5.12 shows the projection, by slices of different inclination bins, of the fitted helium charge collection behavior for different impact positions.

The accuracy of our description depends on the relative abundances of the different nuclei species. Wherever statistics is sufficient, the fit is performed. If not, or if the fit is of insufficient quality, the corresponding bin is set to 0 and treated specifically in the application of the correction factors (Sec. 5.5.3). For each nuclear species, the results of the fits are stored into bi-dimensional maps.

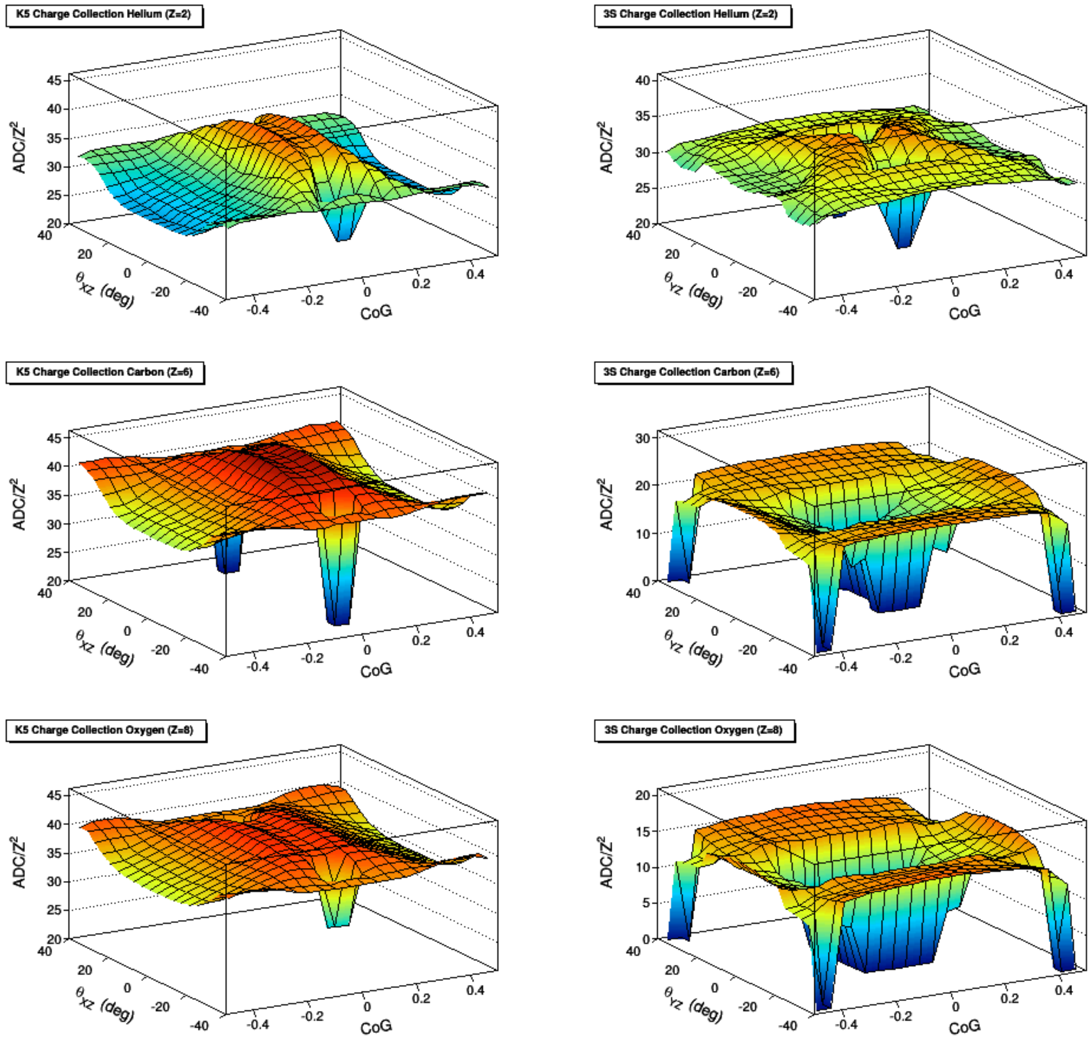

FIGURE 5.11 – K5 (left) and S (right) readout scheme charge collection behavior for selected samples of helium $Z = 2$ (top), carbon $Z = 6$ (middle), and oxygen $Z = 8$ (bottom) nuclei. For each impact position and angle bin is reported the peak value of the fitting function. Empty bins correspond to the cases where the fitting procedure has failed due to lack of statistics, or where the absence of statistics is inherent to the CoG definition of the impact position. With increasing charge, the scale of the charge loss effect tends to decrease.

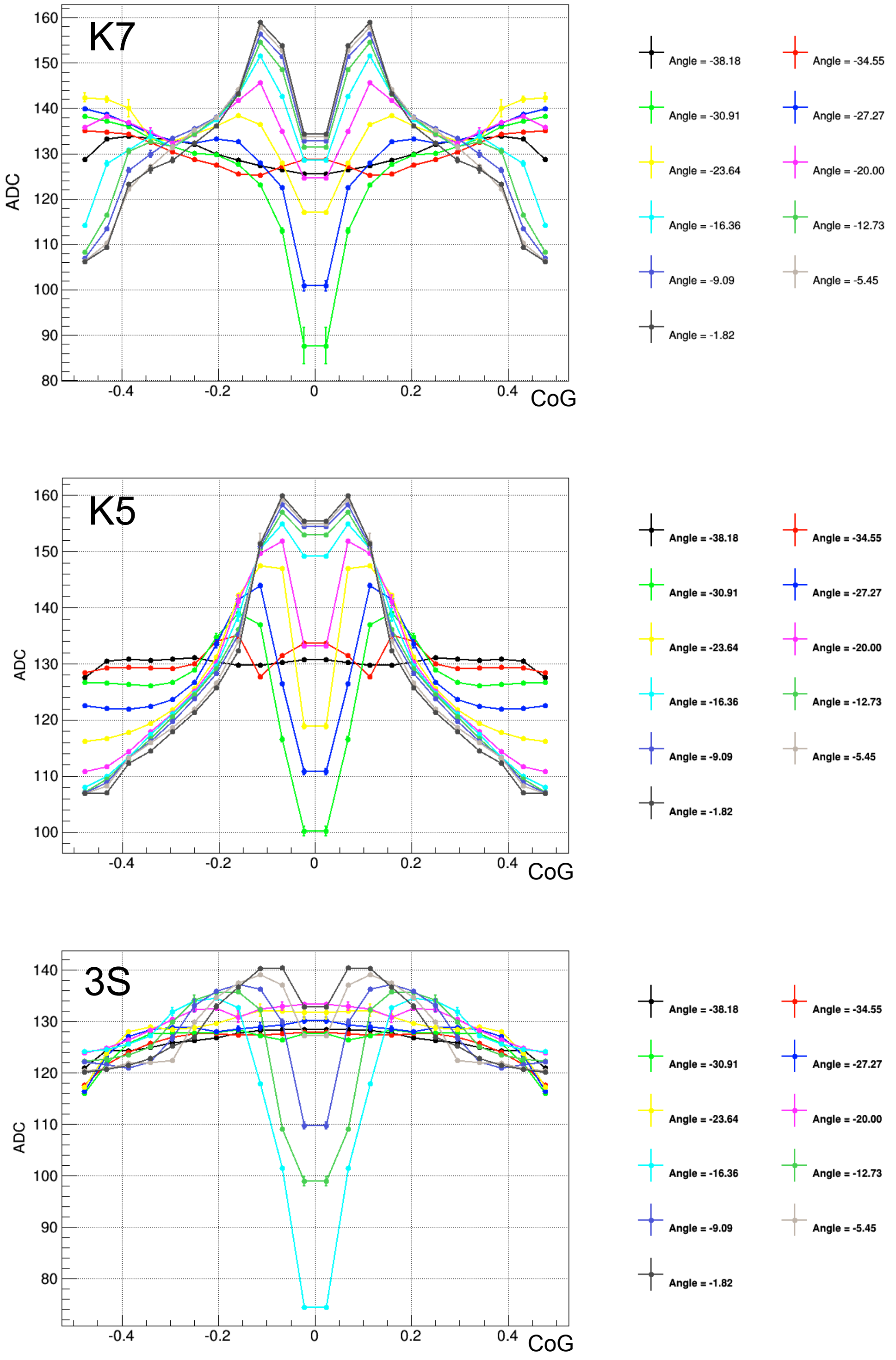

FIGURE 5.12 – Maximum of the fitted function versus the center of gravity CoG for different inclination bins and helium nuclei. The curves are symmetric with respect to CoG=0 since half of the values come from unfolding of the fit results into the previously merged regions. The pronounced gap near CoG=0 is inherent to the CoG definition of the particle impact position.

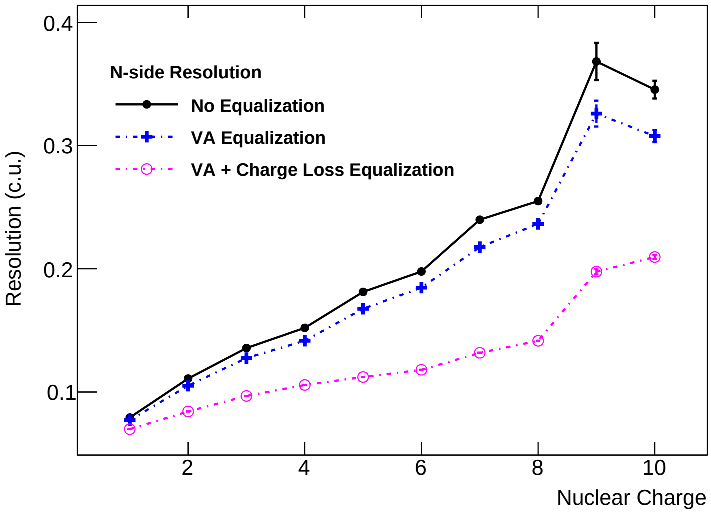

FIGURE 5.13 – N-side charge resolution for nuclei up to neon before and after applying the charge loss correction.

5.5.3 Application of Correction Factors

The equalization is applied to ADC signals by searching for the closest 3-dimensional point in the stored maps. Whenever a point is missing in a given map, the correction algorithm interpolates between the information of the next closest maps. Extensive studies were performed to test the interpolation method. In particular, an interpolation inside the map itself, using the information of the closest group of defined bins, was tested. It was found that this strategy introduced severe biases in the correction factor estimation for maps presenting too many holes. In the process of correcting for the effect of charge loss, the ADC scale of the deposited energy measurement is converted into nuclear charge units. The reference value used for this scale conversion is the weighted mean of fit values.

5.5.4 Results

Figure 5.13 presents the effect of the charge loss correction on the n-side charge resolution for nuclei up to neon ($Z = 10$). The resolution is measured using a multi-gaussian fit (one gaussian per nuclei peak) of the truncated mean distribution of signals before and after applying the corrections, and extracting the widths (1 standard deviation) of the individual gaussians as a sensitive indicator of the resolution. Both K5 and K7 measurements are combined in this result. One observes that the effect of the charge loss correction is substantial, gaining as much as a factor 2 in resolution for certain species. Although the scale of improvement seems to increase with charge, the correction becomes less important for charges above silicon (Z=14) where the n-side saturation starts degrading the measurement but also where the effect of the loss of collection efficiency itself becomes less important.

5.6 Energy Dependences

According to the Bethe-Bloch theory, the shape of the dependence of the ionisation energy loss with the particle energy is not expected to depend on the particle charge. However, we have observed substantial differences in the shape of the energy dependence, especially below the

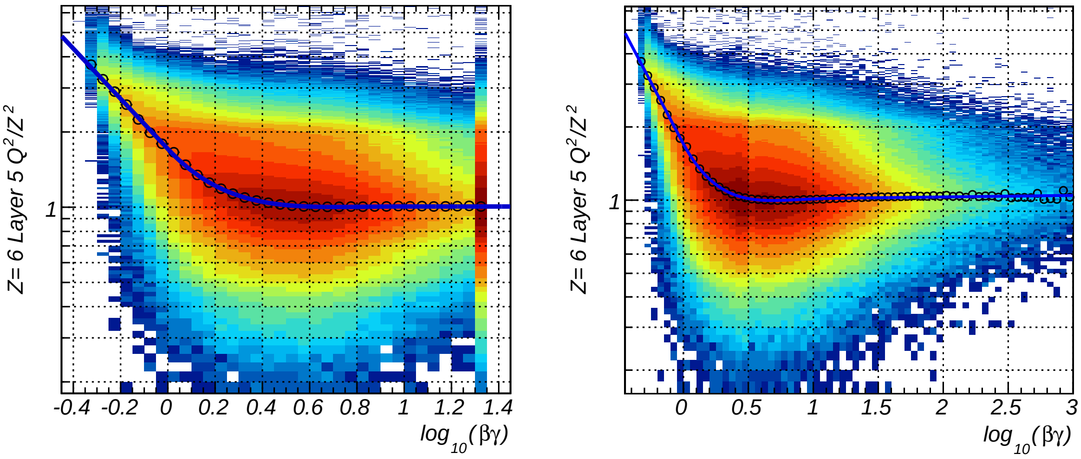

FIGURE 5.14 – Carbon nuclei ionisation energy loss in a single layer as a function of $\beta\gamma$. The left plot describes the dependence using an estimation of the $\beta\gamma$ parameter based on the ToF β measurement only. The right plot uses a combination of the ToF β and tracker rigidity measurement. Each description is parametrized by fitting the corrected pulse height in different energy bins with a Landau function convoluted with a gaussian contribution. The open black circles correspond to the peak values resulting from the fits. This peak profile is then fitted using a function combining two straight lines and a fifth order polynomial. Such parametrization provides a good asymptotic behavior as well as a satisfactory description of the minimum ionizing region. Plots produced by A. Oliva.

minimum ionizing region for different nuclei. Although there is no theoretical support for such charge dependent effect, it seems to be likely that the specific non-linearities and saturation properties of the electronics are at the origin of these features. This has led us to consider a correction procedure based on the observed signal itself, rather than using any theoretical assumptions related to the Bethe-Bloch formula.

5.6.1 Energy Dependence Description

We describe the energy dependence using the universal $\beta\gamma$ parameter, which is equivalent to the momentum over mass value of the particle (p/m). It is in general more convenient to use the logarithm $\xi = \log_{10}(\beta\gamma)$ to consider the energy dependence simultaneously on the full particle energy scale. This parameter can be estimated directly from the ToF β measurement and indirectly from the tracker reconstructed rigidity (R) :

$$\xi_{ToF} = \log_{10}(\frac{\beta}{\sqrt{1-\beta^2}}) \tag{5.5}$$

$$\xi_{Trk} = \log_{10}(R \times \frac{Z}{m}) \tag{5.6}$$

Both estimators are complementary in terms of their specific resolutions. ξ_{ToF} has a better intrinsic resolution at low energies compared to the rigidity measurement which suffers from multiple scattering in the detector. For energies above $\sim$ 2 GeV, ξ_{Trk} becomes the most accurate. ξ_{ToF} presents the advantage of not requiring any information on the charge or mass of the particle, an essential drawback of the rigidity estimation since these properties are in principle not precisely known, in particular for isotopes of a given nucleus.

Two separate descriptions of the energy loss dependence have been derived. The first one uses ξ_{ToF} only. This implies that the logarithmic rise of the energy loss dependence is not described. Therefore, we assimilate all energies corresponding to β >0.999 to a unique characterization. This high energy bin ensures a flat behavior of the description at high energies, in adequacy with the limited ToF resolution. The second description uses a combination of both $\beta\gamma$ estimators, depending on their intrinsic resolutions. Below a β value of 0.95, corresponding to a rigidity around 6 GV, we use ξ_{ToF}. Above this value we switch to the rigidity measurement. Although less accurate at high energies, the ToF based description is additionally produced in order to provide a correction procedure that remains independent of the particle charge and mass properties. An example of the resulting descriptions is presented in Figure 5.14 for a sample of carbon nuclei. The left plot describes the energy dependence in terms of the ToF β measurement alone, with a single characterization of all energies with β >0.999. The right plot is the description obtained using the combination of both ToF and Tracker measurements. Each description is parametrized by fitting the signal in different energy bins with a Landau function convoluted with a gaussian contribution. The open black circles correspond to the peak values resulting from the fits. This peak profile is then fitted using a function combining two straight lines and a fifth order polynomial. Such parametrization provides a good asymptotic behavior as well as a satisfactory description of the minimum ionizing region. The resulting fit (blue curves) are taken as an effective parametrization of the energy loss dependence on $\beta\gamma$ for a given nucleus.

The parametrizations for the two types of descriptions are produced for the most abundant nuclei, from proton to iron, and for each sensor side. Due to the non-linearities in the response function of the p-side, the parametrizations obtained for the n-side are used irrespectively for both sides up to neon ($Z = 10$) in the correction procedure (see 5.6.2). Above neon, specific parametrizations are derived for the p-side. Moreover, one must take into account the energy lost by the particle while traversing the AMS-02 detector. This effect can be important since the ToF measures the β in the middle of the AMS-02 instrument while the amount of material between the tracker layer 1 and the ToF is substantial. This implies that the parametrization must also be implemented for each one of the nine tracker layers, based on an effective β value corrected for the energy lost by the particle while traversing different amounts of material. The resulting parametrizations, for the same carbon nuclei, are given in Figure 5.15 (left plot). While the parametrizations for the inner tracker layers show little difference, strong deviations are observed at low energies for the external layers, as expected. In general the dependence of the correction on different nuclear species is less important, as shown in Figure 5.15 (right plot) for the parameteriztions of the inner tracker layer 5.

5.6.2 Energy Dependence Correction

To correct the cluster signals for the energy dependence, a procedure similar to the one used for the charge loss effect was developed. Both type of descriptions, based on ToF only or on the combined estimator, can be used depending on the type of analysis the user is performing. When both the β and the rigidity of the particle are specified, the procedure corrects the signal using the combined estimator description. If the particle's m/Z value is not provided by the user, an educated guess is made depending on the cluster signal. The resulting m/Z is either the one for proton or for carbon if the signal is characteristic of a charge greater than 1. If the particle rigidity is not specified, or ill-defined, the ToF based correction is applied. These conditions determine the calculation of the $\beta\gamma$ parameter. For a given $\beta\gamma$, the algorithm probes the different parametrizations of the energy loss for the associated layer and sensor side. The resulting relations, in terms of correction factors versus signal values, are systematically

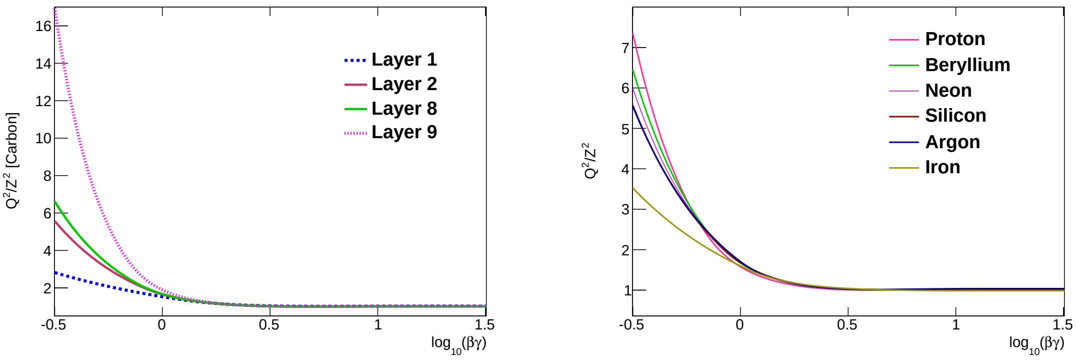

FIGURE 5.15 – *Left* : Parametrization of the energy dependence of the ionisation energy loss of carbon for different tracker layers. The deviations at low energies are due to the additional energy lost by the particle while traversing the AMS-02 material. The deviations are most significant for the two external layers : layer 1 (dashed blue) and layer 9 (dotted magenta). *Right* : The same parameterizations for different nuclei for the inner tracker layer 5. With increasing Z, the energy loss effect becomes less pronounced at low $\beta\gamma$ values.

checked for strict monoticity among the successive values, which are otherwise excluded from the construction. The correction factor is obtained using a cubic interpolation between the constructed relations.

5.6.3 Results

Figure 5.16 shows the result of the energy dependence correction for the n-side charge measurement, for nuclei up to silicon. The correction applied uses the full energy loss description combining the ToF β and Tracker rigidity measurements. We have fitted a simple zeroth order polynomial to each charge sample and calculated the residual distribution for each rigidity bin by comparing the constant value to the peak value of a gaussian fit. For charges up to oxygen, the maximum residual value remains below 1% for all energies. The difference remains below 5% up to iron.

5.7 Final Equalization and Linearization

Due to limited statistics, the equalization procedure described in Section 5.4 uses only proton, helium and carbon nuclei to compute the equalization factors for the n-side measurement and only proton and helium for the p-side equalization. Nevertheless, the equalization for the n-side remains reliable below the saturation region, starting around neon. We thus iterate on the equalization procedure, this time fitting the signal distribution for each single VA with no restriction on impact regions nor on energy, assuming we have efficiently corrected for these effects in the previous steps. The accumulated statistics is enough to extract reference peak values for 19 different nuclei including iron, and perform the extended equalization.

Figure 5.17 shows the results of the final equalization procedure on selected samples of carbon (top) and iron (bottom) nuclei. Each histograms represents the distribution of fitted MPV values for all 3072 VAs, before (black) and after (filled blue) applying the final equalization procedure. The improvement is most significant for carbon where the p-side suffers from the early non-linearities. An overall improvement is observed for all species from proton to iron.

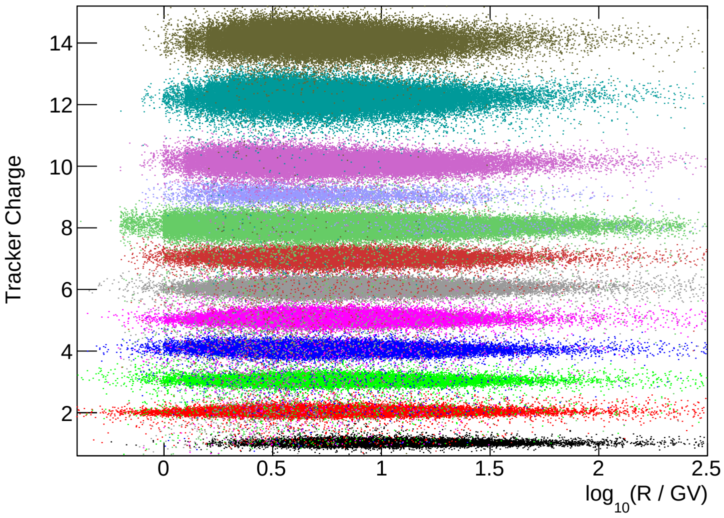

FIGURE 5.16 – Tracker charge estimator for the n-side charge measurement for nuclei up to silicon, after applying the energy dependence correction. The picture allows to see the efficient flattening of the signal distribution with energy.

5.8 Time Stability

We have investigated the potential dependence of our calibration procedure with time. We have binned the two years of statistics in different time intervals depending on the relative nuclei abundance and studied the stability with time of the final tracker charge estimator for the most abundant species : proton, helium, carbon, oxygen, silicon and iron. Figure 5.18 shows the normalized tracker charge estimator for carbon. The black points correspond to the average charge value in each time interval. The RMS of this profile distribution is well below 1% for all charges up to iron and no significant time dependences are found.

5.9 Charge Identification Performance

Figure 5.19 shows the overall improvement in the p (blue) and n-side (red) charge measurements before and after all the calibration steps are applied. The improvement in resolution is most significant for charges up to magnesium ($Z = 12$), after which the n-side response starts saturating, implying a natural degradation of the measurement. For the p-side, a charge distinction power is even achieved around the CNO group.

Assuming the p- and n-side measurements are independent [4], it is possible to profit from both measurements to improve the overall charge identification power. The two measurements are combined using a weighted sum, where the weights are determined from the specific resolutions, depending on the number of points used in the truncated mean computation. The combined charge measurement is then given by :

$$Q = \frac{Q_n w_n + Q_p w_p}{w_n + w_p} \tag{5.7}$$

---

[4] This is only approximately true since an energy deposition in the tail of the Landau distribution on one side will also appear in the tail of the energy loss distribution on the other side.

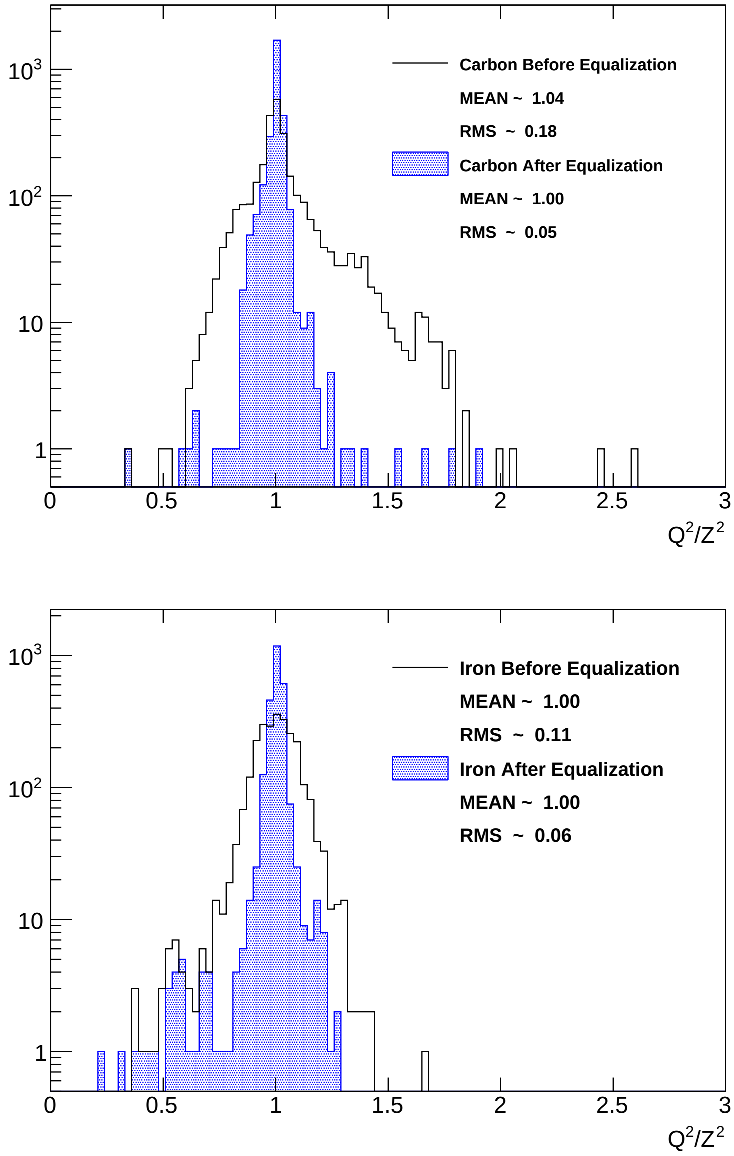

FIGURE 5.17 – The final equalization procedure. The top plot corresponds to the distribution of the 3072 VA MPV values for carbon nuclei, before (black) and after (filled blue) the final equalization procedure. The bottom plot shows the result for iron nuclei.

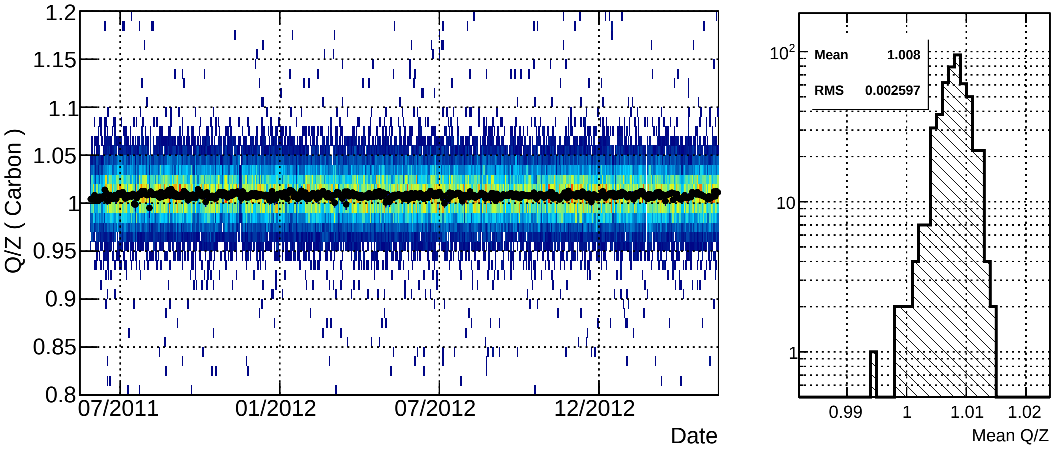

FIGURE 5.18 – *Left* : normalized tracker charge estimator in function of time for carbon nuclei. *Right* : distribution of average Q/Z values for all time intervals.

where the $w_i = 1/\sigma^2(n)$ are the corresponding weight factors that depend on the number of hits n used in the charge determination. We use the resolution curves for the 6 points case as a reference and treat the other cases with simple normalization factors that we assume independent of charge. The distribution of the final combined estimator is shown in Figure 5.20 (top plot) over the full range of charges. Nuclei up to silicon ($Z = 14$) can clearly be separated. Above, nuclei with even charge number can also be distinguished. The iron peak itself is clearly visible due to its natural higher abundance compared to neighboring charges. The bottom plot of Figure 5.20 shows the measured tracker charge resolution. For the combined measurement, we reach a resolution at the level of 0.1 charge units (c.u.) for carbon and lower than 0.3 c.u. up to silicon. The resolutions are obtained by fitting the overall charge estimator distribution using a multi-gaussian fit and extracting the width of each individual gaussian. Fitting the iron peak independently, we estimate a resolution at the level of 0.6 c.u. At 99% selection efficiency, the contamination from neighboring charges is estimated to be lower than 10^{-4} up to oxygen (Z=8) with a mis-identification probability for carbon lower than 10^{-6}.

5.10 Software Implementation

All the information relative to the calibration procedure is saved in tables stored in a dedicated data base easily accessible by all members of the collaboration. The calibration parameters are applied offline and the procedure is essentially transparent to the general user. Based on a tracker track (`TrTrackR` object), there are several methods to access the associated charge measurement :

- $\mathrm{GetQ}(\mathrm{float\ beta} = 1, \mathrm{int\ fit\_id} = -1, \mathrm{float\ mass\_on\_z} = 0, \mathrm{int\ version} = 2)$
- $\mathrm{GetInnerQ}(\mathrm{float\ beta} = 1, \mathrm{int\ fit\_id} = -1, \mathrm{float\ mass\_on\_z} = 0, \mathrm{int\ version} = 2)$
- $\mathrm{GetLayerJQ}(\mathrm{float\ beta} = 1, \mathrm{int\ fit\_id} = -1, \mathrm{float\ mass\_on\_z} = 0, \mathrm{int\ version} = 2)$

which essentially allow to retrieve a particle charge estimation at different levels of the tracker. The single layer evaluation returned by the last method GetLayerJQ() is very useful to study fragmentation in the detector. The user can provide an estimation of the particle velocity

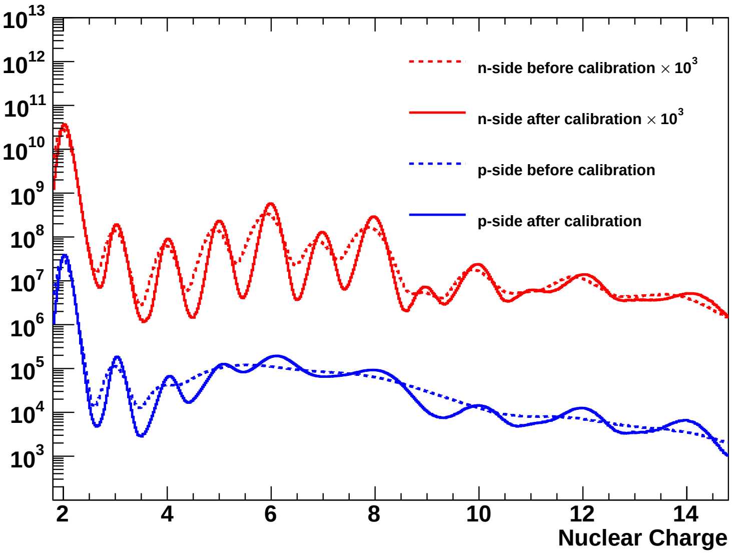

FIGURE 5.19 – Raw abundance distribution for nuclei in the calibration sample before and after applying the equalization and linearization procedure, for the n-side (red) and p-side (blue) measurements. The distributions are not corrected for efficiency and fragmentation.

β, the identification number of the track to access the rigidity measurement, as well as a guess of the m/Z value to help the energy loss dependence correction. The default version is fixed to the latest set of calibration factors but previous calibration results are available. The methods essentially compute a floating point charge estimation based on a truncated mean of all hits belonging to the track. By default, the signals are corrected for all the effects described above. The actual methods used to compute the charge are available through the `TrCharge` class. Ultimately, the user can loop on all hits belonging to a track and retrieve the signal associated to either the x or y cluster. Clusters are managed through the `TrClusterR` class. The GetTotSignal(OptCorr, $\beta, R, m/Z,$ multicplicity) method allows to retrieve the cluster's signal with the desired choice of correction options specified in OptCorr. The available corrections are summarized in Table 5.1.

Corr. Id	**Explanation**
kNoCorr	No Correction Applied
kAsym	Cluster Asymmetry Correction (left/right)
kAngle	Energy Loss Normalization at 300 μm $[cos(\theta)^{-1}]$
kGain	Gain Correction
kLoss	Charge Loss Correction
kLoss2	Charge Loss Correction (alternative to kLoss)
kPN	Normalization to P-Side (probably not working, however not really needed)
kMIP	Normalization to number of MIP
kMeV	Multiply by 300 um MIP energy deposition (estimated to be 81 keV)
kBeta	Beta correction
kRigidity	Rigidity correction
kOld	Use old charge calibration

TABLE 5.1 – Summary of correction options available to correct the signal associated to a tracker cluster.

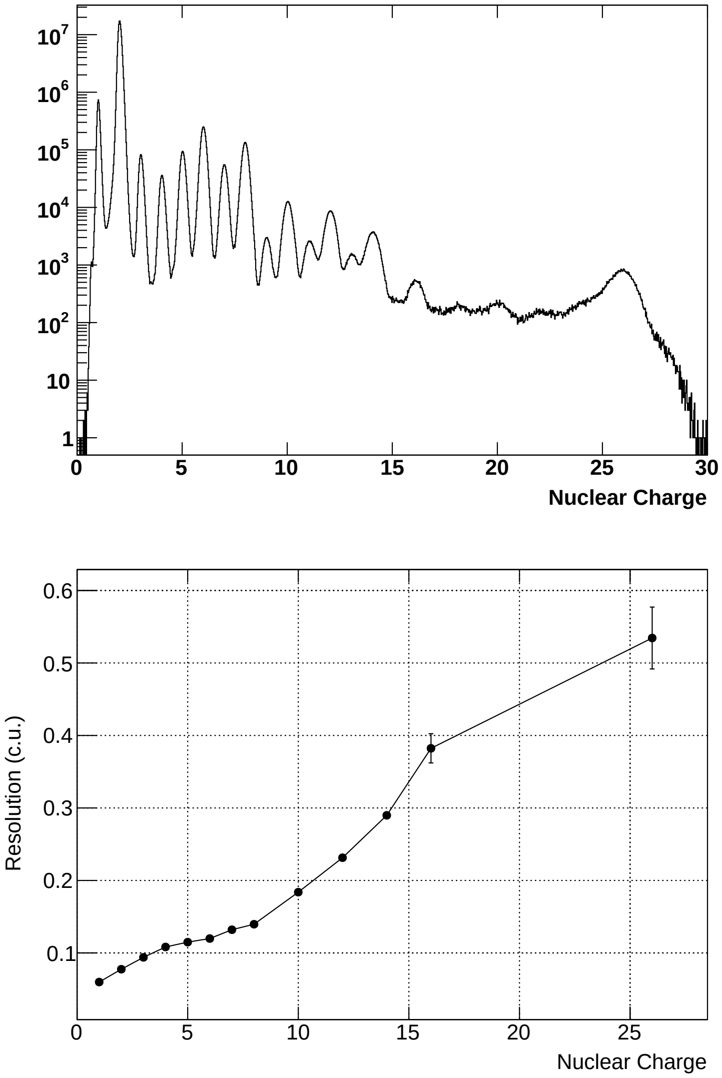

FIGURE 5.20 – *Top* : Raw abundance distribution of nuclei in the calibration sample as a function of the final tracker charge estimator for the combined p- and n-side measurements. The distribution is not corrected for efficiency and fragmentation such that the proton and helium contributions are strongly suppressed. *Bottom* : tracker charge resolution expressed in units of charge from Gaussian fits to the raw abundance distribution. Errors are from the fit.

Chapitre 6

Nuclei Flux Measurements

"This is the end, my friend, the end"

The Doors

In Chapter 5, we have discussed the work done to accurately calibrate the tracker response to cosmic ray nuclei, independently of their energy. The resulting resolution allows to efficiently distinguish nuclei species with the charge Z ranging from 1 (ionized hydrogen) to 14 (silicon). Above, the resolution rapidly degrades due to saturation effects in the electronics, although some distinction power can still be achieved for the most abundant even charge species. Combining the excellent identification power of the tracker with other subdetectors, AMS-02 has the potential to measure relative abundances and absolute fluxes of cosmic ray nuclei from hydrogen up to at least iron ($Z = 26$) in a kinetic energy range from hundreds of MeV to few TeV. With the unprecedented level of statistics accumulated by AMS-02, such measurements will help to better understand the life of cosmic rays in the galaxy, from their origin to their propagation in the interstellar medium.

In this chapter, we discuss a procedure to measure the fluxes of light nuclei based on the inner tracker charge measurement. Although the method is intended to produce in one shot all nuclei fluxes from lithium ($Z = 3$) to silicon ($Z = 14$), we will present preliminary results only up to neon ($Z = 10$) and focus our attention on the most abundant species : boron, carbon, nitrogen and oxygen.

6.1 Nuclei Identification with AMS-02

AMS performs redundant measurements of the absolute charge $|Z|$ along the particle trajectory inside the detector. The tracker identification capabilities have been discussed in the previous chapter. Moreover, each individual layer of silicon possesses its own discrimination power. The tracker charge measurement is complemented by a number of other detection techniques. The ToF instrument performs 4 separate measurements of the charge in each layer of scintillation counters. The resolution of the tracker starts to degrade significantly around silicon ($Z = 14$) while the ToF exhibits an excellent distinction power up to Nickel ($Z = 28$) and perhaps above. The TRD distinction power is also useful for very light nuclei up to oxygen.

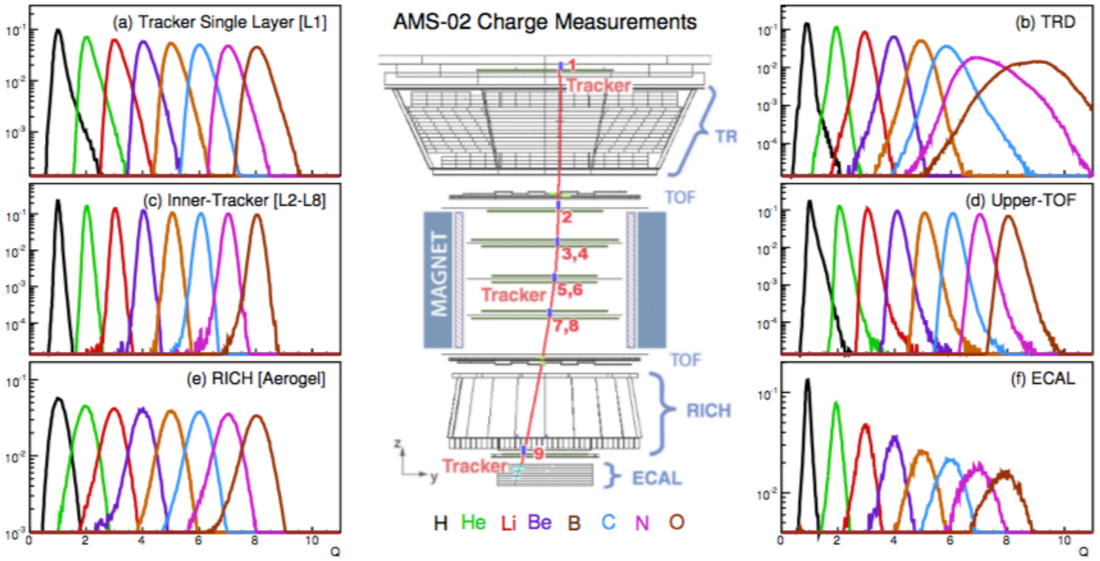

FIGURE 6.1 – Projected $Y-Z$ view of the AMS-02 detector. The red curve represents the trajectory of a particle through the instrument with the various measurements of the particle charge Z at various levels of the instrument [105].

The RICH provides a good charge identification power using the signal created by particles traversing the Aerogel part of the radiator. Finally, although an electromagnetic calorimeter, the first layers of the ECAL also provide some reliable estimation of the charge for light nuclei. Figure 6.1 illustrates the principle of redundant charge measurement inside AMS-02. The six panels show the response of the different subdetector units to light cosmic ray nuclei. A detailed review of the light nucleus identification power of AMS-02 can be found in [105]. These individual measurements are proven to be very useful, in particular to control fragmentation in the detector. For example, the layer 1 can be used to identify a carbon nucleus entering the detector from the top. If a fragmentation occurs in the TRD or in the upper ToF, the inner tracker is typically able to measure the resulting boron product. An example of such a fragmented carbon event is shown in Figure 6.2.

To study the individual response of the various subdetectors to different nuclei, we have considered 9 different estimators of the particle charge : the tracker layer 1, the TRD, the Upper ToF plane, the tracker layer 2, the inner tracker (all 7 layers together), the inner tracker excluding layer 2 (for the unbiased study of the layer 2 response), the lower ToF plane, the RICH Aerogel and the tracker layer 9.

We have intentionally limited our analysis to nuclei up to silicon ($Z = 14$) due to the degrading tracker resolution for higher charges. In the future, the ToF could be used to extend the measurement to heavier nuclei.

6.2 Flux Formula and Analysis Strategy

The differential flux of a given cosmic ray species in a given rigidity interval can be expressed as :

$$\Phi_Z(R, R+\Delta R) = \frac{N_Z(R, R+\Delta R)}{\Delta T \times A_{\text{Geom}} \times \Pi_i \epsilon_i \times \Delta R} \tag{6.1}$$

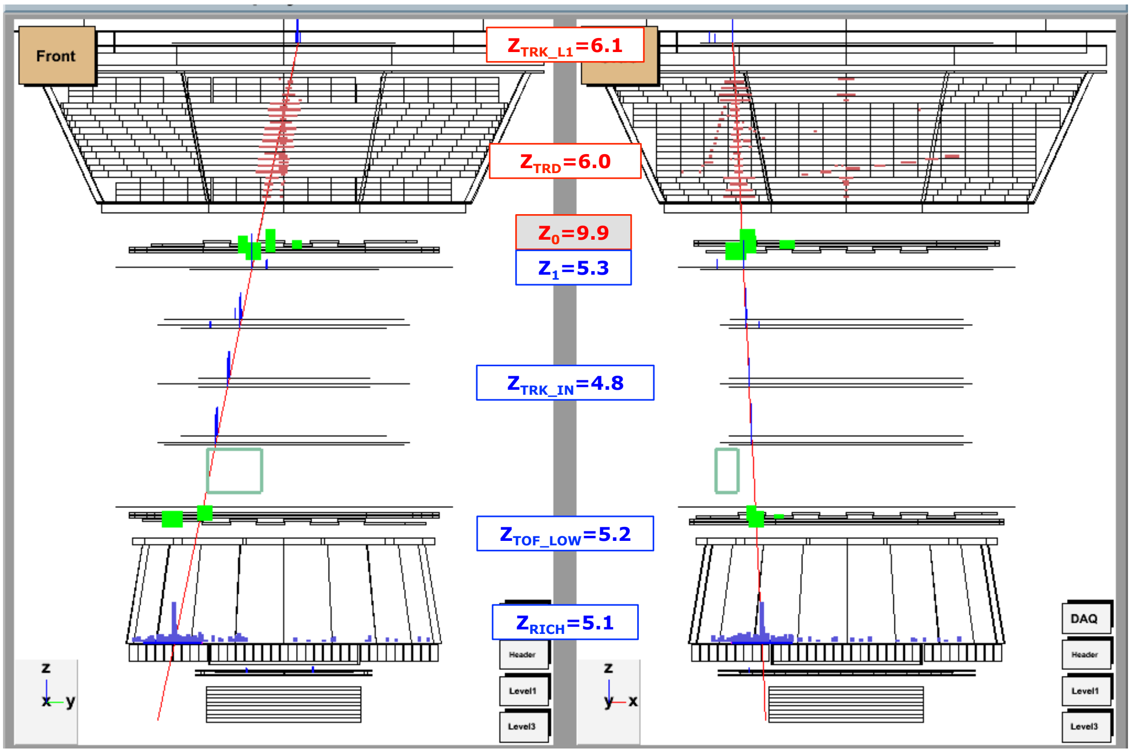
Front
$Z_{TRK\_L1}=6.1$
$Z_{TRD}=6.0$
$Z_0=9.9$
$Z_1=5.3$
$Z_{TRK\_IN}=4.8$
$Z_{TOF\_LOW}=5.2$
$Z_{RICH}=5.1$
DAQ
Header
Level1
Level3
z
x
y

FIGURE 6.2 – Event display (in both bending and non-bending projections) of a carbon nucleus entering the AMS detector from the top and fragmenting into boron in the upper ToF plane. The tracker layer 1 measures a charge of 6.1, the TRD 6.0, while the inner tracker and RICH measure a charge corresponding to boron (Z=5). In the upper ToF plane where the interaction presumably takes place, the measurement integrates the products of the interaction and typically measures a higher charge value. One can also notice from the projection on the right side some activity in the TRD which is most likely due to the production of δ-rays.

where $N_Z(R, R{+}\Delta R)$ is the number of nuclei of charge Z traversing the detector with a rigidity between R and $R + \Delta R$. This number can be obtained by various methods based on different conceptual and technical solutions. ΔT is the exposure time for the analyzed data set. A_{Geom} is the geometric acceptance of the detector and the ϵ_i are the various detector reconstruction efficiencies associated to the specific cuts used in the analysis. We now discuss in more details theses various terms.

6.2.1 Nuclei Counting Method

To measure the nuclei counts $N_Z(R, R + \Delta R)$, we have developed a procedure based on a template fit of the inner tracker charge distribution. The fit provides a first estimation of the total number of nuclei of each species traversing the detector. Due to the matter separating the top of AMS-02 and the inner tracker planes, one expects a substantial contribution from fragmentation initiated above the inner tracker to pollute this measurement. To account for this background, we compute correction factors based solely on the data.

We restrict the geometric acceptance of our analysis to particle tracks passing through the tracker layer 1 and the inner tracker planes. We then study the response of the layer 1 associated to the charge information coming from the inner tracker. The methodology is illustrated in Figure 6.3. The central plot shows the result of the inner tracker template fit of nuclei from boron to nitrogen. Based on this fit, one can select a sample of carbon nuclei (shaded band) with known efficiency and contaminations from neighboring charges. Due to the excellent charge resolution of the inner tracker, a selection efficiency higher than 99% percent with contaminations less than 1% can be achieved up to neon ($Z = 10$). For a pure carbon sample selected in the inner tracker, we now look at the charge distribution of the associated layer 1 hits, as shown in the right plot in Figure 6.3. Several components can be identified. The main peak corresponds to carbon nuclei traversing the layer 1, hence clean events that have not fragmented up to the inner tracker. To the right of the main carbon peak, several heavier nuclei contributions are clearly identified. The latter are associated to fragmentation events. Using a template fit of the layer 1 charge distribution, we can extract the proportion of non fragmenting carbon events traversing the layer 1 and inner tracker. This strategy is applied in different intervals of energy and for all nuclei species up to neon. The final inner tracker corrected count number in a given energy bin can be written as :

$$N_Z(R, R + \Delta R) = \frac{N_{Z,\mathrm{L1,Pure}}(R, R + \Delta R)}{N_{Z,\mathrm{InnerTrk,Pure}}(R, R + \Delta R)} \times N_{Z,\mathrm{InnerTrk,Tot}}(R, R + \Delta R) \tag{6.2}$$

The denominator $N_{Z,\mathrm{InnerTrk,Pure}}$ is the number of nuclei selected in the pure inner tracker sample. $N_{Z,\mathrm{L1,Pure}}$ is the number of corresponding nuclei with the same Z fitted in the layer 1. The ratio of these two terms is a survival fraction correction term for the total number of nuclei fitted in the inner tracker $N_{Z,\mathrm{InnerTrk,Tot}}$. The obtained final count number N_Z must still be corrected for the total survival probability of a given nucleus traversing the material above the inner tracker, which includes the total fragmentation probability and the presence of interactions which can degrade or even prevent any track reconstruction. To measure the fragmentation contribution, a solution would be to fit all fragmentation contributions on the layer 1 for all nuclei such that an estimation of the partial fragmentation cross-sections could be derived. This exercise has been partially conducted but proven to be technically challenging. For the results presented in this analysis, we include the survival probabilities for each nucleus inside the geometric acceptance term, requiring that no fragmentation takes place between the layer 1 and the inner tracker (see Section 6.5).

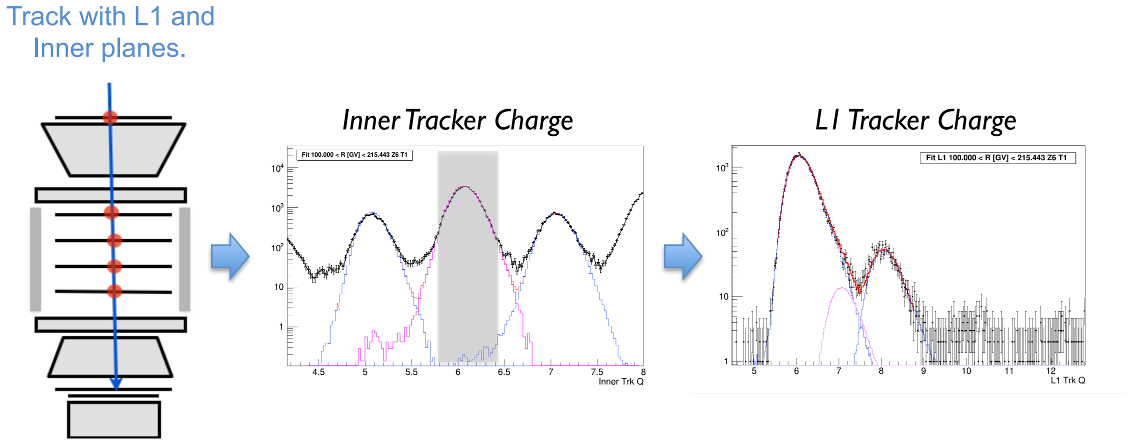

FIGURE 6.3 – Illustration of the strategy of our nuclei counting method. We select tracks with hits in the tracker layer 1 and inner tracker planes. For a pure sample of carbon nuclei selected in the inner tracker (left panel, shaded area), one can estimate the fragmentation background by looking at the associated layer 1 charge distribution (right panel).

The initial motivation behind this counting method was to measure nuclei relative abundances. The method is in fact convenient to extract simultaneously the counts of different nuclei species, providing a straightforward estimation of the relative abundance at different energies. This approach represents also a limitation in terms of individual flux measurements since the energy binning used is essentially dictated by the less abundant species. The procedure is however modular enough to allow a different binning for dedicated analysis for the more abundant BCNO elements.

There is an important and dangerous assumption underlying this counting method, namely that the reconstruction efficiency of tracks with hits in the layer 1 and in the inner tracker is the same for clean events (non-fragmenting) and for fragmentation events. The fragments share the momentum of the mother nucleus such that their magnetic rigidity is almost the same. They thus follow the same trajectory and a track can still be reconstructed. It is legitimate to ask what is the level of inefficiency introduced. Moreover, the track reconstruction efficiency can also be affected by high Z fragmentation events which tend to introduce more activity in the detector (more noise), making the task of the track finding algorithms more difficult. These effects should be carefully studied.

6.2.2 Flux Normalization Factor

The observed number of nuclei N_Z must be corrected for several effects to produce a flux measurement. The detector has a limited field-of-view : the intrinsic acceptance of the instrument is defined by an opening angle depending on the position of the ToF planes (needed to generate a physical trigger) and the ACC counters (which veto particles with too high inclinations traversing the magnetic walls). The geometric acceptance is further reduced by the specific conditions imposed in the analysis. Here we request that particles pass through the layer 1 and the inner tracker. These two requirements reduce the ToF geometric acceptance by roughly a factor 6.

One must also take into account the live-time of the experiment, which is the total time the experiment is in a state ready to accept a new trigger, i.e., measure a new incoming particle. Some time periods can be intentionally rejected due to many different reasons : dedicated calibration of a subdetector, re-filling of the TRD straw tubes with gas, bad temperature periods (high beta angle), commissioning phases, etc. Events acquired in the South Atlantic Anomaly are usually rejected since they are mainly low energy trapped particles from which it is almost impossible to disentangle and reconstruct the primary cosmic ray component. Moreover, due to the Earth's magnetic field, only particles above a certain energy can reach the detector. This energy threshold, called geomagnetic cut-off, is relevant up to few tens of GeV after which primary cosmic ray particles are not affected by the geomagnetic field anymore. Taking into account all the effects contributing to the experiment's dead-time, one can define a total exposure time which depends both on energy and particle type (Section 6.6) and of course on the time period covered by the analyzed data set.

Finally, one must account for the detection and reconstruction inefficiencies of the various subdetectors used in the analysis. For example, how often is the tracker able to reconstruct a track when a particle has indeed passed through all layers of the tracker. The redundant measurements of different particle properties inside AMS offer a convenient way to measure these detector efficiencies in an independent way directly from the data. Another solution is to use the Monte Carlo simulation (see 6.2.3), provided the simulation is reliable. In this analysis, we have extracted all the reconstruction efficiencies from the data. The main reason is that only a limited number of MC nuclei samples was available at the time of this analysis (lithium to oxygen) with sometimes very limited statistics. Since our main motivation is to study all reconstruction efficiencies up to silicon, we have based our parameterizations on the data. We nevertheless present data and MC comparisons when available.

6.2.3 The Monte Carlo Simulation

The AMS-02 Monte Carlo is a complex simulation program that contains a detailed description of the detector : its geometry based on various measurements and mechanical drawings and its composition, with the best estimates possible of the matter density distribution of both active and passive areas in the instrument. The detector description is combined with a simulation of the physical processes that take place inside the detector when a charged particle passes through. This is done by means of the standard `GEANT` package [107]. Once the various energy depositions and interactions of particles inside the detector are described, the hit simulation produces the experimental signals which set the basis for an event reconstruction in the same way as for real data. One ends up with a data structure similar to the one obtained in the data with the additional information of the Monte Carlo generation parameters : which entering particles have been simulated, in which energy range, with what type of spectrum, etc. The simulation code is written and maintained by the collaboration while the MC productions take place in various computing centers around the world.

The Monte Carlo simulation is a fundamental tool to better understand the behavior of the instrument and provide insights in regions of the experimental data with limited or no statistics. The descriptive power comes from the knowledge of the generated particle properties, provided the simulation of the detector and physics processes is accurate. There is no absolute criteria to verify these conditions. One common approach to the validation of the Monte Carlo is to test systematically all reconstructed variables both in the data and in the MC. The best agreement must be found and the MC can be tuned to some reasonable extent to reproduce more accurately the data. The MC can then be used to compensate statistics limitations in the data, for example to construct templates of various quantities. Moreover, the MC can be used to estimate the level of fragmentation expected in the detector. Such estimations are however based on various sources of input (experimental data combined with empirical and semi-empirical models of fragmentation cross-sections), the uncertainties of which may remain significant.

Regarding a flux analysis, the MC can be very useful to group the geometric acceptance factor A_{Geom} and the efficiencies ϵ_i into a single acceptance term. One first checks that all the reconstruction efficiencies are consistent in between data and MC. All the selection cuts of the analysis are then applied to a MC sample of the particle species under study and a single acceptance term can be calculated as :

$$Acc_Z(R, R + \Delta R) = \frac{N_{Z,\text{rec}}(E)}{N_{Z,\text{gen}}(E)} \tag{6.3}$$

where $N_{Z,\text{rec}}$ is the number of reconstructed particles passing all the cuts of the analysis. Normalized to the total number of particles generated in the MC sample $N_{Z,\text{gen}}$, one obtains an overall acceptance term for each nucleus as a function of energy. This simplifies greatly formula 6.2.1 but makes the careful check of the consistency between data and MC a challenging task. Small differences between the MC and the data can be parameterized and the general acceptance term corrected accordingly.

6.3 Data Selection

The evident signature for a particle traversing the AMS detector is to have a track reconstructed by the Tracker, to which is associated a measurement by the ToF of the particle velocity β. The basic requirement of this analysis is to have both objects associated to the reconstructed particles. We then apply a set of quality cuts on the ToF and Tracker variables to ensure the quality of our sample. The selection is applied in order to remove misidentifications, poor reconstructions and the main backgrounds for the signal of interest. The goal is to reject these sources efficiently while keeping the maximum efficiency for the signal of interest. All the cuts of this analysis have been carefully studied to satisfy these conditions simultaneously for all nuclei species from lithium to silicon. This results in looser cuts then what would perhaps be adopted in individual analysis of the various nuclei.

6.3.1 Data Sample

We use a data sample based on more then two years and a half of statistics, from May 2011 to December 2014. For the purpose of nuclei studies, the initial data is reduced to a dedicated ntuple data structure. The reduction code has been written by A. Oliva. Proton and helium contributions are pre-scaled by a factor 1000 and 100 respectively to efficiently reduce the total size of the sample. For each event, the minimum request is to have both a tracker track and a ToF beta object reconstructed. Looping on all reconstructed tracks, the one with the highest average energy deposition on all tracker planes is chosen as the most reliable nuclei candidate. The standard reconstruction of the ToF beta object within the official AMS-02 software utilizes the information from the reconstructed tracks in the tracker. In the reduced data set, a standalone reconstruction of the ToF beta has been added, extremely useful for independent studies of the tracker performance. For the Monte Carlo studies, we have used the latest production of lithium to oxygen nuclei based on the B800 version of the AMS software. The MC production is passed through the same reconstruction and reduction chain as the data.

We exclude runs acquired before the 29th May 2011 corresponding to the commissioning phase of the experiment in space. To reduce the total event data rate, stricter conditions on the ion trigger were applied after this date (see 3.1.10). We also exclude the time period between the 3rd of June and the 4th of June that correspond to special trigger tests. All these exclusions are accounted for in the final exposure time (Section 6.6).

6.3.2 Selection Cuts

We apply loose trigger conditions on the events, the minimum requirement being at least 3 out of 4 ToF signals above high threshold to select charged particles traversing the detector. We then apply all the quality cuts summarized in Table 6.1. The compatibility cuts between the Tracker and ToF variables are intentionally kept very loose to avoid any bias with rigidity since the two measurements have different characteristic resolutions as a function of energy. The compatibility helps however removing bad associations. The efficiency of each single cut has been studied both in ISS data and in the Monte Carlo as a function of the particle rigidity (see Section 6.4). The cuts were grouped in 4 categories :

1. **Beta Reconstruction** : how many times a good beta object is associated to a particle passing inside the ToF fiducial volume.
2. **Inner Tracker Reconstruction** : how many times a good track is associated to a particle passing inside the inner tracker fiducial volume.
3. **Layer 1 Pick-Up Efficiency** : how many times, given a good inner tracker track which extrapolates inside the Layer 1 fiducial volume, a good hit on the layer 1 is attached to the track.
4. **Trigger Efficiency** : given all the selection cuts of the analysis, how many times these conditions are associated with a physical trigger.

The qualification of a *good* track or *good* β is obviously dependent on the specific cuts used in the analysis. The cuts related to the tracker are separated into 2 categories (2 and 3) for practical reasons that will become clear in the next sections.

The cuts related to charge assignments include tests of the cluster quality (cluster at the edge of a sensor, VA with a very low gain or pathological behavior, etc.) and simply add to a total geometrical inefficiency. The Choutko and Alcaraz fitting methods use different technical implementations of the fitting algorithms which offers a good quality check of the reconstructed rigidity. The cut to remove wrong associations was implemented based on inspection of the data and also helps removing singly charged particles such as electrons and pions.

6.4 Reconstruction Efficiencies

The efficiency of a given cut can be defined as the ratio of events passing the cut over the number of good events before the cut. We are interested in the dependence of the efficiency with energy. A flat behavior is the easiest case to treat but is often not verified. One can then either parameterize the observed dependence or quantify the systematic error resulting from the flatness assumption. We measure the efficiencies of all our cuts in function of the particle rigidity for all nuclei up to silicon. For the cuts related to a given subdetector, independent samples of good events are constructed using other subdetectors. For the clarity of the presentation, we present in this section only the plots for elements of the BCNO group. The results for all other nuclei are presented in Appendix B to E.

The efficiency measurement can be interpreted as the parameter of a binomial distribution. The expectation value of the number of events passing a cut is given by the true efficiency

Tracker Track Selection
At least 4 inner hits with a Y cluster
At least 3 inner hits with both a Y and X cluster
At least 1 hit on each inner tracker plane
At least 3 good charge assignments in the inner tracker
Overall inner tracker charge is well defined
A hit on the layer 1 with both X and Y clusters
The charge on the layer 1 is well reconstructed
Chi-square on X : $-2. \leq \log_{10}(\chi^2_Y) \leq 2.$
Chi-square on Y : $-2. \leq \log_{10}(\chi^2_X) \leq 2.$
Fitting method : $\lvert(R_{Choutko} - R_{Alcaraz})/(R_{Choutko} + R_{Alcaraz})\rvert < 0.2$
ToF Selection
At least 3 hits used in the velocity reconstruction
Chi-square : $-3. \leq \log_{10}(\chi^2_T) \leq 3.$
$0.3 < \beta < 1.5$
Compatibility Cuts
Tracker and Tof matching : $-4. \leq \log_{10}(\chi^2_C) \leq 4.$
Wrong associations : $\beta < (0.76 \log_{10} R + 0.96)$
Rigidity compatibility : $\lvert R_{Tof} - R_{Trk}\rvert < 0.4$

Table 6.1 – List of Tracker and Tof based selection cuts used in this analysis.

times the total number of events. One can estimate the efficiency by replacing the expected number of passed events by the observed number of passed events :

$$\epsilon_{Z,cut}(R) = \frac{N_{Z,cut}(R)}{N_{Z,sel}(R)} \tag{6.4}$$

where N_{sel} is the number of good events in the efficiency sample and N_{cut} the number of events passing the cut. We assume a binomial distribution and compute asymmetric errors at the 68% (1 standard deviation) confidence level for the frequentist Clopper-Pearson interval for binomially distributed data[1].

6.4.1 ToF Reconstruction Efficiency

The reconstruction algorithms used to measure the particle velocity β with the ToF instrument are independent from the level-1 trigger logic. While the ToF trigger might be activated by a particle crossing the detector, it can happen that no clusters are judged appropriate to reconstruct the particle velocity. The default velocity reconstruction algorithms use the information from the tracker reconstruction to help find a best track inside the ToF. Each cluster associated to the ToF track can then be assigned a charge estimation, usually combined in an upper ToF plane and lower ToF plane evaluation.

The fiducial volume defined by the inner tracker is well within the ToF planes geometry. We can therefore use the tracker tracks to define our initial sample. Although this reduces the area of the ToF tested for inefficiencies, it remains consistent with the conditions of this particular analysis which requires a tracker hit in the layer 1 and in all the inner tracker planes. Our initial efficiency sample is defined as events and particles passing the following criteria :

- charged particle trigger,
- Tracker track Y hits > 4 and XY hits > 3,
- Hit on layer 1 and all inner planes,
- Chi-square : $-2 \leq \log(\chi^2_{X,Y}) \leq 2$..

Samples of different nuclei are defined using the charge measurement in the layer 1 and in the inner tracker. We apply to the samples the ToF selection from Table 6.1. Figure 6.4 shows the cut breakdown for the ToF beta reconstruction efficiency. Each cut is added on top of the previous one such that the lowest curve indicates the final efficiency. The overall efficiency after applying all the selection cuts remains very high, above 98.5% at all energies. The final efficiency is almost flat with rigidity for all nuclei. Small structures however appear in very narrow energy ranges that cannot be explained by simple statistical fluctuations given the small errors. One possible explanation is that these structures are related to the re-weight of events when correcting for the pre-scaling factors used to produce the reduced data set (see 6.3.1). These effects remain at the percent level and we decide to neglect them in the efficiency parameterization, although included in the systematic error estimation.

Monte Carlo Comparison

In Figure 6.5 we present a comparison between the efficiency measured in the data (blue) and in the MC (green) for the combination of all efficiency cuts. Albeit some small fluctuations in the MC due to limited statistics and the structures in the data already discussed, the

---

[1] This estimation is provided as a standard tool in the Root `TEfficiency` utility (`http://root.cern.ch/root/html/TEfficiency.html`).

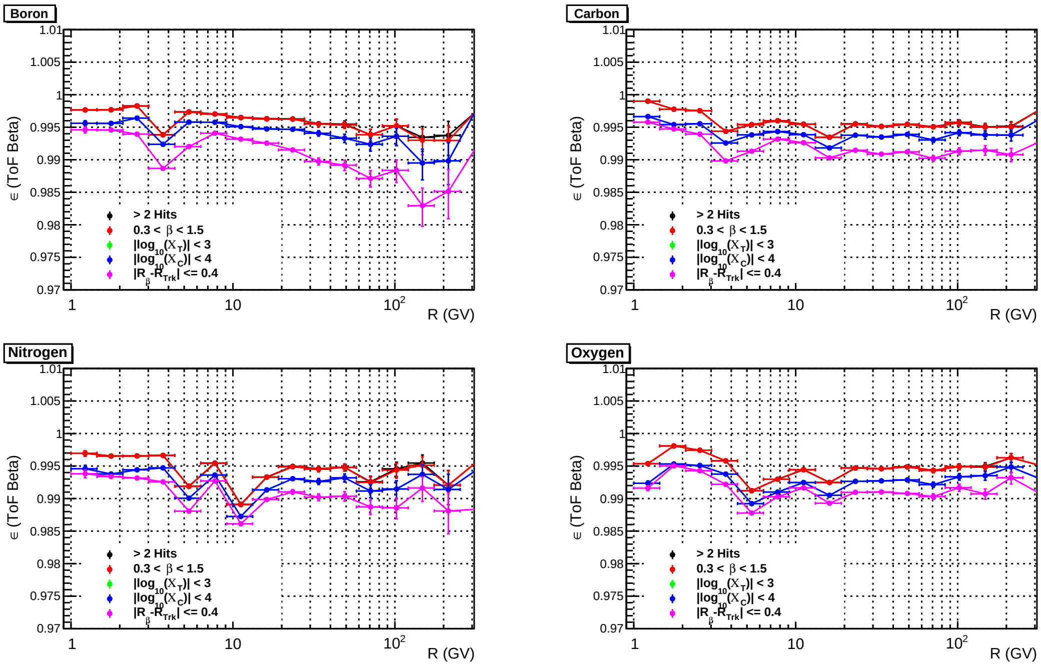

FIGURE 6.4 – Cut breakdown of the ToF beta reconstruction efficiency for BCNO elements.

agreement is within 1% at all energies. The MC efficiency tends to be slightly higher than in the data though above few tens of GV, the comparison is not evident due to the poor MC statistics.

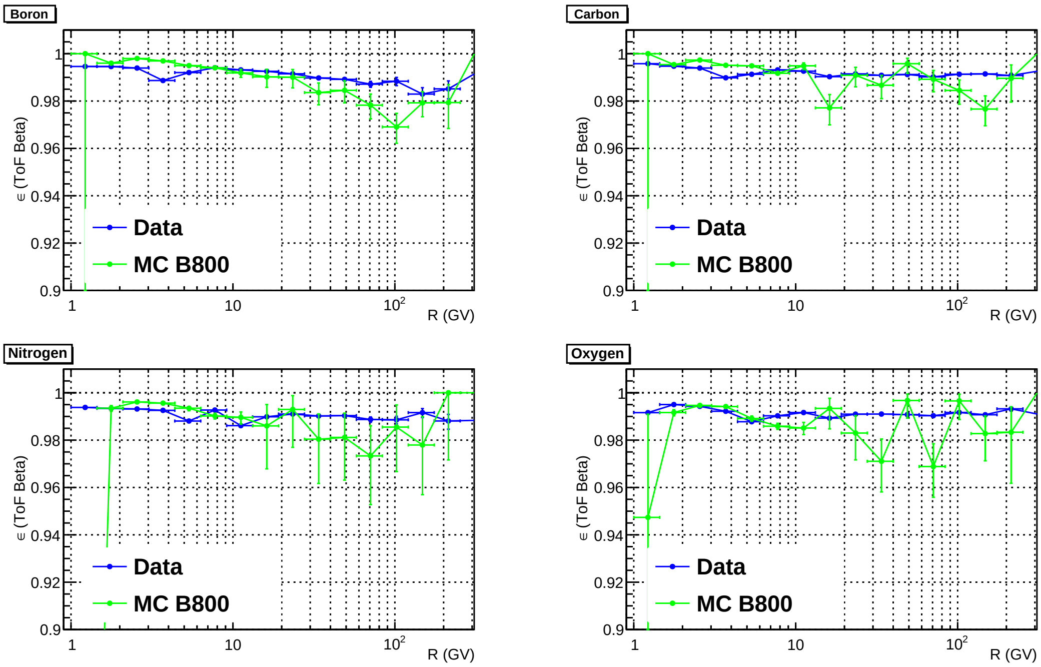

FIGURE 6.5 – Comparison of ToF beta reconstruction efficiencies in data and Monte Carlo. The agreement is good, within 1% at all energies and for all nuclei.

Parameterization

As anticipated, we parameterize all the reconstruction efficiencies from the data. We apply to the efficiency a constant fit. We limit the range of the fit to 200 GV, before the statistics becomes too limited. Figure 6.6 shows the fit result for the BCNO group. There are clear deviations from a constant parameterization but these remain below the percent level for all Z. In Figure 6.7, we show the result of the parameterizations for the most abundant nuclei. The odd Z nuclei above nitrogen are excluded due to higher contaminations in the samples that tend to introduce effects at low rigidities. All efficiencies are above 99% and constant at all rigidities within 1%. Since the efficiency is very high and nearly flat with Z, we use again a constant fit to extract a single efficiency value for all nuclei (dashed red line in Figure 6.7). The maximum deviation between the measured efficiencies and the constant fit is below 0.2%. We save the results of the parameterizations in a special data base with all the information related to the fits.

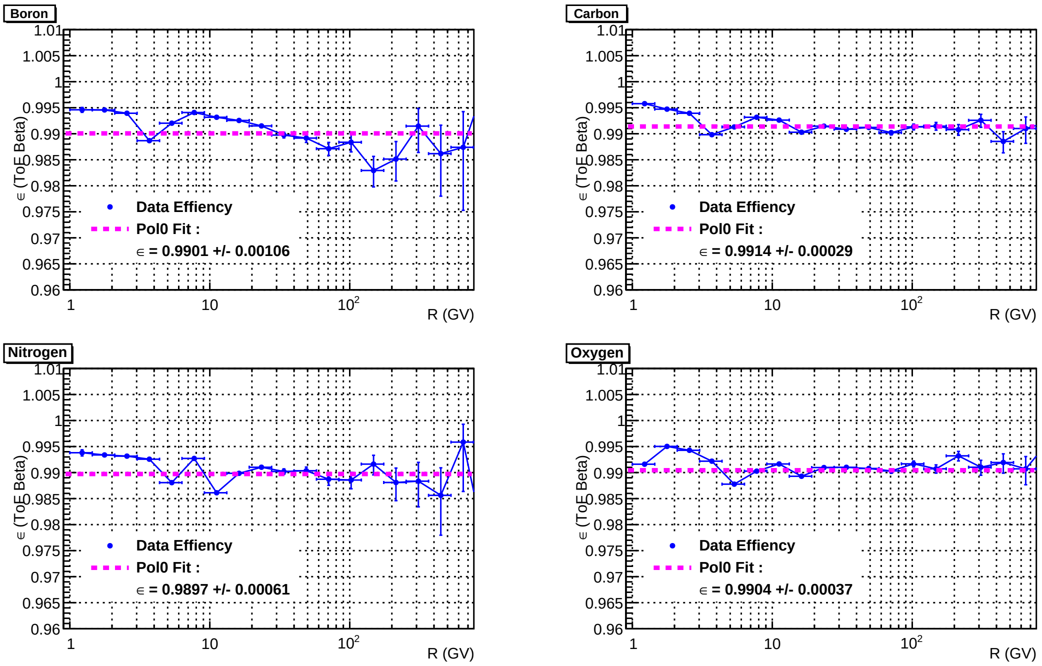

FIGURE 6.6 – Constant parameterization of the ToF beta reconstruction efficiency.

6.4.2 Tracker Reconstruction Efficiency

Since any charged trigger is associated with signals in the ToF system, it is possible to use these signals to build an approximated path of the particle throughout the detector. We profit from the standalone reconstruction of the ToF track to perform an unbiased study of the tracking efficiency. Since the tracker track is not available, one must use an alternative estimator of the particle rigidity. Three estimators have been considered. The first one is based on the measurement of the particle velocity β by the ToF which can be converted into a rigidity estimation (see eq. 5.5 and 5.6). Due to the limited ToF resolution, this estimation is valid only up to about 5 GV. One can also use an estimation of the geomagnetic cutoff rigidity. Based on the ToF track extrapolation, an estimation of the geomagnetic cut-off value is obtained using the Stoermer approximation to which we apply a safety factor of 1.5. The main justification for the use of the cutoff rigidity is that the spectrum of a nucleus is steeply

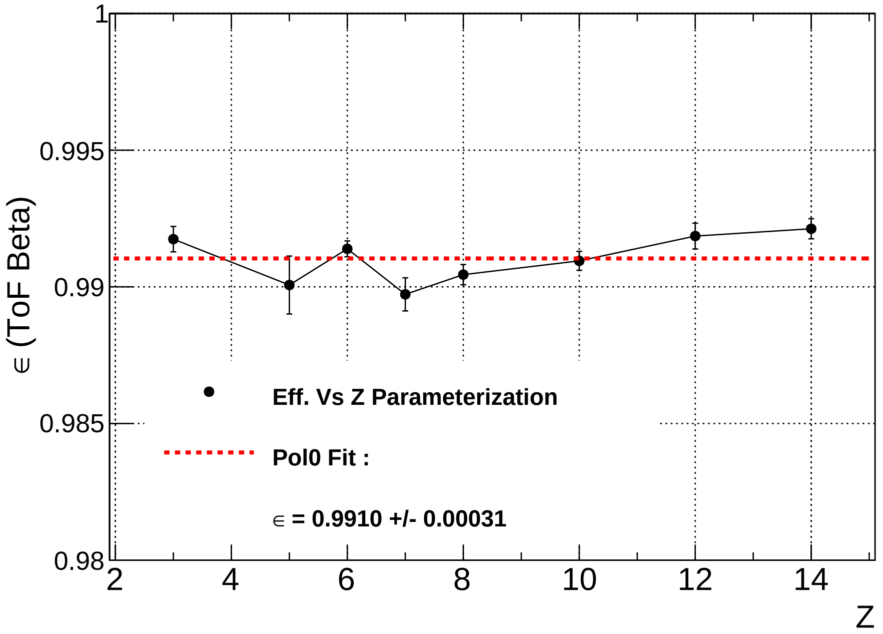

FIGURE 6.7 – Results of the constant parameterizations (black points) of the ToF beta reconstruction efficiency in function of the nuclear charge Z. Odd Z nuclei above nitrogen have been neglected. A single efficiency value for all nuclei is extracted based on a constant fit (dashed red line).

falling such that the geomagnetic cutoff rigidity threshold is representative of the energy of the bulk of particles. This approximation is valid only up to few tens of GV (∼30GV), where geomagnetic effects are relevant. The last estimator is only used as cross-check to the previous estimators and as a potential indicator of trends in the efficiency curve at higher energies. It uses the energy deposition in the Ecal. Obviously, the sample constructed from this estimator has a significantly reduced acceptance. Although the AMS calorimeter is an electromagnetic one, there is an observed correlation between the rigidity of the particle and the calorimetric deposit by hadrons. Figure 6.8 shows the correlation between the tracker full span rigidity and the three estimators discussed here for selected carbon nuclei. Based on the observed correlation, the Ecal rigidity estimator is reliable above few tens of GV up to few hundreds of GV. The rigidity dependence for the track reconstruction efficiency remains one of the weakest points of the efficiency parameterization since one must extrapolate the behavior to high energies. From this point of view, the MC efficiency is the only valid solution to improve the picture.

Our initial sample to test the inner tracker reconstruction efficiency obeys the following criteria :

- charged particle trigger,
- 4 ToF hits,
- $0.3 < \beta < 1.5$,
- chi-square : $-2 \leq log(\chi^2_T) \leq 1.5$,
- ToF track extrapolates into the layer 1 fiducial volume,

where all the ToF-related variables are obtained from the unbiased reconstruction. To define

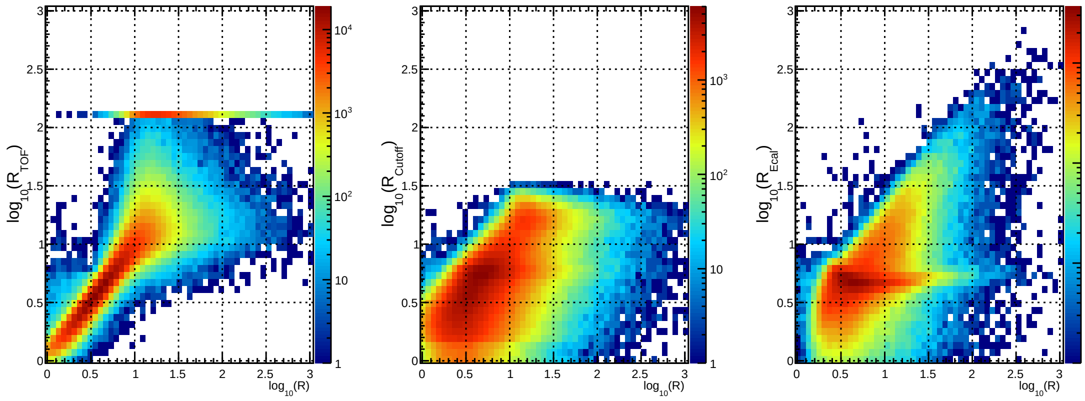

FIGURE 6.8 – Rigidity Estimators. *Left* : rigidity extracted from the ToF velocity measurement versus the tracker full span rigidity. *Center* : geomagnetic cutoff rigidity estimation. *Right* : rigidity estimation from the energy deposition in the Ecal.

the different nuclei samples, we use the unbiased charge evaluations from the upper and lower ToF plane. However, this is not enough to guarantee a clean sample. We therefore add an unbiased estimation of the charge on the layer 1 based on the ToF track extrapolation. Figure 6.9 shows the breakdown of the selection cuts. The rigidity estimator used is the geomagnetic cut-off rigidity which allows to probe the reconstruction efficiency only up to about 20-30 GV. The efficiencies are observed to be rather smooth but exhibit a small decreasing trend with rigidity. In Figure 6.10, we show the efficiency after the last cut is applied for the 3 different rigidity estimators. One can see that a good agreement exists between the different cases.

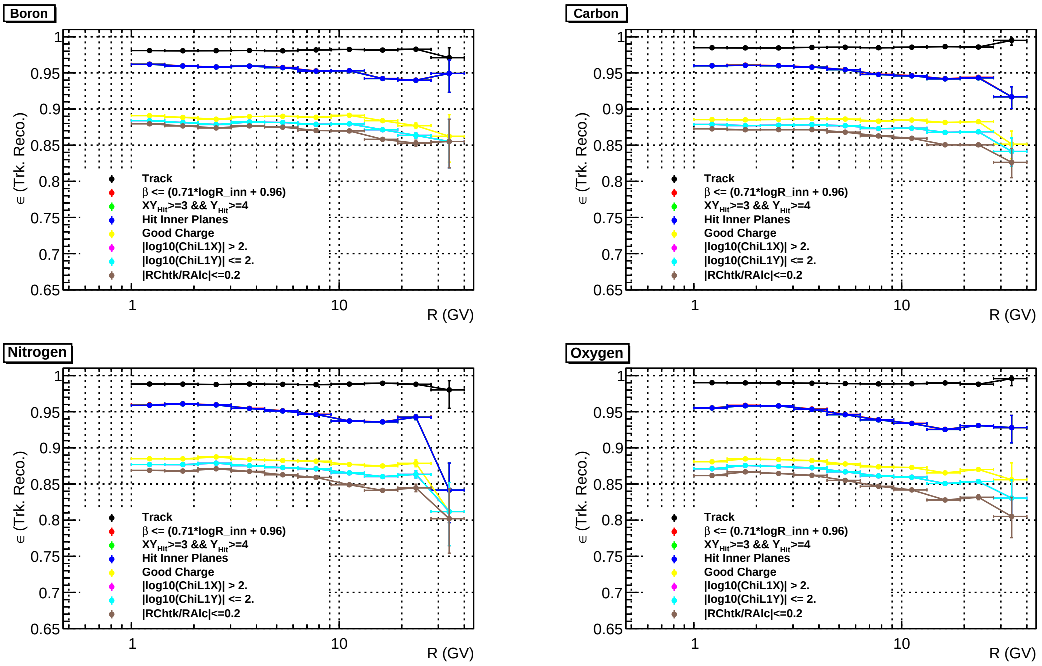

FIGURE 6.9 – Cut breakdown of the inner tracker reconstruction efficiency. The geomagnetic cut-off rigidity is used as the rigidity estimator.

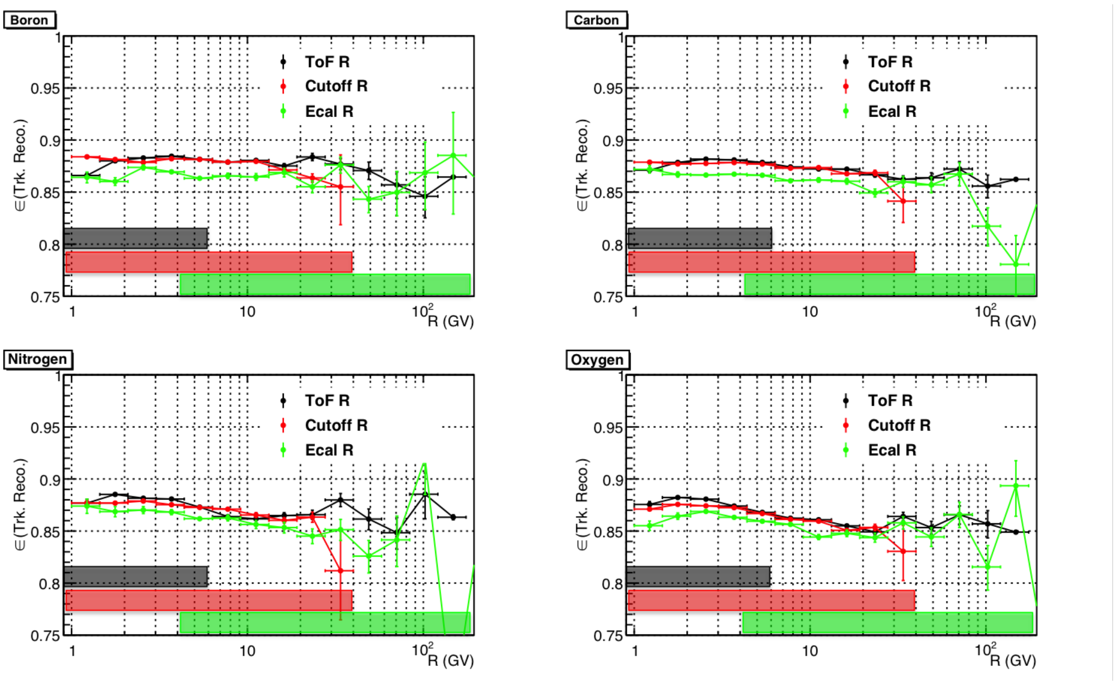

Figure 6.10 – Comparison of the inner tracker reconstruction efficiency measured with the 3 different rigidity estimators. The shaded bands indicate the validity range of the different estimators.

Monte Carlo Comparison

Since independent rigidity estimators only allow to probe an energy range up to few tens of GV, the Monte Carlo is the only tool to understand the behavior of the inner tracker reconstruction efficiency at higher rigidities. We select particles in the MC based on the generated particle information, requiring no fragmentation takes place in the detector. We also ask for the specific geometry of this analysis, i.e. that particle pass through the layer 1 and the inner tracker. Figure 6.11 shows the comparison between the MC (magenta) and the data (blue and green). The black points correspond to the ratio of the data efficiency to the MC efficiency in the range where data measurements exist. One can see that the agreement between the two efficiencies is within 5% at all energies. Although the MC also indicates a small decreasing trend with energy up to $\sim$ 30GV, it seems that the efficiency then flattens out at higher rigidities, although this is not evident for all nuclei (see Appendix C).

Parameterization

We use a straight line to parameterize the efficiency observed in the data. We perform the fit on the cutoff rigidity estimation from 1 GV to 25 GV ($\sim$1.4 in $\log R$). The result of the fit is shown in Figure 6.12. The extrapolation of the fit (magenta line) to higher rigidities seems to be in a reasonable agreement with the behavior suggested by the MC at higher rigidities, although the lack of statistics forbids a clear conclusion at TV energies. Figure 6.13 shows the fitted slope (left plot) and the efficiency value evaluated at $\log R = 1.5$ (right plot) for all nuclei. The slope values are, within errors, almost constant around -0.01 while the efficiency values fluctuate within 2%. Based on these observations, we can conclude that all efficiencies remain above 80% at TV energies. In other words, the efficiency is almost flat with energy. Only more MC statistics could help to understand more clearly the behavior above 400 GV (where the statistics becomes rather limited) and in particular to verify the validity of the

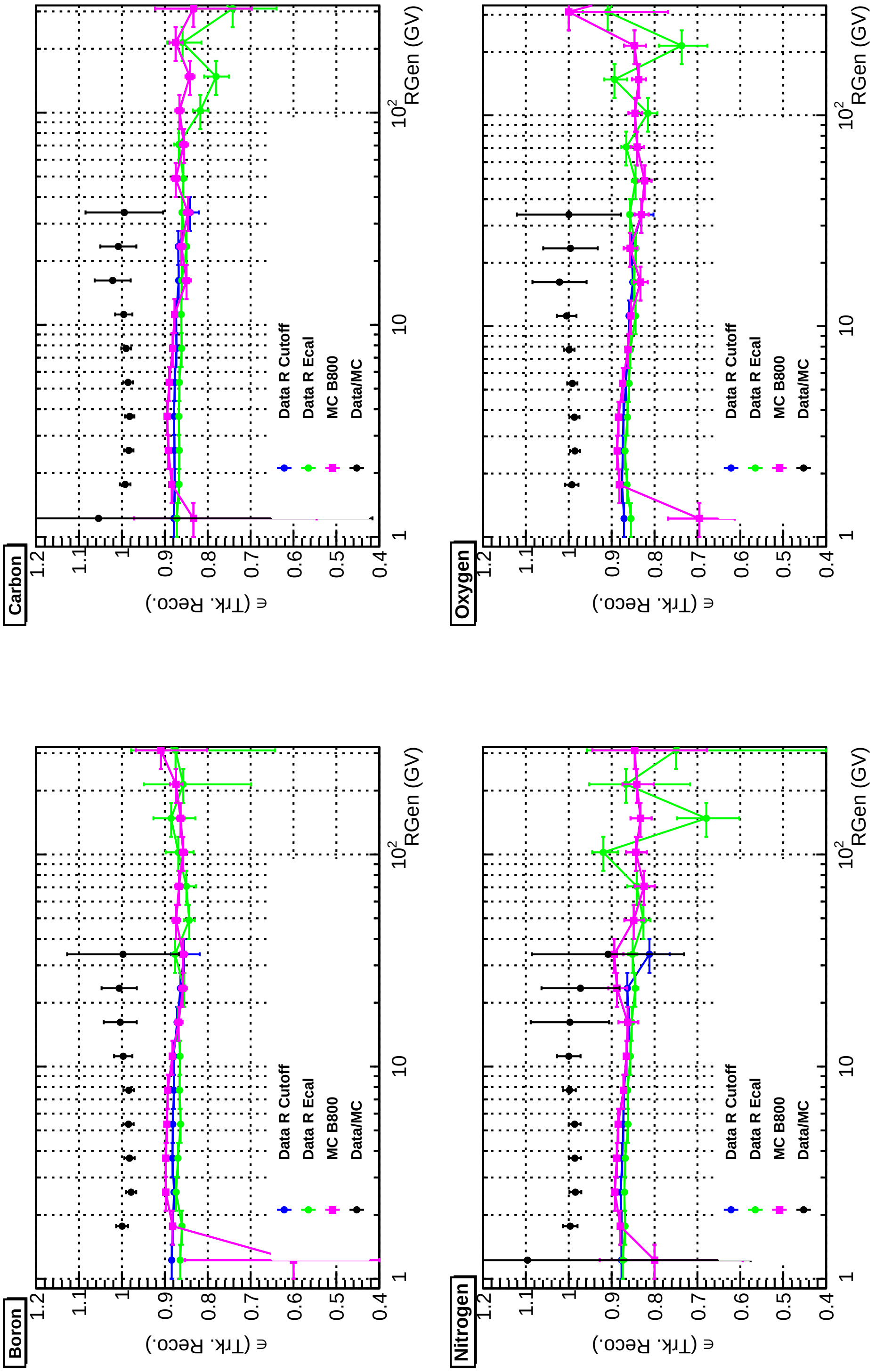

Figure 6.11 – Comparison between data (blue and green) and Monte Carlo (magenta) measured efficiencies. The black points indicate the ratio of blue points to the magenta ones.

extrapolation for nuclei above oxygen.

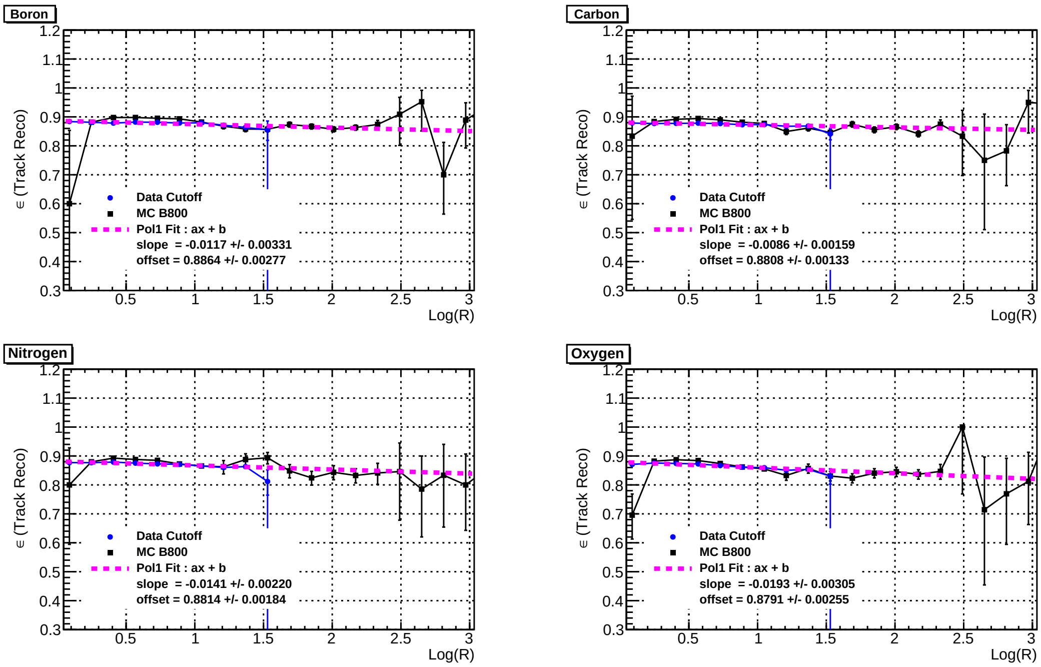

FIGURE 6.12 – Straight line parameterization of the inner tracker track reconstruction efficiency. The fit is applied on the blue points only. The black points correspond to the MC efficiency. The extrapolation of the fit seems in reasonable agreement with the predictions of the MC.

6.4.3 Layer 1 Pick-up Efficiency

The layer 1 pick-up efficiency takes into account geometrical inefficiencies due to the gaps between silicon sensors and silicon ladders as well as potential dead areas in the silicon due to malfunctioning electronics. On top of this geometrical inefficiency, we ask for the layer 1 hit to possess a good reconstructed cluster on both the Y and X side. The former is necessary to ensure a good rigidity reconstruction. The latter is needed due to the intrinsic better charge identification performances of the n-side measurement (see Chapter 5). The total measured inefficiency also includes the performance of the algorithms searching for hit associations on the external layers.

Now that we have provided a measure of the inner tracker reconstruction efficiency, we are free to use tracks reconstructed with the inner tracker combined to the ToF reconstruction as a starting point to measure the layer 1 pick-up efficiency. We define our initial sample as :

- charged particle trigger,
- 4 ToF hits and $0.3 < \beta < 1.5$,
- ToF chi-square : $-2 \leq log\chi^2_T \leq 2$,
- Y hits > 5 and XY hits > 4,
- Tracker chi-square : $-2 \leq log\chi^2_{X,Y} \leq 2$,
- ToF track extrapolates into the layer 1 fiducial volume,
- Inner tracker track extrapolates into the layer 1 fiducial volume.

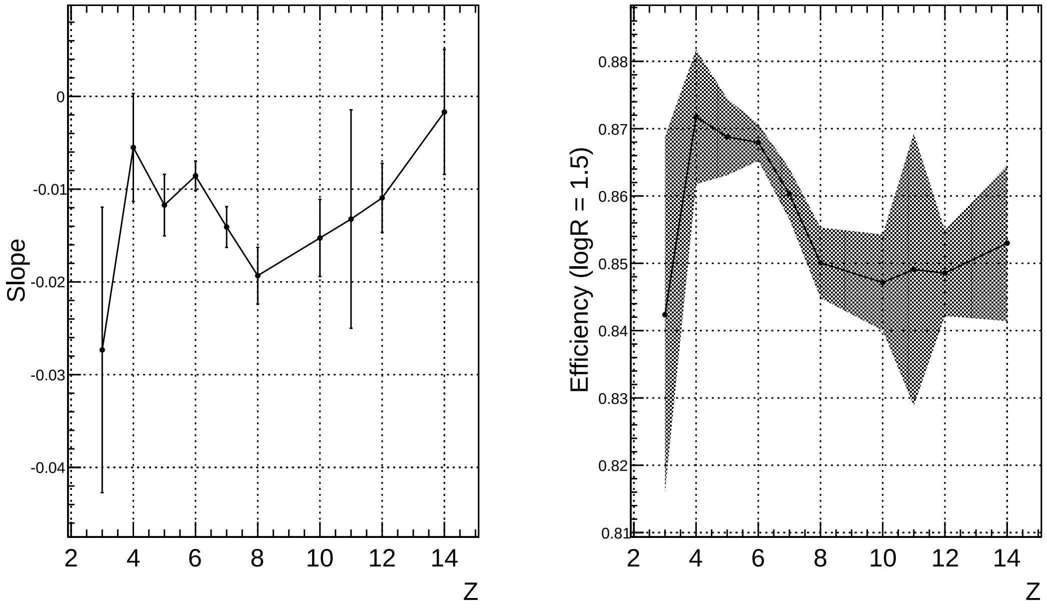

Figure 6.13 – Pol1 parameterization of the inner tracker track reconstruction efficiency for all nuclei from lithium to silicon. The shaded area indicates the variable uncertainties from the fits. Within errors, the slope value is almost constant around -0.01. The efficiency value, evaluated at $\log R = 1.5$ fluctuates within 2% for all nuclei.

We construct the various nuclei samples based on the upper ToF, inner tracker and lower ToF charge measurements. Such selection does however not guarantee that substantial fragmentation has not taken place above or even potentially inside the upper ToF plane and pollutes the efficiency samples. Therefore, we constructed an additional sample based on strict trigger conditions (number of ACC < 3) and the request of having only one track reconstructed in the Tracker. This very clean sample suffers statistical limitations, especially for nuclei above carbon, but can be used as a good cross-check. In Figure 6.14, we show the breakdown of the efficiency value for the successive cuts. Each cut contributes more or less a 10% inefficiency. The behavior is smooth with energy with small structures appearing at the highest energies, though insignificant considering the large errors. For each nucleus, the efficiency increases with rigidity. The reason is a higher inefficiency at lower rigidities caused by the contribution of multiple scattering which makes the searching for hit associations on the layer 1 less efficient.

Figure 6.15 shows the comparison between the efficiencies obtained using the loose selection of nuclei samples (blue) and the stricter one (red). The agreement is within 2% for all nuclei and all rigidities. There is no doubt that the loose definition of the efficiency sample contains contamination from fragmenting events. Figures 6.14 and 6.15 together show that since the pick-up efficiency is very similar for different nuclei, this contamination has only a small effect on the measured efficiency, at least with respect to the cuts used in this analysis.

Monte Carlo comparison

In Figure 6.16, one can appreciate a comparison between the data (blue points) and MC (red points) efficiencies. The black points show the usual ratio of both efficiencies. Although the agreement is very good for boron and in general for all nuclei up to 10 GV, there seems to be a growing disagreement at higher energies. We do not yet understand the origin of this

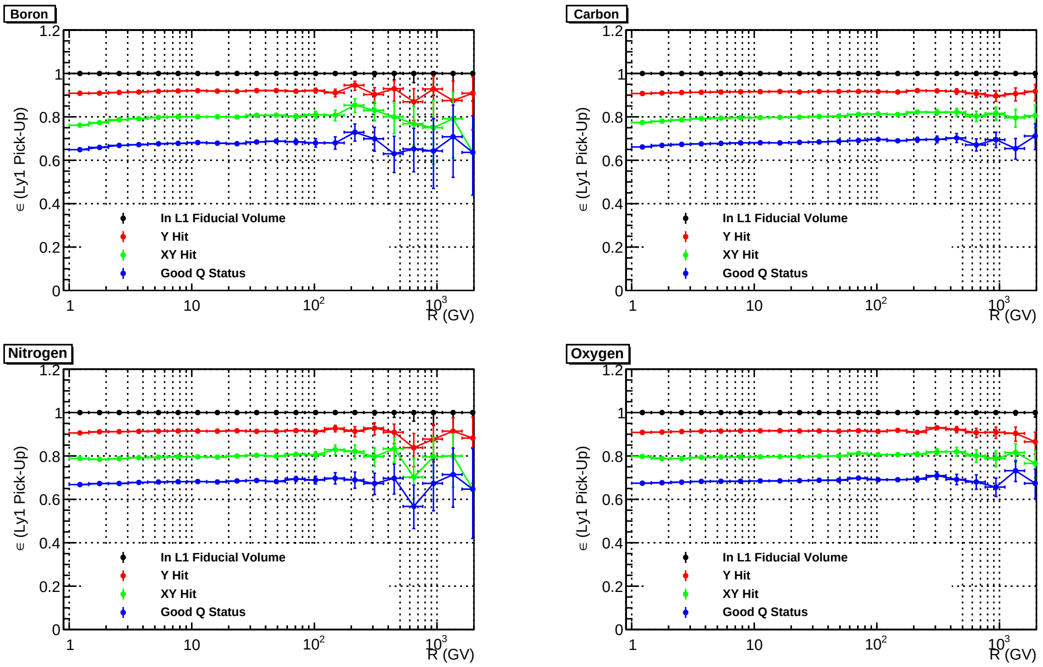

FIGURE 6.14 – Layer 1 hit pick-up efficiency for elements of the BCNO group. The last cut shows an accumulated efficiency above 65% for all nuclei with a slight trend of increasing efficiency with rigidity.

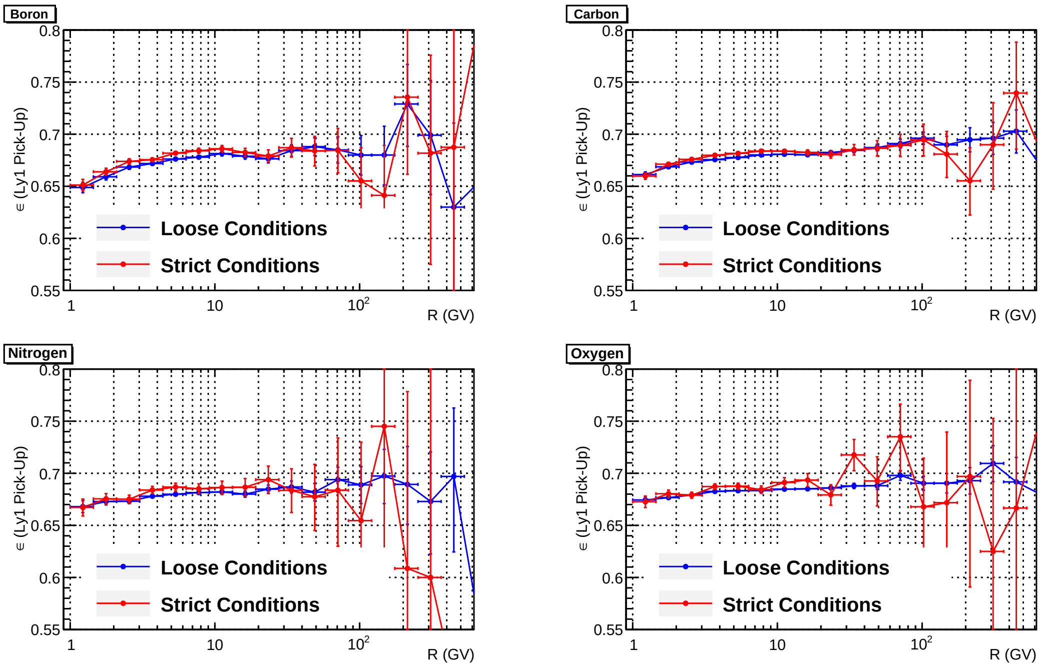

FIGURE 6.15 – Comparison between the layer 1 pick-up efficiencies for two definitions of the efficiency samples. Blue points represent a loose selection with potential contamination from fragmentation while the red points are based on a very strict selection (see text). The agreement is within 2% up to few hundred GV.

effect in the MC which seems to furthermore depend on the nuclei charge.

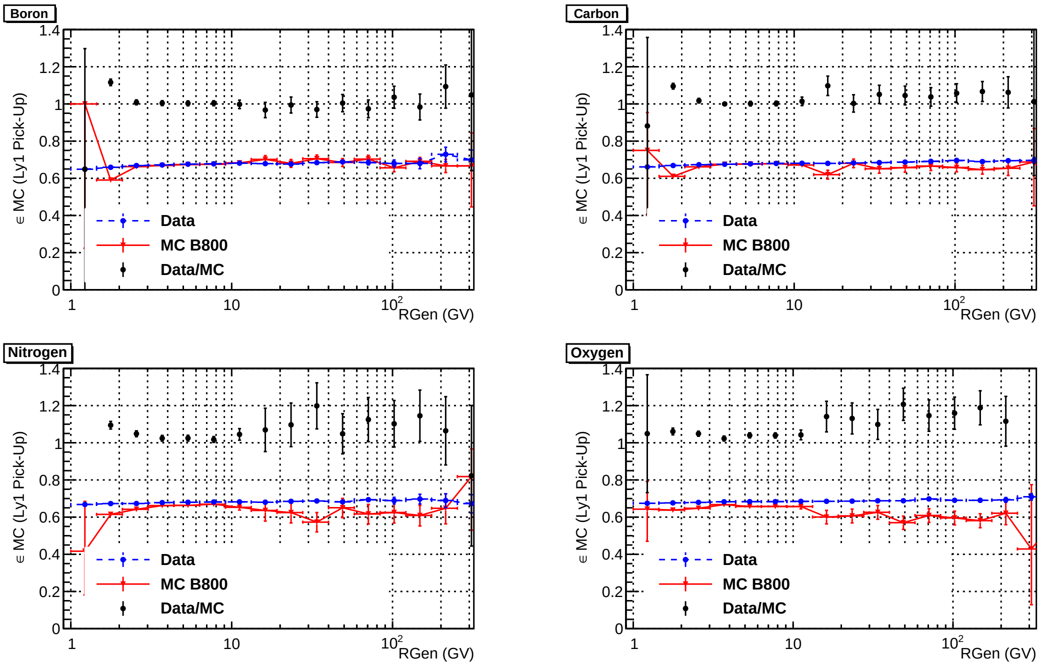

FIGURE 6.16 – Comparison between MC and data layer 1 pick-up efficiencies. The level of agreement, represented by the black points, is within 10% up to 10 GV for nuclei up to oxygen but tends to worsen at higher energies. This effect appears to also increase with Z.

Parameterization

We parameterize the layer 1 pick-up efficiency using a linear function of the logarithm of rigidity for all charges up to silicon. We restrict the range of the fit from 1 GV to 300 GV, assuming the resulting description holds to higher energies. Figure 6.17 shows the resulting parameterizations (dashed magenta line). Figure 6.18 shows the slope and offset values of the fitted functions for all nuclei from proton to silicon. The slope values are very small and do not exhibit any particular trend with Z. The efficiency value, evaluated at $\log R = 1.5$ for all nuclei, varies within 5%. This is probably the combined result of small scale structures in the efficiency curves and different levels of contaminations in the samples.

6.4.4 Trigger Efficiency

Since the trigger requirement will be included in the calculation of the geometric acceptance factor (we need a trigger to select particles), we have verified the agreement of the trigger efficiency in the data and in the MC. We apply all the cuts of the analysis (Table 6.1) except for the trigger requirement and use the un-biased trigger (see 3.1.10) to define the starting sample. We use the charge measured by the upper and lower ToF instruments, as well as the tracker layer 1 and inner tracker planes to define the samples of different nuclei. In the MC, we use the knowledge of the generated charge information and require no fragmentation up to the lower ToF plane. The efficiency measurement is defined by the formula :

$$\epsilon_{\text{Trigger}} = \frac{N_{\text{Physics}}}{N_{\text{Physics}} + 100 \times N_{\text{UnPhysics}}} \tag{6.5}$$

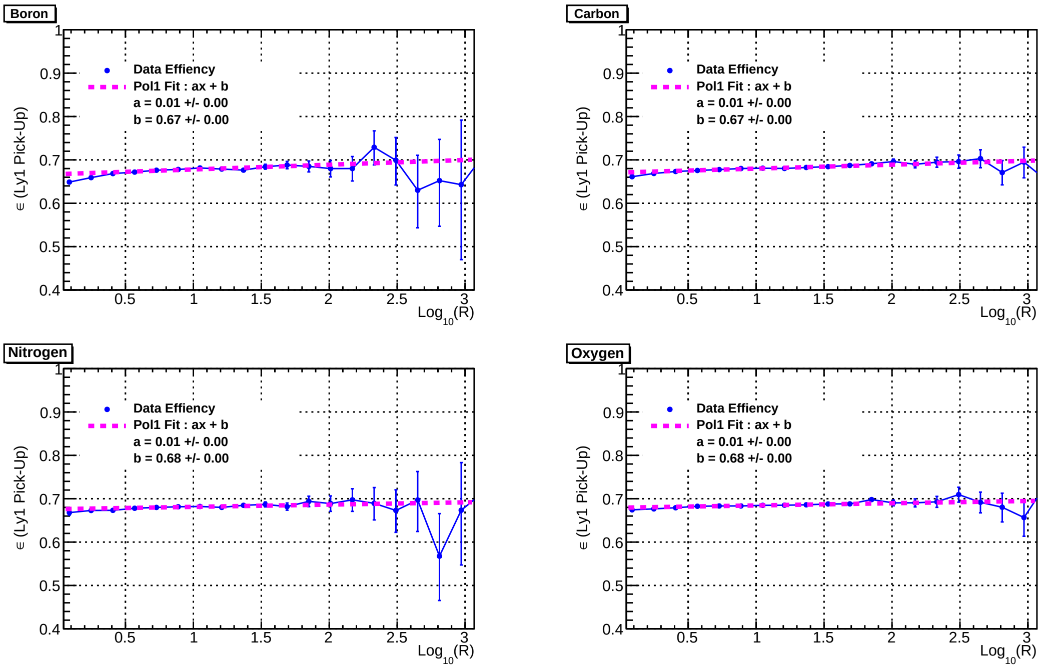

FIGURE 6.17 – Linear parameterization (magenta) of the layer 1 pick-up efficiencies.

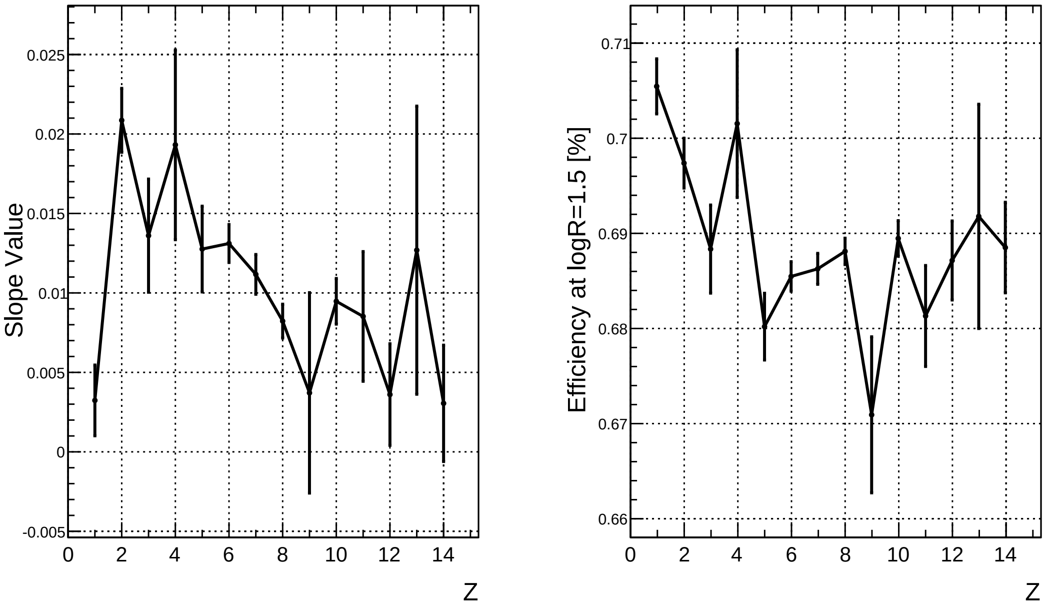

FIGURE 6.18 – Results of the linear parameterizations of the layer 1 pick-up efficiency for all nuclei from proton to silicon. Errors come from the fit.

where N_{Physics} corresponds to all the events passing the selection cuts and have the usual physics trigger set, while $N_{\mathrm{UnPhysics}}$ are the events with the unbiased trigger set but no physics trigger. This unbiased sample is pre-scaled by 100 in the acquisition procedure thus the corresponding multiplication factor in the formula. The measured trigger efficiency in the data is shown in Figure 6.19 for two different geometries. The blue points correspond to a compatibility requirement between the charge measured in the layer 1 and in the inner tracker. The magenta points add the requirement of the layer 9 charge to be compatible with the other measurements of the charge, hence no fragmentation throughout the whole instrument. For the layer 1 plus inner tracker geometry, small structures appear at isolated energies, which are not seen in the full span geometry. In the latter case, particles traverse the detector within the Ecal acceptance and are usually associated to rather clean events, i.e. no ACC triggers, for which the trigger efficiency is thus close to 100%. For the reduced L1 plus inner tracker geometry, particles with high inclinations can trigger more ACC counts due to the production of δ-rays close to the veto counters, a maximum of 5 ACC counts being allowed to accept the event (see 3.1.10). Since the effect seems to appear at smaller energies with increasing particle charge and the size of the effect also increases with Z (see Appendix E), this explanation is also consistent with the fact more δ-rays are produced with increasing energy and increasing charge. The effect is however not seen in the Monte Carlo.

Despite these small effects, the trigger efficiency remains above 99% for all nuclei. In the MC (Figure 6.20), the efficiency is always 1 for all available nuclei at all energies. The disagreement between data and MC is therefore at the level of 1%. This discrepancy is added as a source of systematic error in the final acceptance calculation.

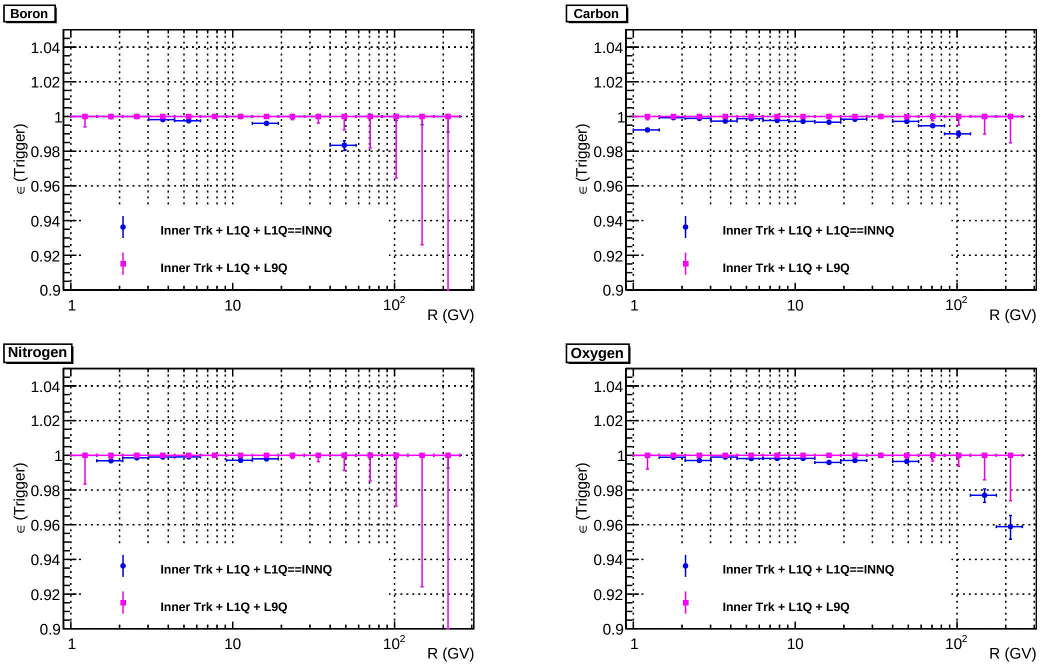

Figure 6.19 – Trigger Efficiency for Boron, Carbon, Nitrogen and Oxygen nuclei for two different definitions of the initial efficiency samples.

6.4.5 Summary

All reconstruction efficiencies have been parameterized from the data. Although a good agreement is found between MC and data for both the ToF beta and inner tracker recons-

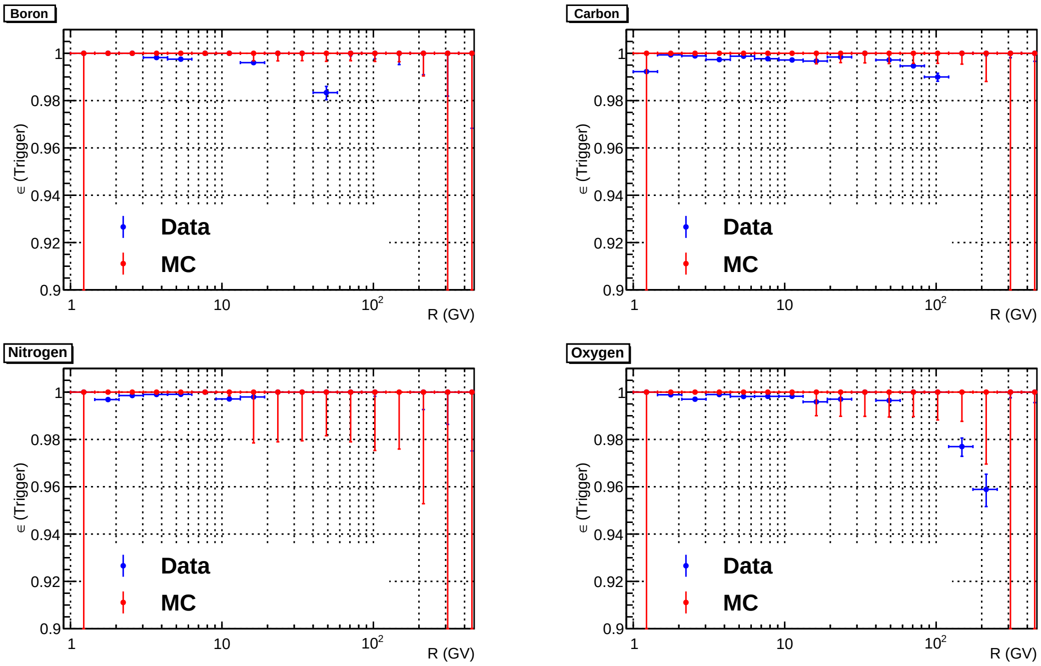

Figure 6.20 – Trigger Efficiency : comparison of Monte Carlo and data.

truction efficiencies, we do not have yet any comparison available for nuclei above oxygen. Moreover, unexplained discrepancies in the layer 1 pick-up efficiencies have been observed. In terms of associated errors, we use the results of the fits and propagate the errors to the various energies and missing nuclei species when needed.

One must finally consider a few caveats in the measurements of the reconstruction efficiencies presented here. The general cuts applied to our data sample in terms of track reconstruction quality are based on fitting tracks with layer 1 and inner tracker planes included. For practical reasons, the track reconstruction efficiency has been determined based on the inner tracker fitting only. We thus make the assumption that the fitting of the inner tracker behaves identically as the larger span fitting in terms of the resulting chi-square values. It is not obvious that this assumption is valid at all energies. One could consider including the chi-square cuts inside the layer 1 pick-up efficiency. This would however make the definition of the efficiency sample more delicate since one would not have a criteria to assess the quality of the sample in terms of the inner track reconstruction.

6.5 Geometrical Acceptance

In the Monte Carlo simulations, the flux of particles is assumed to be isotropic above AMS and is generated uniformly in position and inclination (with respect to the AMS zenith axis) from a plane placed above the instrument. The plane has a surface of $3.9 \times 3.9\mathrm{m}^2$ such that it covers the entire AMS field-of-view. The geometrical acceptance for the generation plane alone is calculated as :

$$A_{\mathrm{top}} = \int_{S,\Omega} d\sigma d\omega = l^2 \int_{\Omega} \sin\theta \cos\theta d\theta d\phi = -\pi l^2 \int_1^0 d\cos^2\theta = \pi l^2 \approx 47.78\mathrm{m}^2 \text{ sr.} \tag{6.6}$$

where $d\sigma$ and $d\omega$ denote respectively an element of surface and solid angle. The geometric acceptance for a given analysis corresponds to the ratio of reconstructed to generated particles :

$$A_{Z,\mathrm{Geom}} = \frac{N_{Z,\mathrm{Rec}}}{N_{Z,\mathrm{Gen}}} \times \pi l^2 \tag{6.7}$$

It is clear that A_{Geom} will represent a significant reduction of the A_{top} factor simply due to the restricted geometry imposed by the narrow AMS field-of-view. Our basic event selection for the acceptance calculation requests the existence of a trigger and that the particle trajectories include the tracker layer 1 and inner tracker planes. This is a pure geometrical requirement without asking for any hits nor tracker tracks to be reconstructed. We select only clean events with no fragmentation up to the lower ToF plane and define the nuclei samples based on the generated charge information. Only nuclei from lithium to oxygen are available in the MC production used. Moreover, the beryllium Monte-Carlo sample suffers an absence of statistics in an intermediate energy range between 20 GV and 200 GV which makes it unusable for the acceptance study.

Figure 6.21 shows the resulting acceptances in function of the generated particle rigidity for 4 different tracker geometries. The red line corresponds to the geometry of this analysis, i.e. particles passing at least through the tracker layer 1 and all inner tracker planes. The acceptances are not flat with rigidity and a significant drop is observed around 10 GV. The fluctuations in the acceptance curves are more evident in Figure 6.22 where we show the proposed parameterization for all available nuclei. The origin of the structure at 10 GV is not yet understood but could be the result of partial cross-section differences due to the use of different interaction models in the simulation code. Below 10 GV, the `Light Ion Binary Cascade` model is used and the `DPMJET` model above, both models being included in the `GEANT4` package. Assuming the `DPMJET` model is more reliable at 10 GV, we parameterize the acceptance with a constant function (magenta) in the flat regime between 10 GV and 120 GV. The fitted acceptance values are displayed in the bottom right plot. Based on these results, it is not possible to justify any specific parameterization of the acceptance in function of Z, which is however needed to estimate the acceptance for the missing nuclei species. The simplest approach is to use a straight line. The final fit (dashed red line) describes rather well the initial acceptances for lithium, boron and oxygen but presents significant deviations for carbon and nitrogen. The error on the final fit parameters obviously translates in large errors in the final acceptance factor. To obtain a reasonable picture on the fluxes, we fix the error to the largest error among the individual acceptance fits, which is about 2%. One should should finally consider that our knowledge of inelastic cross-sections is in fact limited. All models are based on purely theoretical and semi-empirical extrapolations of the few existing measurements. The predictions from different models are in agreement at minimum within 8% at all energies, thus representing a significant source of systematic error for the final flux measurement. This limitation could in principle be overcome by estimating the nuclei survival probabilities from the data itself, therefore making the acceptance term independent of any interaction model. Such measurements remain however very challenging, in particular for the less abundant nuclei species. On another hand, such a measurement, even for a single nuclei species , could help better understand the reliability of various interaction models. This very important topic will be addressed in the future.

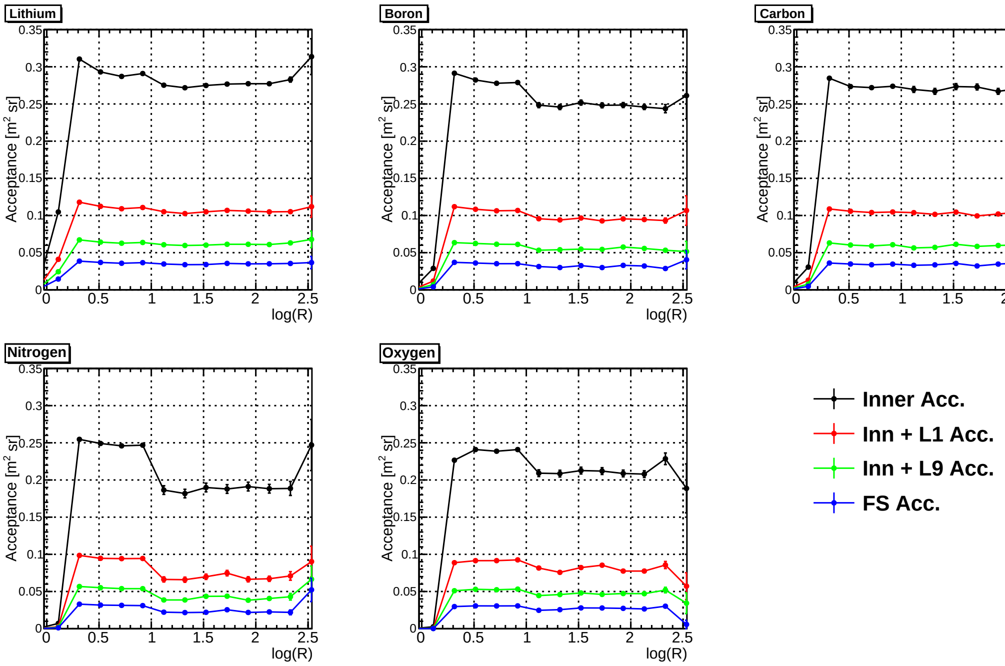

FIGURE 6.21 – The measured MC acceptance for available nuclei. Four geometries are distinguished : particles passing at least through the inner tracker (black), at least through the layer 1 and inner tracker (red), the inner and layer 9 (green) and finally the full span geometry (blue).

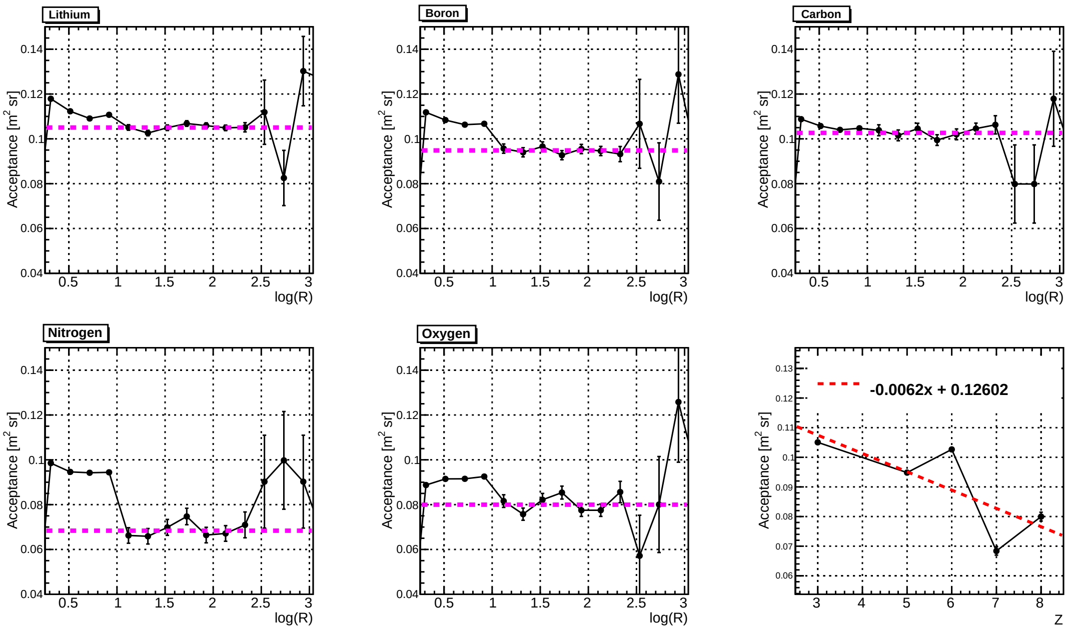

FIGURE 6.22 – Black points are the MC calculated acceptances for the inner tracker plus layer 1 geometry. The magenta dashed lines are constant fits of the acceptances performed between 10 and 100 GV. The bottom right plot shows the result of the fits in function of Z with the simplest parameterization possible (dashed red line).

6.6 Exposure Time

In order to measure an absolute flux, it is necessary to know as precisely as possible the total time the detector was ready to accept events over the whole time period covered by the analyzed data set. This *exposure time* must take into account various sources of dead-time affecting the acquisition (see Section 3.1.10) as well as potential errors occurring during the reconstruction of the raw data. A specific analysis may also reacquire dedicated time periods to be excluded which also contributes to the reduction of the total exposure time.

After careful studies, the AMS collaboration has provided users with a set of standard cuts to remove what must be considered as bad seconds during acquisition. The selection of good seconds is the following :

1. the ratio of triggers to the number of reconstructed events is > 0.98,
2. the detector live-time is above 0.5,
3. the zenith angle of the reconstructed particle is $< 40°$ (AMS field-of-view),
4. the number of errors in reconstruction over the number of reconstructed events is < 0.1,
5. the number of particles must be > 0 and the number of events < 1800,
6. $N_{\text{part}}/N_{\text{trig}} > 0.07/1600 \times N_{\text{trig}}$ and $N_{\text{part}}/N_{\text{trig}} < 0.25$.

The cut number 6 was implemented to remove cases where a high trigger rate is observed but no or very few particles are reconstructed in the detector. This is mainly the case in Polar regions and in the South Atlantic Anomaly where the overwhelming flux of low energy particles generates a lot of activity in the detector which often results in poor reconstruction efficiencies. Less then 1% of all events are removed by these cuts.

For each 23 minutes data acquisition run, we loop over all seconds between the beginning and the end of the run. We correct each second for the live-time of the experiment (lv) and potential errors in reconstruction :

$$dt = \frac{lv \times N_{\text{events}}}{N_{\text{events}} + N_{\text{errors}}} \tag{6.8}$$

For each second, we fill all bins of a histogram for rigidities above the cut-off rigidity times safety factors of 1.3 (1.5) using as weight the corrected time dt. Figure 6.23 shows the resulting exposure time for the current analysis. Two safety factors have been used to search for potential systematic effects resulting from the geomagnetic cut-off rigidity calculation. The final factor used in the analysis is 1.3. The total exposure time above ~40 GV, where geomagnetic effects disappear, is 6.39147×10^7 seconds. The nuclei counts in a given energy bin are divided by the corresponding exposure time value to achieve the proper time normalization to measure absolute fluxes.

6.7 Nuclei Counting Method

For all tracks passing the selection cuts of Table 6.1, we perform a template fit of the inner tracker charge distribution in different intervals of rigidity. Based on the fit results, we define pure nuclei samples in the inner tracker. We then consider the associated charge distribution of hits on the layer 1 and perform another template fit which allows to estimate the survival fraction of each nuclei species between the layer 1 and the inner tracker, as opposite to fragmented events. This correction factor allows to compute the real number of nuclei of a given species traversing the detector without fragmenting.

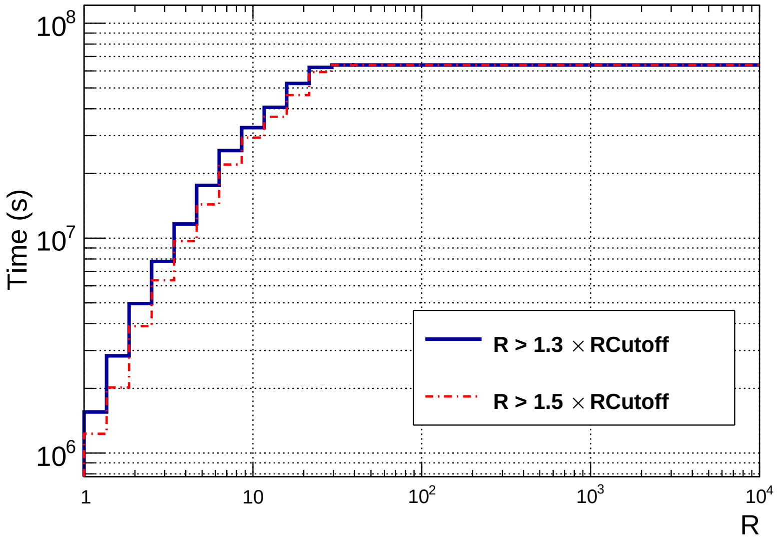

FIGURE 6.23 – Exposure time in function of rigidity for two safety factors on the estimated geomagnetic cutoff rigidity. The total exposure time above ∼40 GV, where geomagnetic effects disappear, is 6.39147×10^7 s.

6.7.1 Charge Templates

We extract the inner tracker and layer 1 charge templates from the data. To study the response of the inner tracker to different nuclei species, we use the upper and lower ToF charge measurements as the basic selector for nuclei up to sulfur ($Z = 16$). For the lowest abundance species, residual contaminations can be important and we add the layer 1, RICH and layer 9 charge estimators to the selection criteria when needed. Even with a data sample of more then 2 years, it was not possible to produce templates in different bins of rigidity due to statistics limitations, in particular for nuclei above oxygen. We have therefore produced the templates in a unique bin of rigidity, assuming the same shape holds at all energies. This should indeed be the case, as the calibration presented in Chapter 5 yields an energy independent charge estimator. However, it is known that the calibration starts being less efficient for nuclei above neon ($Z = 10$) and the errors due to a potential discrepant template shape are treated at the time of the fit and included in the evaluation of the systematic errors.

The two essential criteria to construct the template for a given Z is to maximize its statistical power while minimizing the contamination from neighboring charges. These two constraints are often not met simultaneously and a compromise must be found. We first optimize the template definition for even Z nuclei only. Figure 6.24 shows an example for carbon nuclei. We use 4 different definitions of carbon nuclei based on different combinations of the various charge estimators available. In the upper left plot, the layer 1, upper ToF, lower ToF and RICH measurements are used. In the upper right plot, the layer 9 measurement is added. The two lower plots use strict conditions on the trigger (ACC < 3) and on the number of reconstructed tracker tracks (only 1 track). For each definition, we consider fractions of the estimators resolution (width of gaussian fits to the charge peaks). We choose the final carbon template based on maximum statistics and minimum contamination. In general, we request the contamination to be lower than the per mille level when possible. Even a percent level contamination can induce significant issues in the interpretation of the fit results (see Section 6.7.2).

We then use an interpolation method to produce the missing even Z templates. The results of the interpolation are compared with raw templates extracted from the data for the most abundant odd Z species (lithium, boron and nitrogen). The interpolation is based on the `RooMomentMorph` utility available under the `RooFit` framework [97]. For a given odd Z, we give as input the closest even Z templates. The interpolation technique uses up to the third moments of each input distribution to construct the template at the requested observable value. In Figure 6.25, we show the comparison of raw odd Z templates obtained from the data (blue) and the result of the interpolation (magenta). We observe a good agreement in the template shape around the peak position. The interpolated templates inherit from the contamination present in the even Z templates which becomes significant above oxygen. These are intrinsic limitations of the extraction procedure due to limited statistics and the finite resolution of the tracker.

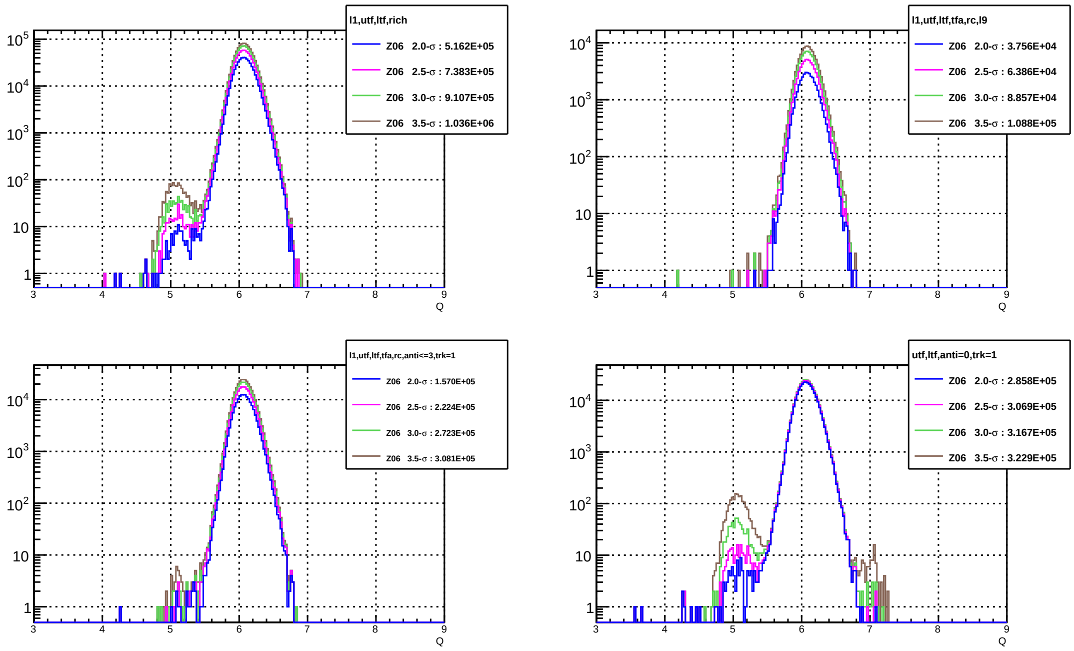

FIGURE 6.24 – Four different definitions of carbon passing through the inner tracker. The final carbon template is chosen based on requirements of maximum statistics and minimum contamination. See text for more information.

For layer 1 templates, we use the same strategy of extracting the even Z from the data and interpolating odd Z templates. However, selecting pure nuclei samples in the layer 1 is extremely challenging due to the significant amount of fragmentation taking place in between the layer 1 and the inner tracker. Using strict trigger conditions ($\mathrm{ACC} < 3$) and the requirement of only one track reconstructed in the tracker allows to clean efficiently the samples. However this results in a drastic reduction of the statistics for charges above oxygen. A seductive alternative is to use the layer 2 response to characterize the layer 1 behavior. High efficiency, low contamination nuclei samples can easily be obtained for the layer 2 using other charge estimators. Figure 6.26 shows a comparison of layer 1 and layer 2 templates for elements of the BCNO group. In general, there is an excellent agreement in the peak position and in the tails description with a discrepancy at the per mille level. For boron (upper left) and nitrogen (lower left), the apparent higher discrepancy is the artifact of residual contaminations that populate the tails of the layer 1 distributions. A good agreement is verified up to neon and

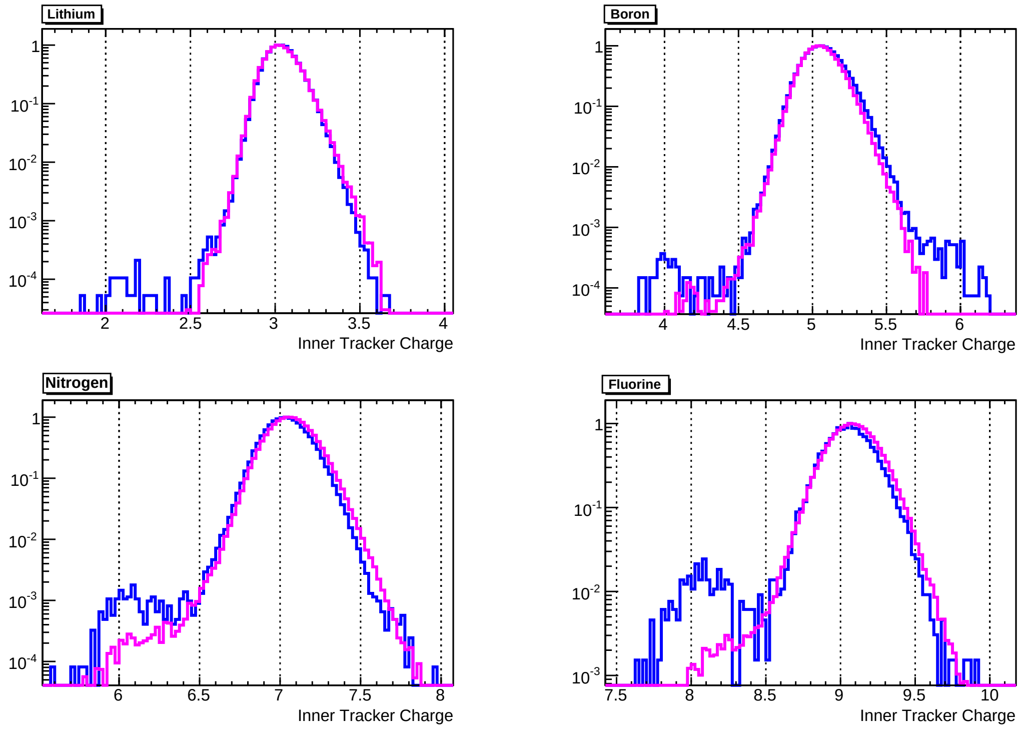

FIGURE 6.25 – Comparison between odd Z raw data templates (blue) and templates obtained using the RooMomentMorph interpolation technique (magenta).

we assume this trend persist at higher Z. This assumption can however not be tested given the statistical limitations for these less abundant species. We also know the tracker resolution starts degrading around neon so it is natural to expect some stronger deviations between the layer 1 and layer 2 response for these charges. In the present state, our best solution remains to use the layer 2 response to produce the templates for all nuclei up to sulfur (Z=16).

6.7.2 Inner Tracker Template Fit

In Figure 6.27, we show the inner tracker charge distribution in different representative bins of rigidity. The binning used is uniform in logarithm with 30 bins between 1 GV and 10 TV. The binning of the inner tracker charge estimator contains 1280 bins from 0 to 32. Only rigidities above 1.3 times the cut-off rigidity are considered to ensure we are selecting primary particles. The last bin shown is at an energy of about 1 TV where the statistics for fitting nuclei components other than BCNO becomes limited.

For each nuclei component in each rigidity bin, we use an extended maximum likelihood fit where the probability density function used is the combination of templates for 3 neighboring charges. This allows to estimate the contamination from $Z-1$ and $Z+1$ populations for any arbitrary selection of the nuclei under study. We assume the contamination from the next-to-closest ($Z-2$ and $Z+2$) nuclei are negligible up to neon. Above neon, the p.d.f. combines the templates for 5 neighboring charges to account for this additional source of contamination.

In a first iteration, we fit single peak contributions with their associated templates, allowing the template position to shift around its initial peak value. The goal is to find the template position that gives the best agreement with the data around the peak region. The fit quality is

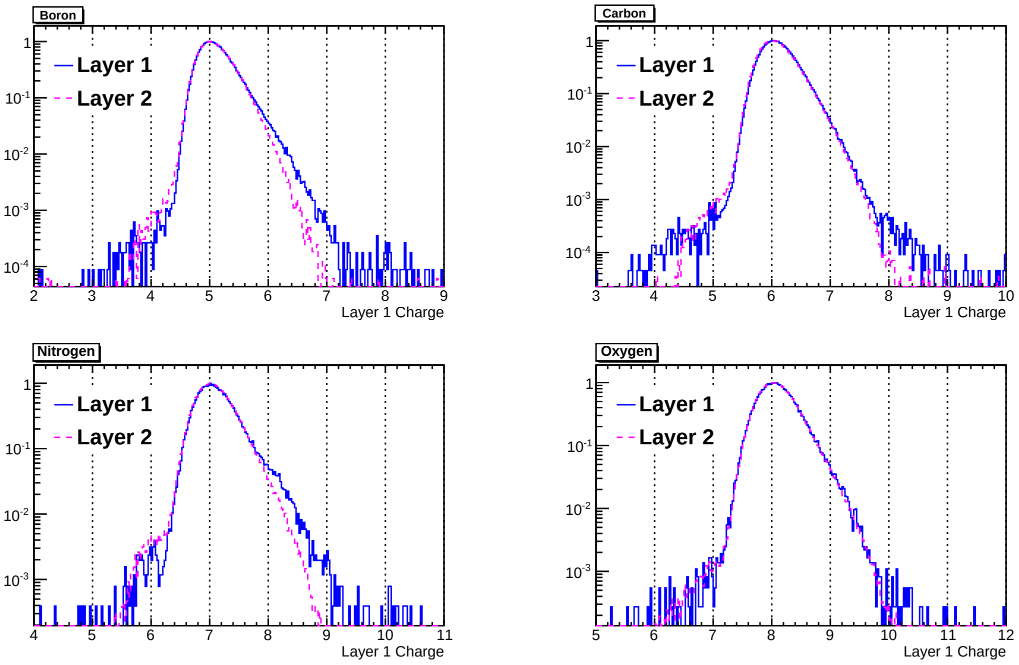

Figure 6.26 – Comparison between layer 1 and layer 2 templates for elements of the BCNO group.

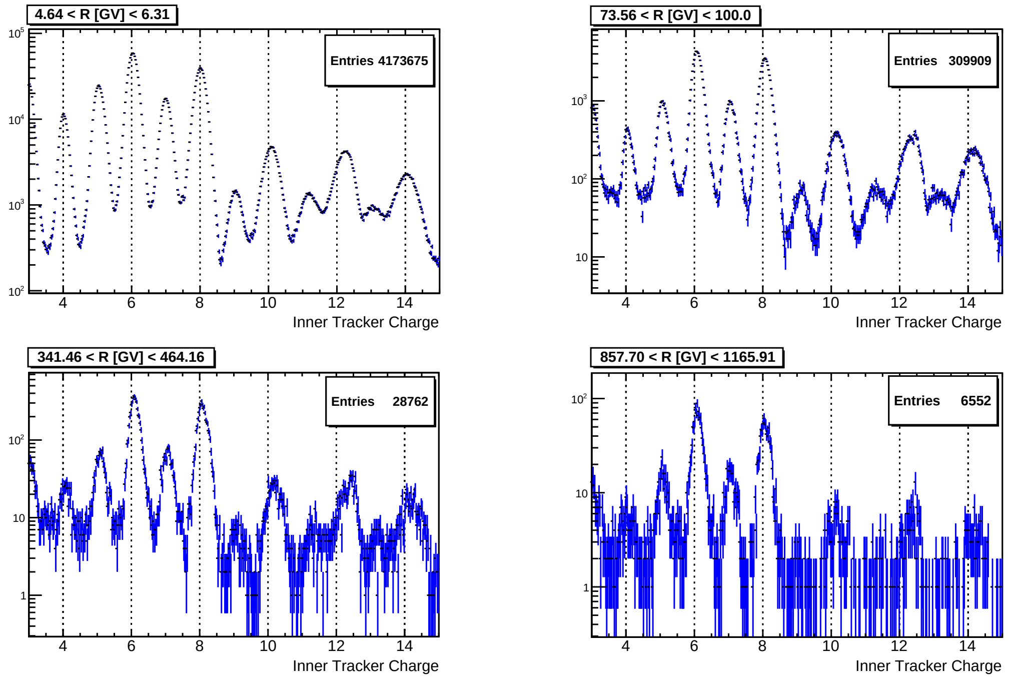

Figure 6.27 – Examples of inner tracker charge distributions for 4 different energy bins.

tested based on the projected pull distributions. We choose the fit with minimum RMS of the pull distribution as the best fit. Once the optimal position of the template is found, we fix it for the next iteration of the fit. The adjustment of the peak position was found to be relevant mostly for nuclei above neon, where we know the tracker calibration becomes less accurate.

We then combine the templates for three neighboring charges with variable normalization into a single p.d.f. for the final fit. Figure 6.28 and 6.29 show the fit results for boron and carbon in the same energy bins previously shown. Figures 6.30 and 6.31 show the associated pull distributions for each fit. It can be seen that in general the valleys in between the charge peaks are not well described by the templates. The discrepancy is greater at energies below 10 GV, suggesting a residual dependence of the inner tracker response with energy. However, it is also plausible that the observed excess of events in the valleys is the result of interactions in the detector (for example the production of δ-rays) correlated with bad reconstructions and spurious charge assignments. If this is the case, identifying clearly this residual background would help reduce the systematic errors from the fit.

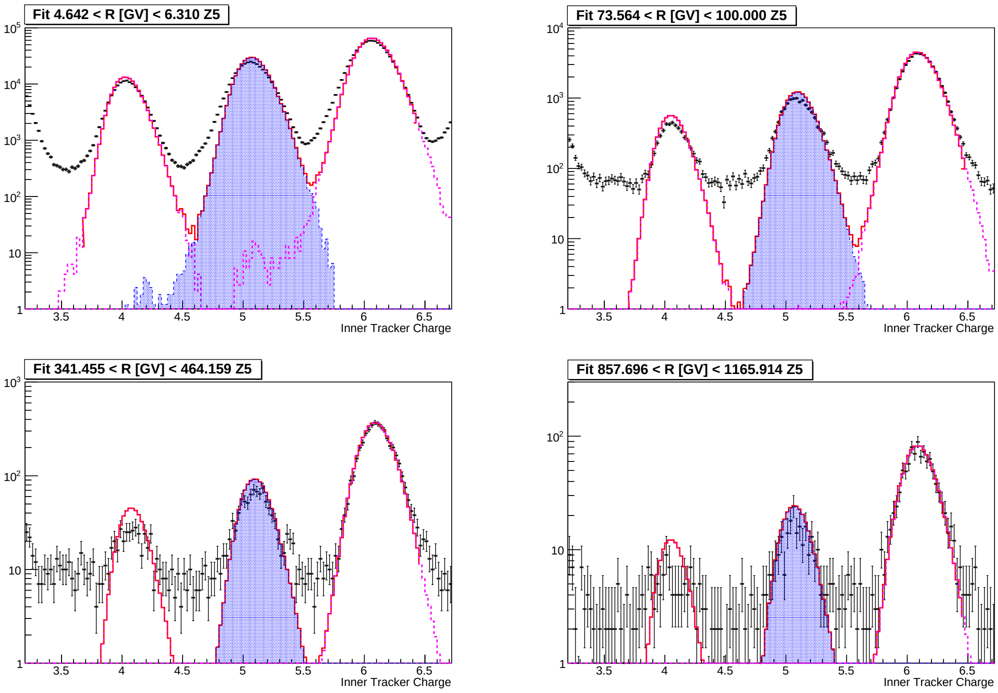

FIGURE 6.28 – Inner tracker template fit results for boron nuclei. Both the full p.d.f. (red line) and p.d.f. components are shown. The blue histogram is the fitted boron template while the magenta templates are the resulting templates for the neighboring charges, beryllium and carbon.

6.7.3 Contamination and Pure Sample Selection

We define high purity samples of each nucleus inside the inner tracker using numerical integration of the fitted templates in 6 different ranges corresponding to fractions of the inner tracker charge resolution (Section 5.9), namely 0.5σ, 1.0σ, 1.5σ, 2.0σ, 2.5σ, $3.\sigma$. The best selection interval is required to have less than 5% contamination together with maximum selection efficiency. For nuclei of the BCNO group, it is always possible to reach a 99% purity with maximum statistics, i.e., with a selection at the 3-σ level. Above neon, the contamination requirement is hardly met for odd Z and a looser cut is adopted. Table 6.2 gives an example

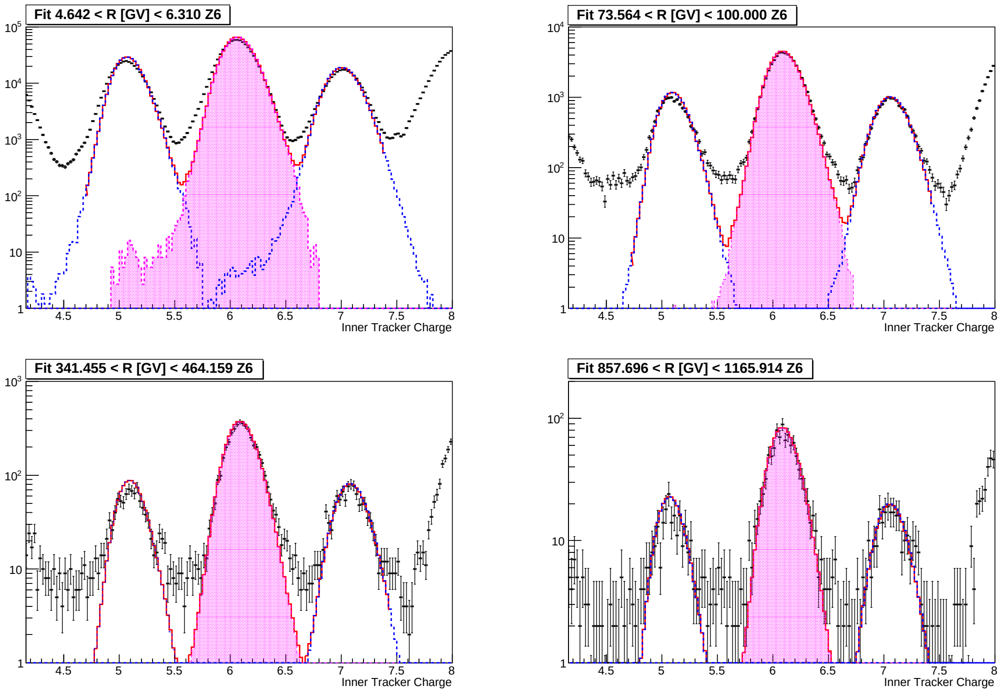

FIGURE 6.29 – Inner tracker template fit results for carbon nuclei. The red line is the combined template p.d.f. The magenta histogram is the fitted carbon template while the blue templates are the resulting templates for the neighboring charges, boron and nitrogen.

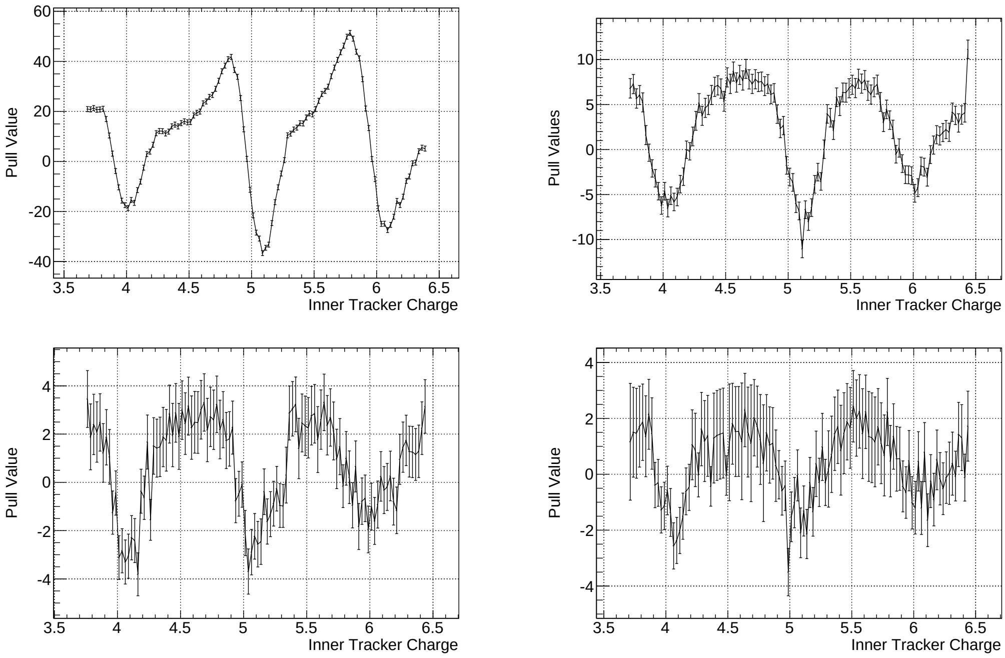

FIGURE 6.30 – Distribution of pull values in the range of the respective inner tracker template fits for boron (Figure 6.28). One can observe that for beryllium ($Z = 4$), both the peak position and the tails are not well described by the templates. For boron and carbon, the discrepancy seems to be mainly in the description of the tails and the valleys in between the peaks.

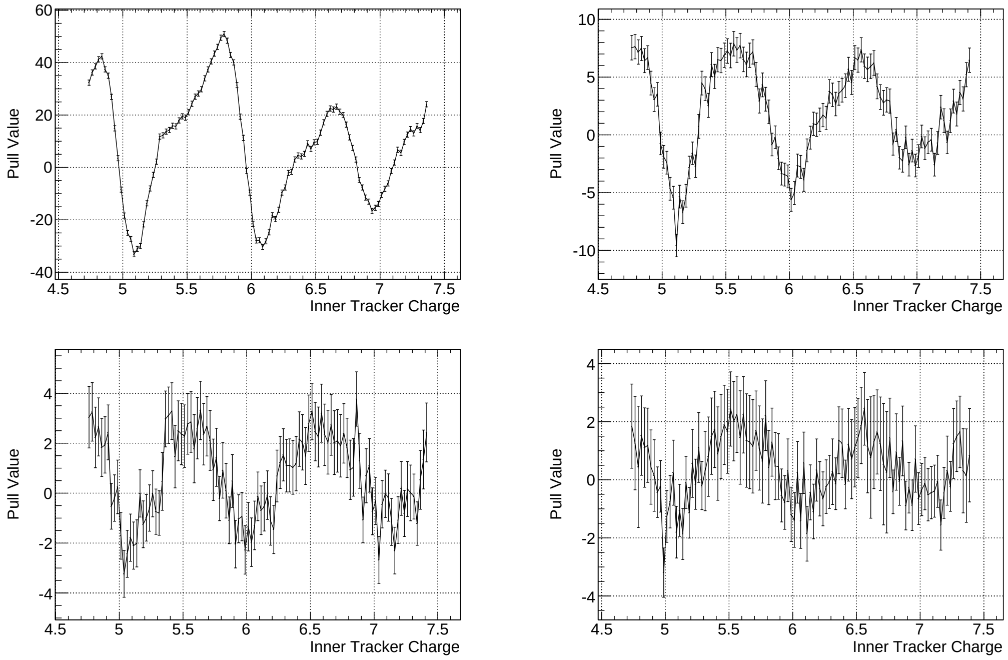

FIGURE 6.31 – Distribution of pull values in the range of the respective inner tracker template fits for carbon (Figure 6.29). The templates do not describe well the tails of the charge peak positions as well as the valleys in between the different nuclei contributions. The effect is worse at low energies.

of the measured contaminations for the boron sample. Contaminations are below the per mille level at all energies. One can observe that the contamination from carbon ($Z+1$) increases with energy since the ratio of boron to carbon is expected to decrease with energy.

6.7.4 Layer 1 Template Fit

For each pure nucleus sample selected in the inner tracker, we fit the associated charge distribution of hits on the layer 1. Figure 6.32 shows the results of the fit for carbon. For the lowest energy bin (upper left plot), there is a clear population to the left of the main carbon peak. This is mainly the result of wrong hit associations and remains below the percent level in all cases. Since our main goal is to estimate the fraction of carbon nuclei in the inner tracker which are also identified as carbon in the layer 1, we do not try to fit all components of the distribution. To avoid any bias in the estimation of the main peak contribution, we nevertheless take into account the two adjacent nuclei contributions. The range of the fit is varied until the best fit is found according to minimum spread of the projected pull distribution.

6.7.5 Corrected Nuclei Counts

The true number of nuclei of a given Z traversing the detector is given by the formula quoted in Section 6.2.1 which we recall here :

$$N_Z(R, R+\Delta R) = \frac{N_{Z,\mathrm{L1,Pure}}(R, R+\Delta R)}{N_{Z,\mathrm{InnerTrk,Pure}}(R, R+\Delta R)} \times N_{Z,\mathrm{InnerTrk,Tot}}(R, R+\Delta R)$$

The fraction term on the right hand side is essentially the fraction of nuclei with charge Z

Z	R [GV]	Sigma	Sel. Eff. [%]	$Z-1$ [%]	$Z+1$ [%]
5	1.604	3.00	99.674	0.013	0.066
5	2.180	3.00	99.541	0.006	0.063
5	2.963	3.00	99.541	0.002	0.055
5	4.028	3.00	99.674	0.001	0.055
5	5.476	3.00	99.759	0.001	0.063
5	7.443	3.00	99.674	0.002	0.059
5	10.118	3.00	99.674	0.001	0.062
5	13.754	3.00	99.759	0.001	0.065
5	18.697	3.00	99.759	0.001	0.070
5	25.415	3.00	99.759	0.001	0.076
5	34.549	3.00	99.759	0.001	0.084
5	46.964	3.00	99.674	0.002	0.090
5	63.841	3.00	99.674	0.002	0.095
5	86.782	3.00	99.674	0.002	0.099
5	117.968	3.00	99.674	0.002	0.109
5	160.360	3.00	99.674	0.002	0.108
5	217.987	3.00	99.674	0.005	0.109
5	296.322	3.00	99.674	0.002	0.116
5	402.807	3.00	99.541	0.002	0.116
5	547.558	3.00	99.674	0.006	0.112
5	744.327	3.00	99.541	$< 10^{-3}$	0.106
5	1011.805	3.00	99.541	0.001	0.099
5	1375.404	3.00	99.674	0.007	0.122

Table 6.2 – Contaminations and selection efficiencies for boron. The Sigma value corresponds to the final selection interval (in units of the tracker resolution) which maximizes the selection efficiency while minimizing the total contamination.

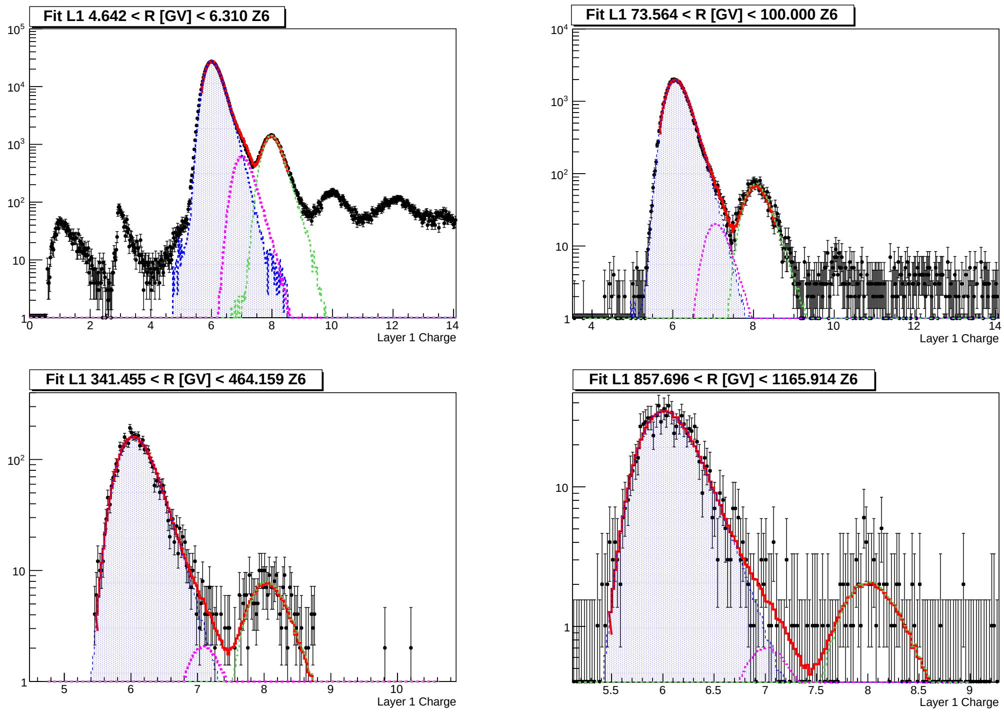

FIGURE 6.32 – Template fit of the charge distribution of the layer 1 hits (black points) for the pure carbon sample selected in the inner tracker. The red line is the combined p.d.f. fit result. The filled blue histogram is the resulting carbon template while the magenta and green histograms are respectively the nitrogen and oxygen contributions.

surviving up to the inner tracker. Figure 6.33 shows the value of this correction factor for the BCNO group (left plot) and other less abundant species (right plot). The errors come from propagation of the different sources of errors associated to the fits (see Section 6.7.6). All survival fractions tend to exhibit a similar shape with an increase from low rigidities to about 100 GV and a decrease at higher rigidities. The second trend is however more pronounced for odd Z nuclei and beryllium. The correction factor is in fact the convolution of fragmentation effects and nuclei relative abundances. The latter seems to have the largest effect. Even Z nuclei become increasingly dominant over odd Z ones with energy, which implies a larger proportion of fragmentation from heavier nuclei into the inner tracker lower abundance nuclei samples. Although an asymmetric *bell-type* shape is distinguished for all nuclei, there are clear fluctuations, most likely due to poor fits, since these points are usually associated with large errors. In few selected regions, mainly above 400 GV, we apply an interpolation to smoothen the correction curves (dashed lines in Figure 6.33). The interpolation is applied only if the result is compatible within errors with the raw measurements. It would be extremely interesting in the future to conduct the exercise of simulating these curves using the Monte Carlo, assuming some reasonable nuclei spectra and using the standard fragmentation cross-sections available.

6.7.6 Fit Systematics and Total Error

To estimate the total error from the fit procedure, we characterize the discrepancy between the fitted templates and the data. We integrate the templates and the data in a reasonable range around each peak position. Since there is no absolute definition for the integration range, we use a statistical approach, repeating the integration in increasingly larger intervals according to the following definition of the integration interval :

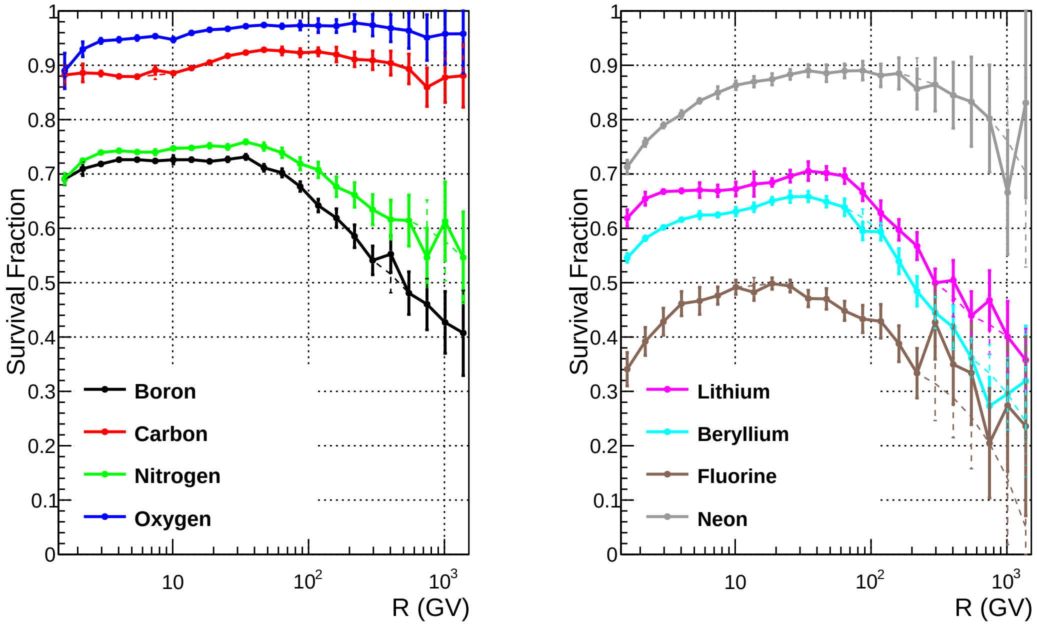

FIGURE 6.33 – Measured survival fractions as a function of rigidity for elements of the BCNO group (left) and other less abundant species (right). The dashed lines are the results of a smoothing of the measured survival fractions for energies where the fit errors are particularly large (see text for more details).

$$[x_1; x_2] = [T_C - \frac{\sigma}{2}(j+2); T_C + \frac{\sigma}{2}(j+2)] \tag{6.9}$$

where T_C is the template center position, evaluated as the center of the template bin with maximum content, and σ is the known tracker resolution (Section 5.9). The index j runs from 0 to 3. We measure the systematic error as the percentage difference between the results of the data and template integrations. To avoid counting statistical errors twice, we subtract it when it does not dominate the error measurement. Formally,

$$\Delta_{Sys} = \begin{cases} \dfrac{\left| \left| \int_{x_1}^{x_2} \text{Data} - \int_{x_1}^{x_2} \text{Temp} \right| - \Delta_{\text{Stat}} \right|}{\int_{x_1}^{x_2} \text{Data}} & \text{if } \Delta_{\text{Stat}} < \Delta \left| \int_{x_1}^{x_2} \text{Data} - \int_{x_1}^{x_2} \text{Temp} \right| \\ \dfrac{\left| \int_{x_1}^{x_2} \text{Data} - \int_{x_1}^{x_2} \text{Temp} \right|}{\int_{x_1}^{x_2} \text{Data}} & \text{otherwise.} \end{cases}$$

Figure 6.34 shows the calculated percentage difference for the inner tracker fits. The percentage difference decreases as the integration range increases. This indicates that the tails of the charge peaks are not well represented. At low rigidities, the percentage difference is larger due to a worse agreement of the templates with data, as discussed in Section 6.7.2. With increasingly larger integration ranges, one obviously expects the percentage difference to increase again as it will start including other nuclei contributions. We choose the last integration range in Figure 6.34 as a conservative starting point to the total systematic error evaluation [2].

---

[2] A more refined analysis, where we systematically search for the turning point (in terms of the integration interval) where the percentage difference starts increasing again, is under investigation. The latter should in principle allow to perform an exact evaluation of the systematic error instead of making a conservative choice as done here.

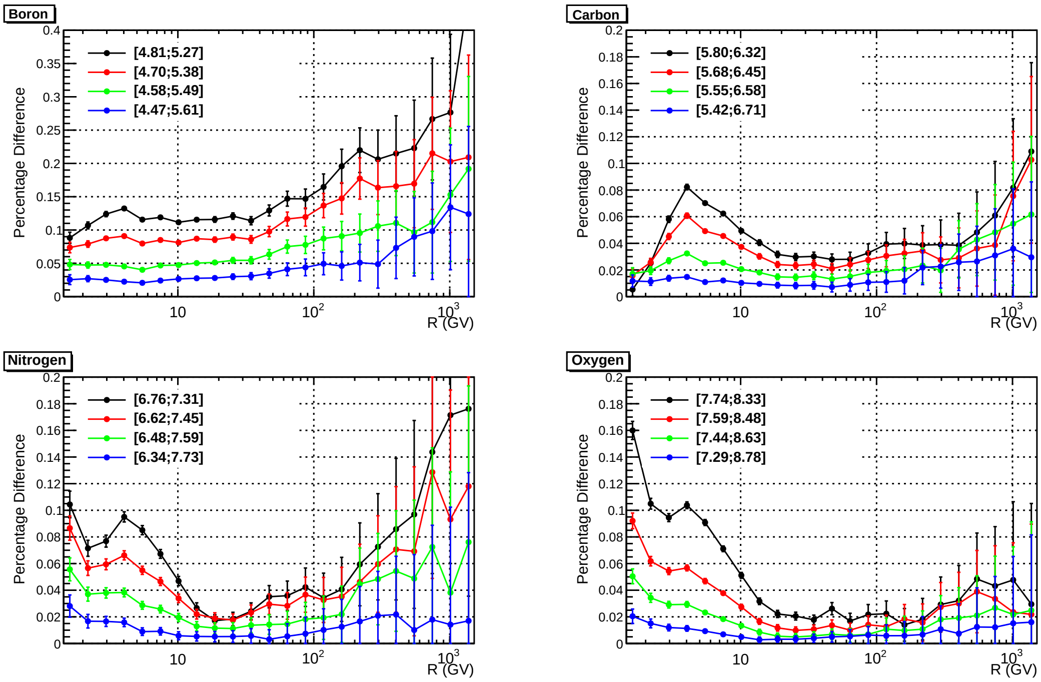

FIGURE 6.34 – Percentage difference between the data and template integration in increasing integration ranges. Errors are statistical.

A detailed decomposition of the fit errors is presented in Figure 6.35. Blue points represent the percentage difference between the integration of the data and the fitted templates. The black points are the statistical errors on the data which naturally increase with rigidity. The final error corresponds to the magenta points which are the percentage error (blue points) subtracted from statistical errors where appropriate, and the value of the upper error edge on the percentage difference otherwise. The final systematic errors from the fits are shown in Figure 6.36. The error remains below 10% for carbon and oxygen at all energies while it remains below 10% for all nuclei up to about 700 GV.

The total error on the final corrected inner tracker count number is obtained by propagation of the different error components :

$$\Delta N_Z(R, R+\Delta R) = \Delta C \times N_{Z,\text{Inn,Tot}} + \Delta N_{Z,\text{Inn,Tot}} \times C \tag{6.10}$$

where C corresponds to the survival fraction correction term such that :

$$\Delta C = \sqrt{\frac{\Delta N_{Z,L1}}{N_{Z,\text{Inn,Sel}}} + \frac{\Delta N_{Z,\text{L1}} \times N_{Z,\text{Inn,Sel}}}{N^2_{Z,\text{Inn,Sel}}}} \tag{6.11}$$

$$\Delta N_{Z,\text{Inn,Tot}} = \sqrt{\Delta^2_{\text{sys}} + \Delta N^2_{\text{stat}}} \tag{6.12}$$

6.8 Nuclei Fluxes

The differential flux is calculated by normalizing the nuclei count number N_Z to the total exposure time, the various reconstruction efficiencies, the geometric acceptance and the

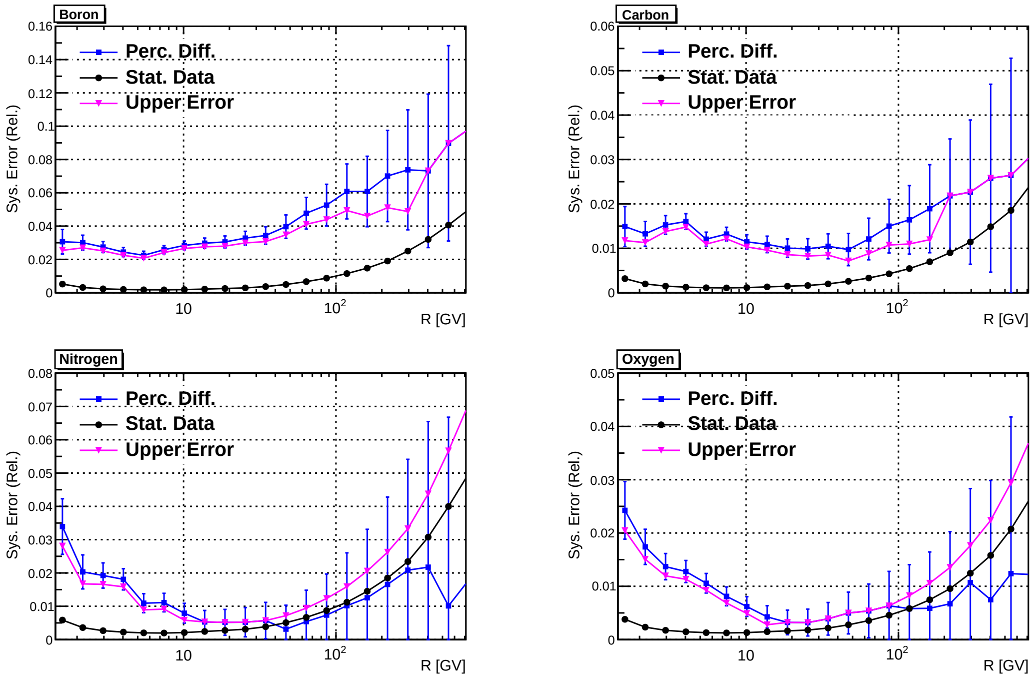

Figure 6.35 – Decomposition of fit errors for the inner tracker template fit of boron nuclei. See text for more information.

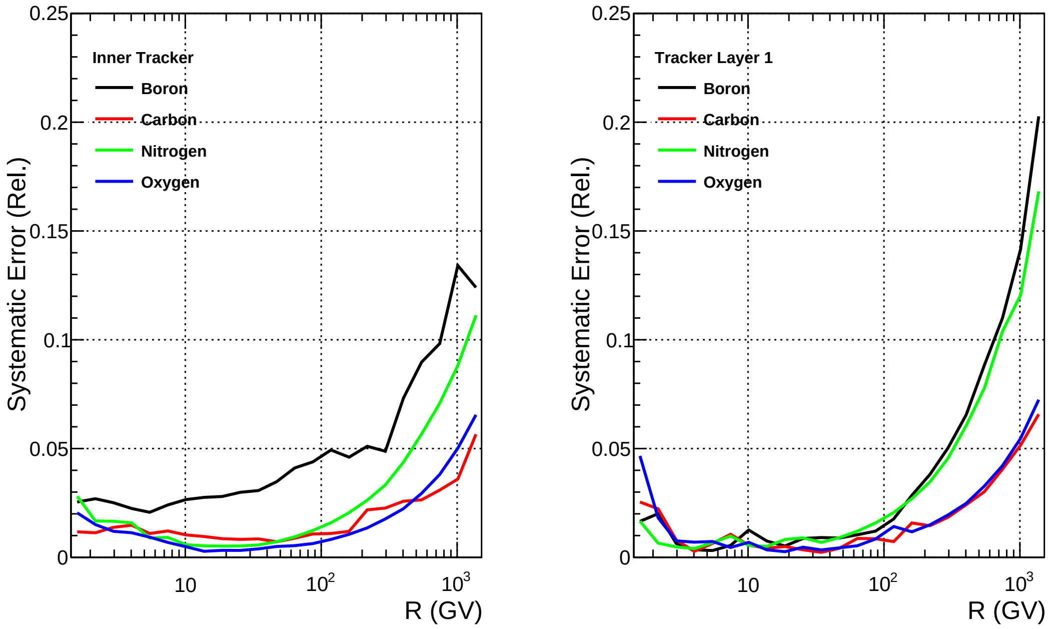

Figure 6.36 – Final systematic errors for the inner tracker template fit (left) and the layer 1 template fit (right).

corresponding energy bin width according to equation 6.2. The total error is obtained by propagating the various sources of errors affecting each term and adding them in quadrature. We have assumed a conservative 1% error on the exposure time value, constant with energy. Figure 6.37 shows the resulting fluxes of nuclei from lithium ($Z = 3$) to neon ($Z = 10$) in logarithmic scale, both in flux and energy. Except for carbon, the fluxes have been scaled by different values for an easier comparison. The fluxes appear smooth with energy with apparently very similar spectral slopes. The relative errors on the fluxes are shown in Figure 6.38. Above few hundreds of GV, the error is dominated by the systematics from the fitting procedure which translate in much larger uncertainties for the lowest abundance nuclei (lithium, beryllium and fluorine). In general, the last two high energy points in the TV region should not be trusted for all presented fluxes since the fitting procedure is known to be unstable and also because we are at the edge of the tracker resolution for the layer 1 plus inner tracker fitting configuration (see Section 3.1.2). An unfolding of the nuclei spectra from the effects of the finite tracker resolution is an important ingredient missing from the current analysis and which can have substantial effects on the flux measurement at the highest energies. The contribution of the various sources of errors to the total flux error is shown in Figure 6.39. It is clear that above 300 GV, the error is completely dominated by the error from the fitting procedure (black points). However, at intermediate rigidities (between 10 GV and 100 GV), the acceptance term (green points) is in fact the dominant source of error for most nuclei species. This means that at these energies, the acceptance is, as anticipated, a limiting factor of the analysis. This is even more true considering we have not taken into account the overall uncertainty coming from nuclear interaction models (see 6.5).

Figure 6.37 provides only a qualitative picture of the fluxes, based on the simple inspection of the spectral shape. The double logarithmic scale tends to hide potential structures in the measurements. In Figure 6.40, we present the BCNO fluxes scaled by $E^{2.7}$ in comparison with previously published results. Figure 6.41 displays the fluxes of less abundant species in the same scale. All our fluxes are in reasonable agreement with previous results, although they may appear slightly higher. The maximum difference is around 10 to 20% but mainly depends on what results we choose for the comparison. Considering the limitations faced in the extraction of the geometric acceptances from the Monte Carlo, it is clear that more simulations are needed to assess the validity of our flux normalizations. It must be emphasized that most of the previous results are balloon measurements which makes a direct comparison delicate due to the unavoidable atmospheric overburden affecting the measurements. Moreover, the energy measurement is often a calorimetric one, which allows to probe directly the particle kinetic energy, and not the rigidity. The comparison is therefore intrinsically biased by the assumptions used to convert the measurements from one energy scale to another. For lithium, beryllium and boron, the number of existing measurements is low. Although the results of this analysis are only preliminary, one can only admire the potential AMS has to provide precise measurements over a wide range of energies in these poorly understood channels.

There is a convenient way to assess the reliability of our flux results. Ratios of different nuclei species are expected to be free of several systematic effects which affect the measurement of absolute fluxes. For example, the exposure time can reasonably be assumed equal for neighboring nuclei and potential systematic effects cancel when taking the ratio. This is also true for part of the reconstruction efficiencies. This is one of the important benefits of measuring secondary to primary nuclei ratios. In fact several experiments have published measured boron to carbon ratios without necessarily publishing the associated fluxes. There is therefore more comparisons available for the ratios with often smaller uncertainties. This analysis was not optimized for such measurements but we can estimate the ratios based on our measured fluxes converted beforehand in kinetic energy per nucleon, using the following formula :

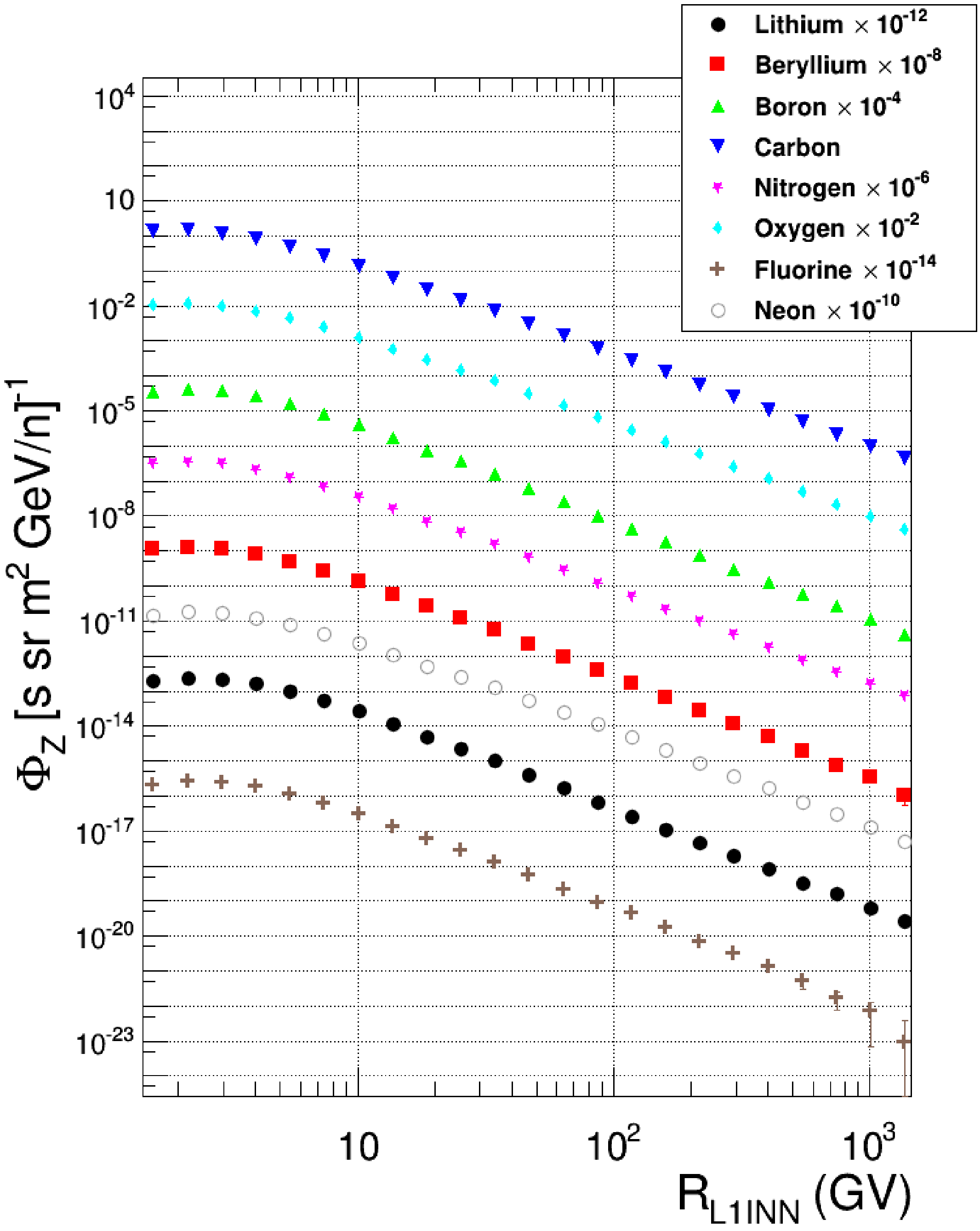

FIGURE 6.37 – Fluxes of all nuclei from lithium to silicon. To facilitate the visualization, the various components have been scaled by different factors, except for carbon.

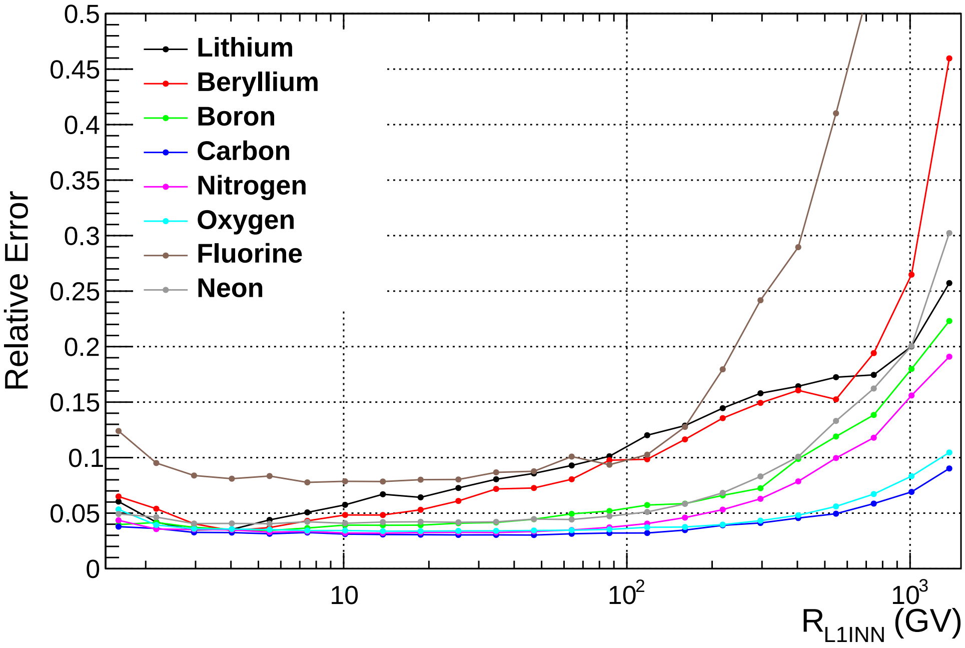

FIGURE 6.38 – Total relative error on the flux measurement of nuclei from lithium ($Z = 3$) to neon ($Z = 10$). The error is dominated by the systematics from the fitting procedure. The latter are correlated to the abundance of the nuclei, hence beryllium (red) and fluorine (brown) have particularly large errors.

$$E_k/N = \frac{(M^2 + (Z \times R)^{1/2}) - M}{A} \tag{6.13}$$

where we use for M an average mass value based on existing measurements of isotopic abundances for each nuclei, as reported in Table 6.3. The values correspond to measurements at solar minimum performed by the ACE-CRIS experiment [3]. We consider up to the 3 most abundant isotopes in the average mass calculation.

Various ratios are shown in Figures 6.42 and 6.43. The secondary boron over primary carbon ratio in Figure 6.42 is certainly the best measured ratio up to date and is most useful to constrain models of propagation of cosmic rays (Sec. 2.4). Our results for the boron over carbon (BC), carbon over oxygen (CO) and nitrogen over oxygen (NO) ratios are in good agreement with existing results, in particular with the AMS-02 result presented at the 2013 ICRC conference (open green circles). The observed agreement strongly supports the methodology of our counting method. The lithium over carbon ratio is perhaps not as good in agreement, in particular with previous AMS-01 data. It is suspected that the selection cuts used in this analysis might introduce a small bias for lithium which could partially explain the observed discrepancy. This however needs to be assessed by careful studies of reconstruction efficiencies specifically dedicated to lithium.

---

[3] `http://www.srl.caltech.edu/ACE/ASC/DATA/level3/`

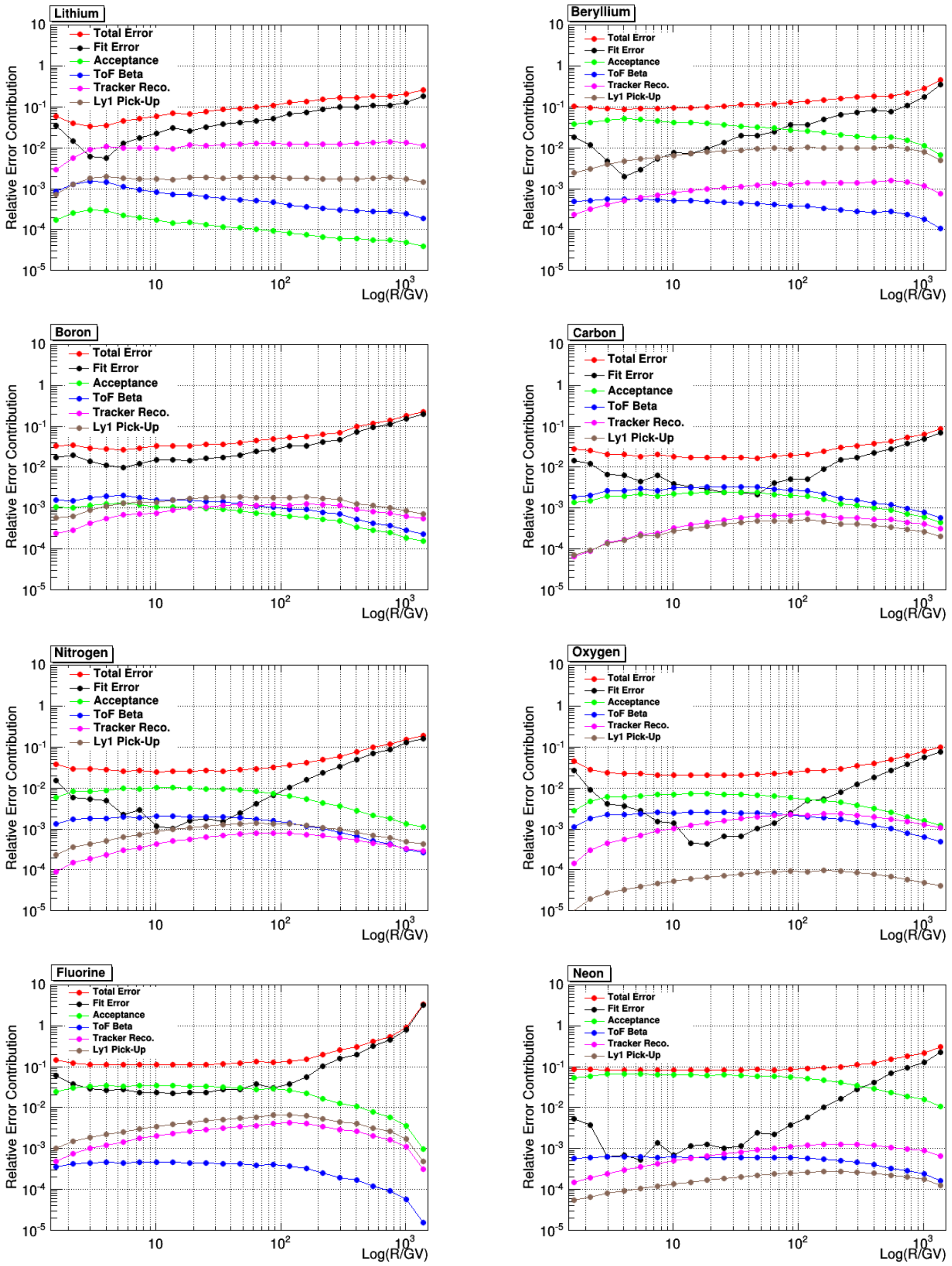

FIGURE 6.39 – Breakdown of the various error contributions to the total flux error for nuclei from Lithium to Neon. Above few hundreds of GV, the error is dominated by the systematics from the fitting procedure (black). The red points are the total flux errors reported in Figure 6.38. In green is the contribution from the acceptance term, in blue from the ToF reconstruction efficiency while magenta and brown are respectively the inner tracker reconstruction and layer 1 pick-up efficiency contributions.

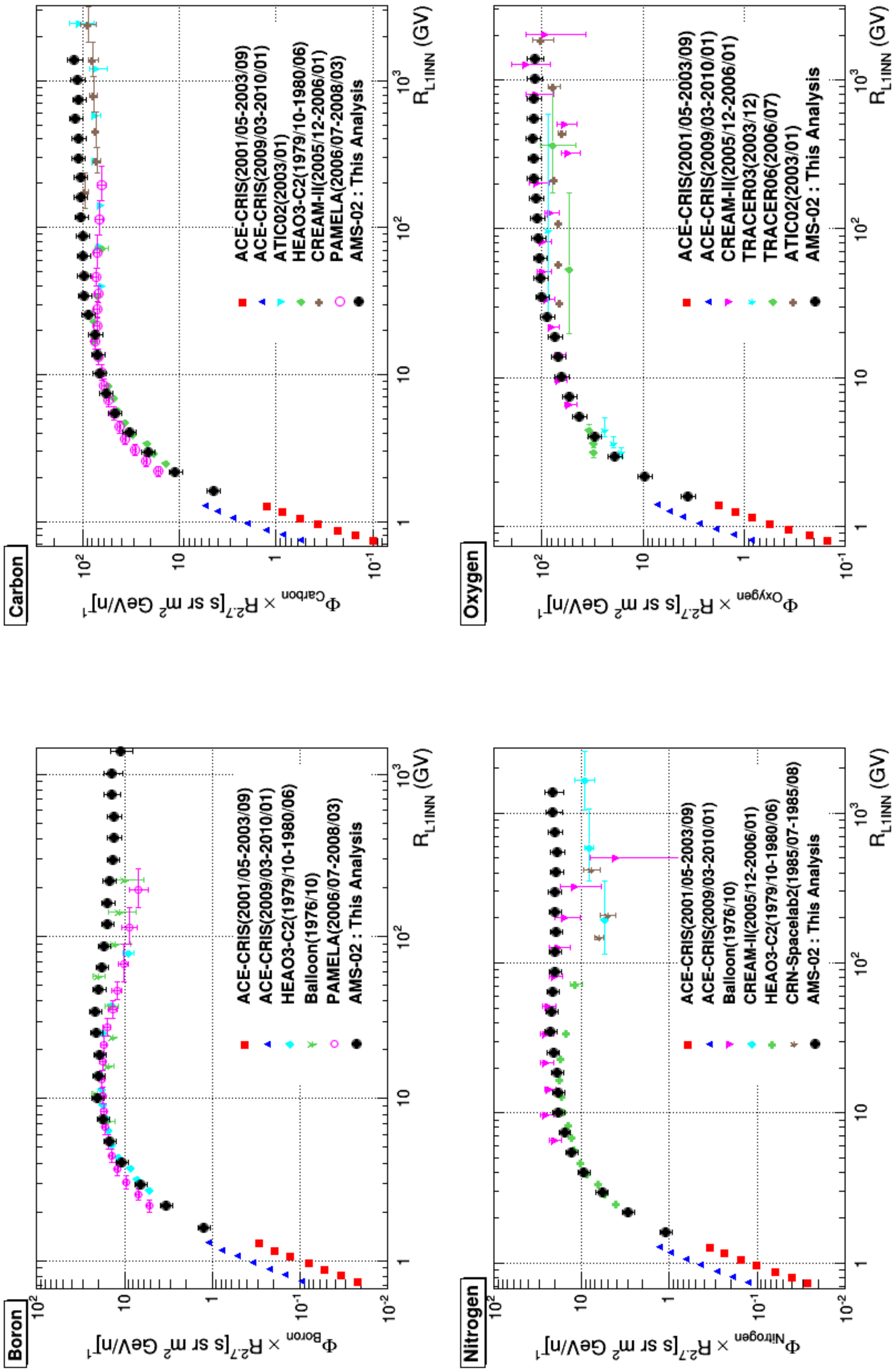

FIGURE 6.40 – Fluxes of BCNO elements scaled by $R^{2.7}$ compared with previously published results.The data are extracted from the Cosmic Ray Database [108].

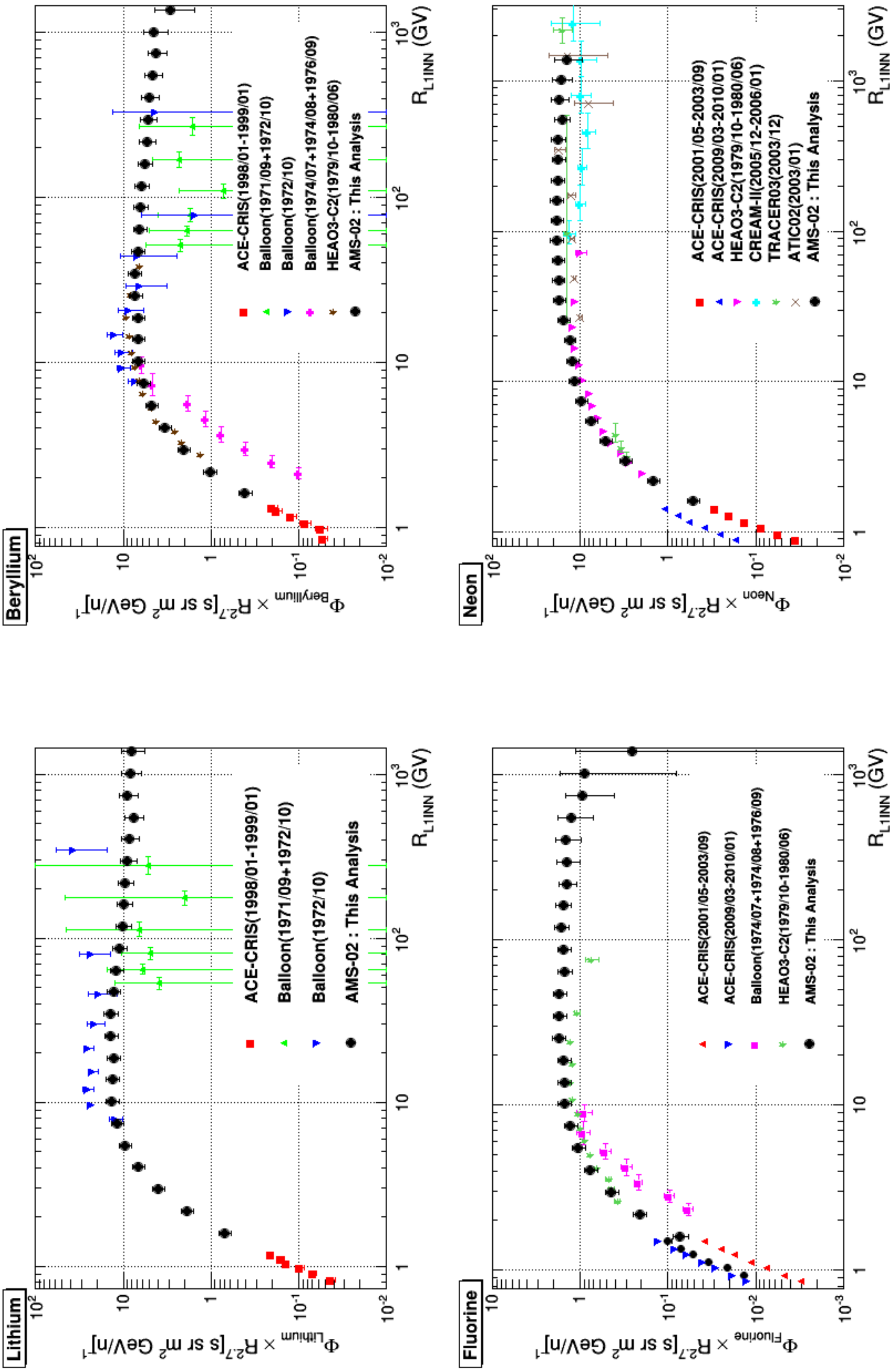

FIGURE 6.41 – Fluxes of lithium, beryllium, fluorine and neon scaled by $R^{2.7}$ compared with previous results [108].

	Energy	A	Abundance [%]	Error [%]
Li (Z=3)	49-127 MeV/nuc	6	53.1	2.2
		7	46.9	2.2
Be (Z=4)	60-157 MeV/nuc	7	59.9	2.9
		9	36.2	3.1
		10	3.8	0.8
B (Z=5)	65-172 MeV/nuc	10	30.0	0.6
		11	70.0	0.6
C (Z=6)	75-199 MeV/nuc	12	94.09	0.18
		13	5.91	0.18
N (Z=7)	81-214 MeV/nuc	14	48.9	0.5
		15	51.1	0.5
O (Z=8)	88-236 MeV/nuc	16	97.19	1.12
		17	1.25	0.08
		18	1.56	0.05
F (Z=9)	92-245 MeV/nuc	19	100.	0.
Ne (Z=10)	98-264 MeV/nuc	20	55.6	0.8
		21	12.0	0.44
		22	32.4	0.6
Na (Z=11)	103-278 MeV/nuc	23	100.	0.
Mg (Z=12)	110-298 MeV/nuc	24	69.6	1.1
		25	14.6	0.7
		26	15.8	0.5
Al (Z=13)	114-310 MeV/nuc	26	4.22	0.38
		27	95.78	0.38
Si (Z=14)	121-320 MeV/nuc	28	86.92	0.36
		29	7.32	0.27
		30	5.76	0.21

Table 6.3 – Cosmic ray isotopic composition measured at solar minimum by the ACE-CRIS experiment. The values are the result of measurements from December 1997 through September 1999.

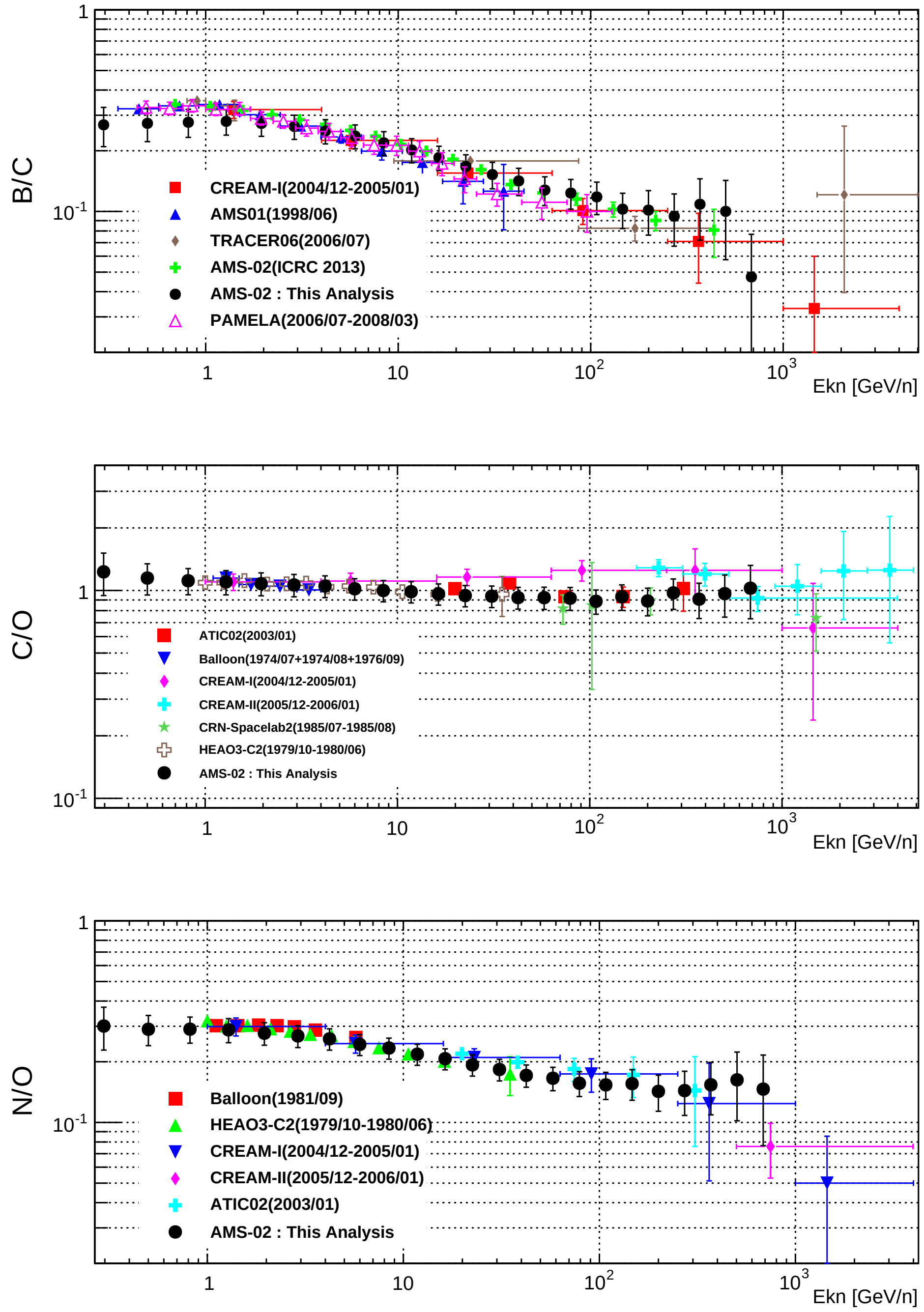

FIGURE 6.42 – Comparison of boron to carbon, carbon to oxygen and nitrogen to oxygen nuclei ratios in kinetic energy per nucleon with previous measurements [108].

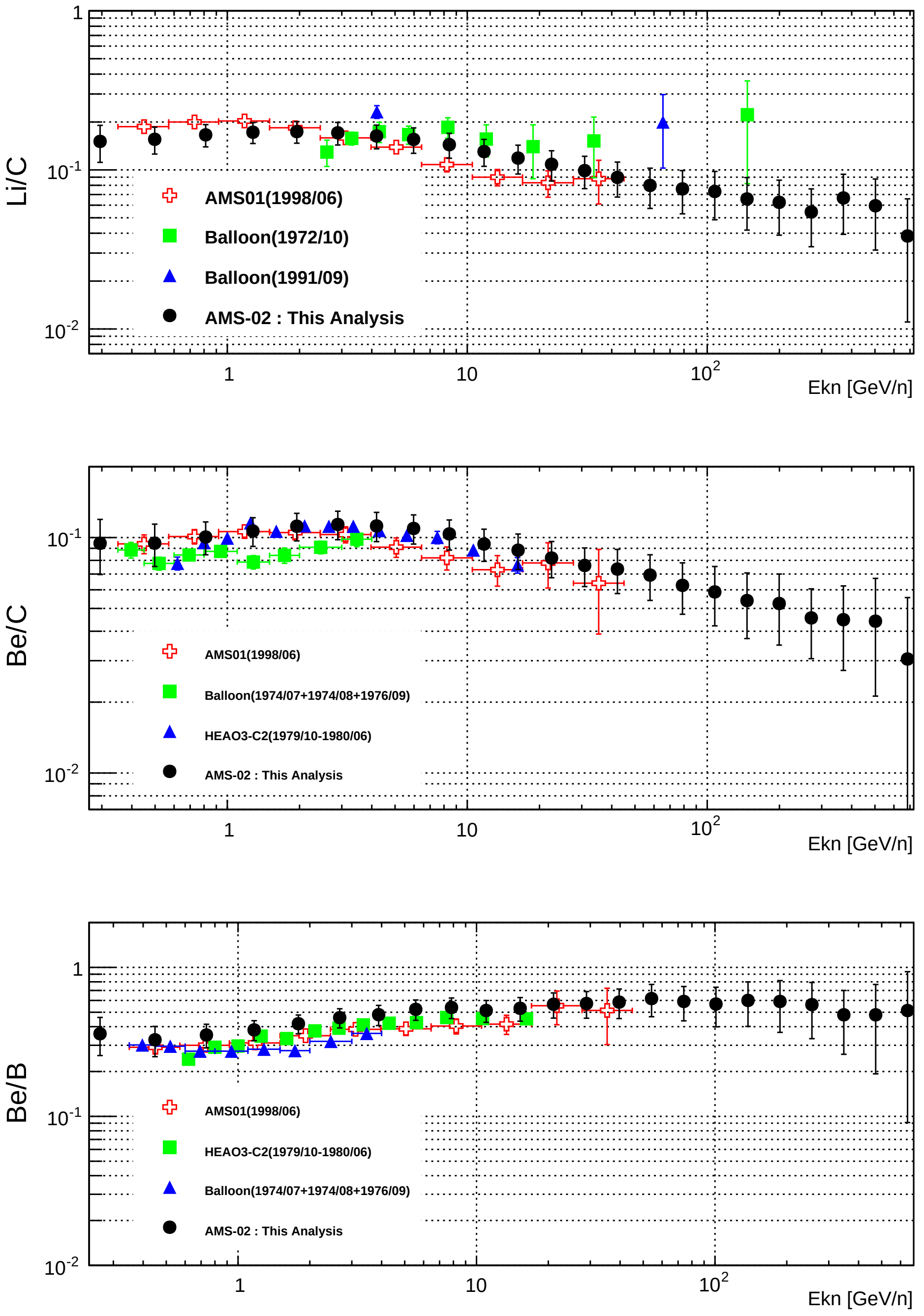

FIGURE 6.43 – Comparison of boron to carbon, carbon to oxygen and nitrogen to oxygen nuclei ratios in kinetic energy per nucleon with previous measurements [108].

6.9 Conclusion and Outlook

We have presented in the previous sections a measurement of the fluxes of nuclei from lithium to neon from 1 GV to slightly above 1 TV. The high end of the energy range is determined by statistics and systematics from the counting method as well as the rigidity determination. The results are in good agreement with existing measurements, although an overall normalization issue might be at play. It is obvious from this work that the lack of Monte Carlo nuclei simulations is currently the most limiting factor of the analysis. Our parameterization of the geometrical acceptance in function of the nuclei charge Z is based on limited MC statistics and only 5 simulated nuclei species. It is expected that a new MC production with a simulation of nuclei up to silicon should take place in the near future, depending on the availability of computing resources. A better understanding of the geometric acceptance is necessary and should also help reduce the systematic errors related to the current parameterization. The new simulations will also help conducting important cross-checks of our parameterizations of the inner tracker reconstruction efficiencies for nuclei above oxygen.

The errors associated to our fluxes are largely dominated by the systematic uncertainties from the fitting procedure used to extract nuclei counts in the inner tracker. At low energies, the charge templates are observed to be in worse agreement with the data. This could be due to residual dependences of the tracker response on the particle rigidity but could also be the result of background events polluting the inner tracker measurement. Careful studies are needed to asses the origin of the discrepancies. The first approach is to produce templates at different energies, despite the statical limitations, and check for potential dependences of the template shape. It was already observed that for carbon the tracker response tends to be broader at low energies. The valleys in between the charge peaks are in general not well represented by the templates, for all nuclei, and at all energies. Identifying and removing a potential source of background in these regions, combined with a better definition of the templates, would clearly help reducing the systematic errors from the fit. The improvement expected for the layer 1 template fitting is limited since fragmentation is an unavoidable background to the study of the layer 1 response. The agreement between the layer 2 and layer 1 templates is reasonable up to oxygen but cannot currently be verified above.

At the highest energies, where the errors are the largest, it is expected that some improvement can still be achieved in the fitting but ultimately, only more statistics will help reducing significantly the errors. An additional improvement could in principle come from including the full span geometry into our analysis. A better rigidity resolution could be achieved and the range of the measurement extended.

Finally, there are few important ingredients missing in the procedure. There is a substantial amount of material above the tracker layer 1 plane which inevitably induces additional fragmentation. The fragmentation probability above the layer 1 has not been estimated in this analysis but was studied by various collaborators in the AMS collaboration. Based on Monte Carlo simulations, it was found the probability is below 1% for carbon and oxygen, although our understanding of these effects above a few tens of GV is limited. Fragmentation effects could be experimentally measured by exposing targets representative for the materials present in AMS to suitable ion beams at accelerator facilities. Such experimental measurements would be of great interest for many cosmic ray experiments given that only very few fragmentation cross-sections have been measured at all, and often in limited energy ranges.

The resolution of the tracker rigidity measurement is finite and depends on the span of the fitted tracks (see Section 3.1.2). The finite resolution introduces deviations in the measured spectrum which must therefore be unfolded from the instrument response. The procedure is called unfolding. Standard tools exist to invert the matrix that represents the array of effects caused on the true spectrum. The results of the unfolding are significant at the highest energies where the resolution rapidly degrades but where the measurements also represent the highest scientific interest. A precise study of the unfolding depends largely on the availability of Monte Carlo simulations.

Chapitre 7

Conclusions

The fluxes of completely ionized nuclei in cosmic rays, as well as secondary-to-primary ratios such as the boron over carbon ratio, are important information to better understand the production, acceleration and propagation of cosmic rays in the galaxy. A challenging aspect of measuring nuclei fluxes with AMS-02 is the precise understanding of fragmentation processes inside the detector. The single layer charge identification capability of the silicon tracker provides an important tool for tagging the nuclear fragmentation appearing at different levels in the detector. A precise calibration is thus essential for many physics topics.

In Chapter 5, we have presented a procedure to optimize the charge identification capabilities of the silicon tracker. After correcting for the most relevant effects degrading the charge measurement, we reach a resolution of 0.1 charge units for carbon and below 0.3 c.u. up to silicon. Due to non-linearities in the response of the electronics, the tracker resolution starts degrading around silicon ($Z = 14$). In the next years, AMS-02 will continue accumulating new data and some limitations of the current calibration procedure might be addressed. Given the life-time of the AMS mission, expected to be as long as 18 years or more, one crucial aspect of the tracker calibration will be to verify the stability with time of the electronics behavior.

In Chapter 6, we have presented preliminary flux measurements of nuclei from lithium to neon from 1 GV to few TV. The measurements are based on a fit of the inner tracker charge distribution that we correct for the fragmentation background from heavier nuclei using the information of hits on the tracker layer 1. The motivation for our method was to produce in one shot the fluxes of all nuclei, providing a direct path to the measurement of nuclei relative abundances. Our preliminary results are in good agreement with the existing data. Despite few ingredients missing in our results, such as the unfolding of the measured spectra, it is clear that the unprecedented level of statistics accumulated in only three years of operation of AMS-02 sets a new basis for precision measurements of cosmic ray spectra. In particular, our results show clearly the potential AMS-02 has to provide precise measurements in poorly understood channels such as for lithium or beryllium nuclei. The most limiting factor in the present analysis deals with the lack of Monte Carlo simulations. With new simulations expected in a near future, several cross-checks will be required to validate definitively the methodology proposed in this work and achieve a final flux measurement for nuclei up to silicon.

List of Figures

1.1 Pictures of the ATIC (left) and CREAM (right) instruments. 20

1.2 The entire sky observed by FERMI for γ-rays with energies above 1 GeV [14]. Brighter colors indicate brighter sources. One can observe the concentrated emission around the galactic center. 21

1.3 Illustration of the various instrumentations and techniques used to detect extensive air showers on ground (credits K. Bernlöhr [1]) 23

1.4 Recent measurements of the positron fraction [29]. The grey band is the expectation from models of particle interaction and propagation in the Galaxy. The current measurements show a clear deviation from the predictions above 10 GeV. 25

1.5 Measured energy spectra for proton and helium nuclei. The black points from PAMELA indicate a clear deviation from a smooth power-law. An extrapolation of the proton break observed by PAMELA seems consistent with the flux measured by the ATIC (open purple circles) and CREAM (green squares) experiments at higher energies. A pronounce discrepancy is however observed for the helium flux. Plot taken from [32]. 26

2.1 Left : Various components of the cosmic ray flux measured by different experiments. Picture taken from [40]. Right : Relative flux of primary cosmic ray nuclei from hydrogen to iron [41]. 30

2.2 Flux of UHE cosmic ray particles measured by various experiments [41]. The differential cosmic-ray flux is multiplied by $E^{2.6}$. A significant suppression of the the flux of cosmic rays is observed above 4×10^{19} eV. 33

2.3 Sky map in equatorial coordinates presenting the arrival directions of cosmic ray showers measured at the Pierre Auger observatory (filled red circles). The blue asterisks indicate the position of AGNs from different catalogs. The squares correspond to events measured with the HiRes telescope. Picture taken from [58]. 35

2.4 Relative abundance of cosmic ray nuclei at an energy around 1 GeV/n (normalization to Si $\times100$). Filled triangles represent solar system abundances [58]. The black points are a compilation by Simpson [59] of different experimental results. Courtesy of Prof. Israel for the Advanced Explorer experiment [2]. 36

2.5 Remnant of SN-1572 as seen in X-ray light from the Chandra X-ray Observatory [3]. The blueish rim at the edge of this type Ia SNR is the first evidence for magnetic filed amplification at the shock front of SNRs. 41

2.6 Hillas plot : the lines represent the maximum energy of a proton (blue) and iron (red) in different accelerator sites (β=1/300 for non-relativistic shock, β=1 for relativistic shocks). The gray blobs in the plot are characteristic of the astronomical objects magnetic field sizes and radii. Any class of objects above the diagonal line will be able to accelerate the proton/iron nuclei to the marked energies. Picture taken from [68]. 42
2.7 Radial distribution of atomic and molecular hydrogen as deduced from radio surveys of the Galaxy in the 21-*cm* line of atomic hydrogen and from millimetre surveys of the molecular emission line of carbon monoxide [70]. 44
2.8 Predicted gamma-ray energy spectra from each secondary particle produced in p+ISM interactions for a photon energy of 150 GeV, here only from baryon decay contributions. Plot taken from [81]. 47
2.9 Parameterization of the diffused gamma rays emission [76]. Black points are the local effective emissivity of the ISM per hydrogen atom measured by the Fermi collaboration. The lines correspond to the predictions based on different photo-production cross-section parameterizations. 48
2.10 Black points are the local effective emissivity of the ISM per hydrogen atom measured by the Fermi collaboration. The lines correspond to the predictions based on different parameterizations of the CR proton and helium fluxes measured at Earth. Delahaye et al. [76]. 50

3.1 Schematic view of the AMS-02 spectrometer [88], presented in the bending plane of the magnetic field. Pictures of the nine silicon tracker layers are also shown. . 52
3.2 Detailed drawing (to scale) of AMS-02 [89]. The various detectors are labelled. 53
3.3 *Left* : Picture of the AMS-02 permanent magnet. The very same magnet was operated during the STS-91 Space Shuttle Discovery mission in 1998. *Right* : Magnetic field configuration of the AMS-02 magnet. The uniformity of the field inside the magnet defines the reference frame for the instrument, with its X axis running along the magnetic filed lines, and its Y coordinate describing the bending direction. Pictures taken from [90]. 54
3.4 The lower ToF plane (left) [90] and the charge measured by the upper ToF plane (right) in a data sample with a pre-scaled H component [91]. 55
3.5 Detection principle of the TRD [92]. The Figure depicts a single element of the fleece radiator and proportional chamber layered combination. The AMS-02 TRD is made of 20 of such elements. 56
3.6 Left : exploded view of the various elements of the RICH instrument. From top to bottom : the radiator plane, the conical reflector walls and the bottom layer of PMT detectors. Right : Example of the type of events reconstructed by the RICH. Particles can either emit Čerenkov radiation in the NaF part of the radiator or the silicon aerogel. The ring of the Čerenkov emission cone is reconstructed by the PMTs detected signals. Pictures taken from [89]. 57
3.7 Picture of the ECAL detector [90]. Each wire is connected to the PMTs inserted in the lateral slots on all sides of the structure. 58
3.8 Illustration of the ACC purpose in rejecting certain types of events in the AMS trigger [89]. 59
3.9 Left : picture of one Star Tracker camera placed on top of the magnet case [90]. The camera points at a 40° w.r.t. the AMS zenith. Right : The GPS receiver integrated on top of AMS [89]. 60
3.10 Diagram of the AMS-02 Data Acquisition architecture [90]. 64

3.11 Picture of the AMS-02 instrument place on its mission site on the ISS. Credits to Nasa. 65
3.12 Scheme of electrical interfaces between AMS-02 and the ISS [90]. TDRS : Tracking and Data Relay Satellite, POCC : Payload Operations and Control Center, M&C : Monitoring and Command. 66
3.13 Illustration of the beta angle definition (*Wikipedia*). 67
3.14 Picture of the AMS POCC at Cern Prévessin [89]. A big central screen displays the position of the ISS at any moment in time. 69

4.1 Schematic view of a double-sided silicon sensor. Plot created by N. Saouter ^{4}. . 72
4.2 Architecture of the connection between the p-side of a sensor and the associated S-side Hybrid. One can recognize the 10 VAs used to amplify and shape the signals from the p-side strips. 73
4.3 Schematic view of the signal routing for both sides of a typical AMS-02 ladder [98]. The specific routing of the n-side introduces an ambiguity in the hit position. 74
4.4 The AMS-02 inner tracker planes [90]. One can appreciate the double layered structure of each plane with the two columns of ladders running parallel. . . . 75
4.5 Schematic illustration of the special K7 routing scheme. A sensor is separated into 7 sub-groups of 32 readout channels. Two sub-groups on each edge of the sensor possess a specific routing scheme alternating between 1 out of 1 strip and 1 out of 2 strips (usual K5 implementation) readout by the electronics. 76
4.6 Example of the different naming schemes for the tracker layer 9. 77
4.7 Asymmetry in the n-side signal CoG distribution due to the multiplexed reading of the VA chips (blue filled curve). Correcting for this effect allows to partially recover the original symmetry of the signal (blue curve). 79

5.1 Draw chart of the architecture of the charge calibration procedure of the silicon tracker. 82
5.2 Illustration of the nuclei selection procedure. The black curve represents a typical n-side truncated mean distribution in units of $\sqrt{ADC}$. The peaks of nuclei up to oxygen ($Z = 8$) are clearly visible. The gaussian fits allow to select the different nuclei with minimum contamination from neighboring charges, as indicated by the colored hashed areas. 83
5.3 Dependence of the raw signal on the impact position of the particle and its inclination for a selected sample of helium nuclei. The maximum of collection efficiency appears when the particle traverses at vertical incidence, impinging directly on a readout strip, i.e. $IP = 0$ and $\theta_{XZ} = 0$. 85
5.4 *Left* : Correlation between the charge and the raw cluster signal for the p-side (top plot) and n-side (bottom plot) measurements of a single tracker ladder during the 2003 test beam [87]. *Right* : the same correlation is measured for another AMS-02 tracker ladder with ISS data for the p-side (solid blue) and n-side (solid red). 86
5.5 The scatter plot presents the cluster signal, in units of ADC, for a selected sample of helium nuclei, vs the 10 p-side VAs of a single AMS-02 ladder (TkID +307). For this extreme case, the maximum difference in the peak position (black points from fitting) amounts to 22%. 87
5.6 Landau convoluted with gaussian fit of 6 N-side VAs and the 5 first P-side VAs of ladder +103. For each VA, two separate categories are defined depending on the impact position of the particle (see text). 89

5.7 *Left* : Relation of the MPV values for a given VA as function of the reference MPV values. Horizontal error bars are the RMS of the reference MPV distributions. The inverse of the slope value gives the equalization factor for the given VA. *Right* : distribution of n-side MPV values before (black) and after (red) applying the equalization factors. All three nuclei sample are combined in this plot. 90

5.8 Cluster signal signal distribution (in ADC) for ladder -201 in the two readout and non-readout regions. Three different type of VA categories can be identified among these 6 n-side VAs. VA 10 ,11 and 12 are tagged as bad VAs (10 and 12 are dead while 15 shows very pathological behavior). VA 12 and 13 are golden VAs and VA 14 is considered as silver since the signal has a well defined shape but has a very low gain. 91

5.9 Effect of the VA equalization on the overall charge separation power for a selected range of nuclei for the n (top) and p-side (bottom) measurements. Dashed lines indicate the results before applying the equalization. 92

5.10 Average relative difference between fitted MPV values in the readout and non-readout regions, for individuals layers. A distinctive feature appears for layer 2, probably due to different signal-to-noise thresholds settings for cluster reconstruction. 93

5.11 K5 (left) and S (right) readout scheme charge collection behavior for selected samples of helium $Z = 2$ (top), carbon $Z = 6$ (middle), and oxygen $Z = 8$ (bottom) nuclei. For each impact position and angle bin is reported the peak value of the fitting function. Empty bins correspond to the cases where the fitting procedure has failed due to lack of statistics, or where the absence of statistics is inherent to the CoG definition of the impact position. With increasing charge, the scale of the charge loss effect tends to decrease. 95

5.12 Maximum of the fitted function versus the center of gravity CoG for different inclination bins and helium nuclei. The curves are symmetric with respect to CoG=0 since half of the values come from unfolding of the fit results into the previously merged regions. The pronounced gap near CoG=0 is inherent to the CoG definition of the particle impact position. 96

5.13 N-side charge resolution for nuclei up to neon before and after applying the charge loss correction. 97

5.14 Carbon nuclei ionisation energy loss in a single layer as a function of $\beta\gamma$. The left plot describes the dependence using an estimation of the $\beta\gamma$ parameter based on the ToF β measurement only. The right plot uses a combination of the ToF β and tracker rigidity measurement. Each description is parametrized by fitting the corrected pulse height in different energy bins with a Landau function convoluted with a gaussian contribution. The open black circles correspond to the peak values resulting from the fits. This peak profile is then fitted using a function combining two straight lines and a fifth order polynomial. Such parametrization provides a good asymptotic behavior as well as a satisfactory description of the minimum ionizing region. Plots produced by A. Oliva. 98

5.15 *Left* : Parametrization of the energy dependence of the ionisation energy loss of carbon for different tracker layers. The deviations at low energies are due to the additional energy lost by the particle while traversing the AMS-02 material. The deviations are most significant for the two external layers : layer 1 (dashed blue) and layer 9 (dotted magenta). *Right* : The same parameterizations for different nuclei for the inner tracker layer 5. With increasing Z, the energy loss effect becomes less pronounced at low $\beta\gamma$ values. 100

5.16 Tracker charge estimator for the n-side charge measurement for nuclei up to silicon, after applying the energy dependence correction. The picture allows to see the efficient flattening of the signal distribution with energy. 101
5.17 The final equalization procedure. The top plot corresponds to the distribution of the 3072 VA MPV values for carbon nuclei, before (black) and after (filled blue) the final equalization procedure. The bottom plot shows the result for iron nuclei. 102
5.18 *Left* : normalized tracker charge estimator in function of time for carbon nuclei. *Right* : distribution of average Q/Z values for all time intervals. 103
5.19 Raw abundance distribution for nuclei in the calibration sample before and after applying the equalization and linearization procedure, for the n-side (red) and p-side (blue) measurements. The distributions are not corrected for efficiency and fragmentation. 104
5.20 *Top* : Raw abundance distribution of nuclei in the calibration sample as a function of the final tracker charge estimator for the combined p- and n-side measurements. The distribution is not corrected for efficiency and fragmentation such that the proton and helium contributions are strongly suppressed. *Bottom* : tracker charge resolution expressed in units of charge from Gaussian fits to the raw abundance distribution. Errors are from the fit. 105

6.1 Projected $Y - Z$ view of the AMS-02 detector. The red curve represents the trajectory of a particle through the instrument with the various measurements of the particle charge Z at various levels of the instrument [105]. 108
6.2 Event display (in both bending and non-bending projections) of a carbon nucleus entering the AMS detector from the top and fragmenting into boron in the upper ToF plane. The tracker layer 1 measures a charge of 6.1, the TRD 6.0, while the inner tracker and RICH measure a charge corresponding to boron (Z=5). In the upper ToF plane where the interaction presumably takes place, the measurement integrates the products of the interaction and typically measures a higher charge value. One can also notice from the projection on the right side some activity in the TRD which is most likely due to the production of δ-rays. 109
6.3 Illustration of the strategy of our nuclei counting method. We select tracks with hits in the tracker layer 1 and inner tracker planes. For a pure sample of carbon nuclei selected in the inner tracker (left panel, shaded area), one can estimate the fragmentation background by looking at the associated layer 1 charge distribution (right panel). 111
6.4 Cut breakdown of the ToF beta reconstruction efficiency for BCNO elements. . 117
6.5 Comparison of ToF beta reconstruction efficiencies in data and Monte Carlo. The agreement is good, within 1% at all energies and for all nuclei. 117
6.6 Constant parameterization of the ToF beta reconstruction efficiency. 118
6.7 Results of the constant parameterizations (black points) of the ToF beta reconstruction efficiency in function of the nuclear charge Z. Odd Z nuclei above nitrogen have been neglected. A single efficiency value for all nuclei is extracted based on a constant fit (dashed red line). 119
6.8 Rigidity Estimators. *Left* : rigidity extracted from the ToF velocity measurement versus the tracker full span rigidity. *Center* : geomagnetic cutoff rigidity estimation. *Right* : rigidity estimation from the energy deposition in the Ecal. . 120
6.9 Cut breakdown of the inner tracker reconstruction efficiency. The geomagnetic cut-off rigidity is used as the rigidity estimator. 120

6.10 Comparison of the inner tracker reconstruction efficiency measured with the 3 different rigidity estimators. The shaded bands indicate the validity range of the different estimators. . . . 121

6.11 Comparison between data (blue and green) and Monte Carlo (magenta) measured efficiencies. The black points indicate the ratio of blue points to the magenta ones. . . . 122

6.12 Straight line parameterization of the inner tracker track reconstruction efficiency. The fit is applied on the blue points only. The black points correspond to the MC efficiency. The extrapolation of the fit seems in reasonable agreement with the predictions of the MC. . . . 123

6.13 Pol1 parameterization of the inner tracker track reconstruction efficiency for all nuclei from lithium to silicon. The shaded area indicates the variable uncertainties from the fits. Within errors, the slope value is almost constant around -0.01. The efficiency value, evaluated at $\log R = 1.5$ fluctuates within 2% for all nuclei. . . . 124

6.14 Layer 1 hit pick-up efficiency for elements of the BCNO group. The last cut shows an accumulated efficiency above 65% for all nuclei with a slight trend of increasing efficiency with rigidity. . . . 125

6.15 Comparison between the layer 1 pick-up efficiencies for two definitions of the efficiency samples. Blue points represent a loose selection with potential contamination from fragmentation while the red points are based on a very strict selection (see text). The agreement is within 2% up to few hundred GV. . . . 125

6.16 Comparison between MC and data layer 1 pick-up efficiencies. The level of agreement, represented by the black points, is within 10% up to 10 GV for nuclei up to oxygen but tends to worsen at higher energies. This effect appears to also increase with Z. . . . 126

6.17 Linear parameterization (magenta) of the layer 1 pick-up efficiencies. . . . 127

6.18 Results of the linear parameterizations of the layer 1 pick-up efficiency for all nuclei from proton to silicon. Errors come from the fit. . . . 127

6.19 Trigger Efficiency for Boron, Carbon, Nitrogen and Oxygen nuclei for two different definitions of the initial efficiency samples. . . . 128

6.20 Trigger Efficiency : comparison of Monte Carlo and data. . . . 129

6.21 The measured MC acceptance for available nuclei. Four geometries are distinguished : particles passing at least through the inner tracker (black), at least through the layer 1 and inner tracker (red), the inner and layer 9 (green) and finally the full span geometry (blue). . . . 131

6.22 Black points are the MC calculated acceptances for the inner tracker plus layer 1 geometry. The magenta dashed lines are constant fits of the acceptances performed between 10 and 100 GV. The bottom right plot shows the result of the fits in function of Z with the simplest parameterization possible (dashed red line). 131

6.23 Exposure time in function of rigidity for two safety factors on the estimated geomagnetic cutoff rigidity. The total exposure time above ~40 GV, where geomagnetic effects disappear, is 6.39147×10^7 s. . . . 133

6.24 Four different definitions of carbon passing through the inner tracker. The final carbon template is chosen based on requirements of maximum statistics and minimum contamination. See text for more information. . . . 134

6.25 Comparison between odd Z raw data templates (blue) and templates obtained using the RooMomentMorph interpolation technique (magenta). . . . 135

6.26 Comparison between layer 1 and layer 2 templates for elements of the BCNO group. . . . 136

6.27 Examples of inner tracker charge distributions for 4 different energy bins. . . . 136
6.28 Inner tracker template fit results for boron nuclei. Both the full p.d.f. (red line) and p.d.f. components are shown. The blue histogram is the fitted boron template while the magenta templates are the resulting templates for the neighboring charges, beryllium and carbon. 137
6.29 Inner tracker template fit results for carbon nuclei. The red line is the combined template p.d.f. The magenta histogram is the fitted carbon template while the blue templates are the resulting templates for the neighboring charges, boron and nitrogen. 138
6.30 Distribution of pull values in the range of the respective inner tracker template fits for boron (Figure 6.28). One can observe that for beryllium ($Z = 4$), both the peak position and the tails are not well described by the templates. For boron and carbon, the discrepancy seems to be mainly in the description of the tails and the valleys in between the peaks. 138
6.31 Distribution of pull values in the range of the respective inner tracker template fits for carbon (Figure 6.29). The templates do not describe well the tails of the charge peak positions as well as the valleys in between the different nuclei contributions. The effect is worse at low energies. 139
6.32 Template fit of the charge distribution of the layer 1 hits (black points) for the pure carbon sample selected in the inner tracker. The red line is the combined p.d.f. fit result. The filled blue histogram is the resulting carbon template while the magenta and green histograms are respectively the nitrogen and oxygen contributions. 141
6.33 Measured survival fractions as a function of rigidity for elements of the BCNO group (left) and other less abundant species (right). The dashed lines are the results of a smoothing of the measured survival fractions for energies where the fit errors are particularly large (see text for more details). 142
6.34 Percentage difference between the data and template integration in increasing integration ranges. Errors are statistical. 143
6.35 Decomposition of fit errors for the inner tracker template fit of boron nuclei. See text for more information. 144
6.36 Final systematic errors for the inner tracker template fit (left) and the layer 1 template fit (right). 144
6.37 Fluxes of all nuclei from lithium to silicon. To facilitate the visualization, the various components have been scaled by different factors, except for carbon. . . 146
6.38 Total relative error on the flux measurement of nuclei from lithium ($Z = 3$) to neon ($Z = 10$). The error is dominated by the systematics from the fitting procedure. The latter are correlated to the abundance of the nuclei, hence beryllium (red) and fluorine (brown) have particularly large errors. 147
6.39 Breakdown of the various error contributions to the total flux error for nuclei from Lithium to Neon. Above few hundreds of GV, the error is dominated by the systematics from the fitting procedure (black). The red points are the total flux errors reported in Figure 6.38. In green is the contribution from the acceptance term, in blue from the ToF reconstruction efficiency while magenta and brown are respectively the inner tracker reconstruction and layer 1 pick-up efficiency contributions. 148
6.40 Fluxes of BCNO elements scaled by $R^{2.7}$ compared with previously published results.The data are extracted from the Cosmic Ray Database [108]. 149
6.41 Fluxes of lithium, beryllium, fluorine and neon scaled by $R^{2.7}$ compared with previous results [108]. 150

6.42 Comparison of boron to carbon, carbon to oxygen and nitrogen to oxygen nuclei ratios in kinetic energy per nucleon with previous measurements [108]. 152
6.43 Comparison of boron to carbon, carbon to oxygen and nitrogen to oxygen nuclei ratios in kinetic energy per nucleon with previous measurements [108]. 153

B.1 Cut breakdown of the ToF beta reconstruction efficiency all nuclei from lithium ($Z = 3$) to silicon ($Z = 14$). 180
B.2 Constant parameterization of the ToF beta reconstruction efficiency for all nuclei from lithium ($Z = 3$) to silicon ($Z = 14$). 181

C.1 Inner Tracker reconstruction efficiency : cut breakdown. The rigidity is estimated through the geomagnetic cutoff rigidity. 184
C.2 Straight line parameterizations of the inner tracker reconstruction efficiency. The black points are the Monte Carlo measured efficiencies, available only for a limited number of nuclei. The green points are the efficiencies measured in the data using the Ecal energy deposition as the rigidity estimator. 185

D.1 Cut breakdown of the layer 1 hit pick-up efficiency for all nuclei from lithium ($Z = 3$) to silicon ($Z = 14$). 188
D.2 Straight line parameterization (dashed magenta line) of the layer 1 pick-up efficiency (blue points). 189

E.1 Trigger Efficiency for all nuclei from lithium ($Z = 3$) to silicon ($Z = 14$) for two different tracker geometries. See text for more information. 192

List of Tables

2.1 Contribution of the most abundant nuclei species to the diffuse γ-ray emission according to the simple scaling model of Norbury and Townsend. First column gives the assumed ISM abundance normalize to proton. The third column uses the same normalization to produce the expected additional γ-ray flux (in % of the proton contribution). 49

3.1 List of the various technical challenges faced by the design of space qualified electronics for AMS-02. Table adapted from [90]. 60

5.1 Summary of correction options available to correct the signal associated to a tracker cluster. 104

6.1 List of Tracker and Tof based selection cuts used in this analysis. 115
6.2 Contaminations and selection efficiencies for boron. The Sigma value corresponds to the final selection interval (in units of the tracker resolution) which maximizes the selection efficiency while minimizing the total contamination. . . 140
6.3 Cosmic ray isotopic composition measured at solar minimum by the ACE-CRIS experiment. The values are the result of measurements from December 1997 through September 1999. 151

A.1 Gain parameter database for VAs of ladder +103. 177

Bibliographie

[1] P. Blasi. The origin of galactic cosmic rays. *Astron. Astrophys. Rev.*, 21 :70, 2013.

[2] Alessandro. Angelis. *L'enigma dei raggi cosmici : Le più grandi energie dell'universo.* I Blu, Pagine di Scienza,. Springer Milan,, Milano :, 2012.

[3] V. Hess. Über Beobachtungen der durchdringenden Strahlung bei sieben Freiballonfahrten. *Wien. Sitz. Ber.*, 120(13) :1084–1091, 1912.

[4] W. Kolhörster. Messungen der Durchdringenden Strahlung im Freiballon in Grösseren Höhen. *Physikalishe Zeitschrift*, 14 :1153–1156, 1913.

[5] W. Bothe and W. Kolhörster. *Zeitschr. f. Phys.*, 56 :751, 1929.

[6] L. Alvarez and Compton A. A Positively Charged Component of Cosmic Rays. *Phys. Rev.*, 43(10) :835–836, May 1933.

[7] Carl D. Anderson. The Positive Electron. *Phys. Rev.*, 43 :491–494, Mar 1933.

[8] Seth H. Neddermeyer and Carl D. Anderson. Note on the Nature of Cosmic-Ray Particles. *Phys. Rev.*, 51 :884–886, May 1937.

[9] C. M. G. Lattes, P.S. Occhialini, and C. F. Powell. Observations on the tracks of slow mesons in photographic emulsions. *Nature*, 160 :486–492, October 1947.

[10] M. Schein, W. P. Jesse, and E. O. Wollan. The nature of the primary cosmic radiation and the origin of the mesotron. *Phys. Rev.*, 59 :615–615, Apr 1941.

[11] G.V. Kulikov and G.B. Khristiansen. Particle-number spectrum of extensive air showers at sea level. *JETP Letters*, 18 :207, 1958.

[12] C. Macolino and the Pierre Auger Collaboration. Anisotropy Studies with the Pierre Auger Observatory. *Journal of Physics : Conference Series*, 375(5) :052002, 2012.

[13] J. Chang et al. An excess of cosmic ray electrons at energies of 300-800 GeV. *Nature*, 456, November 2008.

[14] D.J. Thompson. The Gamma-ray Sky with Fermi. *Nucl.Phys.B*, 2013.

[15] T. Antoni et al. The Cosmic ray experiment KASCADE. *Nucl.Instrum.Meth.*, A513 :490–510, 2003.

[16] G. Navarra, T. Antoni, W.D. Apel, F. Badea, K. Bekk, et al. KASCADE-Grande : A large acceptance, high-resolution cosmic-ray detector up to 10^{18} eV. *Nucl.Instrum.Meth.*, A518 :207–209, 2004.

[17] N. Chiba, K. Hashimoto, N. Hayashida, K. Honda, M. Honda, et al. Akeno giant air shower array (AGASA) covering 100-km^2 area. *Nucl.Instrum.Meth.*, A311 :338–349, 1992.

[18] J. Abraham and al. Properties and performance of the prototype instrument for the Pierre Auger Observatory. *Nuclear Instruments and Methods in Physics Research Section A : Accelerators, Spectrometers, Detectors and Associated Equipment*, 523(1–2) :50 – 95, 2004.

[19] J.A. Hinton. The Status of the H.E.S.S. project. *New Astron.Rev.*, 48 :331–337, 2004.

[20] Daniel Ferenc. The MAGIC gamma-ray observatory. *Nuclear Instruments and Methods in Physics Research Section A : Accelerators, Spectrometers, Detectors and Associated Equipment*, 553(1–2) :274 – 281, 2005. Proceedings of the fifth International Workshop on Ring Imaging Detectors Fifth International Workshop on Ring Imaging Detectors.

[21] T.C. Weekes, C. Akerlof, S. Biller, A.C. Breslin, J.H. Buckley, et al. VERITAS : Very energetic radiation imaging telescope array system. *Astroparticle Physics*, 17 :221–243, 2002.

[22] R.M. Baltrusaitis, R. Cady, G.L. Cassiday, R. Cooper, J.W. Elbert, et al. The utah FLY's Eye Derector. *Nucl.Instrum.Meth.*, A240 :410–428, 1985.

[23] H. Kawai and al. Telescope Array Experiment. *Nuclear Physics B - Proceedings Supplements*, 175–176(0) :221 – 226, 2008. Proceedings of the XIV International Symposium on Very High Energy Cosmic Ray Interactions.

[24] O. Adriani, G. C. Barbarino, and al. PAMELA Results on the Cosmic-Ray Antiproton Flux from 60 Mev to 180 Gev in Kinetic Energy. *Phys. Rev. Lett.*, 105 :121101, Sep 2010.

[25] B. Agrinier, Y. Koechlin, and al. East-west asymmetry and charge sign ratio of primary cosmic-ray electrons at 8.3 gv rigidity cut-off. *Lettere al Nuovo Cimento*, 1(1) :53–56, 1969.

[26] O. Adriani and al. Cosmic-ray positron energy spectrum measured by PAMELA. *Phys. Rev. Lett.*, 111 :081102, Aug 2013.

[27] M. Ackermann and al. Measurement of Separate Cosmic-Ray Electron and Positron Spectra with the Fermi Large Area Telescope. *Physical Review Letters*, 108(1) :011103, January 2012.

[28] M. Aguilar et al. First Result from the Alpha Magnetic Spectrometer on the International Space Station : Precision Measurement of the Positron Fraction in Primary Cosmic Rays of 0.5 to 350 GeV. *Phys.Rev.Lett.*, 110(14) :141102, 2013.

[29] S. Coutu. Positrons galore. *Physics*, 6 :40, Apr 2013.

[30] A.D. Panov, Jr. Adams, J.H., H.S. Ahn, G.L. Bashinzhagyan, J.W. Watts, et al. Energy Spectra of Abundant Nuclei of Primary Cosmic Rays from the Data of ATIC-2 Experiment : Final Results. *Bull.Russ.Acad.Sci.Phys.*, 73 :564–567, 2009.

[31] H.S. Ahn and al. Discrepant Hardening Observed in Cosmic-ray Elemental Spectra. *Astroparticle Particle Physics Journal Letters*, 714 :89–93, May 2010.

[32] O. Adriani et al. PAMELA Measurements of Cosmic-ray Proton and Helium Spectra. *Science*, 332 :69–72, 2011.

[33] S. Thoudam and Jorg R. Horandel. Nearby supernova remnants and the cosmic-ray spectral hardening at high energies. *ArXiv e-prints*, 2011.

[34] Peter L. Biermann, Julia K. Becker, Jens Dreyer, Athina Meli, Eun-Suk Seo, and Todor Stanev. The Origin of Cosmic Rays : Explosions of Massive Stars with Magnetic Winds and Their Supernova Mechanism. *The Astrophysical Journal*, 725(1) :184, 2010.

[35] A. E. Vladimirov, G. Johannesson, I. V. Moskalenko, and T. A. Porter. Testing the Origin of High-energy Cosmic Rays. *The Astrophysical Journal*, 752(1) :68, 2012.

[36] Nicola Tomassetti. Origin of the Cosmic-Ray Spectral Hardening. *Astrophys.J.*, 752 :L13, 2012.

[37] S. Haino and al. Precision Measurement of the Proton Flux with AMS. 2013. Proceedings of the 33rd International Cosmic Ray Conference (to be published).

[38] V. Choutko and al. Precision Measurement of the Cosmic Ray Helium Flux with the AMS Experiment. 2013. Proceedings of the 33rd International Cosmic Ray Conference (to be published).

[39] J. Lavalle. Impact of the spectral hardening of TeV cosmic rays on the prediction of the secondary positron flux. *MNRAS*, 414 :985–991, jun 2011.

[40] Anthony M. Hillas. Cosmic Rays : Recent Progress and some Current Questions. *ArXiv e-prints*, 2006.

[41] J. Beringer and al. Particle Data Group. *Phys. Rev.*, 86, 2012.

[42] Jörg R. Hörandel. On the knee in the energy spectrum of cosmic rays. *Astroparticle Physics*, 19(2) :193 – 220, 2003.

[43] W. D. Apel and al. Ankle-like feature in the energy spectrum of light elements of cosmic rays observed with KASCADE-Grande. *Phys. Rev. D*, 87 :081101, Apr 2013.

[44] M. G. Aartsen and al. Measurement of the cosmic ray energy spectrum with IceTop-73. *Phys. Rev. D*, 88 :042004, Aug 2013.

[45] P. Sokolsky and G.B. Thomson. Highest Energy Cosmic Rays and results from the HiRes Experiment. *J.Phys.*, G34 :R401, 2007.

[46] P. Sokolsky. Results from the Telescope Array and review of HiRes. *EPJ Web of Conferences*, 52(2), 2013.

[47] J. Abraham and al. Measurement of the Depth of Maximum of Extensive Air Showers above 10^{18} ev. *Phys. Rev. Lett.*, 104 :091101, Mar 2010.

[48] Tadeusz Wibig and Arnold W. Wolfendale. At what particle energy do extragalactic cosmic rays start to predominate ? *J.Phys.*, G31 :255–264, 2005.

[49] Veniamin S. Berezinsky, S.I. Grigorieva, and B.I. Hnatyk. Extragalactic UHE proton spectrum and prediction for iron-nuclei flux at $10^8 - 10^9$ GeV. *Astropart.Phys.*, 21 :617–625, 2004.

[50] R. Aloisio, V. Berezinsky, Pasquale Blasi, A. Gazizov, S. Grigorieva, et al. A dip in the UHECR spectrum and the transition from galactic to extragalactic cosmic rays. *Astropart.Phys.*, 27 :76–91, 2007.

[51] W. Bietenholz. The most powerful particles in the Universe : a cosmic smash. *ArXiv e-prints*, 2013.

[52] L.J. Gleeson and W.I. Axford. The Compton-Getting Effect. *APSS*, 2 :431–437, Dec 1968.

[53] M. Amenomori et al. A Northern sky survey for steady TeV gamma-ray point sources using the Tibet Air Shower Array. *Astrophys.J.*, 633 :1005–1012, 2005.

[54] T. Antoni et al. Search for cosmic-ray point sources with KASCADE. *Astrophys.J.*, 608 :865–871, 2004.

[55] G. Guillian et al. Observation of the anisotropy of 10-TeV primary cosmic ray nuclei flux with the Super-Kamiokande-I detector. *Phys.Rev.*, D75 :062003, 2007.

[56] M. Amenomori. Anisotropy and Corotation of Galactic Cosmic Rays. *Science*, 314 :439–443, 2006.

[57] M. Salvati and B. Sacco. The Milagro anticenter hot spots : cosmic rays from the Geminga supernova ? *Astron.Astrophys.*, 485 :527–529, 2008.

[58] Johannes Blümer, Ralph Engel, and Jörg R. Hörandel. Cosmic rays from the knee to the highest energies. *Progress in Particle and Nuclear Physics*, 63(2) :293 – 338, 2009.

[59] G. M. Comstock, C. Y. Fan, and J. A. Simpson. Energy Spectra and Abundances of the Cosmic-Ray Nuclei Helium to Iron from the Ogo-I Satellite Experiment. *APJ*, 155 :609, February 1969.

[60] N. E. Yanasak and al. Measurement of the Secondary Radionuclides ^{10}Be, ^{26}Al, ^{36}Cl, ^{54}Mn, and ^{14}C and Implications for the Galactic Cosmic-Ray Age. *The Astrophysical Journal*, 563(2) :768, 2001.

[61] W. Baade and F. Zwicky. Remarks on Super-Novae and Cosmic Rays. *Phys. Rev.*, 46 :76–77, Jul 1934.

[62] E. Fermi. On the Origin of the Cosmic Radiation. *Phys. Rev.*, 75 :1169–1174, Apr 1949.

[63] D. Caprioli, E. Amato, and P. Blasi. Non-linear diffusive shock acceleration with free escape boundary. *Astropart.Phys.*, 33 :307–311, 2010.

[64] F. Giordano, M. Naumann-Godo, J. Ballet, K. Bechtol, S. Funk, et al. *Fermi*-LAT Detection of the Young SuperNova Remnant Tycho. *ArXiv e-prints*, 2011.

[65] V.A. Acciari, E. Aliu, T. Arlen, T. Aune, M. Beilicke, et al. Discovery of TeV Gamma Ray Emission from Tycho's Supernova Remnant. *Astrophys.J.*, 730 :L20, 2011.

[66] G. Morlino and D. Caprioli. Strong evidences of hadron acceleration in Tycho's Supernova Remnant. *Astron.Astrophys.*, 538 :A81, 2012.

[67] E.G. Berezhko, L.T. Ksenofontov, and H.J. Völk. The nature of gamma-ray emission of Tycho's supernova remnant. *Astrophys.J.*, 763 :14, 2013.

[68] G. Sigl. High energy neutrinos and cosmic rays. *ArXiv e-prints*, 2012.

[69] D. Maurin. USINE : A new public cosmic ray propagation code. Basic phenomenology, sample results, and a bit of USINE. *ICATPP Conference on Cosmic Rays for Particle and Astroparticle Physics, Como : Italy (2010)*, pages 420–434, 2010.

[70] J. Binney and M. Merrifield. *Galactic Astronomy.* Princeton University Press, 1998.

[71] S. Longair. *High Energy Astrophysics.* Cambridge University Press, 2011.

[72] D. Maurin. *Propagation des rayons cosmiques dans un modèle de diffusion : une nouvelle estimation des paramètres de diffusion et du flux d'antiprotons secondaires.* PhD thesis, LAPTH, Annecy, France, 2002.

[73] D. Maurin, F. Donato, R. Taillet, and P. Salati. Cosmic Rays below Z=30 in a Diffusion Model : New Constraints on Propagation Parameters. *The Astrophysical Journal*, 555(2) :585, 2001.

[74] Miguel Pato, Dan Hooper, and Melanie Simet. Pinpointing Cosmic Ray Propagation With The AMS-02 Experiment. *JCAP*, 1006 :022, 2010.

[75] A. Oliva and al. Precision Measurement of the Cosmic Ray Boron-to-Carbon Ratio with AMS. 2013. Proceedings of the fifth International Cosmic Ray Conference (to be published).

[76] T. Delahaye et al. The GeV-TeV galactic gamma-ray diffuse emission. I. Uncertainties in the predictions of the hadronic component. *Astroparticle and Astrophysics*, 531, 2011.

[77] S. D. Hunter, D. L. Bertsch, et al. EGRET observations of the Diffuse Gamma-Ray Emission from the Galactic Plane. *The Astrophysical Journal*, 481(1) :205, 1997.

[78] M. Mori. The Galactic diffuse gamma-ray spectrum from cosmic ray proton interactions. *Astrophys.J.*, 478 :225–232, 1997.

[79] F.W. Stecker, S.D. Hunter, and D.A. Kniffen. The likely cause of the EGRET GeV anomaly and its implications. *Astroparticle Physics*, 29(1) :25 – 29, 2008.

[80] The Fermi-LAT Collaboration. Fermi-LAT Observations of the Diffuse Gamma-Ray Emission : Implications for Cosmic Rays and the Interstellar Medium. *ArXiv e-prints*, February 2012.

[81] C.-Y. Huang, S.-E. Park, M. Pohl, and C.D. Daniels. Gamma-rays produced in cosmic-ray interactions and the TeV-band spectrum of RX j1713.7-3946. *Astroparticle Physics*, 27(5) :429 – 439, 2007.

[82] Y. Shikaze, S. Haino, et al. Measurements of 0.2–20 GeV/n cosmic-ray proton and helium spectra from 1997 through 2002 with the BESS spectrometer. *Astroparticle Physics*, 28(1) :154 – 167, 2007.

[83] Tuneyoshi Kamae, Niklas Karlsson, Tsunefumi Mizuno, Toshinori Abe, and Tatsumi Koi. Parameterization of gamma, $e^{\pm}$, and Neutrino Spectra Produced by p-p Interaction in Astronomical Environments. *The Astrophysical Journal*, 647(1) :692, 2006.

[84] J. Lavalle. Impact of the spectral hardening of TeV cosmic rays on the prediction of the secondary positron flux. *Mon.Not.Roy.Astron.Soc.*, 414 :985L, 2011.

[85] M. Aguilar et al. The Alpha Magnetic Spectrometer (AMS) on the International Space Station. I : Results from the test flight on the space shuttle. *Phys.Rept.*, 366 :331–405, 2002.

[86] C. Adloff et al. The AMS02 lead-scintillating fibers Electromagnetic Calorimeter. *Nuclear Inst. and Methods in Physics Research, A*, 714 :147–154, 2013.

[87] J. Alpat et al. Charge determination of nuclei with the AMS-02 silicon tracker. *Nucl.Instrum.Meth.*, A540 :121–130, 2005.

[88] G. Ambrosi and al. AMS-02 Track Reconstruction and Rigidity Measurement. 2013. Proceedings of the 33rd International Cosmic Ray Conference (to be published).

[89] R. Battiston and A. Oliva. AMS-02 Web Page.

[90] The AMS Collaboration. AMS on ISS : Construction of a Particle Physics Detector on the International Space Station. Technical Design Report (unpublished).

[91] V. Bindi et al. Calibration and performance of the AMS-02 time of flight detector in space. *Nuclear Instruments and Methods in Physics Research Section A : Accelerators, Spectrometers, Detectors and Associated Equipment*, 743(0) :22 – 29, 2014.

[92] Melanie Heil. *Measurement of the positron fraction in cosmic rays from 0.5 - 350 GeV with the AMS-02 detector on the International Space Station.* Dr., KIT, 2013. KIT, Diss., 2013.

[93] M. Aguilar-Benitez and al. In-beam aerogel light yield characterization for the AMS RICH detector. *Nuclear Instruments and Methods in Physics Research Section A : Accelerators, Spectrometers, Detectors and Associated Equipment*, 614(2) :237 – 249, 2010.

[94] M. Vecchi. The electromagnetic calorimeter of the AMS-02 experiment. *Instrumentation and Detectors*, 2012. Proceedings of SF2A conference 2012.

[95] C. Lin. Trigger Logic Design Specifications. Internal Note, 2005.

[96] M. Duranti. *Measurement of the Atmospheric Muon Flux on Ground with the AMS-02 Detector.* PhD thesis, Universita degli Studi di Perugia, Italie, 2011.

[97] R. Brun and al. Root web page : http ://root.cern.ch/, 2001.

[98] P. Azzarello. *Tests And Production Of The AMS-02 Silicon Tracker Detectors.* PhD thesis, Université de Genève, Genève, Suisse, 2005.

[99] B. Alpat et al. High precision tracking and charge selection with silicon strip detectors for relativistic ions. *Nucl.Instrum.Meth.*, A446 :522–535, 2000.

[100] J. Alcaraz et al. The alpha magnetic spectrometer silicon tracker : Performance results with protons and helium nuclei. *Nucl.Instrum.Meth.*, A593 :376–398, 2008.

[101] E. Nygard et al. CMOS low noise amplifier for microstrip readout Design and results. *Nucl.Instrum.Meth.*, A301 :506, 1991.

[102] A. Oliva. *High Charge Cosmic Rays Measurement with the AMS-02 Silicon Tracker.* PhD thesis, Universita degli studi di Perugia, Perugia, Italy, 2006.

[103] G. Ambrosi and al. In-flight operations and efficiency of the AMS-02 silicon tracker. 2013. Proceedings of the 33rd International Cosmic Ray Conference (to be published).

[104] G. Ambrosi and al. Alignement of the AMS-02 Silicon Tracker. 2013. Proceedings of the 33rd International Cosmic Ray Conference (to be published).

[105] G. Ambrosi and al. Identification of Light Cosmic-Ray Nuclei with AMS-02. 2013. Proceedings of the 33rd International Cosmic Ray Conference (to be published).

[106] H. Bichsel. A method to improve tracking and particle identification in TPCs and silicon detectors. *Nuclear Instruments and Methods in Physics Research Section A : Accelerators, Spectrometers, Detectors and Associated Equipment*, 562(1) :154 – 197, 2006.

[107] S. Agostinelli and al. Geant4 — a simulation toolkit. *Nuclear Instruments and Methods in Physics Research Section A : Accelerators, Spectrometers, Detectors and Associated Equipment*, 506(3) :250 – 303, 2003.

[108] D. Maurin, F. Melot, and R. Taillet. A database of charged cosmic rays. *ArXiv e-prints*, 2013.

Appendices

Annexe A

VA Equalization DataBase

All the information relative to the VA equalization procedure is stored by means of text files in a dedicated data base. Each file (one for N-side VAs and one for P-side VAs), contains a table with the following parameters. The first column gives the ladder identification in TkID format. The second column is the VA identification number (0 to 9 for p-side Vas, 10 to 15 for N-side VAs). Five bits of information are then used for the VA classification. If all bits are set to 0, than the VA is of golden type. If either bit 1 or 2 are set, then the VA is either dead or of very bad quality and must be excluded from any analysis. Bit 3 indicates a VA of lower quality while bit 4 indicates a VA with low gain. The last bit used to indicate that the equalization factor was extracted based on a restricted number of points (usually due to low statistics). The categories are of course not exclusive since a lower quality VA is usually associated with a lower gain value or with low statistics. The following two parameters are the gain and offset value to correct the VA response. Finally, the last column gives the RMS measure of the fit quality (Section 5.4). Table A.1 gives a snapshot of the text file structure for VAs of the ladder with TkID +103.

TkID	VA	0	1	2	3	4	Gain	Offset	SysDev
103	0	0	0	0	0	0	0.87	2.24	9.877E-02
103	1	0	0	0	0	0	0.93	0.89	3.906E-02
103	2	0	0	0	0	0	0.91	1.12	5.044E-02
103	3	0	0	0	0	0	0.94	0.61	3.189E-02
103	4	0	0	0	0	0	0.96	0.32	2.004E-02
103	5	0	0	0	0	0	0.96	0.48	2.414E-02
103	6	0	0	0	0	0	0.96	0.67	3.229E-02
103	7	0	0	0	0	0	0.91	0.94	4.359E-02
103	8	0	0	0	0	0	0.87	1.46	6.329E-02
103	10	0	0	0	0	0	0.97	-0.35	8.585E-03
103	11	0	0	0	0	0	0.98	-0.73	2.624E-02
103	12	0	0	0	0	0	0.96	-0.56	2.241E-02
103	13	0	0	0	0	0	0.97	-0.31	9.638E-03
103	14	0	0	0	0	0	0.97	0.12	1.563E-02
103	15	0	0	0	0	0	0.96	-0.31	5.667E-03

TABLE A.1 – Gain parameter database for VAs of ladder +103.

Annexe B

ToF Beta Reconstruction Efficiency

Figure B.1 shows the ToF beta reconstruction efficiency for all nuclei from lithium to silicon. Although the efficiency behavior is flat within 2% for almost all charges, significant structures appear for sodium ($Z = 11$) and aluminium ($Z = 13$). We suspect such dependences are due to contaminations in the initial samples. Given the degrading tracker resolution around silicon ($Z = 14$) and the lower abundance of the odd Z species, it is in fact very hard since it is very hard to select pure samples for these nuclei with sufficient statistics. Therefore, the final efficiency value for these nuclei is interpolated using the results for neighboring nuclei and assuming the ToF beta reconstruction efficiency is flat with Z (see Figure 6.7). In Figure B.2, we however propose individual parameterizations of all nuclei.

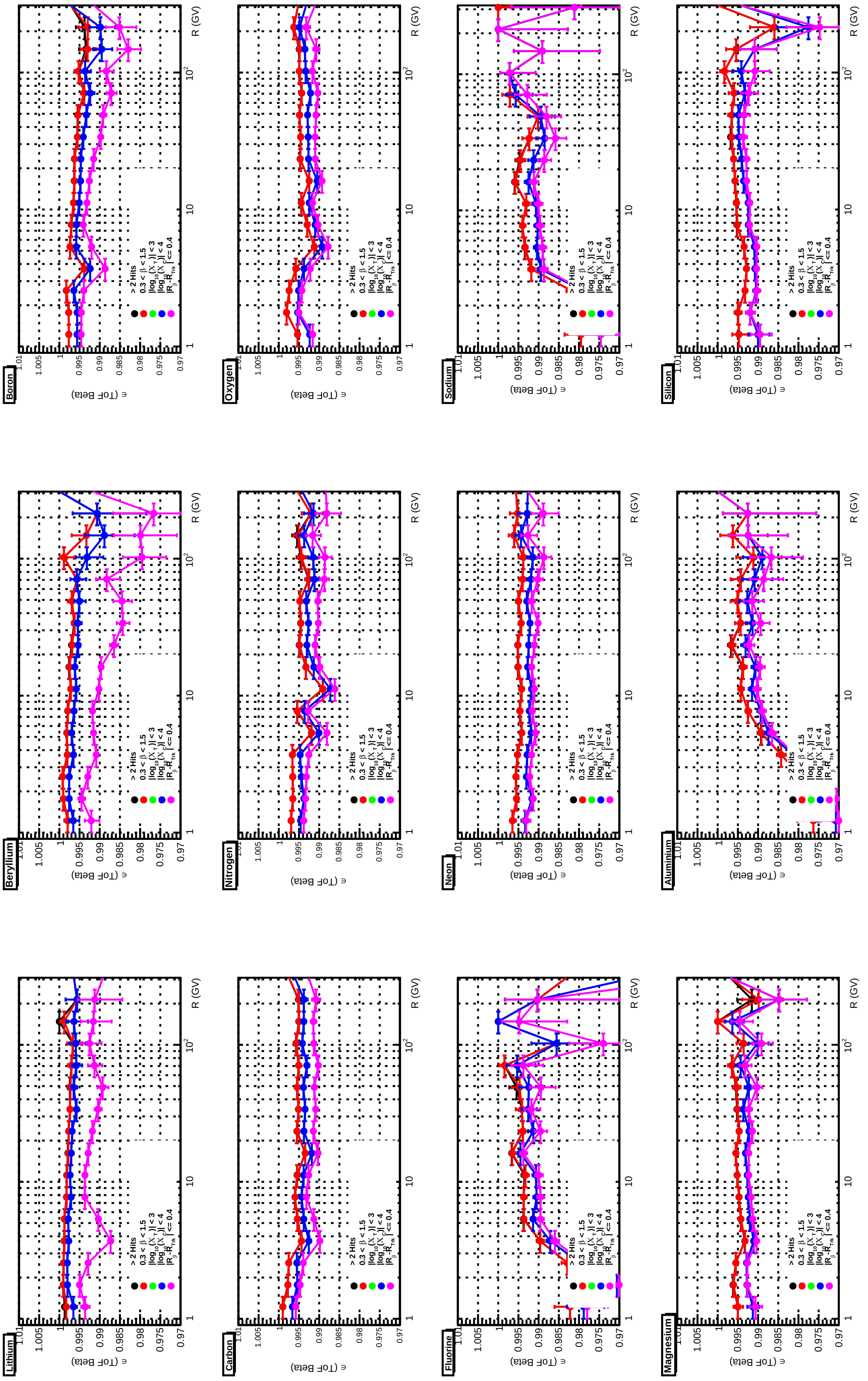

FIGURE B.1 – Cut breakdown of the ToF beta reconstruction efficiency all nuclei from lithium ($Z = 3$) to silicon ($Z = 14$).

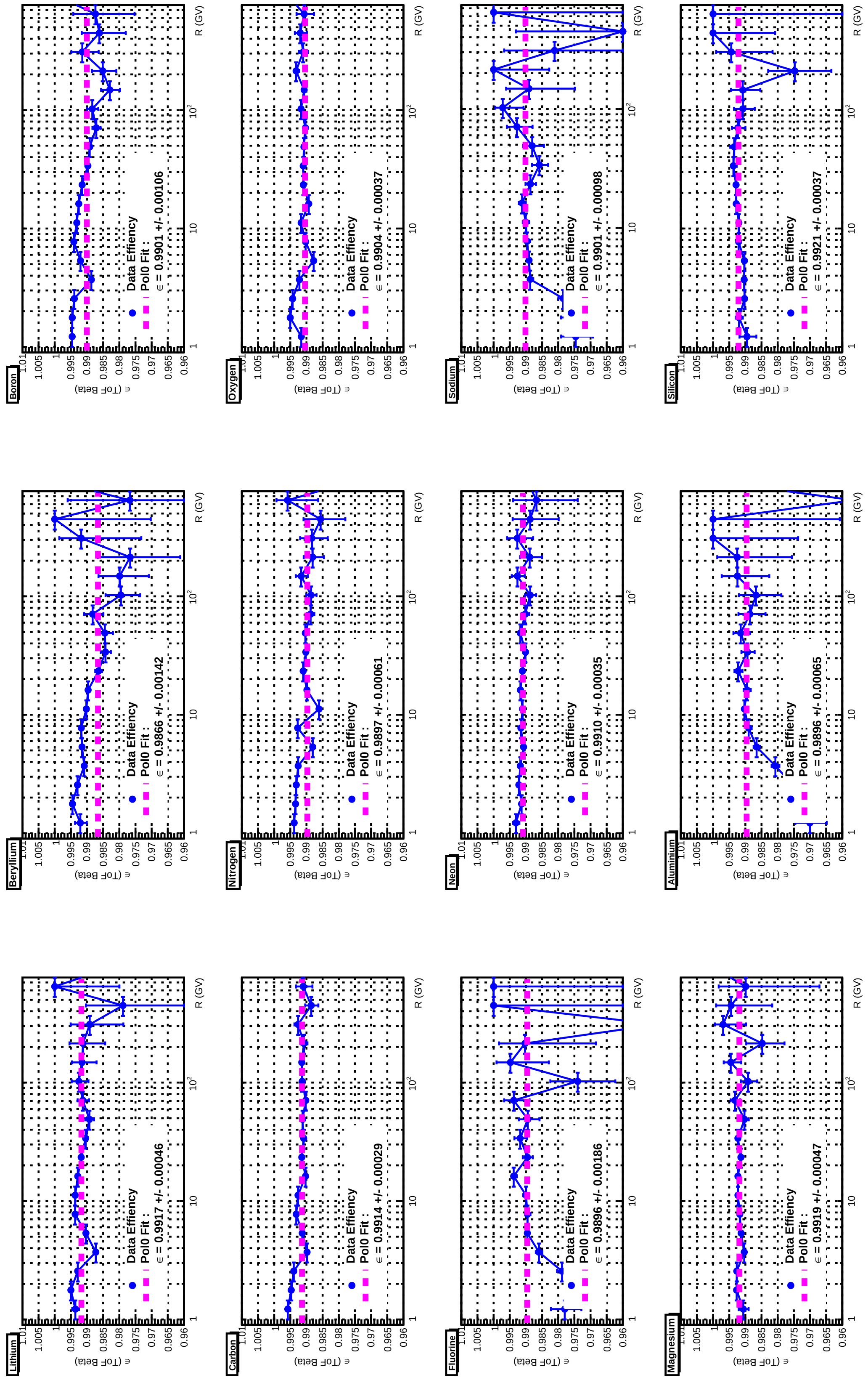

FIGURE B.2 – Constant parameterization of the ToF beta reconstruction efficiency for all nuclei from lithium ($Z = 3$) to silicon ($Z = 14$).

Annexe C

Track Reconstruction Efficiency

Figure C.1 shows the cut breakdown for the inner tracker reconstruction efficiency for all nuclei from lithium ($Z = 3$) to silicon ($Z = 14$). The behavior of the efficiency curve under the successive cuts is very similar, the last cut indicating a slight decrease of the efficiency with rigidity. One can also notice the efficiency decreases with increasing nuclear charge. The effect is however small since the average difference between the efficiency for lithium and silicon is at maximum 2% for energies between 1 and 10 GV. Figure C.2 shows the proposed linear parameterization (dashed magenta line) of the final efficiency (blue points) for all nuclei. When available, the Monte Carlo efficiencies are also plotted (black points). One can see the extrapolations of the fits are in reasonable agreement with the predictions of the MC. For beryllium, there is no statistics in the MC sample between 1 GV and $\approx$ 160 GV. The good agreement between the parameterization and the small energy regions available is however comforting. We have also plotted the efficiency measured using the Ecal deposited energy as the rigidity estimator. The behavior of the latter is again in good agreement with the extrapolation of the fit results.

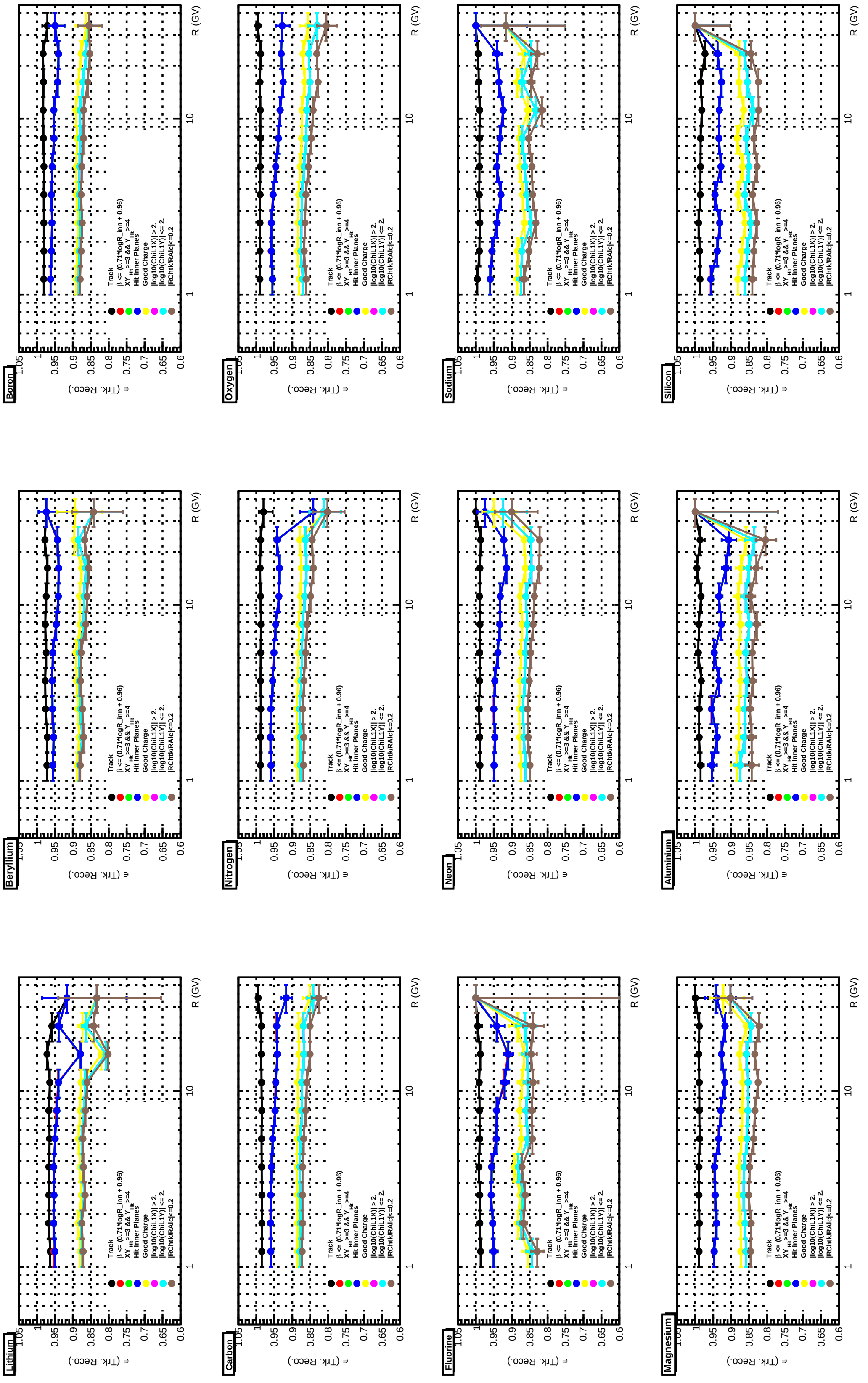

FIGURE C.1 – Inner Tracker reconstruction efficiency : cut breakdown. The rigidity is estimated through the geomagnetic cutoff rigidity.

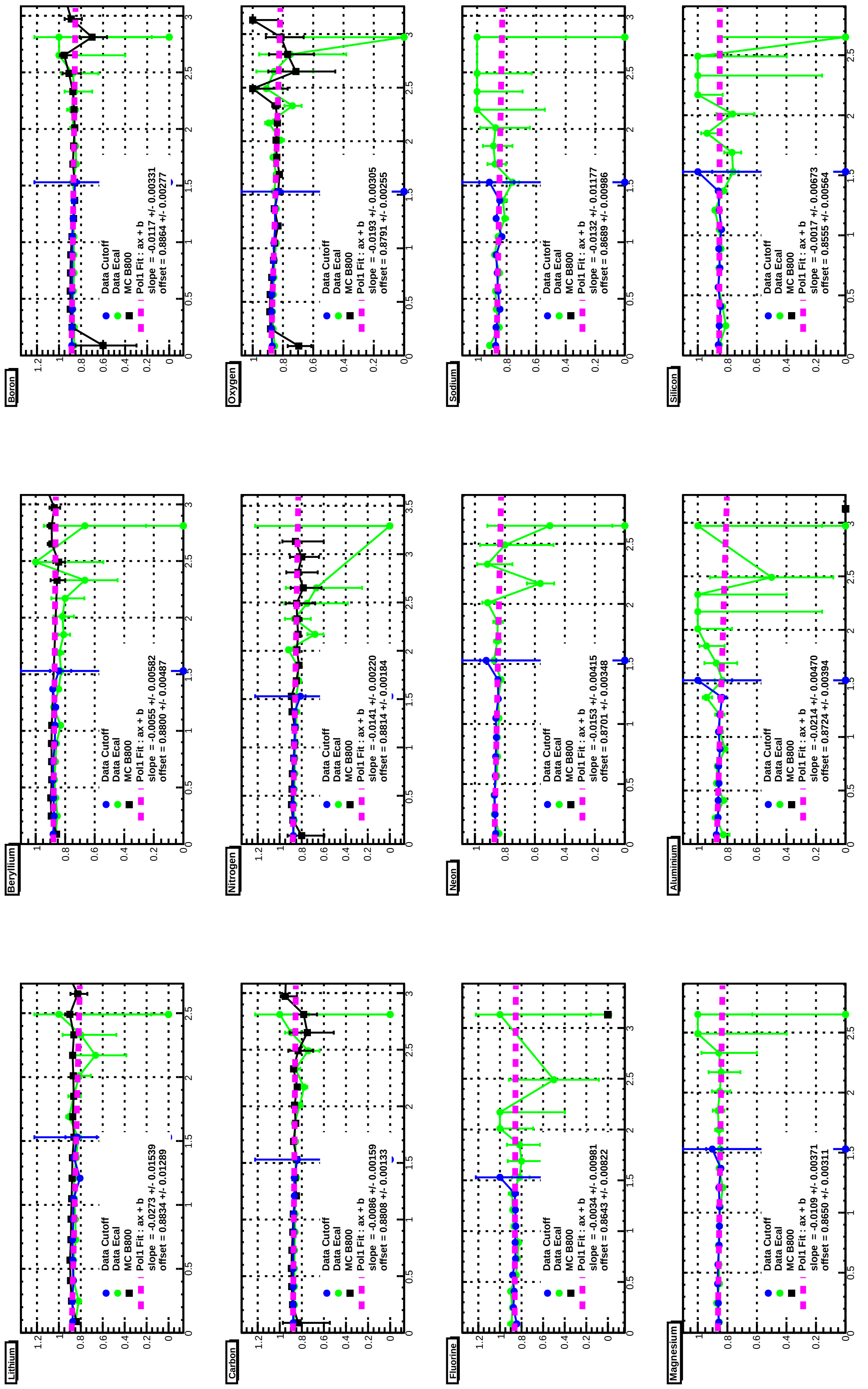

FIGURE C.2 – Straight line parameterizations of the inner tracker reconstruction efficiency. The black points are the Monte Carlo measured efficiencies, available only for a limited number of nuclei. The green points are the efficiencies measured in the data using the Ecal energy deposition as the rigidity estimator.

Annexe D

Layer 1 PickUp Efficiency

Figure D.1 shows the cut breakdown for the hit pick-up efficiency of the layer 1 for all nuclei from lithium ($Z = 3$) to silicon ($Z = 14$). The behavior of the efficiency curve under the successive cuts is very similar for the different nuclei. The last efficiency cut shows a significant increase of the efficiency with the rigidity for all nuclei. This can be explained by the fact the algorithms searching for hit associations in the external layers are helped by larger energy depositions. Figure D.2 shows the straight line parameterization applied to the final efficiency.

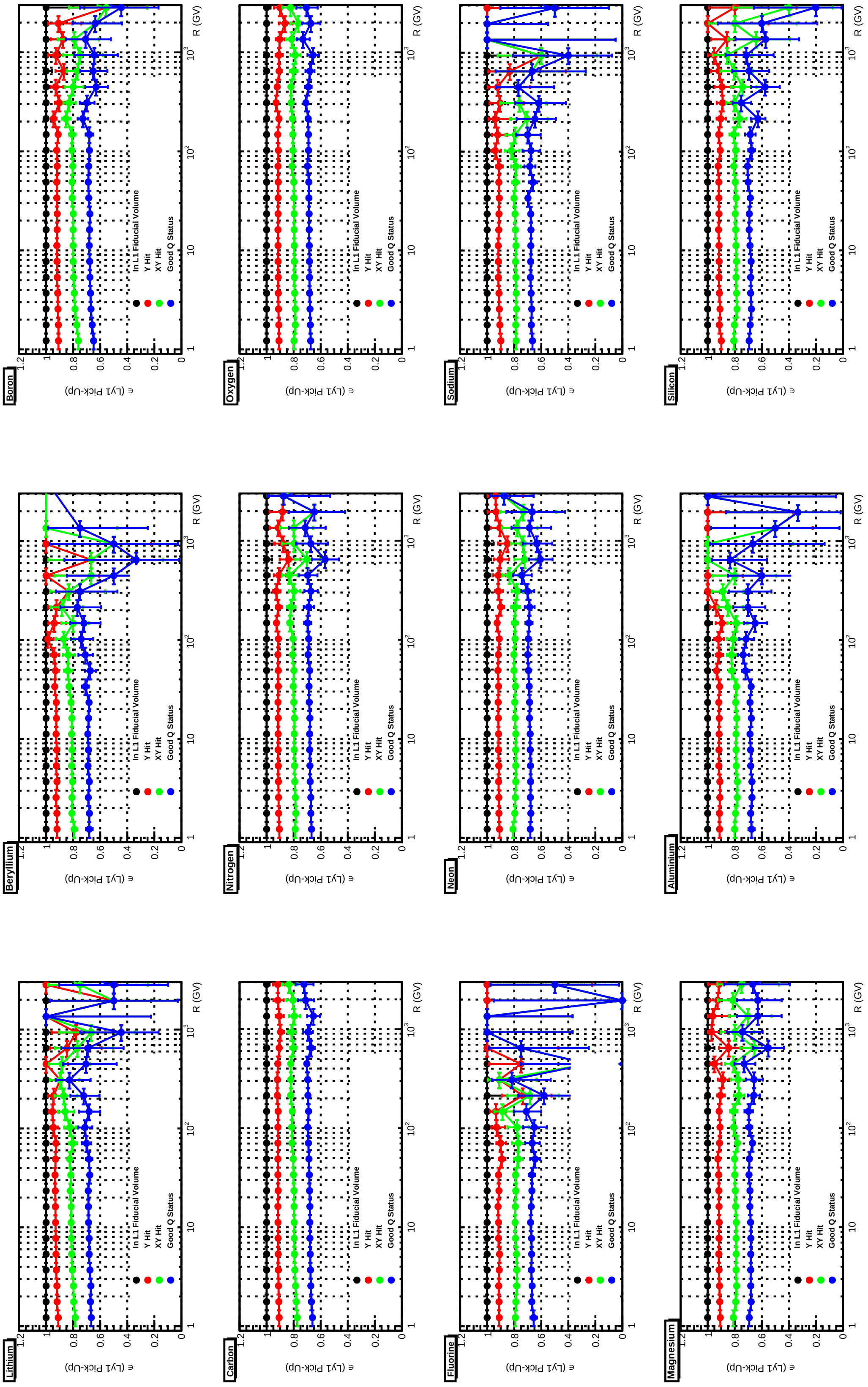

FIGURE D.1 – Cut breakdown of the layer 1 hit pick-up efficiency for all nuclei from lithium ($Z = 3$) to silicon ($Z = 14$).

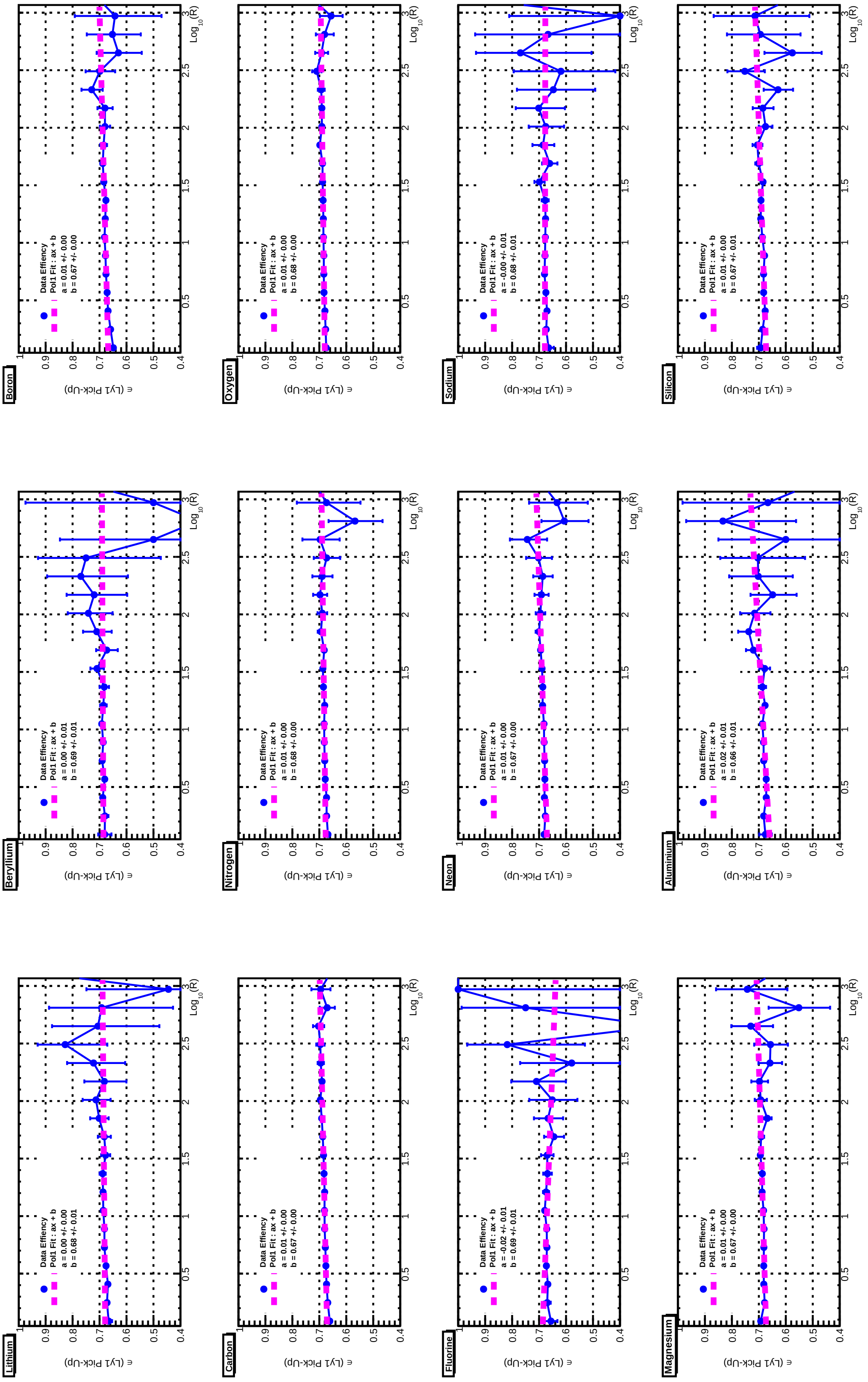

FIGURE D.2 – Straight line parameterization (dashed magenta line) of the layer 1 pick-up efficiency (blue points).

Annexe E

Trigger Efficiency

Figure E.1 shows the trigger efficiency measured in the data for two different tracker geometries. The blue points correspond to a compatibility requirement between the charge measured in the layer 1 and in the inner tracker while the magenta points add the same compatibility request on the layer 9, hence selecting very clean events that have undergone no fragmentation throughout the whole detector. It can be seen that the trigger efficiency for the layer 1 plus inner tracker geometry shows small structures that tend to appear at smaller energies with increasing nuclear charge, the scale of the effect also increasing with Z. One possible explanation is that the trigger efficiency is influenced by the restrictions imposed on the tracker event size to respect the downlink and buffering capabilities on the ISS, i.e. a restriction on the number of ACC counts to be < 5 (see Section 3.1.10). Since heavier nuclei interact more in the detector material, they are usually correlated with increasing ACC counts. The full span geometry does not see this effect because it tends to select cleaner events (no fragmentation throughout the whole detector). The effect is neither seen in the Monte Carlo.

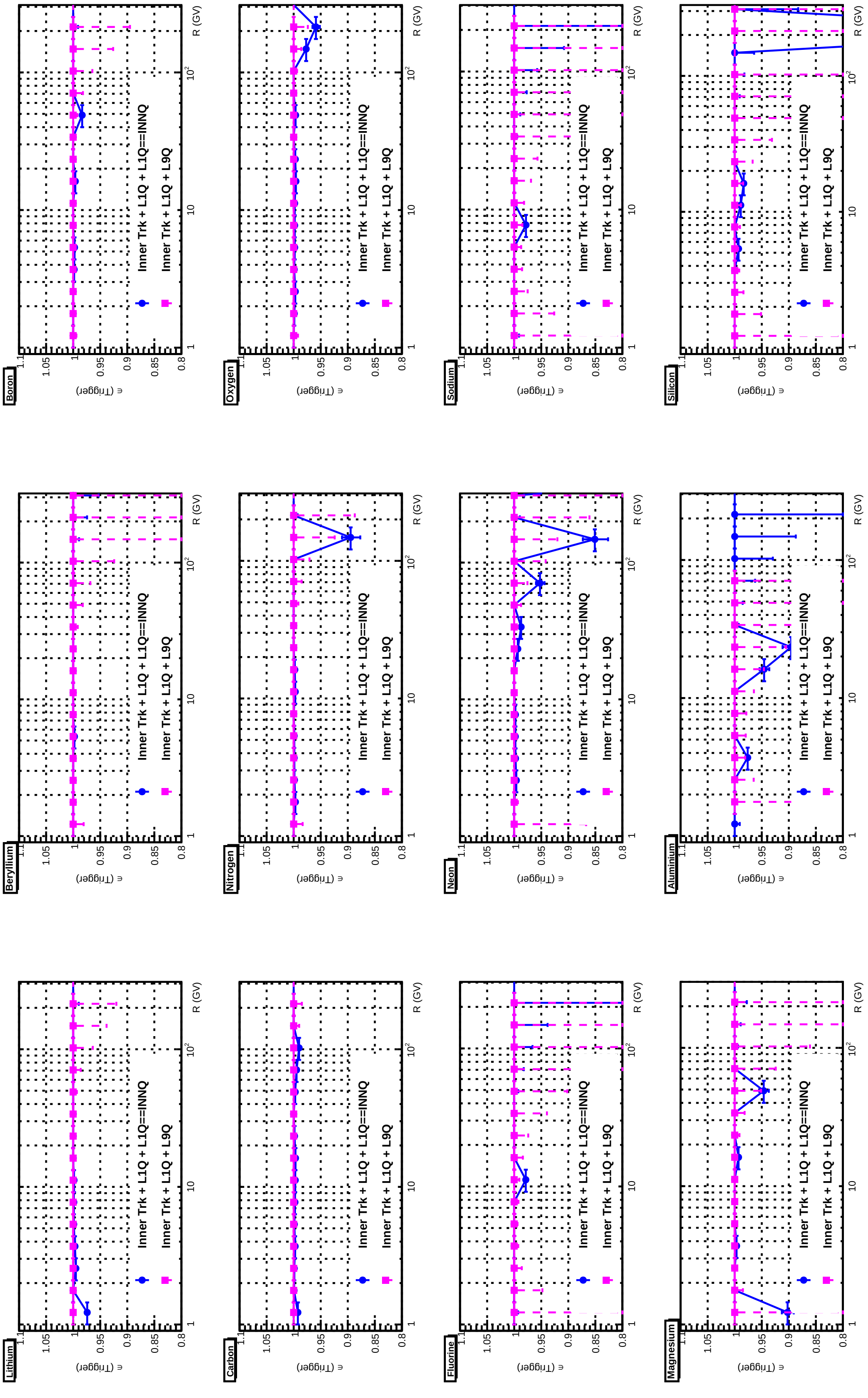

FIGURE E.1 – Trigger Efficiency for all nuclei from lithium ($Z = 3$) to silicon ($Z = 14$) for two different tracker geometries. See text for more information.